

Copyright
by
Jerome Anthony Bellian
2009

**The Dissertation Committee for Jerome Anthony Bellian Certifies that this
is the approved version of the following dissertation:**

**Laser-Mapping and 3D Reconstruction of the Lower Ordovician El Paso
Group Breccia Collapse Breccias, Franklin Mountains, Texas**

Committee:

Charles Kerans, Supervisor

Xavier Janson

David Mohrig

Robert Loucks

F. Jerry Lucia

Ron Steel

**Laser-Mapping and 3D Reconstruction of the Lower Ordovician El Paso
Group Breccia Collapse Breccias, Franklin Mountains, Texas**

by

Jerome Anthony Bellian, B.A.; M.S.

Dissertation

Presented to the Faculty of the Graduate School of
The University of Texas at Austin
in Partial Fulfillment
of the Requirements
for the Degree of

Doctor of Philosophy

**The University of Texas at Austin
August 2009**

Dedication

I dedicate this to my son Jacob Olaf Bellian.

Acknowledgements

I would like to thank Charlie Kerans, my great friend, mentor, and supervisor...in that order. Thank you for believing in me and supporting my research with your time, funding, and friendship. I would also like to thank the Reservoir Characterization Research Laboratory (RCRL) at the Bureau of Economic Geology, within the Jackson School of Geosciences. This project would not have been possible without financial support. The RCRL including but not limited to Jerry Lucia, Xavier Janson, Chris Zahm, Jim Jennings, Bob Loucks, and the wagon trail of staff and students who have helped along the way. I would also like to thank my committee members for their thoughtful and helpful comments and support for this study. I would also like to thank Dr. Scott Tinker, director of the Bureau of Economic Geology for encouragement to pursue my doctorate. Special thanks goes to Reuben Reyes from the Bureau of Economic Geology, for the countless hours of brainstorming, "chalk talk" accompanied with strange hand contortions and computer code and sharing chocolate. Thanks a million Reuben, you are the bomb!

Funding for the airborne lidar for this project was provided by the Dr. Charles Kerans faculty startup grant (Jackson School of Geosciences, Department of Geological Sciences) and the Reservoir Characterization Research Laboratory (RCRL) industrial associates consortium at The University of Texas at Austin, Jackson School of Geosciences Bureau of Economic Geology (<http://www.beg.utexas.edu/indassoc/rcrl/index.htm>). Funding for the Devil's Sinkhole lidar scanning portion of this research came from: TPWD, Bureau of Economic Geology, the National Speleological Society, Texas Cave Management Association, The National Cave and Karst Research Institute, Bat Conservation International, The Devil's Sinkhole Society, PMI, Daniel Holeman Photography, Kevin McGowan Photography, George Veni and Associates and private contributions from Will Howie, Don Auburn, and Jerry Atkinson. Access to the Devil's Sinkhole is restricted by season due to biological conservation.

The only way in or out of the sink is by rope, requiring a 45 m vertical repel into and a 45 m vertical climb out. Thanks to the coordination of the survey expeditions was conducted with the

guidance of Randy Rosales of the TPWD and Geary Schindel of the Texas Cave Management Association everyone had a safe trip down and up!

I would also like to thank Dr. John Repetski from the U.S.G.S office in Reston, VA for his assistance in the conodont identification, thoughtful comments and critical review of Chapter 1; Dr. Stephen Leslie, James Madison University, kindly assisted in processing conodont samples while the USGS labs were closed for renovation. Dr. Richard Beck for assistance and technical direction with the hyperspectral analysis and Dr. Ted E. Playton for his valuable assistance in bleeding all over my rocks in the field and many fruitful discussions on the breccia systems described in this work. The Texas Parks and Wildlife Department staff at Wyler Aerial Tramway and Franklin Mountain State Park for always being supportive and smiling, moreover for always being a phone call away and watching my back; thank you Beto, Nancy, Gilbert, Estaban, and Adrian. Chapter 3 field work assistants were Dr. Chris "Fred Flintstone" Zahm and Joseph "Tiny" El Azzi.

Commercial software packages used for data analysis include Polyworks (InnovMetrics, Toronto, Canada), Rockware (Denver, Colorado), Gocad (Paradigm B.V. Amsterdam, The Netherlands), Landmark (Halliburton, Houston, Texas), Expert GPS (Stow, Massachusetts) , and Google Earth.

I'd especially like to thank my number one hero, my father Joseph G. Bellian, my late mother Joan Carol Bellian and my fantastic family for giving me the tools to become the man I am today and the support and encouragement to pursue my PhD. Also, my amazing extended family, sadly, now-former neighbors in the Austin, Texas; may we keep our friendship through the coming years. Viva la Captains of the Chess Team!

MOST importantly I'd like to thank my beautiful, wonderful, brilliant wife Dr. Mary M. Guisinger for inspiring and supporting me get through this while being an amazing mother to our child(ren!), best friend, life partner, respected scientist AND simultaneously working on her own PhD in integrative biology and beating me in the doctorate race by three days. You are the reason I push harder every day, you are my lobster, I love you more than everything. Although it isn't much for everything you do and have done, you get your very own page.

**Laser-Mapping and 3D Reconstruction of the Lower Ordovician El Paso
Group Breccia Collapse Breccias, Franklin Mountains, Texas**

Publication No. _____

Jerome Anthony Bellian, Ph.D.
The University of Texas at Austin, 2009

Supervisor: Charles Kerans

Abstract:

The Lower Ordovician El Paso Group is a >400-m-thick carbonate succession exposed in the Franklin Mountains, El Paso, Texas. The El Paso Group contains multiple breccias related to collapsed-paleocave systems. These breccias have been documented as having formed during the top-Lower Ordovician Sauk depositional supersequence lowstand. Evidence presented in this study suggests that cave formation may have been as much as 350 millions years younger and related to Laramide oblique right lateral compression. Regardless of the timing of formation, the breccias mapped in this study are of collapsed paleocave origin based on breccia clast organization and matrix content.

Speleogenetic models are compared against observations of breccia distribution by direct field observations and mapping on sub-meter airborne light detection and ranging or lidar data. Point vectors were defined for every point within study area to highlight subtle changes in outcrop erosional profile for mapping geological features directly on

the lidar point cloud. In addition, spectral data from airborne photography and hyperspectral image analysis were used assist in geological contact definition.

A digital outcrop model was constructed from 3D geologic mapping results from which spatial statistic were extracted and used to reconstruct collapsed paleocave breccia bodies. The resultant breccia geometries were compared against laser-scanned modern cave dimensions, from Devil's Sinkhole, Rocksprings, Texas, and used in analysis of conceptual models for cave formation.

The breccias of the southern Franklin Mountains follow linear trends that closely match Riedel shear fracture patterns predicted from right-lateral oblique compression. Stress orientations that match right-lateral oblique compression in the Phanerozoic of the El Paso region are related to the Laramide orogeny. The relationship of observed structures and the orientation of collapse breccias may indicate that southern Franklin Mountain breccia bodies are the result of a solution-enhanced tectonic karst system.

Table of Contents

List of Tables	xiii
List of Figures	xiv
List of Illustrations	xviii
Introduction	1
Chapter 1 The Great American Carbonate Bank, Southern Franklin Mountains, El Paso, Texas	5
Abstract	5
1.1 Introduction	6
1.2 General Paleoclimate Setting of the Ordovician	9
1.3 General Stratigraphic of the El Paso Region	12
1.4 Facies Associations	16
1.5 Lower Paleozoic Lithostratigraphy of the Southern Franklin Mountains	19
1.6 Sequence Stratigraphy	39
1.7 EP 1 Third-Order Sequence	39
1.8 EP 2 Third-Order Sequence	42
1.9 EP 3 Third-Order Sequence	42
1.10 EP 4 Third-Order Sequence	43
1.11 Montoya and Fusselman Sequences	44
1.12 Breccias of the El Paso Group	45
1.13 Spatial Distribution of Breccia Types	47
1.14 Micropaleontology of the Breccia Systems	57
1.15 Discussion	60
1.16 Conclusions	64
Chapter 2 Paleocave Mapping and Reconstruction with Hyperspectral, Airborne, and Ground-based Lidar Data; Franklin Mountains, El Paso, Texas	67
Abstract	67
2.1 Introduction	69
2.2 El Paso Region Geologic Overview	71
2.3 Models for Timing of Cave Formation	75
2.4 Methods and Data	76

2.4.1 Field methods and paleontology	77
2.4.2 Airborne lidar data acquisition	78
2.4.3 Lidar data processing	81
2.4.4 DOM construction and modeling.....	85
2.4.5 Breccia extrapolation and simulation	87
2.4.6 Ground-based lidar of a modern cave	88
2.6 Discussion.....	97
2.7 Conclusions	99
Chapter 3 Origin of Breccia Bodies within the Southern Franklin Mountains Fault Block, El Paso, Texas	101
Abstract.....	101
3.1 Introduction	102
3.2 Geologic Background	106
3.2.1 Stratigraphy.....	106
3.2.2 Diagenetic overview	110
3.2.3 Breccias	111
3.2.4 Structural history and critical elements	115
3.3 Models for Breccia Origin	118
3.3.1 Fault breccia/gouge model.....	119
3.3.2 Second-order depositional sequence meteoric karst model.....	121
3.3.3 Third order composite cave model.....	123
3.3.4 Solution-enhanced Tectonic Karst	124
3.4 Methods	125
3.5 Observations.....	133
3.5.1 Main boundary faults.....	133
3.5.2 Breccia locations and geometries	134
3.5.3 Fracture plane orientation and breccia geometry	136
3.6 Discussion.....	142
3.6.1 Fault breccia/gouge model.....	142
3.6.2 Second-order depositional sequence meteoric karst model.....	142
3.6.3 Third-order composite cave model	146
3.6.4 Solution-enhanced tectonic karst.....	148
3.6.5 Analogous solution-enhanced tectonic karst model	152
3.7 Conclusions	154

Appendix A Franklin Mountain LIDAR Project Metadata	155
Appendix B DOM results for 3 interpolations and 9 simulations	159
Appendix C El Paso Group Conodont Samples.....	172
Appendix D Palynology Report.....	194
References	198
Vita	210
Plate printer requirements	211
Plates.....	end of document

List of Tables

Table 1.1:	Conodont sample locations	59
Table 2.1:	Devil's Sinkhole cave volume	95
Table 2.2:	Devil's Sinkhole ellipticity	96
Table 2.3:	Breccia body diameters	97
Table 3.1	Rotation of fault planes compared to breccia geometry	135
Table 3.2	Breccia area and width measurements	140
Table 3.3	Tabular breccia dimensions	141

List of Figures

Figure 1.1:	Location map of study area	8
Figure 1.2:	Paleogeography of Laurentia.....	10
Figure 1.3:	Ordovician through Silurian stratigraphy	11
Figure 1.4:	Facies Associations	18
Figure 1.5:	Bowen Formation facies photograph	20
Figure 1.6:	Hag Hill Formation facies photographs	22
Figure 1.7:	Chamizal Formation facies photograph	24
Figure 1.8:	McKelligon Canyon Formation facies photograph.....	25
Figure 1.9:	Cindy Formation facies photograph.....	27
Figure 1.10:	Ranger Peak Formation facies photograph	28
Figure 1.11:	Montoya Formation facies photograph	29
Figure 1.12:	El Paso-Montoya Group unconformity.....	31
Figure 1.13:	Cable Canyon Sandstone infilling Ranger Peak grike.....	32
Figure 1.14:	Dolomitized Ranger Peak-Upham Formation contact	34
Figure 1.15:	Aleman Formation facies photograph.....	35
Figure 1.16:	Cutter Formation field photos	36
Figure 1.17:	Fusselman Formation facies photographs	38
Figure 1.18:	Base of EP 1 sequence, base of Bliss Sandstone	41
Figure 1.19:	Airborne lidar of southern Franklin Mountains	48
Figure 1.20:	Breccia locations of east face of southern Franklin Mountains	50
Figure 1.21:	Lechuguilla Breccia vertical stacking	51
Figure 1.22:	Quarry Breccia upper and lower breccia stacking	52
Figure 1.23:	Contact of Lechuguilla Breccia with McKelligon Canyon Formation	55
Figure 1.24:	Ceiling beam thickness calculation diagram	55

Figure 1.25	Breccia <i>pipe</i> clasts from Cindy Canyon	59
Figure 2.1:	Location map of study area	72
Figure 2.2	El Paso through Fusselman stratigraphy.....	74
Figure 2.3:	Airborne lidar flight plan	80
Figure 2.4:	Lidar points, vectors, and colors	84
Figure 2.5:	Geocellular model of SFM	90
Figure 2.6:	Fault offset of stratigraphic grid	91
Figure 2.7:	Devil's Sinkhole location	92
Figure 2.8:	Lidar data of Devil's Sinkhole and "Devil's Cave"	93
Figure 2.9:	Devil's Cave overlain on Lechuguilla Breccia	96
Figure 2.10:	Extrapolation of Lechuguilla Breccia in 3D	97
Figure 3.1:	Location map of study area	104
Figure 3.2:	El Paso through Fusselman stratigraphy.....	105
Figure 3.3:	Paleogeography of the Early Ordovician	108
Figure 3.4:	Geohistory diagram of El Paso Region for the Phanerozoic	109
Figure 3.5:	Breccias of the east face of the SFM.....	114
Figure 3.6:	Cave formation models.....	117
Figure 3.7:	Breccia geometry ternary diagram.....	120
Figure 3.8:	Second-order supersequence exposure paleocave evolution	122
Figure 3.9:	Fault-plane projection technique.....	129
Figure 3.10:	Fault-scarp tracing	130
Figure 3.11:	Fault-plane projection	131
Figure 3.12:	Rotation of fault planes an breccias.....	132
Figure 3.13:	Breccia body rotation	140
Figure 3.14:	Rose diagram of fractures and faults.....	141

Figure 3.15:	Block diagram of Laramide oblique compression.....	150
Figure 3.16:	Dent fault model.....	151
Figure B.1:	Appendix B model results	160
Figure B.2:	Appendix B model results	161
Figure B.3	Appendix B model results	162
Figure B.4	Appendix B model results	163
Figure B.5	Appendix B model results	164
Figure B.6	Appendix B model results	165
Figure B.7	Appendix B model results	166
Figure B.8	Appendix B model results	167
Figure B.9	Appendix B model results	168
Figure B.10	Appendix B model results	160
Figure B.11	Appendix B model results	170
Figure B.12	Appendix B model results	171
Figure C.1	Appendix C conodont sample location map	173
Figure C.2	Appendix C conodont sample 2368 field photo	174
Figure C.3	Appendix C conodont sample 2368 photomicrographs.....	175
Figure C.4	Appendix C conodont sample 2369 polarized light and CL.....	176
Figure C.5	Appendix C conodont sample 2369 field photo	177
Figure C.6	Appendix C conodont sample 2369 photomicrograph	178
Figure C.7	Appendix C conodont sample 2372 field photo	179
Figure C.8	Appendix C conodont sample 2372 photomicrograph	180
Figure C.9	Appendix C conodont sample 2372 field photo	181
Figure C.10	Appendix C conodont sample 2373 photomicrograph	182
Figure C.11	Appendix C conodont sample 2395 field photo	183

Figure C.12	Appendix C conodont sample 2395 photomicrograph	184
Figure C.13	Appendix C conodont sample 2405 field photo	185
Figure C.14	Appendix C conodont sample 2405 photomicrograph	186
Figure C.15	Appendix C conodont sample 2412 field photo	187
Figure C.16	Appendix C conodont sample 2412 photomicrograph	188
Figure C.17	Appendix C conodont sample 2428 field photo	189
Figure C.18	Appendix C conodont sample 2429 field photo	190
Figure C.19	Appendix C conodont sample 2435 field photo	191
Figure C.20	Appendix C conodont sample 2447 field photo	192
Figure C.21	Appendix C conodont sample 2472 field photo	193

List of Illustrations

Plate I Correlation Chart for Lower Paleozoic	end of document
Plate II Geological Map of El Paso Region	end of document
Plate III Representative Stratigraphic Section of Study Area	end of document
Plate IV Oblique Air Photograph of east face of study are	end of document

NOTE: Plates require large-format printer (at least 36 inches wide) to properly print.

Introduction

Mapping modern caves is a complex task. Extrapolating ancient cave system geometries and their potential origin from outcrop remnants of those systems that have collapsed is much more complicated. This study focused on applying new technology such as laser scanning and spectral imaging to better constrain the geometry, spacing, and indirectly, the timing of paleocave formation within the Lower Ordovician collapsed paleocave breccias in the southern Franklin Mountains. The mapping and modeling for this study were carried out on a 3D digital base map referred to as a digital outcrop model, or DOM (Bellian et al. 2005) generated from airborne lidar (light detection and ranging), aerial photography, and hyperspectral imagery. A 3D geostatistical reconstruction of paleocave geometry and spacing was conducted using geocellular modeling techniques similar to those used in subsurface hydrocarbon reservoir modeling.

The Lower Ordovician El Paso Group carbonates formed the southwestern margin of what R. N. Ginsburg (1982) called the "Great American Bank." The Great American Carbonate Bank extends from southwestern Texas and eastern New Mexico all the way to Newfoundland and is more appropriately a carbonate platform that rimmed Laurentia, which was more than half submerged during the Early Ordovician (plate I). The sediments of the Lower Ordovician were deposited in shallow tropical seas reaching thicknesses of well over 450 m within the study area in El Paso, Texas.

Various conceptual models to explain the timing and formation of the original caves that made up the southern Franklin Mountain paleocave system were evaluated against each other and then compared to a modern cave of comparable dimension to aid in pre-collapse reconstruction. The modern cave was scanned with ground-based lidar and then theoretically compacted to estimate a post-collapse paleocave breccia volume. These dimensions could then be directly compared with the collapsed paleocave outcrop dimensions to better understand the scale and possible orientation of the paleocave system. Finally, an updated geological map of the

southern Franklin Mountains area was created that incorporates the paleocave breccia bodies, formation-scale stratigraphy, and previously unidentified faults.

Within the thick succession of marine carbonates of the El Paso Group several breccia bodies have been identified and interpreted to have formed as a result of caves that have collapsed (Lucia 1995). Additional breccia bodies to those mapped by Lucia (1995) have been documented of the westward dipping monocline that makes up the southern Franklin Mountains. This study agrees with the previous interpretation (Lucia 1995) that the breccias are of collapsed cave origin, but questions still remain as to the timing of emplacement of these breccia bodies. Integration of Tertiary structural data with breccia body geometry discussed in chapter three calls into question the timing of dissolution and collapse. This system may have been a product of uplift and dissolution during Laramide compression. Alternatively, as proposed by Lucia (1971), these caves may be part of a top-Sauk, late Lower to Middle Ordovician karst system.

This study is organized into three publications submitted as stand-alone papers. Chapter one is in review (Bellian et al. *in review*) by the Society for Sedimentary Geology (SEPM) Wilson Memorial Special Publication on the Great American Carbonate Bank. A version of this manuscript is presented here as an overview and update of the sequence stratigraphy and biostratigraphy of the El Paso Group, an outcrop equivalent of the productive Ellenburger Group hydrocarbon subsurface reservoir. The Ellenburger of Texas has long been recognized as containing significant amounts of breccia similar to those observed in the Franklin Mountains (Loucks 1999; Lucia 1995; 1968; Loucks and Anderson 1994; Kerans and Lucia 1989, Kerans, 1989; 1988). Chapter one describes the third-order depositional sequences mapped in the southern Franklin Mountains and places the breccias within this context. In addition, chapter one discusses conodont biozones from material recovered from within the breccia matrices and offers a fold-out summary chart (plate I) detailing sedimentation controls and contributors of the Cambrian, Ordovician, and Silurian. A revised geological map is presented in this chapter (plate II) that accurately locates breccia bodies within the stratigraphy. Chapter one is intended to

provide the reader with sufficient background information to set the stage for chapters two and three.

Chapter two builds upon a previously published paper in the Geological Society of America's digital publication *Geosphere* (Bellian et al. 2007). This chapter incorporates a high-resolution airborne lidar data set that was used to build a stratigraphic, digital outcrop model, or DOM (*cf.* Bellian et al. 2005), including delineation of paleocave-related breccias and a 3-D simulation of breccia bodies. This chapter also discusses the process of populating the DOM with geologically meaningful, quantitative observations and preliminary testing of model validity by integrating dimensional data from a modern sinkhole. The Devil's Sinkhole near Rocksprings, Texas, was scanned and returned to its pre-sinkhole cave status to extract dimensional data for cave reconstruction. Devil's Sinkhole is the third deepest cave in Texas, and it has been recognized as one of the best examples of a vertical sinkhole in the United States (Palmer 2007). For this reason, the Devil's Sinkhole was chosen to use for comparison to the best exposed, vertically extensive collapsed paleocave breccias in the United States, those exposed in the southern Franklin Mountains.

Chapter three compares four models for breccia origin in the study area. These models are the currently accepted second-order supersequence model (Lucia 1995), a third order deposition sequence model that emphasized the *coalesced collapsed-paleocave hypothesis* (Loucks 1999), a fault gouge/breccia model based on fault damage zone cataclastic-type brecciation based on previous studies of "fault rocks" by Sibson (1977), and a new model that incorporates solution-enhanced tectonic karst similar to previous work along the Dent fault in northwestern England (Woodcock et al. 2008). These models are reviewed on the basis of field observations and lidar interpretation to evaluate which may be most appropriate for explaining the observed breccia patterns in the SFM.

An overarching result of this study is the development of quantitative approach to creating 3D outcrop analogue models to help understand complexity, subsurface, brecciated hydrocarbon reservoir architecture.

Chapter One:

The Great American Carbonate Bank, Southern Franklin Mountains, El Paso, Texas

Abstract:

This paper reviews and synthesizes lithostratigraphy, biostratigraphy, chronostratigraphy, breccia types, and paleokarst geometries of the southwestern part of the Great American Carbonate Bank in the southern Franklin Mountains, El Paso, Texas. Primary units of focus are the Lower Ordovician El Paso and Upper Ordovician Montoya Groups; however, Precambrian, Silurian, and Tertiary units are discussed briefly. Specific attention is paid to the impact of the top-Sauk second-order supersequence with a ~10-m.y. exposure event that separates Upper and Lower Ordovician carbonates and that has been previously documented as a significant karst horizon at the top Sauk supersequence boundary across much of North America.

New approaches in this work include integration of traditional field mapping with high-resolution airborne lidar (24 km²) and biostratigraphic data to construct a detailed geological map and stratigraphic correlation chart of the southern Franklin Mountains and accurately place karst-related collapsed breccia bodies within stratigraphic and geographic positions. Breccia bodies present within the El Paso Group are described within a sequence stratigraphic context, and breccia facies are related to paleocave collapse to better understand vertical and lateral distribution of the breccias that formed primarily within the limestone units of the El Paso Group. Results of this work suggest that the El Paso Group breccias may not be a suitable analogue for subsurface hydrocarbon brecciated reservoirs and mining districts, such as Ellenburger, Arbuckle Group, St. George, Knox, Beekmantown, and Prairie du Chien of North America.

1.1 Introduction:

The Franklin Mountain outcrops are amongst the most complete and best exposed vertical successions of Lower Paleozoic strata exposures in North America (Lucia *in press*). The Franklin Mountains in El Paso, Texas, form a westward-dipping fault block that is the result of Laramide through Paleogene Basin and Range/Rio Grande Rift tectonism (Lovejoy 1969) that exposes Precambrian through Devonian strata. The southern Franklin Mountains (SFM), the focus of this study, dip between 25° and 35° west-southwest with a regional strike of 340°. Several large fault blocks are bounded on the east and west by regional normal faults parallel to regional strike. Evidence of compressional, extensional, and shear tectonics have been documented by recent studies (Stacy et al. 1992; Fetzner 1992; Wu 2002; Carciumaru 2005; Scharman 2006; Carciumaru and Ortega 2008) and place the SFM within a transition zone between thick skinned deformation to the north and thin-skinned deformation to the south of the study area (figure 1.1) (Carciumaru and Ortega 2008).

The term *paleocave* is used in this work to describe a relic cave system that is no longer actively being modified significantly by ongoing karst processes. Breccias within the El Paso and Montoya Groups were first mapped by Lucia (1971) and interpreted as the product of a two-part meteoric karst system. The upper 60 m of the El Paso Group contains a laterally continuous collapsed paleocave system interpreted by Lucia (1971) to be part of a water-table-controlled aquifer setting. The second system comprises a laterally restricted cave system that ranges between 85 and 250 m wide in outcrop dimension following regional strike. These collapsed-paleocave breccias are very large (>100 m wide) from what has been predicted by ceiling-span stability of individual modern cave passages (*cf.* Loucks 1999). The question addressed in this study is therefore, are these breccias the product of a single large collapsed cave or multiple events?

To address this question, 1:2000 mapping of stratigraphic units and collapse breccias was conducted on high-resolution airborne lidar (light detection and ranging) data with 0.7 m point

spacing. Survey details are located in Appendix A. The study area includes a 24 km² area of Cambrian through Silurian shallow-marine strata (plate I). These data were used to create a digital base map that was used to combine new field observations with previously published biostratigraphy, lithostratigraphy, sequence stratigraphy, karst diagenesis, and basic structure of the El Paso Group. A geological map is presented (plate II) for the SFM at the formation level that includes locations of breccia bodies. Breccias mapped in this study are characterized by vertical stacking of internal paleocave fill and compared with those predicted by the coalesced-collapsed paleocave breccia hypothesis of Loucks (1999). Vertical facies successions within the host rock and breccia bodies are discussed within a sequence stratigraphic context, and provide a template from which future geological research.

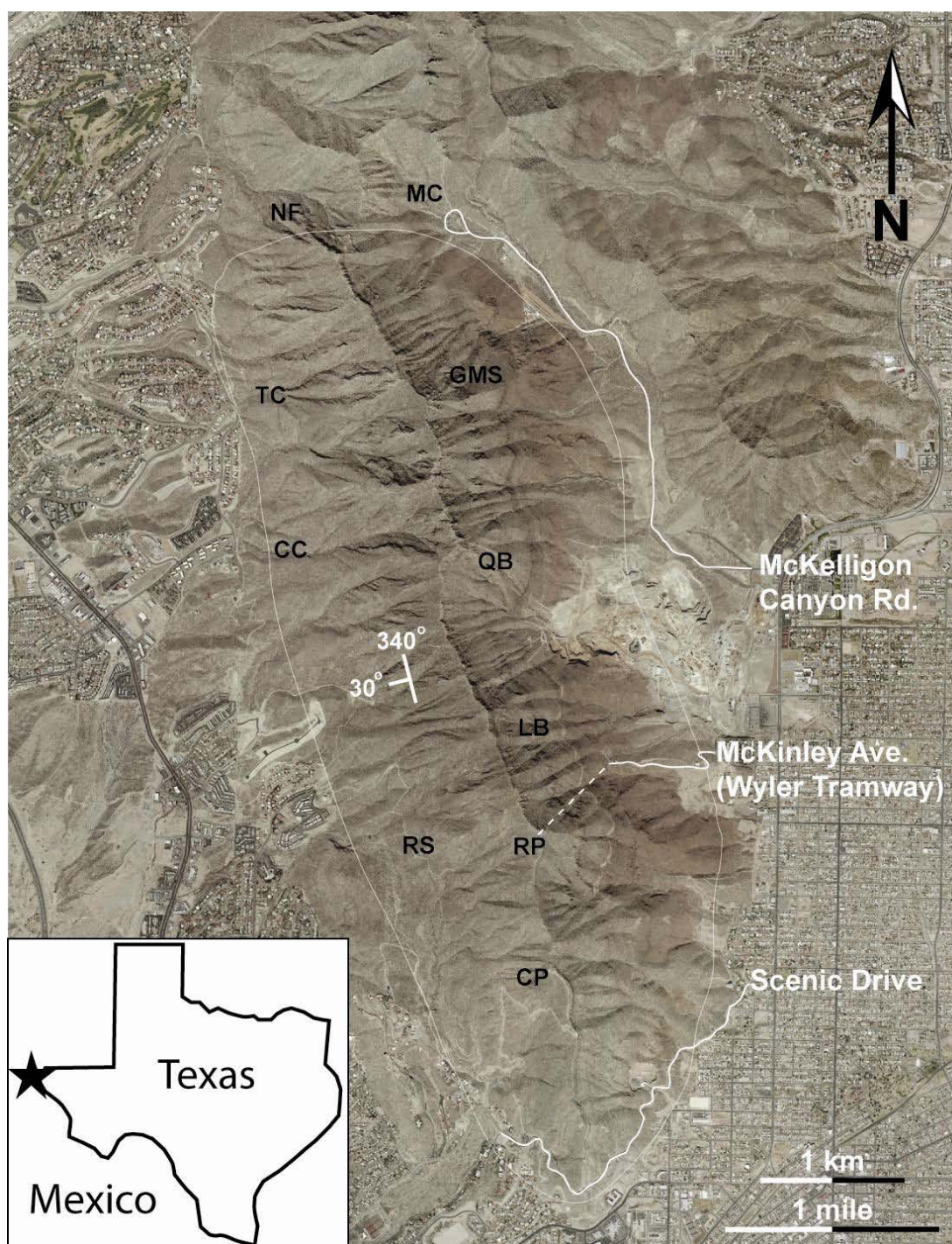


Figure 1.1: The southern Franklin Mountains (SFM) are surrounded by the city of El Paso, Texas. The study area (star on inset map) covers 24 km² of the southernmost Franklin Mountains outlined by the thin line. Average strike and dip are 340° and 30°, respectively. CP = Comanche Peak, RP = Ranger Peak, RS = Rock Slide, LB = Lechuguilla Breccia, QB = Quarry Breccia, CC = Cindy Canyon, TC = Transition Canyon, GMS = Great McKelligon Sag (breccia), MC = McKelligon Canyon (breccia), and NF = North Face (breccia).

1.2 General Paleoclimate Setting of the Ordovician:

The Ordovician Period was unique in several ways. First, it was a period of extraordinarily high sea level. Some of the highest sea levels in the Paleozoic, and arguably the entire Phanerozoic, occurred in the Ordovician (Gradstein et al. 2004; Markello et al. 2006). Ordovician global sea level rose from 300 to nearly 600 m above present-day sea level (plate I). Greenhouse conditions in addition to the relatively small, exposed, tropical land masses of Laurentia (figure 1.2) created open-marine global circulation patterns (Markello et al. 2006) that aided in development of an enormous carbonate epeiric platform—"The Great American Bank" (Ginsburg 1982), also referred to as the "Great American Carbonate Bank." The deposits of this very extensive platform covered most of Laurentia, comprising what today are eastern North America, Greenland, and parts of Europe (figure 1.2 and plate I).

North American supersequences of the Sauk and Tippecanoe (Sloss 1963) include all of the pre-Devonian rocks of the Paleozoic and are separated by a significant top-Sauk unconformity. The top-Sauk unconformity is recognized across much of North America and has been widely recognized as a karst surface associated with numerous caves and collapse breccias (figure 1.2; shaded area). This widespread karst system is somewhat enigmatic as the global emergence and diversification of vascular plants did not occur until the Devonian (Murphy 2005) and lack of well-documented paleosols during the Ordovician would have limited formation of aggressive water to carry out meteoric dissolution (Palmer 2007; Ford and Williams 2008). However, Ordovician paleoatmospheric conditions are interpreted to have had extremely high PCO_2 , 16 times higher than present day (Yapp and Poths 1992, Berner 1997). These extremely high atmospheric PCO_2 levels could have been sufficient for acidification of meteoric water and hence dissolution of exposed carbonates, despite potentially limited soil availability typically associated with carbonic acidification of meteoric water. The widespread evidence across North America for cave formation at the top Sauk supersequence boundary (figures 1.2 and 1.3) clearly shows that some acidification mechanism was active over large areas for cave development.

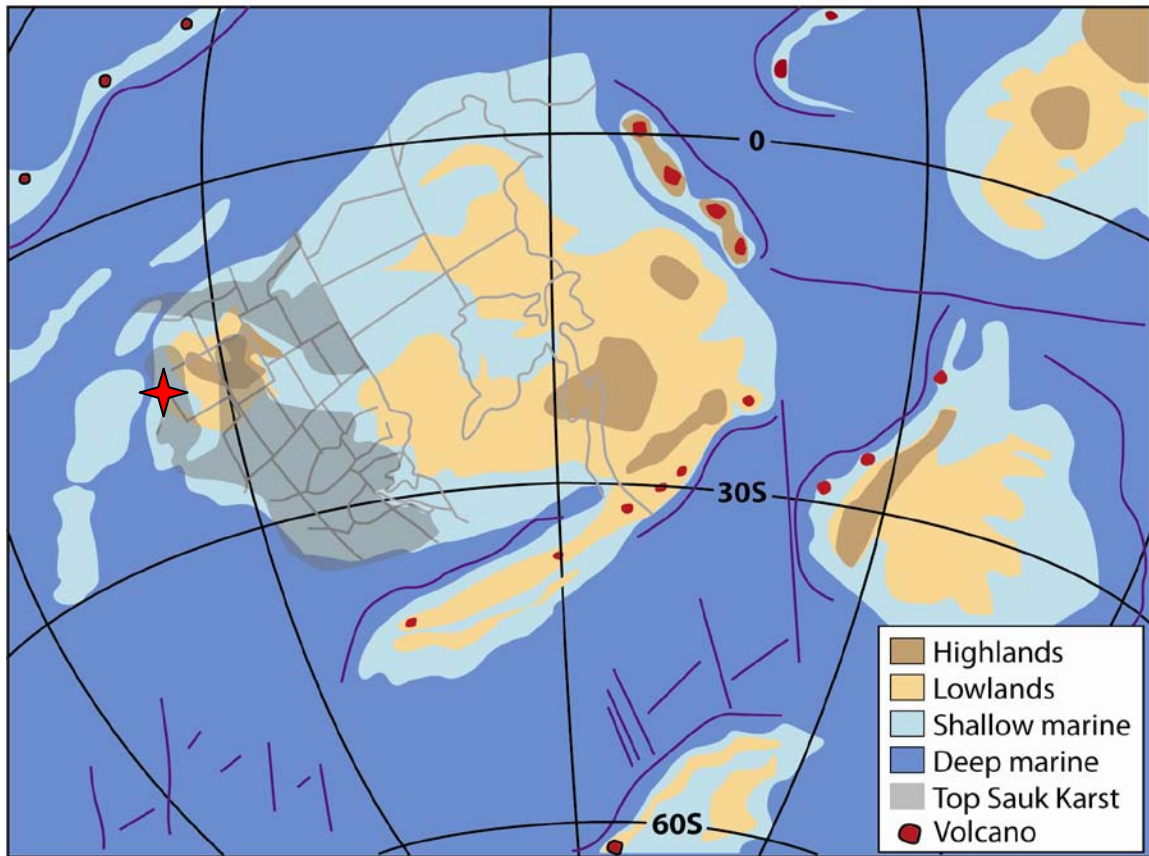


Figure 1.2: Paleogeography of Laurentia during the Lower Ordovician at 470 m.a. with regional patterns of top-Sauk supersequence-related paleokarst in gray (Paleogeography after Scotese 1986; Top-Sauk karst outline after Palmer and Palmer 1989). Red star identifies the study area.

Franklin Mountains, West Texas

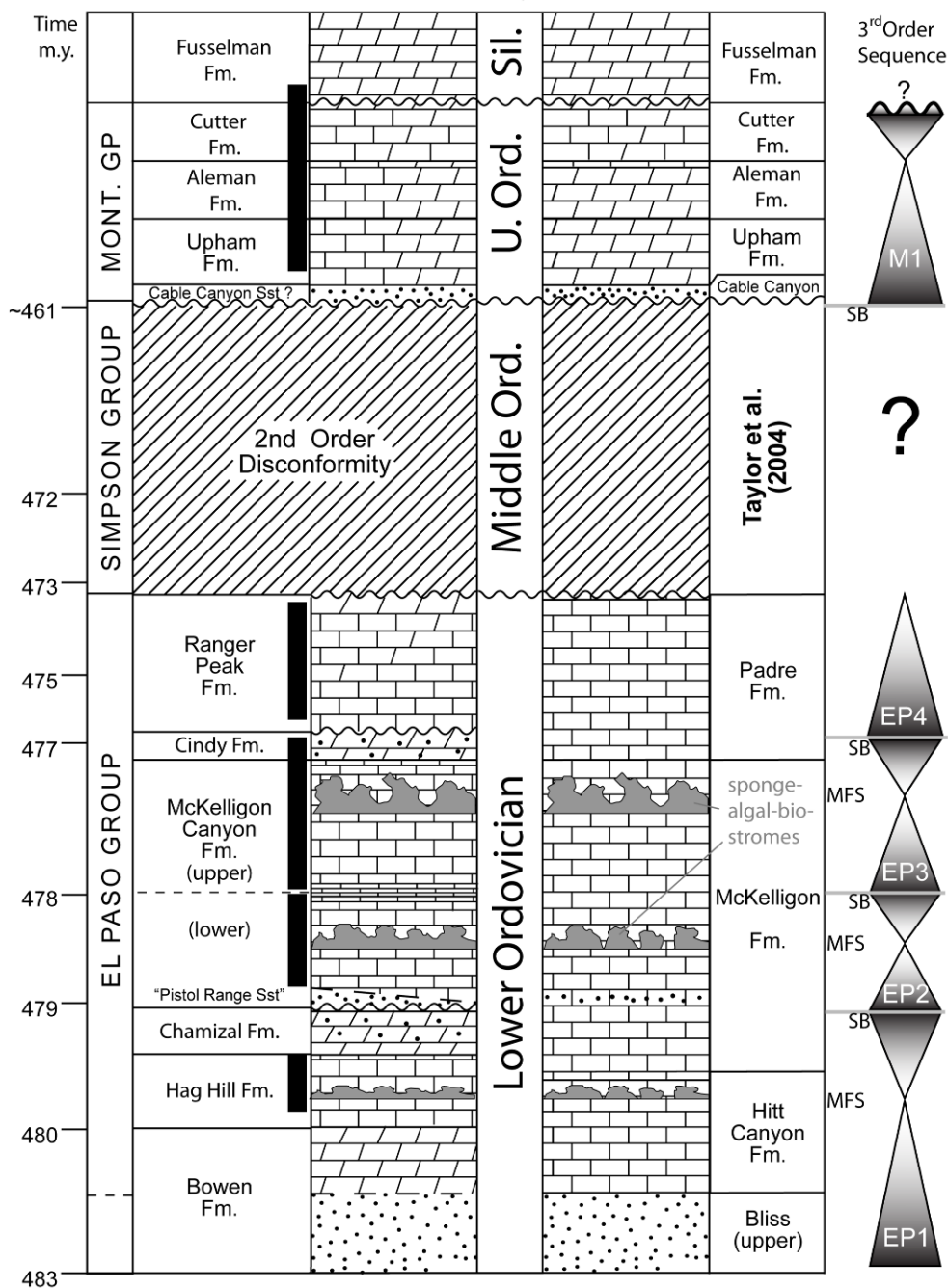


Figure 1.3: Third-order sequences EP1–4 described in text. Triangle points indicate high sea level and the maximum flooding surface zone as explained in the text. SB = sequence boundary, MFS = maximum flooding surface, black bars are breccia body-prone intervals. Diagonal hachures indicate non-deposition or erosion. Stratigraphic chart modified from Goldhammer et al. (1993) and Bellian et al. (2007) correlated to recent work by Taylor et al. (2004).

1.3 General Stratigraphy of the El Paso Region:

In the past century, the stratigraphy of the SFM, El Paso, Texas (figure 1.1) has been studied in detail by various workers (Richardson 1909; Cloud and Barnes 1948; Lucia 1968, LeMone 1969; Flower 1969; Harbour 1972; Hayes 1975; Kerans and Lucia 1989; Goldhammer et al. 1993; Taylor et al. 2004). It was Richardson (1904) who first recognized Ordovician strata in the Franklin Mountains. Richardson later (1909) subdivided the Lower and Upper Ordovician into the El Paso and Montoya Formations (figure 1.3), respectively, on the basis of biostratigraphic evidence and noted the absence of Middle Ordovician fauna. Lucia (1968) subdivided the El Paso Group into six formations on the basis of gross depositional and diagenetic packages. The Montoya was elevated to group status and divided into four formations from outcrop studies in Texas and New Mexico (Cloud and Barnes 1948; Kelley and Silver 1952). The nomenclatures of Lucia (1968) and Kelley and Silver (1952) are described in detail later and will be used in this study.

In the SFM the Lower Ordovician El Paso Group overlies the Cambrian Bliss Sandstone which fines upward into a medium- to fine-grained quartz arenite within a few meters from the granitic gravel-lag at the Precambrian-Cambrian boundary. The Bliss Sandstone is well-sorted with 5-15-cm-high cross bedding (plate III). Transition from the Bliss Sandstone to the lowermost El Paso Group unit, the Bowen Formation, is gradational but indicates a steady decrease in siliciclastic sediment input associated with continued transgression of the Lower Ordovician shoreline over the exposed Precambrian landmass (figure 1.3).

Carbonate deposition within the El Paso Group in this region vacillated between moderate (<10 m) to shallow-subtidal and peritidal environments along the western passive margin of Laurentia (figure 1.2 and plate I) in a semitropical environment, with siliciclastics concentrated near third-order sequence boundaries (Goldhammer et al. 1993). Low-relief granite islands referred to as the "Thunderbird Islands" (Kottlowski et al. 1969), named for the erosional pattern

resembling a thunderbird, crop out ~2 km north-northwest of the study area along the western dip slope of the SFM. The Thunderbird outcrop displays onlap of lowermost El Paso Group strata onto weathered Precambrian Red Bluff granite, which was a paleo high during deposition of the lower half of the El Paso Group (Kottowski et al. 1969). Scattered, low-relief granite islands like this one were likely the source for siliciclastic detritus throughout El Paso Group deposition.

The Lower Ordovician El Paso Group of west Texas is the temporal equivalent of the Ellenburger Group in the Permian Basin and central Texas (Cloud and Barnes 1948; Hendricks 1952; Mound 1968; Clemons 1998; Kerans and Lucia 1989; Goldhammer et al. 1993; Haubold 1999). The El Paso Group is composed of four partial third-order carbonate-dominated depositional sequences (plate I and figure 1.3) that record passive-margin drift-phase deposition during greenhouse conditions (Kerans and Lucia 1989; Goldhammer et al. 1993) along the southwestern margin of the Laurentian paleocontinent (figure 1.2). The lower Ordovician deposits compose the upper Sauk supersequence. The El Paso Group subtidal limestone-dominated sequences are commonly capped by siliciclastics and/or peritidal dolomudstones. Extensive tidal flats were common and indicate sea-level inflection points that punctuate subtidal-intertidal deposits (Goldhammer et al. 1993). The shallow subtidal to intertidal environment of the Early Ordovician was dominated by microbial communities with abundant but relatively low diversity invertebrate fauna (Harper 2006). These faunas accumulated in intrashelf bioherm complexes composed of sponge-algal mats trapping and/or binding grains. They now compose 1-5 m-thick laterally extensive biostromal units within the El Paso Group across the entire study area (figure 1.1).

Recent work by Taylor et al. (2004) in the SFM was built upon the stratigraphic nomenclature of Hayes (1975) and divided the El Paso Group into three formations, the Hitt Canyon, McKelligon Canyon, and Padre Formations (figure 1.3). These subdivisions were defined on mappable lithologies primarily working from New Mexico, south and east into west Texas. An alternative division of the El Paso Group, which was established by Lucia (1968), is

also based on genetic depositional units. These formations are, in stratigraphic succession, the Bowen, Hag Hill, Chamizal, McKelligon Canyon, Cindy, and Ranger Peak Formations (figure 1.3). A correlation of Taylor et al. (2004) and Lucia (1995) is presented for reference in figure 1.3.

Golhammer et al. (1993) added chronologic ages based on high-frequency cycle-stacking pattern analyses using Harland et al.'s (1989) geologic time scale applied to Lucia's (1968) formation divisions. The nomenclature and chronology of Goldhammer et al. (1993) were adapted in this study but fit by linear interpolation to the most recent geological time scale (Gradstein et al. 2004) (figure 1.3). This adaptation reduced the duration of the Middle Ordovician disconformity from the previously proposed 30 m.y. duration (Goldhammer et. al. 1993) to ~10 m.y. The motivation for using Lucia's (1968) nomenclature is that this scheme uses gross sedimentary packages to delineate shallow-subtidal, dolomitic limestone of the Hag Hill, McKelligon Canyon, and Ranger Peak Formations from medium-to-thin bedded dolostone, siliciclastic-rich dolostone, and peritidal facies associations of the Bowen, Chamizal and Cindy units. This division more logically follows third-order sequence subdivisions preserved within the strata.

The upper three-quarters of the ~500 m thick El Paso Group exhibits extensive breccia bodies first recognized and interpreted as collapsed paleocaves by Lucia (1971). These breccias locally penetrate more than 300 m down into El Paso Group strata from the top Sauk surface and are composed of matrix-rich, collapsed-cave deposits (*sensu* Loucks 1999) that have been subsequently preferentially and extensively dolomitized (Lucia 1971, 1995). The largest continuously mappable breccia bodies observed in outcrop are concentrated within the dolomitic limestone units of the El Paso Group.

A significant tectono-eustatic sea-level fall occurred near the latest Lower Ordovician to early Middle Ordovician (Sloss 1963, 1988)—the Sauk–Tippecanoe first-order megasequence boundary (figure 1.3 and plate I). Laurentia was rimmed by the carbonate megabank at this time but underwent nearly continent-wide subaerial exposure, as evidenced by widespread top-Sauk-related paleokarst across North America (figure 1.2-shaded area). On the basis of previous

biostratigraphic analysis in the SFM (Cloud and Barnes 1948; Flower 1969; Repetski 1982) no Middle Ordovician sediments have yet been found *in situ*. In this study, I sampled breccia matrix material within the El Paso Group breccia bodies for conodont analysis (table 1.1), but no evidence for Middle Ordovician conodonts were found in the paleocave system. The nearest documented Middle Ordovician strata are in the Beach and Baylor Mountains, some 175 km east-southeast of the SFM (Suhm and Ethington, 1975). Precisely how much dissolution of the El Paso Group has occurred cannot be determined. However, the latest Early Ordovician, Blackhillsian *Reutterodus andinus* conodont biozone (plate I) is represented in the uppermost 65 m of the El Paso Group at the southern end of the SFM (Repetski 1982), and index species of this biozone were found from multiple localities within breccia matrix material (table 1.1). There is no indication of Early Ordovician biozones younger than *R. andinus* from the matrix material collected in this study.

The Late Ordovician was a period of great biodiversification (Webby et al. 2004, Harper 2006). Open-marine seas flooded the karst-modified El Paso Group surface (Harbour 1972), and carbonate production resumed along the tropical ramp, as is evidenced by abundant tabulate corals, cephalopods, nautiloids, and diverse brachiopods (Flower 1969, LeMone 1969) of the Montoya Group. Kelley and Silver (1952) elevated the Montoya from Formation to Group status and defined four formations, the Cable Canyon Sandstone, and Upham, Aleman, and Cutter Formations. Howe (1959) expertly synthesized the Montoya lithostratigraphy and paleontology, which was further expanded upon by Flower (1969). The Upham Formation is the most extensively preserved of the Montoya Group units within the study area, with the Aleman and Cutter decreasing in outcrop area. At the karst-modified El Paso-Montoya Group contact an occasional thin layer of siliciclastic Cable Canyon Sandstone infilled 1-3 cm-wide grikes along the upper few meters of this karst surface. There is also a lack of any macrofauna within the breccia and/or matrix material in this and previous breccia studies (Lucia 1995).

The Fusselman Formation rests disconformably upon the Montoya Group (Flower 1969). The Fusselman Formation is only represented in the SFM by a few meters that contain a marker bed of dark tan colored, dolomitized pentamerid brachiopod (*Virgiana decussata*) rudstone that stands out abruptly against the light-gray to white Cutter Formation (figure 1.3). The Fusselman is not described in this work, although it is mentioned because large 20- to 40-cm clasts of the brachiopod rudstone have been identified within breccias near the Montoya-El Paso contact. This brachiopod rudstone indicates that open conduits were present or created during or after the Fusselman lithification.

1.4 Facies Associations:

For this overview, I rely on a suite of depositional facies associations to document the development of the four third-order depositional sequences within the Lower Ordovician El Paso Group. These depositional facies associations (I-V) represent deposition from offshore to inter-supratidal (figure 1.4) and are intended to simplify the ten subfacies proposed by Goldhammer et al. (1993). The vertical organization of these facies associations will be discussed in the sequence stratigraphy section later. Relevant subfacies correlations with Goldhammer et al. (1993) are listed at the end of each description:

- I. High-Energy Outer Shelf: sponge-thrombolite-microbial bafflestone with scalloped/scoured tops infilled and flanked by coarse bioclastic-intraclastic grainstones. These outer shelf buildups are rich in *Renalcis*, *Girvanella*, *Pulchrilamina*, *Archeoscyphia* and *Calathium*. This facies association is similar to Goldhammer et al.'s (1993) subfacies (1), Sponge-Algal Bioherm Complexes.
- II. Moderate-Energy Open Shelf: thrombolitic-oncolitic wacke-packstones with thin to medium bedding with intermittent wind-blown eolian red siltstone. Open marine fauna are common, including trilobites, brachiopods, and echinoderms. This facies association closely corresponds to Goldhammer et al.'s (1993) subfacies (2)

Intercalated Heterolithic Thin Bed, (3) Oncolite-Digitate-Thrombolite Wackestone-Packstones, and (5) Laterally Linked to Stacked Hemispheroid Stromatolites.

- III. Mixed-Low-Energy Intertidal: interbedded red (oxidized) siltstone and coarse planar to trough crossbedded skeletal grainstone. This facies associations is what Goldhammer et al. (1993) referred to as *ribbon rock* or subfacies (6) Wavy-Lenticular-Bedded Limestone and Red Siltstone. In addition, subfacies (4) Bioturbated Dolomitic Mudstone-Wackestone is included in this facies association.
- IV. High-Energy Upper Shoreface: planar to crossbedded medium- to coarse-grained subangular quartz arenite with carbonate cement. This facies association is equivalent to Goldhammer et al.'s (1993) subfacies (10) Cross-Bedded Quartz Arenite to Dolomitic Sandstone.
- V. Low-Energy Inter-Supratidal: interbedded algal-laminated, mud-cracked, fenestral, mudstone-wackestone with thin, rippled, siliciclastic sands. This facies association is equivalent to Goldhammer et al.'s (1993) subfacies (8) Mud-Cracked Flaser-Bedded and Wavy-Bedded Thin Beds and (9) Wavy-Bedded and Planar-Bedded Mud-Cracked Laminites.

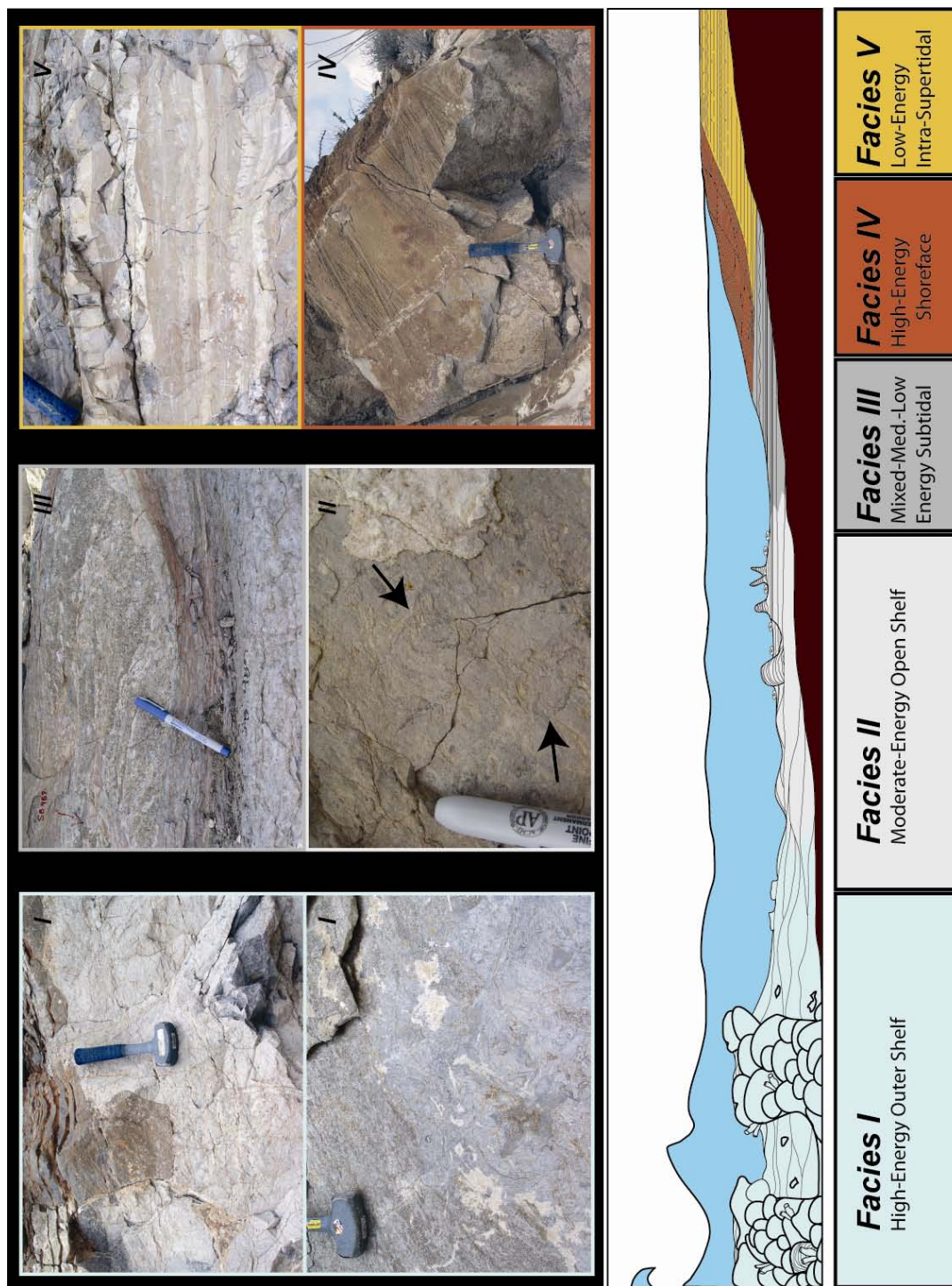


Figure 1.4: A conceptual depositional model has been constructed to relate vertical facies stacking to environment of deposition. Facies/subfacies correlations with those by Goldhammer et al. (1993) are explained in the text. Note that colors of facies belts correspond to facies photo border colors. Black arrows in image II point out digitate algal fingers within dolomitized the Chamizal formation, pen in image II is 5 cm long.

1.5 Lower Paleozoic Lithostratigraphy of the Southern Franklin Mountains:

El Paso and Montoya Group stratigraphy with its exceptional outcrop exposures in the Franklin Mountains has been well documented over the past 100 years beginning with the detailed mapping of the area in 1909 by Richardson, whose 1:125,000 scale surface map stands for the most part correct today. In recent years significant attention has been devoted to the extensive breccia systems developed in the El Paso Group and associated Montoya strata (Lucia 1995, Bellian et al. 2007). In particular, these breccia systems have been considered as a possible outcrop analogue for breccias from the laterally equivalent, Ellenburger Group breccias in the subsurface that form significant hydrocarbon reservoirs in the subsurface of west Texas (Kerans 1988, 1989; Loucks and Anderson 1984; Lucia 1995; McDonnell et al. 2007). To date limited work has been published to link the detailed stratigraphy of the SFM system to the breccia bodies, and no geographically precise geological maps have been published to include formation-level interpretations and breccia locations.

The next three sub-sections review the lithostratigraphy of the El Paso Group, Montoya Group, and Fusselman Formation, from which a sequence stratigraphic interpretation is assembled in the following section. This summary of the El Paso Group is based on field observations from this study combined with previously published descriptions (Lucia 1968; LeMone 1969; Harbour 1972; Goldhammer et al. 1993; Clemons 1989; Seager and Mack 2003). A measured stratigraphic section from the non-brecciated area of the El Paso Group and a geological map for the SFM study area are included as plates II and III. The Montoya Group and Fusselman Formation are similarly described from field observations but rely heavily on previous work (Kelley and Silver 1952; Pray 1953; Howe 1959; Lucia 1968; Clemons 1989; Seager and Mack 2003) from the El Paso and surrounding region because exposures, especially the upper Montoya and Fusselman, are sparse within the study area.

The El Paso Group:

The *Bowen Formation* is the oldest preserved Lower Ordovician section within the El Paso Group. The Bowen Formation rests unconformably above the Bliss Sandstone and shown by absence of diagnostic conodont biozones (Repetski 1988); however, sequence stratigraphically there is no compelling evidence for disruption in sedimentation between the Bliss and Bowen Formations. Deposition appears to be continuous from Cambrian transgression, beginning during recorded by the Bliss Sandstone deposition (Lucia 1968). The lower contact of the Bowen is difficult to recognize in the field because of similarities in facies and lithology to the uppermost Bliss Sandstone. The Bowen Formation (figure 1.5) is between 50 and 60 m in thickness, and consists predominantly of facies IV High-Energy Upper Shoreface, with planar-tabular dolomitic



Figure 1.5: The Bowen Formation contains decreasing a percentage of tan to orange siliciclastic sands (white arrows) upward and gradually becomes more carbonate rich. Other than the siliciclastic tidal flat sand (tidal bundles?) the Bowen has been entirely dolomitized. This photograph is from the upper portion of the Bowen approximately 7 m below the contact with the Hag Hill Formation and shows a high concentration of siliciclastic tidal bundles, indicating a possible high-frequency cycle boundary within the overall transgressive system. Pencil is 11 cm long.

sandstone with low-angle cross-stratification and thin ripple-laminated units in the lower half of the formation. These thin-bedded facies grade upward into mixed carbonate-siliciclastic grainstones having similar 5- to 20-cm (2- to 8-inch) planar to low-angle crossbedding.

The Bowen Formation is interpreted to record the continued transgression onto the Late Cambrian to Early Ordovician western Laurentian craton (figure 1.2 and plate I) with the transition from shoreline-proximal siliciclastics to open-shelf, mixed carbonate and siliciclastic facies. A shallow subtidal setting is consistent with the sparse open marine biota, absence of fine-grained sediments, and the dominance of medium-scale crossbedding. Transgression ensued and the siliciclastic source shifted gradually landward, and a passive-margin carbonate-dominated system was established (Lucia 1968) with a lower concentration of siliciclastic sediment being contributed.

The Hag Hill Formation contact with the Bowen Formation is gradational. The Hag Hill is ~82 m thick and overall consists of both facies I and facies II Moderate-Energy Open Shelf shallow subtidal thrombolite-oncolite deposits in the lower half of the formation. Facies II represents the establishment of carbonate production dominance in the sediment supply with little siliciclastic input. Facies II is overlain by facies I High-Energy Outer Shelf, represented by < 1 m sponge-algal bioherm-bearing cycles that indicate a more distal position to the paleoshoreline but within a higher-energy environment of deposition. Cycle thicknesses within the Hag Hill Formation of the SFM are >1 m thick packages of facies I overlain by facies II.

The Hag Hill Formation was deposited during continued transgression and highstand of the relative sea level over the Bowen Formation. The dominant lithologies are limestone with wispy seams of dolomite and localized dolostone bodies (figures 1.4 and 1.6).

The Chamizal Formation contact with the Hag Hill Formation is also gradational. The Chamizal Formation is ~27 m thick. It is composed of facies IV High-Energy Upper Shoreface

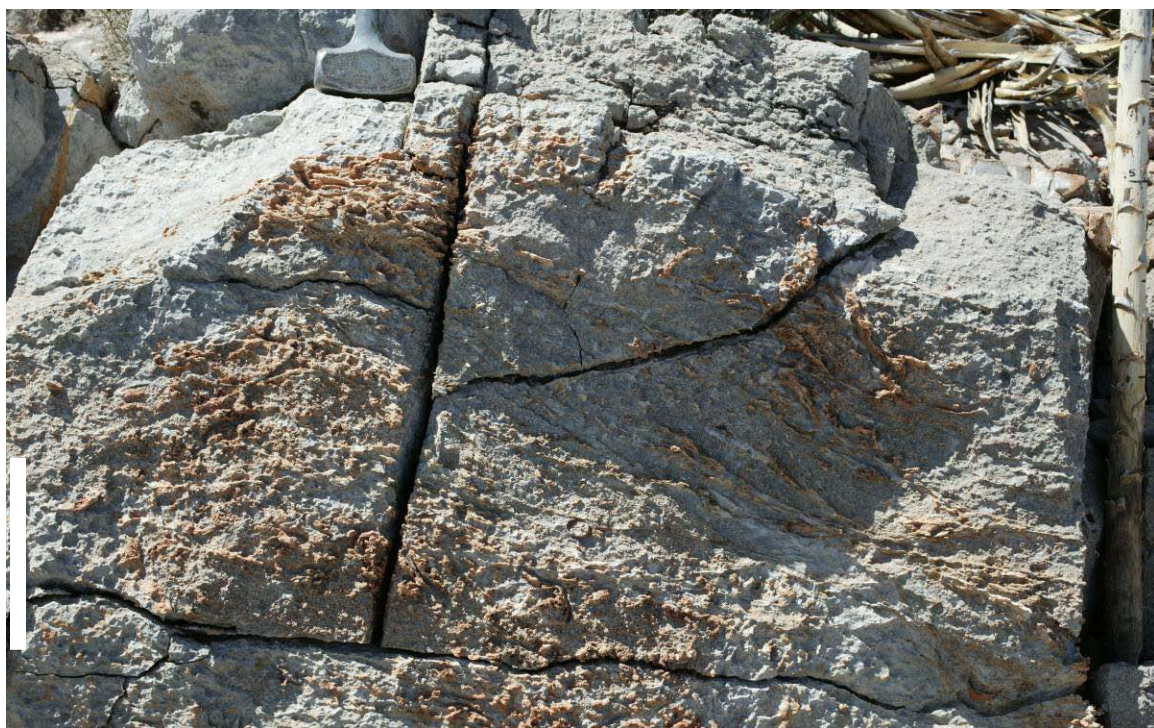


Figure 1.6: Lower section of Hag Hill contains 1-2 cm wide digitate thrombolites (white arrows upper photo), sponges (black arrows), and dolomitized and orange-weathered, chert-filled burrows. Orange-weathered chert highlights a 30-50 cm high sponge-algal mounds (lower photo). The white scale bar (left) is 10 cm.

siliciclastic sandstones as it transitions into facies V Inter-Supratidal mud-cracked and fenestral wackestones to mudstones (figure 1.4). The upper few meters exhibit the first obvious subaerial exposure evidence (figure 1.7) in the El Paso Group in this locality including mud cracks, and fenestrae.

The dominant lithology of the Chamizal is siliciclastic-rich dolowackestone deposited in a tidal-flat environment based on the occurrence of abundant mud cracks and fenestrae. The Chamizal is reported to have undergone early, reflux dolomitization (Lucia 1995; *c.f.* Montañez and Read 1992), resulting in fine-grained (<20 μm) dolowackestones and dolomudstones. The Lower Ordovician granitic "Thunderbird Islands" (Kottowski et al. 1969) ~2 km to the northwest are the most likely provenance for the siliciclastic sand mixed in with the mud-dominated dolopackstone to dolowackestone of the Chamizal Formation.

The McKelligon Canyon Formation contact with the Chamizal Formation is disconformable. The McKelligon Canyon Formation is 210 m thick, twice as thick as any of the other Formations within the El Paso Group, and it likely records peak carbonate production of the El Paso Group.

In general the McKelligon Canyon Formation is composed of facies I, II, III, and subordinate facies IV (figure 1.4). A thin, 0.75 m discontinuous siliciclastic sandstone (facies IV) with 5-15 cm herringbone cross-bedding is present at the base of this Formation, and is best observed along the Scenic Drive section (figure 1.1 and figure 1.7 upper). This siliciclastic sandstone was previously called the Pistol Range Sandstone (Goldhammer et al. 1993). It is only an effective marker bed for the base of the McKelligon Canyon Formation along Scenic Drive as it pinches out within a few hundred meters and only sporadically returns across the SFM exposures. Except for the Pistol Range bed, coarse siliciclastic sandstones are not present within the McKelligon Canyon Formation. Fine red silt is located within thin beds of facies III where bedding is less than 20 cm (plate III).

The McKelligon Canyon Formation records a rise in relative sea-level flooding over tidal flats of the Chamizal Formation. The dominant lithology is limestone with selectively dolomitized



Figure 1.7: Mud-cracked (white arrows), fenestral (black arrow) dolopackstone to dolowackestone of the Chamizal Formation (upper photograph) is overlain by the herringbone crossbedded (black arrows) siliciclastic sandstone (bottom photo) of the lowermost McKelligon Canyon Formation.

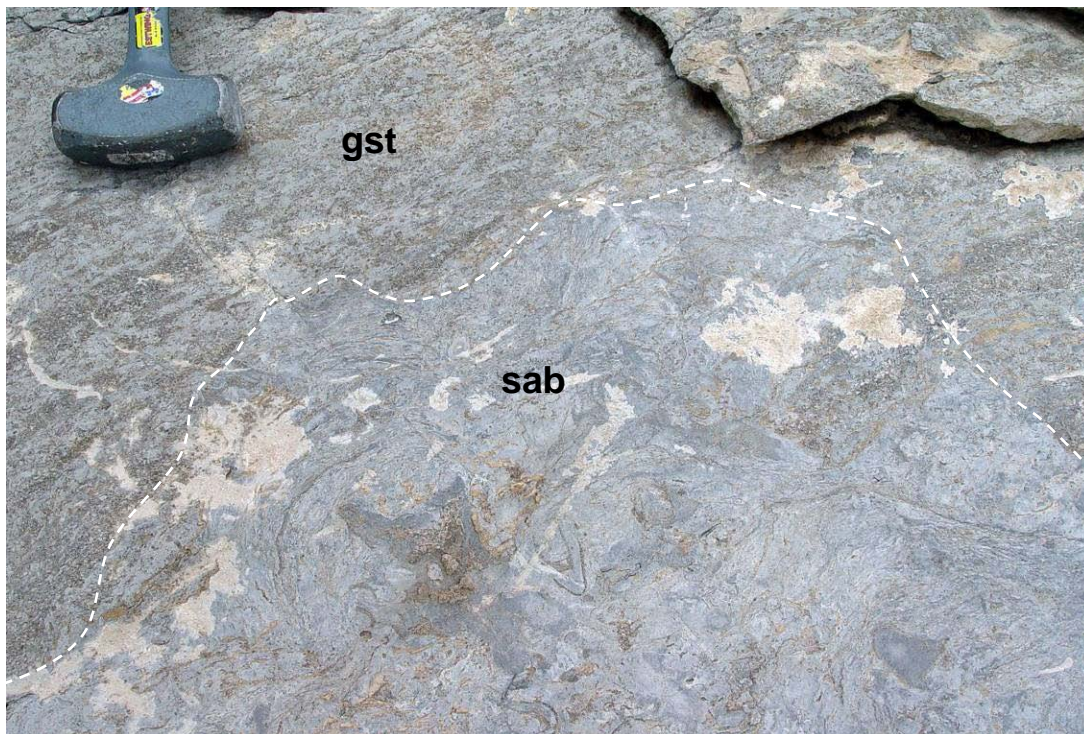
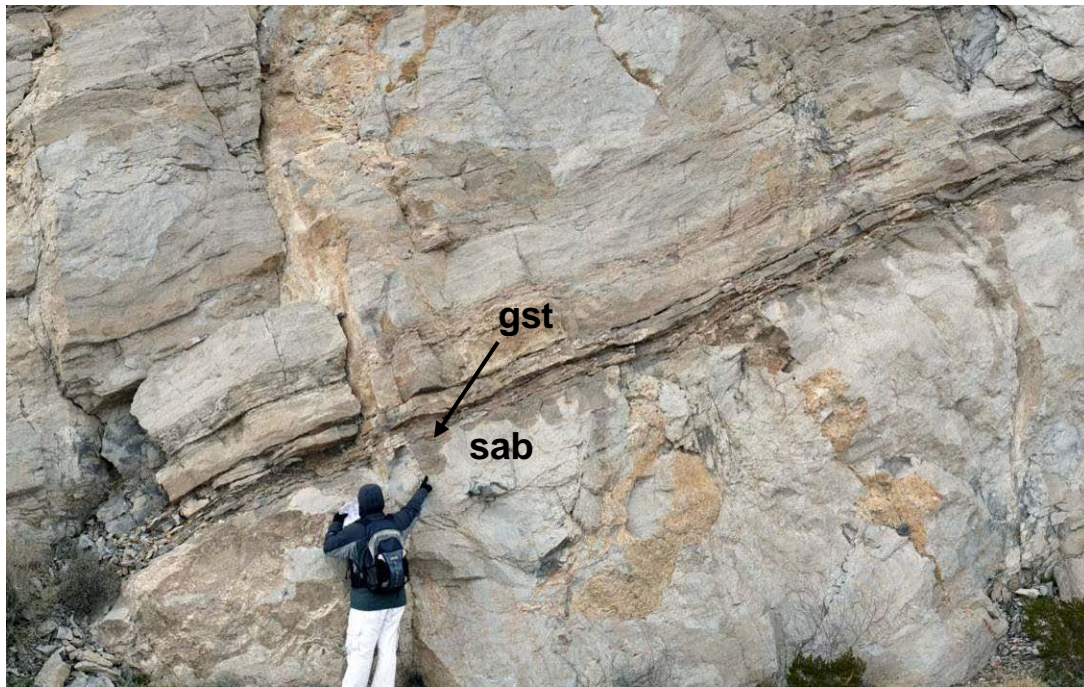


Figure 1.8: McKelligon Canyon Formation (top photo) contains skeletal grainstone-filled irregular channels on biostrome tops (dark tan-brown pointed to by person). Facies photo (lower) of skeletal grainstone infill (gst) around sponge-algal/microbial buildup (sab) contact highlighted by white dashed line. Bivalve fragments, lithisid sponges, thrombolites, and small digitate algal fingers dominate the light gray buildup core and darker brown near hammer is skeletal grainstone fill.

burrows and thin, red silt beds within intercalated thin beds of coarse skeletal grainstones to packstones.

The Cindy Formation contact with the McKelligon Canyon Formation is gradational and conformable. The Cindy Formation is 34 m thick and preserves the second distinct subaerial exposure horizon within the El Paso Group. The Cindy is dominated by facies IV and V, with thin interbedded siliciclastic sandstone and algal-laminated mudstones and packstones containing well preserved fenestrae, mud rip-up clast horizons, and pristine mud cracks similar to but more well-developed than those observed in the Chamizal Formation (figures 1.7 and 1.9). Siliciclastic sandstone thin-beds (0.5-10 cm) are common within the Cindy Formation.

The Cindy Formation, like the Chamizal, ranges between dolopackstone and dolomudstone, with thin, interbedded, siliciclastic sandstones. The Cindy, like the Chamizal records predominantly a tidal-flat depositional environment and associated early reflux dolomitization (Lucia 1995) resulting in fine crystalline dolomite ($<20\text{ }\mu\text{m}$) everywhere it crops out in the SFM.

The Ranger Peak Formation contact with the Cindy Formation is disconformable. The Ranger Peak Formation in the SFM is a maximum of 76 m thick when limestone but is on average 16 m thinner, or 60 m thick where it is brecciated and dolomitized (Lucia 1995). The original depositional thickness of the Ranger Peak Formation cannot be accurately determined because the Sauk–Tippecanoe unconformity truncates the top of this Formation. However, the SFM do offer one of the most complete sections of this unit in the region (Howe 1959) as the entire El Paso Group is erosionally thinned to the north (Kottlowski et al. 1969). The Ranger Peak Formation consists of facies II and III, with wavy-bedded limestone containing 10- to 50-cm dolostone beds and occasional small 5-10 cm sponge-algal bioherms. Chert is common in the upper 20 m (figure 1.10). The thickest preserved sections of the Ranger Peak Formation such along Scenic Drive contain a dolomitic, fissile, silty mud-dominated wackestone (figure 1.11).



Figure 1.9: Disrupted algal laminations within the Cindy Formation with interbedded siliciclastic sands (black arrows). Mud cracks and fenestrae are common. Frequent syndepositional intraformational breccias and mud-rip-up horizons are present as above (white circled area) with rare, partially in-filled vugs lined with saddle dolomite (red arrows).



Figure 1.10: The Ranger Peak Formation is a burrowed packstone with burrows of abundant chert (not pictured) and dolomitized burrows (white arrows point to a few examples). Cycles in the Ranger Peak Formation are 10-50 cm thick on average. Pencil is 11 cm long.



Figure 1.11: Montoya (Upham Formation) contact with the uppermost El Paso Group (Ranger Peak Formation) at Scenic Drive locality with a dolomitic, fissile, silty dolomitic wackestone.

The Ranger Peak Formation was deposited in an open-shelf, marine environment in the late Early Ordovician. This formation contains dolomitized burrows and occasional 10-20 cm strataform dolostone beds, but it has no indication of peritidal facies associations or subaerial exposure. In brecciated regions it is dolostone. The upper contact of the Ranger Peak Formation with the Montoya Group is karst modified with 1-3 m of localized erosional relief.

The Montoya Group:

The *Cable Canyon Sandstone Formation* is the oldest formation within the Montoya Group, and its presence in the SFM is somewhat controversial. It is a fine- to medium-grained siliciclastic sandstone deposited on the eroded El Paso Group strata (Harbour 1972). Some authors (Howe 1959; Flower 1969) suggested that this sandstone may be related to the Harding/Winnipeg Sandstone of the western United States. There is no conclusive evidence to validate this interpretation. In this study, we follow the interpretation of Harbour (1972) that it is a distal remnant to the Cable Canyon Sandstone of the Montoya Group described by Kelley and Silver (1952) in the Caballo Mountains of New Mexico, ~100 km north-northwest of the SFM.

Where present in the SFM (Howe 1959; Flower 1969; Bellian et al. 2007), the Cable Canyon Sandstone reaches a maximum thickness of 0.1 m. It was laid down by late Ordovician transgression across the karst-modified upper surface of the Ranger Peak Formation. Locally, 30-cm flat-clasts of the uppermost Ranger Peak are incorporated within the Cable Canyon Sandstone (figure 1.12 - lower). The thin sandstone mantles the karst surface (figure 1.12) and filters down into small, 1- to 3-cm-wide grikes as much as 2 m into the Ranger Peak Formation (figure 1.13).



Figure 12: This contact with El Paso and Montoya Groups shows strong evidence of epikarst erosion with thin (0.3 cm) grike fill into the Ranger Peak Formation (upper photo, black arrow) with up to 1-2 m of erosion into the Ranger Peak Formation. Lower photo shows large, 20- to 30-cm, flat, rip-up clasts (black arrows) of the uppermost Ranger Peak encased in Cable Canyon Sandstone, indicating some level of surface karst and erosion before Montoya deposition.



Figure 1.13: Brecciated contact of El Paso Group with Montoya Group containing a 2-cm-wide, Cable Canyon Sandstone-filled grike (finger pointing to) coming down from the Sauk-Tippecanoe unconformity (white line) surface into brecciated Ranger Peak Formation. This indicates that breccia was present before Cable Canyon Sandstone was deposited in the Upper Ordovician or that the sandstone was not cemented at the time of brecciation and filtered down into fracture. Overlying Montoya beds (M in photo) show minor crackle brecciation.

The *Upham Formation* crops out as the first dark gray to brown ledge-forming unit, along the ridge-line across a large portion of the SFM and is exposed as the dip-slope surface on the west face of the SFM. The Upham Formation contact with the Cable Canyon Sandstone is diffuse and is more appropriately described as a transition to lower siliciclastic sand content. Siliciclastics go to zero within the basal 50 cm of the Upham Formation. In the study area the Upham reaches a

maximum thickness of 34 m thick. It is composed of low-energy open-shelf facies, similar to facies III of the El Paso Group, but macrofossils are more abundant. One of the largest biodiversifications at the genus level occurred in the Middle and Upper Ordovician, which makes the Upham stand out from the relatively macrofossil-poor El Paso Group. The Upham Formation is a burrowed dolopackstone to dolograinstone (figure 1.14) that contains abundant tabulate corals, solitary corals, cephalopods, brachiopods, and receptaculids (Howe 1959; Flower 1969).

The Upham Formation is interpreted to have been deposited in open-marine, subtidal shelf conditions on the passive margin of southwestern Laurentia (Flower 1969). Everywhere north of the Wyler Tramway (figure 1.1) the Upham is medium-crystalline dolopackstone and weathers to a lightly mottled dark-brown to dark gray (figure 1.14). No *in situ* outcrop of the Montoya between the first N-S ridge north of Ranger Peak/Wyler Aerial Tramway and Comanche Peak has been identified (plate II). South of Comanche Peak, the Upham is a fossiliferous burrowed packstone to grainstone that weathers to a mottled light-gray, with dark-gray burrows (figure 1.11).

The *Aleman Formation* conformably overlies the Upham Formation with a gradational contact. The formation, 46 m thick, contains both limestone and dolomite beds (figures 1.15 and 1.16), with large chert nodules occasionally cored with dolostone (Howe 1959). In the SFM, the Aleman is a chert-rich skeletal packstone to wackestone. The Aleman contains bryozoans, brachiopods, trilobites and echinoderm fragments in a fine-to-medium crystalline dolomite with abundant chert.

The Aleman was deposited in a slightly deeper subtidal shelf with open-marine circulation during a period of global cooling and possible onset of glaciation. Previous isotopic studies examining the phosphate content of chert within the Montoya (Pope 2002) indicate cold-water upwelling from the onset of Late Ordovician icehouse conditions.

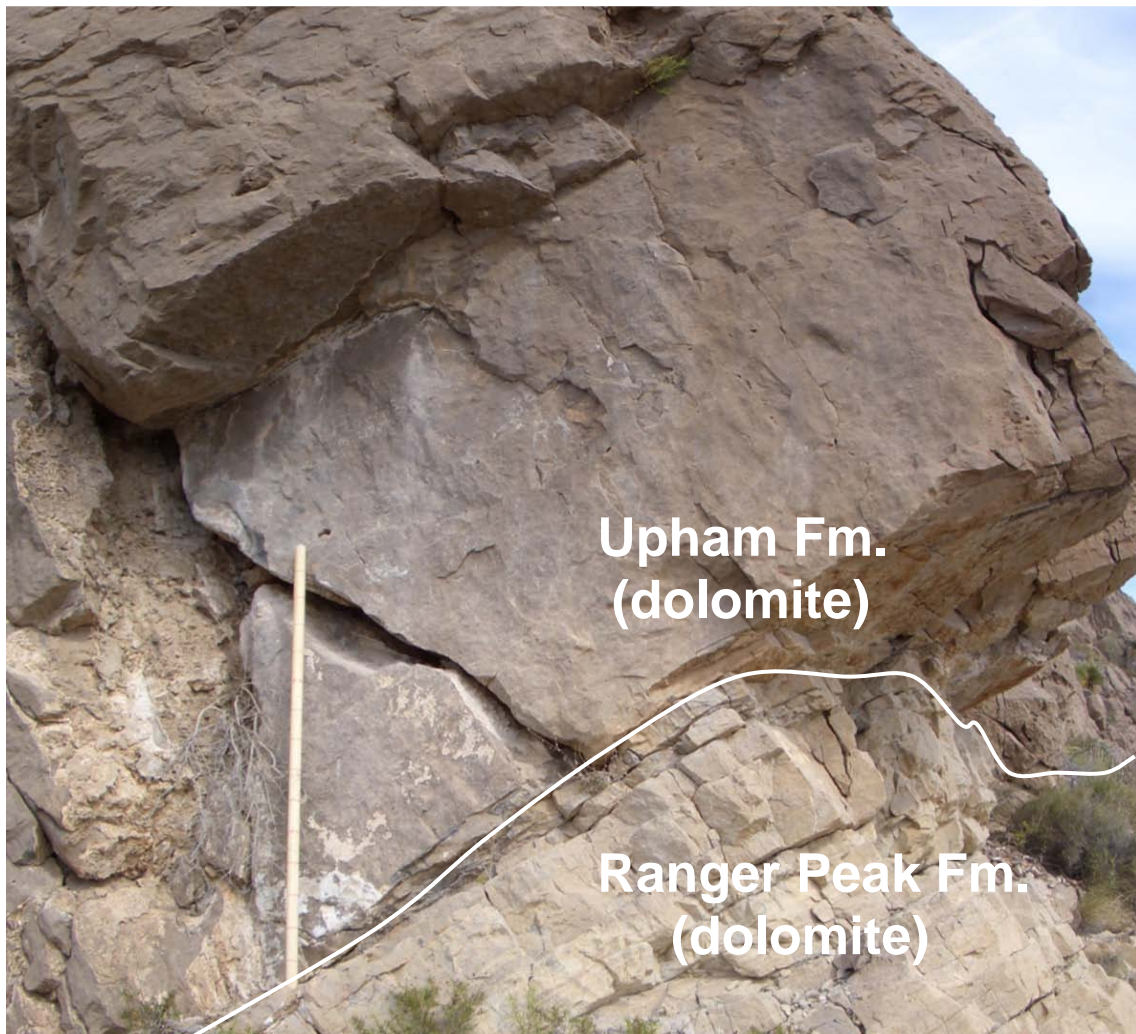


Figure 1.14: Dolomitized Upham Formation of the lowermost Montoya is darker brown and mottled texture. The lighter tan-colored bed is the uppermost Ranger Peak Formation separated by the Sauk-Tippecanoe unconformity (white line). Note the absence of the silty-dolomitic wackestone that is present in figure 1.11 along Scenic Drive. Jacob's staff for scale is 1.5 m long. Photograph from first outcrop of Montoya along ridgeline north of Wyler Aerial Tram tower.

The *Cutter Formation* has a sharp-based contact and reaches a thickness of 46 m. The basal part of the Cutter is commonly recessive (figure 1.16) in outcrop, followed by an abrupt color change from the darker chert-bearing Aleman to the lighter, yellowish-tan to off-white Cutter Formation. The Cutter Formation has been dolomitized, but ghosts of echinoderms and brachiopods as well as silicified brachiopods and some horn corals have been reported (Clemons 1998) in what was likely a skeletal packstone before fabric-destructive dolomitization. The Cutter

has a somewhat restricted marine fauna of small (1-3 cm) brachiopods and bryozoans (Pope 2002).



Figure 1.15: Chert nodules (white arrows) 5-10 cm across within the open-shelf, dolomitized Aleman Formation. Pencil is 10 cm long.

The Cutter Formation may represent a slight shallowing from deeper subtidal to shallower subtidal or lagoonal in cooler waters associated with Late Ordovician glaciation and cool-water upwelling along the passive margin of Laurentia (Pope 2002). These analyses were derived from phosphate extracted from the abundant chert extracted from the Montoya by Pope and Steffen (2003). The Cutter Formation has been dolomitized by a fine crystalline dolomite (Howe 1959).



Figure 1.16: Light-tan beds in the foreground (upper photo) are the Cutter Formation (C) overlain by the Silurian Fusselman Dolomite. Below the Cutter Formation, the Aleman (A), Upham (U) and Ranger Peak (RP) Formations can be identified. The lower photo shows dolomitized Cutter Formation, pencil is 10 cm long. Red dashed line is down-to-east fault; this image was taken facing north-northeast.

The Fusselman Formation:

The *Fusselman Formation* records a shallow subtidal shelf depositional environment (likely deeper than El Paso or Montoya Groups) with abundant fauna, and its contact with the Cutter is disconformable (Clemons 1998). The Fusselman reaches a maximum thickness of 450 m in the Florida Mountains (Clemons 1998) and is 300 m in the Franklin Mountains north of the study area (Richardson 1909; Pray 1953). Only a few meters of the Fusselman are preserved on isolated knobs along the western dip slope of the SFM. Reported fossils include a diagnostic pentamerid brachiopod (*Virgiana decussata*), solitary and colonial corals, stromatoporoids, gastropods, cephalopods, bryozoans, crinoids, algae, and conodonts (Clemons 1998). A karst surface separates the Fusselman from the Cutter Formation (LeMone 1968; Lucia 1968; Clemons 1998; Seager and Mack 2003). Transported clasts of the pentamerid brachiopod rudstone have been identified in this study *within* breccias near the Ranger Peak–Upham Formation contact (figures 1.16 and 1.17). Contact with the overlying Devonian is also disconformable, although not exposed in the SFM study area (Lucia 1995; Clemons 1998; Seager and Mack 2003).



Figure 1.17: Diagnostic marker bed for the Silurian Fusselman Dolomite is a pentamerid brachiopod lag (*Virgiana decussata*) exposed in the study area where the Fusselman crops out (upper photo). Clasts of this lag have been found (lower photo) ~120 m below its equivalent stratigraphic level. Lower photo is a chaotic breccia near the El Paso-Montoya Group contact containing Fusselman clasts.

1.6 Sequence Stratigraphy:

Sequence stratigraphy of the El Paso Group and Lower Ordovician in general records gradual semi-symmetrical transgressions and regressions that reflect the low-amplitude eustatic signal in a greenhouse global climate setting (Read 1982; Montañez and Osleger, 1993). The high-frequency cycles (5th order) documented by Goldhammer et al. (1993) record gradual deepening and thickening during transgression and highstand followed by a rapid thinning of high frequency cycles as accommodation space is filled. This stacking pattern has been previously described in the SFM by Kerans and Lucia (1989) and Goldhammer et al. (1993). Cycles of the El Paso Group stack together to make four 3rd order depositional sequences. In three of the four depositional sequences in the SFM, 3rd order sequence boundaries are sharp and marked by some evidence of exposure and erosion. At the EP 2 sequence boundary, only a change in cycle stacking pattern marks the sequence boundary, and no single master exposure surface can be identified. This gradual turnaround at EP 2 is analogous to the sequence boundary zones (SBZ) recognized by Montañez and Osleger (1993) for the Cambrian of Nevada.

The Bliss Sandstone, not formally part of the El Paso Group, is included in the measured section in plate III. The contact of the Bliss Sandstone with the Precambrian basement is an erosional, gravel to coarse-grained sandstone lag that incorporates clasts of granite (figure 1.18). As previously stated, the contact of the Bliss Sandstone with the lower Bowen Formation is a diffuse zone of increasing carbonate (now dolomite) content and gradually reduced siliciclastic sandstone. The sequence stratigraphic discussion will begin with the Bowen Formation with the assumption that the Bliss Sandstone deposition occurred during initial transgression of the Precambrian granite and continued transgression and deposition of the Bowen Formation.

1.7 EP 1 Third-Order Sequence:

The diffuse contact between the Bliss and Bowen Formations makes it difficult to determine the exact location of initial El Paso Group transgression. Regional biostratigraphic work is

ongoing (Taylor et al. 2004, Myrow P.M., Colorado College, pers. comm. 2007). Deposition of the lower Bowen Formation occurred near sea level, as indicated by the planar-tabular- to herringbone crossbedded fabric with a gradual upward increase of carbonate grains (Lucia 1968). The Bowen Formation was deposited during continued relative sea-level rise (TST). The Hag Hill Formation is interpreted to record continued transgression during the TST. The upper Hag Hill Formation contains digitate thrombolites, and sponge bioherms (figure 1.3, plate III) the most offshore facies within EP 1.

The exact position of maximum flooding surface (MFS) within the EP 1 Bowen-Hag Hill-Chamizal sequence is difficult to isolate as the water depth in the entire sequence likely never exceeded 10 m during greenhouse conditions. The MFS is constrained within a zone, similar to the sequence boundary zones described previously (Montañez and Osleger 1993) that coincides with the thickest biohermal cycles. From this point on, accommodation is more limited and more proximal to shoreline facies dominate, indicating progradation of the shoreline. EP 1 is capped by peritidal algal laminite cycles and thin, crossbedded siliciclastic sandstones of the Chamizal Formation sourced by the Thunderbird Island northwest of the study area (Kottlowski et al. 1969). Exposure indicators within the early, reflux dolomitized Chamizal Formation (Lucia 1995) are fenestrae, mud cracks, and algal laminites that occur just below the transgressive “Pistol Range” sands.



Figure 1.18: The contact of the Bliss Sandstone with the Precambrian granite (middle of the hammer handle). Note the decomposed, weathered granite surface near the hammer head with low-angle crossbedded Bliss Sandstone.

1.8 EP 2 Third-Order Sequence:

The EP 2 sequence consists of the uppermost Chamizal Formation through the lower third of the McKelligon Canyon Formation. The upper few meters of the Chamizal Formation indicate initiation of the next TST as tidal-flat dolomudstones to dolowackestones of the previous sequence are overlain by upper-shoreface siliciclastics of the *Pistol Range Sandstone* (Goldhammer et al. 1993), which crops out just south of the El Paso Police Department firing range along Scenic Drive (figure 1.1). On top of the localized Pistol Range Sandstone, carbonate deposition quickly resumed. The skeletal packstone succession of the lower McKelligon Canyon Formation is characterized by subtidal firm grounds (bored and burrowed surfaces) a few meters above the *Pistol Range Sandstone* are covered or colonized by oncoids, small sponges, and digitate algal fingers during the late TST. These small buildups were taken over by large sponge-algal biostrome colonies that amalgamated to form the McKelligon Canyon Formation's lower biostrome, indicating the MFS of EP 2. This 2- to 3-m-thick biostromal unit is laterally extensive throughout the entire study area. High-frequency depositional cycles above the lower biostrome become thinner with increased siliciclastic contribution forming what Goldhammer et al. (1993) referred to as *ribbon rock* and is interpreted as shallow subtidal deposits of the HST. Evidence of subaerial exposure is not present in this third-order sequence but rather a sequence boundary zone exists, as previously discussed, and composed of thin, siliciclastic-beds indicating the turn-around from EP 2 HST to EP 3 LST.

1.9 EP 3 Third-Order Sequence:

Sequence EP 3 consists of the upper two thirds of the McKelligon Canyon Formation and the majority of the Cindy Formation. The high-frequency depositional cycle thicknesses within the McKelligon Canyon Formation show the now-familiar gradual but distinct thickening upward above the EP 2 third-order sequence boundary zone. Selection of the exact sequence boundary surface again is based on recognition of a zone of a few meters in thickness where stacking

patterns begin to transition from upward thinning to upward thickening cycles. The same evolution of the TST through HST from EP 2 is present in this sequence, except that larger 3-4.5 m, well-developed sponge-algal biostromes occur (figure 1.8) approaching the MFS. More detailed work focused on these biostromal units may reveal lateral variability within these buildups at the high-frequency cycle scale. It is likely internal evidence for progradation or retrogradation could be found with detailed analysis of each of these biostromal units.

Deposition of shallower water Cindy Formation laminite-dominated cycles over the McKelligon Canyon Formation indicates platform progradation. The Cindy, like the Chamizal from the top of sequence EP 1, contains algal-laminated and fenestral dolomudstones with thin, interbedded, siliciclastic sandstones. This sequence provides a "type sequence" for the El Paso Group that records a transition from a diffuse sequence boundary zone through establishment of the carbonate factory with gradual colonization of the sea floor and formation of small biological communities followed by large, reef-like sponge algal biostromes during peak transgression (MFS zone). The biostromes are eroded and covered over by more proximal to the shore facies and gradually buried as accommodation is filled. The EP 3 sequence is also the maximum transgression of the El Paso Group second-order supersequence.

1.10 EP 4 Third-Order Sequence:

The TST of this sequence begins within the last few beds of the Cindy Formation and continues through the entire Ranger Peak Formation (figure 1.3), where the sequence is truncated. The last few beds within the Cindy Formation do not show distinct tidal flat laminations and well developed mud cracks but are still mud-rich cycles that illustrate an upward-thickening trend and transition into the lower Ranger Peak Formation less abruptly than previously noted with the EP 1 sequence. The Sauk–Tippecanoe megasequence unconformity surface truncates the EP 4 depositional sequence before a definitive cycle stacking change can be defined. The Sauk-Tippecanoe unconformity marks the end of preserved Lower Ordovician rocks in the SFM.

Determining how thick this last partially preserved depositional sequence may have been is not possible from the outcrop evidence in the SFM. However, it is obvious from the irregular and karst-modified contact with the Upham Formation of the Montoya Group that this surface underwent subaerial exposure and considerable carbonate strata have likely been removed. Previous works by Kottlowski (1969), Lucia (1971), Kerans and Lucia (1989), and Goldhammer et al. (1993) indicate thinning of the El Paso Group to the north, east and west of the SFM study area.

The entire Middle Ordovician Simpson Group is absent here, probably never having been deposited or, possibly, having been completely eroded before deposition of the Upham Formation. Suhm and Ethington (1975) have reported 22.6 m and 33.7 m of Simpson Group strata at sections 175 km southeast of El Paso, Texas, in the Beach and Baylor Mountains, respectively. No Simpson-equivalent strata or fauna have been reported within the SFM or the greater El Paso region, and none were observed in this study.

1.11 Montoya and Fusselman Sequences:

The Upper Ordovician Montoya crops out in only a few locations in the study area, so the sequence stratigraphic architecture is not discussed here. Recent work of Pope (2002), Pope and Steffen (2003), Seager and Mack (2003), and previous work by Howe (1959), Hayes (1975), and Clemons (1998) are suggested sources for further detail. In general the Montoya Group likely represents a single third-order sequence beginning with the LST indicated by the siliciclastic Cable Canyon Sandstone and rapid transition to open-marine-fauna-dominated packstones of the Upham to the deeper subtidal chert-rich Aleman Formation wacke-packstone (maximum flood zone) and finally the skeletal packstone Cutter Formation with subaerial exposure (MI sequence in figure 1.3).

The Silurian Fusselman Formation is present in only a few thin remnants in the study area and will not be discussed here (plates I and II). Examination of the sea-level curve (plate I)

indicates two significant (>100 m) sea-level-fall events at the Ordovician–Silurian and Silurian–Devonian boundaries. Very little sea level fall is noted at the top Sauk in comparison to these other two events. The global sea-level curve presented in plate I is a global curve, so relative sea level does not necessarily need to correspond directly to this pattern. Summaries by Pray (1953, 1958), Clemons (1998), and Seager and Mack (2003) are suggested for more detailed analysis of the Fusselman Formation.

1.12 Breccias of the El Paso Group:

The El Paso Group is the host rock within which several collapsed-cave breccias have been documented (Lucia 1971, 1995). Two dominant breccia types have been identified on the basis of geometry and occurrence: laterally extensive and laterally restricted breccia systems. Lucia (1971) interpreted these breccias as the result of the collapse of the "El Paso Caverns" (figures 1.1 and 1.19). The breccias were noted to have two primary orientations within the upper El Paso Group. A laterally extensive cave system formed within the upper 60 m of the El Paso Group Ranger Peak Formation limestone. This Ranger Peak cave system has been interpreted as a meteoric karst system forming along the post-Lower Ordovician water-table. A second laterally restricted cave system extends down from the Sauk-Tippecanoe unconformity over 300 m into the El Paso Group (figure 1.19 and plate IV) and is best preserved within the McKelligon Canyon Formation limestone. Both breccia system geometries are pervasively dolomitized with an associated dolomite halo that penetrates several meters into the surrounding host rock of the El Paso Group (Lucia 1995; Tillotson 2003).

All breccia matrix material observed in the study area is dolomitized, and where laminated, laminations have been reported as parallel to the structural bedding dip (Lucia 1995) of the SFM (~30° W), but the irregularity of lamina likely due to compaction makes this observation difficult to validate. No measurements of lamina orientations have been published. In general, both clasts and matrix sediment are dolomitized, and trace amounts of siliciclastics are frequently scattered

within the matrix material. Despite dolomitization of all matrix material observed, large blocks of the McKelligon Canyon Formation within the lower reaches of the laterally restricted breccias are preserved as limestone. These limestone blocks are dominantly composed of biostromal Facies I and II (figure 1.4).

Breccia nomenclature used here is adopted from Kerans (1989) and Loucks' (1999), vertical stacking and collapsed-cave breccia classification. Below is a summary of breccia types used in this study:

- Chaotic-breccia clasts have been transported away from the protolith and can be mono or polymictic. As the name implies, this fabric is poorly sorted and can be either clast- or matrix-supported. Matrix, if present between clasts can be laminated to massive, with void spaces that may be partially or completely cement filled. A vague trend of decreasing clast size toward the contact with host rock may be observed. Pressure-solution seams between touching clasts are common.
- Mosaic-breccia fabric is defined by clast arrangements, suggesting only minor clast transport (a few centimeters) from original position. Proximity of clasts to original position can often be identified by adjacent broken fragments. Rarely have preserved void spaces been documented in this type of breccia in the SFM. Both massive to laminated internal sediments and dolomite cements occlude porosity between clasts.
- Crackle-breccia types are the least spatially altered. Crackle breccias are basically fractured in place and later infilled by sediment and/or cement. Matrix within this type can be absent but may also range from mud to coarse sand. By definition, matrix is a subordinate component of this breccia type. Most often these breccias are observed near the edges of breccia bodies within the host

rock, potentially along walls or ceilings of paleocaves, and are the result of compaction and/or failure of the strata.

1.13 Spatial Distribution of Breccia Types:

Laterally restricted collapse breccias occur dominantly within thick packages of limestone such as the Hag Hill, McKelligon Canyon and Ranger Peak Formations within the El Paso Group. A partial sample bias exists, as there are few vertical outcrops of the full Montoya Group in the study area. Several linear breccia bodies along the west side of the SFM have been identified in this work, and others have also been re-mapped from previous work (Lucia 1971). The following section discusses the large, laterally restricted breccias that penetrate several hundred meters down into the El Paso Group from the Sauk-Tippecanoe unconformity and then briefly discusses the laterally extensive breccias that occur dominantly within the Ranger Peak Formation and the linear breccias that crop out along the western dip slope of the SFM.

Large, laterally restricted breccias, such as the Ranger Peak Breccia (located just below the geographic location of Ranger Peak), Lechuguilla, Quarry, and Great McKelligon Sag Breccias extend between 150 and 450 m deep from the Sauk–Tippecanoe unconformity downward. All of these breccias except the Ranger Peak Breccia have continuous collapse breccia, up to and including the Upham Formation of the Montoya Group. These breccia exposures range in width from 170 to 370 m and range in outcrop area from ~8,000 to 60,000 m² (figure 1.20 and plate IV). These laterally restricted breccias are evenly spaced at 1000 m +/- 100 m when measured parallel to regional strike (340°). Similar spacing was reported by Lucia (1995).

Laterally restricted breccias mapped in figure 1.20 (LB, QBu, QBI, RP, and GMS) have similar vertical breccia-fabric successions as those recognized by Kerans (1988, 1989) in subsurface Ellenburger cores of the Permian Basin, Texas. The vertical progression from breccia base to top El Paso Group transitions from angular, clast and slab-supported chaotic breccias to matrix-supported, smaller clast (5–30 cm) breccias, and finally to mosaic- to crackle-breccia

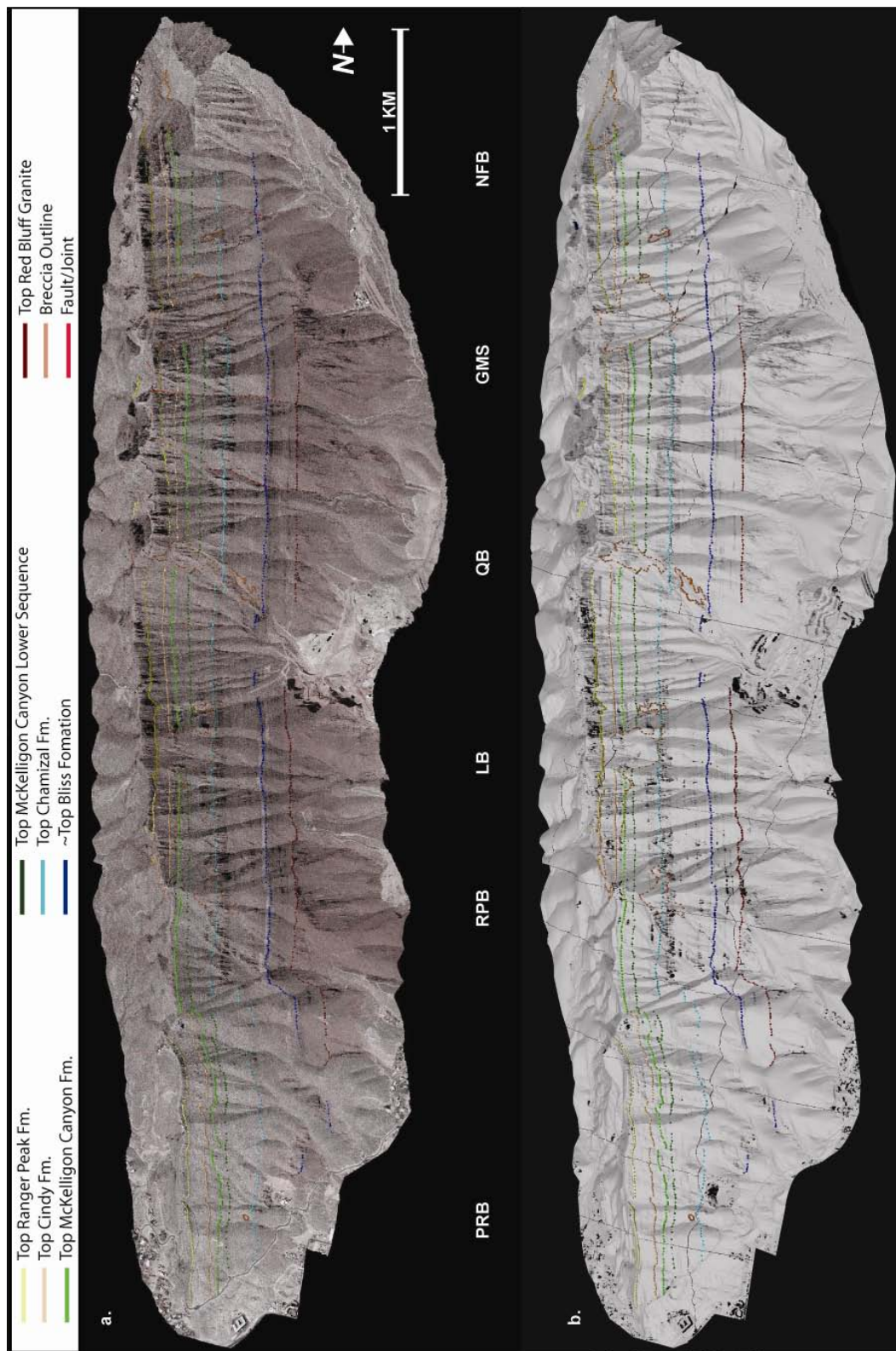


Figure 1.19: (a) Co-registered 30-cm air-photograph-draped lidar point cloud and (b) triangulated irregular network (TIN) showing interpretation of main stratal surfaces. Main breccia bodies are also labeled, PRB = Pistol Range Breccia, RPB = Ranger Peak Breccia, LB = Lechuguilla Breccia, QB = Quarry Breccia, GMS = Great McKelligon Sag, and NFB = North Face Breccia. Vertical exaggeration is 50%.

zones (Kerans 1988, 1989) have been observed in outcrop (figures 1.21 and 1.22).

Matrix material nearly always fills intraclast voids with rare vuggy porosity often infilled by coarse crystalline calcitic or saddle dolomite cement. Matrix material is always dolomitized with minor siliciclastic content (<1%) with occasional abraded and/or corroded dolomite rhombs observed under cathodoluminescence (Appendix C, sample 2368). Typically the matrix weathers red to orange in the lower sections of the breccias and more tan to white in the upper regions. Matrix coloration often makes identification of clast boundaries less ambiguous in the field. In some regions, especially within the Ranger Peak Formation the weathering of the matrix and host rock are so similar, that it is often extremely difficult to determine if the rocks are brecciated or simply dolomitized, burrowed, Ranger Peak Formation.

Large, open voids, several thousands of cubic meters in size must have been present to allow for slabs to be transported >50 m stratigraphically downward, as in the Lechuguilla Breccia, Quarry Breccia complex, and Great McKelligon Sag. Limestone slabs of biostromal units (facies I) are found near the base of the Lechuguilla Breccia, Great McKelligon Sag and near the base of the upper Quarry Breccia and filling most of the lower Quarry Breccia (figures 1.20 and 1.21). These stratigraphically-downward displaced slabs can be as much as 10 × 2 m in size and dip up to 90° to original bedding. Sediment infill around these slabs is typically red, dolomitic, and contains small dolomitized rock fragments with silt. In modern cave-mapping terminology (Palmer 2007), this type of breccia would be classified as a *breakdown* from roof-collapse material transported downward stratigraphically into an open void. Kerans (1989) referred to this as "lower collapse zone" in his models based on extensive Ellenburger core data.

Up-section within laterally restricted breccias (figure 1.21), clast composition becomes more obviously heterolithic or polymictic with decreasing clast size, and fewer to no clasts are left undolomitized. Clasts of the dolomitized Ranger Peak Formation are intermixed with Cindy and

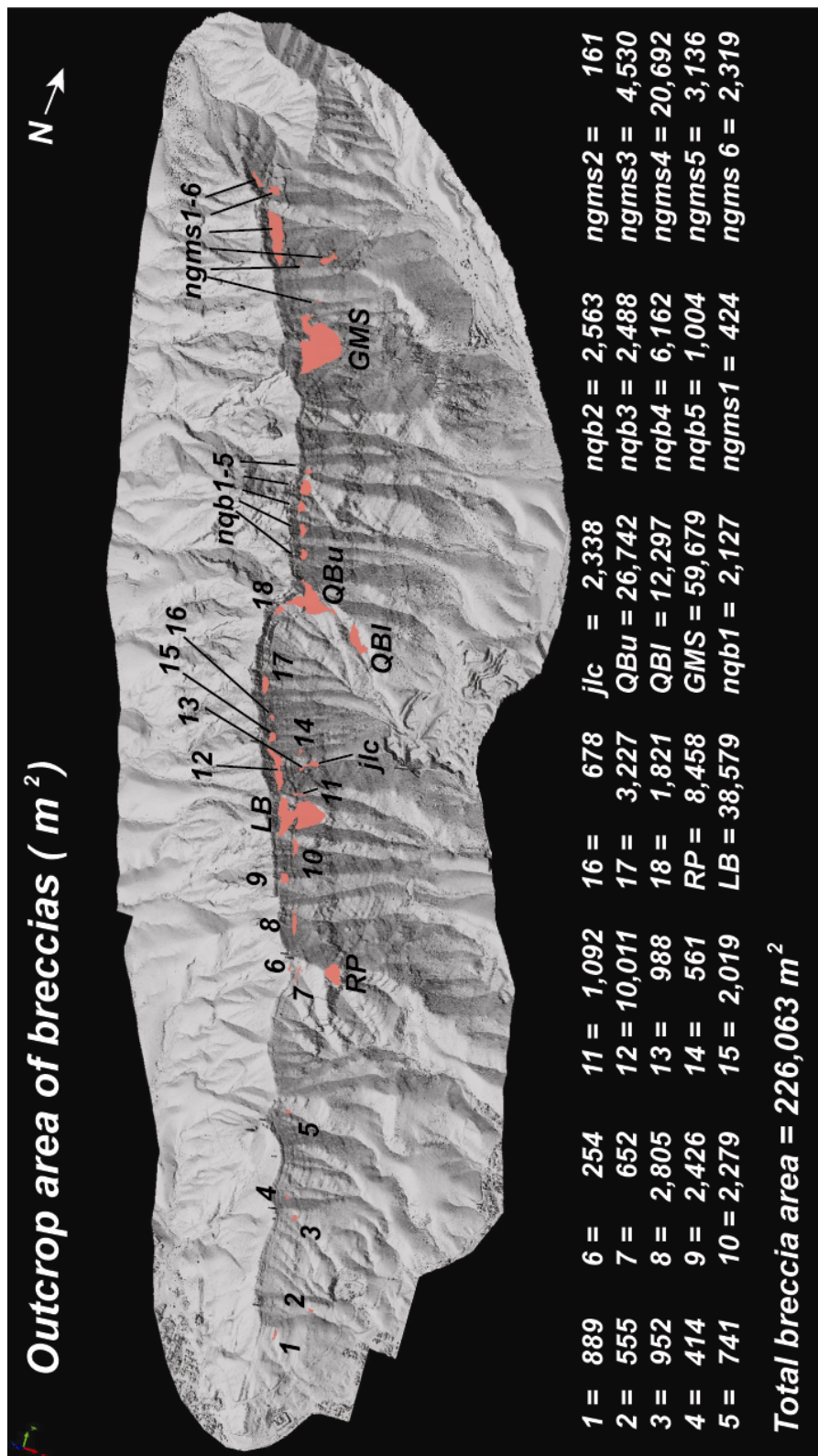


Figure 1.20: Breccia bodies that outcrop along the east face of the SFM. RP = Ranger Peak Breccia, LB = Lechuguilla Breccia, jlc = Jerry Lucia Cave, QBI and QBu are Quarry Breccia lower and upper respectively, GMS = Great McKelligon Sag, nqb = north of Quarry Breccia (1-5), ngms = north of Great McKelligon Sag (1-6). All numerical breccia names increase in value from south to north. For example, nqb1 is the southernmost nqb breccia and nqb5 is the northernmost. A photographic panorama of the east face may be found on plate IV.

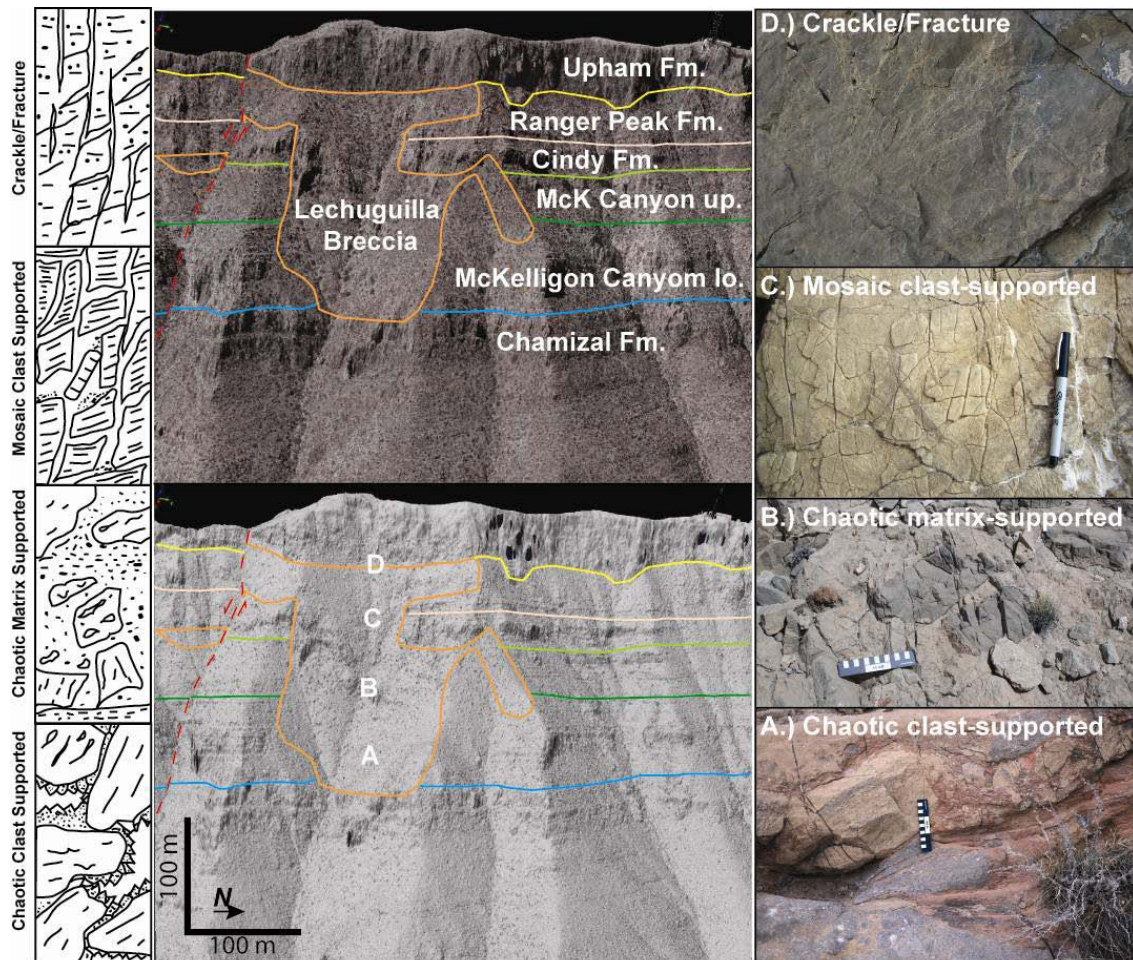


Figure 1.21: The idealized breccia stacking (left) of Kerans (1989) illustrates the breccia stacking character observed in the Lechuguilla Breccia (top-center). Stratigraphy and breccia outlines are duplicated on a color-draped (top-center) and a sun-shaded (center-bottom) lidar images. The ability to shift between the color-draped and sun-shaded lidar pointclouds reduced uncertainty in direct interpretation of lidar data and highlighted areas that required additional field scrutinization. There is no vertical exaggeration in these images but structural dip has been removed to return bedding to pre-Basin and Range/Rio Grande Rift deformation. Breccia facies photos (far right) are taken from locations A-D within the Lechuguilla Breccia. McKelligon Canyon up. and lo. are the upper and lower informal divisions separated by the EP 2 sequence boundary (figure 1.3).

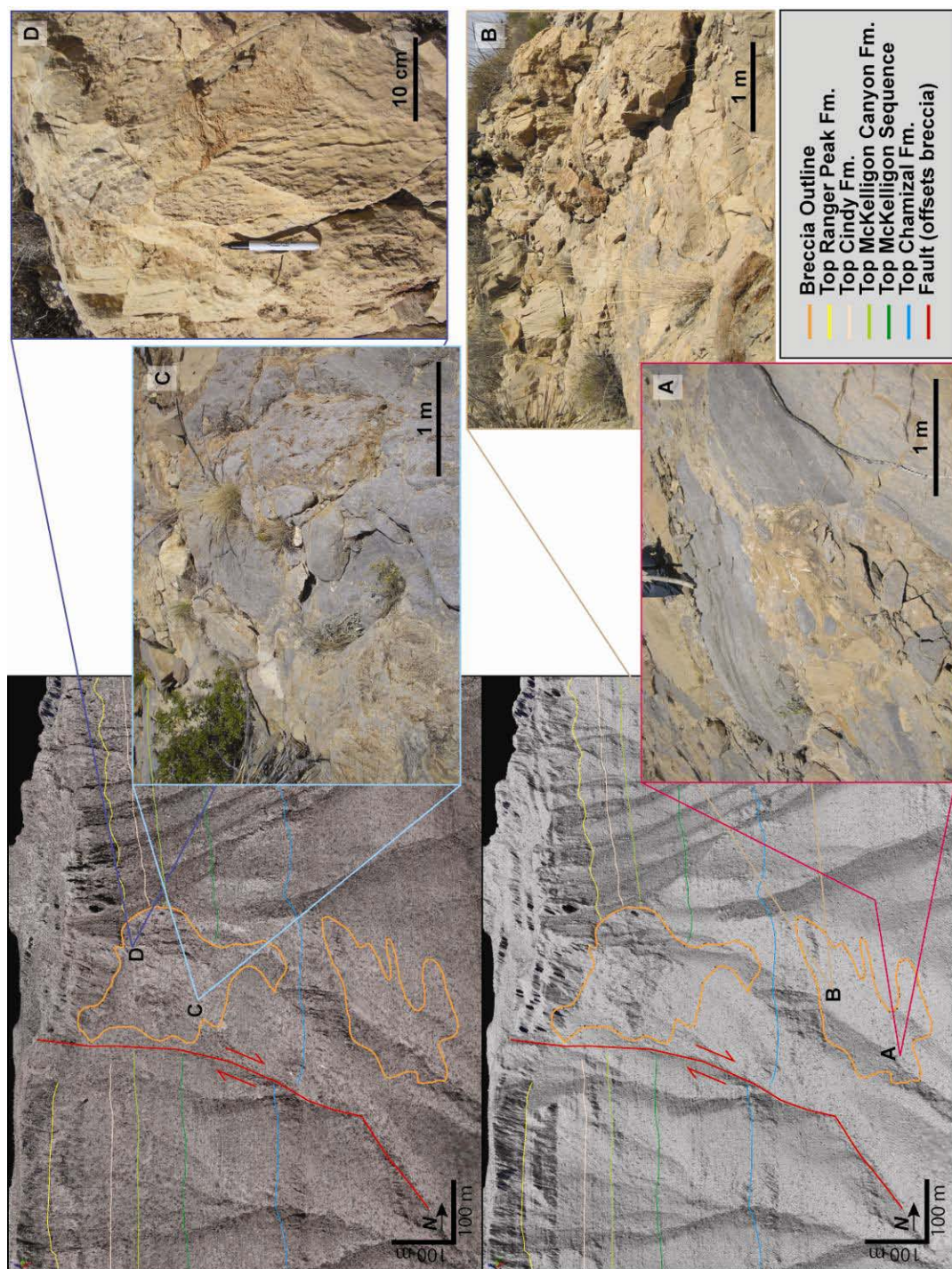


Figure 1.22: The Quarry Breccia has two separate breccia bodies with similar fill pattern to Lechuguilla Breccia (figure 1.21). The lower breccia (A and B inset) is dominantly large clast and matrix supported chaotic breccia. The upper breccia has similar fill to the lower but contains a zone of smaller clast sizes near the top (C and D); the two breccias appear to be a continuum following Kerans (1989) stacking.

Upham Formation dolomite blocks within a dolomitized matrix. Nowhere in the SFM have limestone Ranger Peak, or limestone Upham Formation clasts been observed within breccias. Dolomitized clasts of the Upham and Aleman Formations have been identified as much as 200 m below the contact of the Montoya and El Paso Groups within the Lechuguilla and Great McKelligon Sag breccia bodies. In addition, large (20-30 cm) clasts of the Fusselman Formation pentamerid brachiopod lag have been identified within the upper reaches of the Ranger Peak Formation breccias ~125 m below the stratigraphic equivalent strata (figure 1.17) within the upper Quarry Breccia.

Mosaic breccias are less commonly observed in SFM breccias except in areas where beds overhang or sag down stratigraphically into breccias below such as the lower Upham Formation above brecciated Ranger Peak in the Lechuguilla and Upper Quarry Breccias and the lower Chamizal above the brecciated Hag Hill in the lower Quarry Breccia (figure 1.22, plate IV), which transitions from chaotic to crackle along most of the contact. Mosaic breccias are typically found only within the upper few meters of laterally restricted breccias. Near-vertical host-rock contacts show far less, if any brecciation. The transition from chaotic breccia to intact host rock occurs within a few centimeters (figure 1.23) with little to no evidence of mosaic or crackle brecciation. It is logical that collapsed cave type breccias would have abrupt transitions along vertical walls because compaction would likely not disturb cave walls or floors in the same manner as a roof may be disrupted under compaction (Ford and Williams 2008).

The dimensions of the laterally restricted breccia bodies of the El Paso Group are extremely large compared to those predicted to be stable as single cave passages (figure 1.24) (Loucks 1999). The average NW-SE breccia body dimension exposed along the east face of the SFM is well over 100 m. This size indicates either the breccia bodies mapped are aligned to the long dimensions of vertical to subvertical tabular cave passages or these are part of a coalesced collapsed paleocave system. The lack of evidence for multiple cave passages, such as repeated



Figure 1.23: Vertical contact of chaotic breccia body of the Lechuguilla Breccia (LB), with the intact host rock of the McKelligon Canyon Formation (McK). Note extremely sharp contact with the host rock.

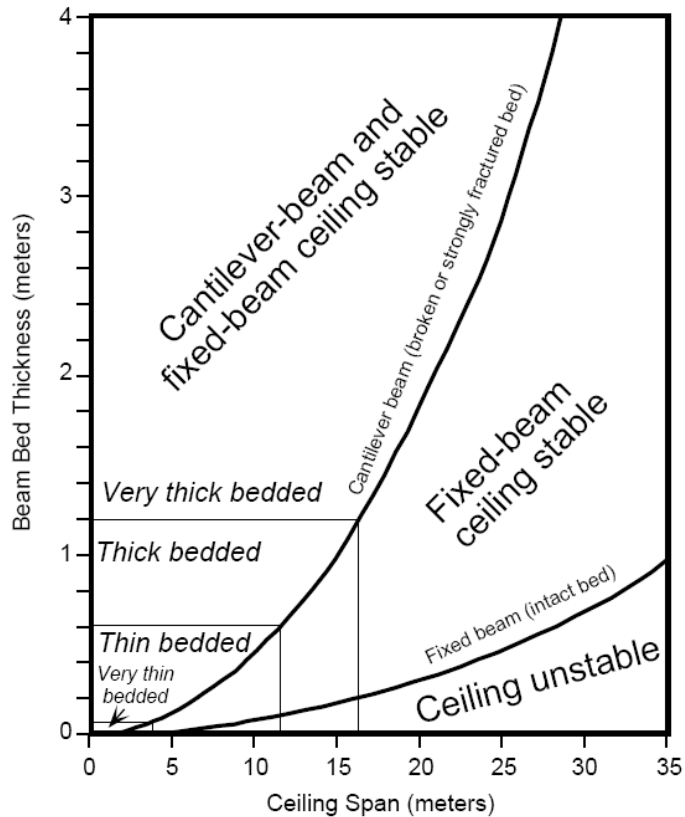


Figure 1.24: This diagram (after Loucks 1999) illustrates the important relationship of fractured versus non-fractured ceiling beam. Actual ceiling span is dependent on the rock strength (compressive strength) of the beam in question. This diagram is related to the actual ceiling span assuming a non-arched chamber therefore, as commonly is the case, an arched chamber may create a room substantially wider than 35 m (which would be outside the reasonable limits of this chart) wide even if heavily fractured. This is because the actual span required by an arched chamber may only be a few meters for a chamber with dimensions well over 50 m in diameter. Flat-ceiling caves are most common in bedding-plane parallel cave system.

zones of breakdown and cave sediment infill through mosaic and crackle breccias that would stack in an idealized vertical cave fill to roof collapse succession (figure 1.21), indicates these breccias were likely formed from a single large collapse chamber rather than a composite cave system. Additional analysis is needed to better constrain parameters such as porosity redistribution and breccia volumes, topics that are outside the scope of this discussion but will be addressed in the following chapters.

The laterally extensive breccia system as originally defined (Lucia 1971) does not exhibit the same degree of organized vertical arrangement of breccia facies as observed in laterally restricted breccias. These breccias are quite variable in texture and can be chaotic, matrix-supported polymictic breccias like those exposed north of Quarry Breccia (plate IV, breccias nqb1-5) and are typically not "laterally extensive" but are relatively small in outcrop area (figure

1.20) and simply closely spaced. The laterally extensive breccia system is dominantly observed within the Ranger Peak Formation, but small breccias similar to those found within the Ranger Peak Formation are located throughout the SFM study area (figure 1.20 and plate IV). Other breccias similar to those of the Ranger Peak Formation are present within the El Paso Group (figure 1.20 and plate IV; breccias 3, 5-8, 10, 11, 13, 14, jlc, and ngms1-3). The matrix material of these breccias can be tan to yellow-to-white dolostone but may have red silt with dolomitized and re-brecciated, fractured clasts. In the ngms1-3 breccias, rounded clasts of El Paso Group, Montoya Group, and saddle dolomite have been observed (plate IV, inset photo ngms2b) in the lower McKelligon Canyon Formation.

The individual breccia bodies of the laterally extensive system occur within the Ranger Peak Formation (figure 1.20 and plate IV breccias 1, 4, 9, 12, 15-17, nqb1-5, and ngms4-6). The margins of these breccias are difficult to identify due to pervasive dolomitization of both the breccia bodies and intervening Ranger Peak Formation. Neither lidar data nor air photographs alone were sufficient to accurately interpret breccias within the Ranger Peak Formation, and undoubtedly some may have been missed. The dolomitization of the breccias and host rock can be identified from high-resolution air photos, but the boundary between dolomitized breccia and dolomitized host rock is indistinguishable. Ranger Peak Formation breccias with larger clasts and clearly disrupted bedding, such as those to the north of Quarry Breccia (nqb in figure 1.20) can be roughly identified on lidar and whenever possible were field checked. Even in the field, pervasive dolomitization makes breccia identification difficult, especially when breccias are composed of primarily dolomitized Ranger Peak Formation within a dolomitized matrix material (plate IV). Chaotic slab-supported breccias observed in the stratigraphically lower, laterally restricted breccia bodies have not been observed within the Ranger Peak Formation breccias.

Vertical breccia *pipes* (Lucia 1995) have been documented passing from the Ranger Peak Formation through the entire exposed Montoya Group on the west side of the SFM in both Cindy and Transition Canyons. Mapping conducted in this study indicates that these pipes are

near-vertical tabular breccia bodies, some of which have offset, down to the east. A total of 10 tabular breccias have been identified in this study; they are between 50 and 500 m in length and 30 and 75 m in width (plate II). Composition of these tabular breccias is variable but typically consists of chaotic clast-supported and matrix supported breccias with no indication of crackle or mosaic breccias preserved in outcrop. Boulders of the Aleman, Cutter, and Fusselman Formations have been documented within these breccias (Lucia 1995). They are angular to subrounded (figure 1.25), and both clasts and matrix material are dolomitized. Several of these linear features tend to align in a general 340° orientation (plate II), but others are trend along north and northeast orientations. Additional discussion of these features will be presented in chapter 3 of this study.

1.14 Micropaleontology of the Breccia Systems:

To constrain the upper age limit of infill of these collapse features, twelve 3- to 5-kg samples were collected and processed to extract conodonts from various breccia matrices along the eastern face of the SFM. Lithified breccia matrix material was sampled to constrain the latest open phase of cavern fill before final compaction of the breccias. Eight samples yielded identifiable conodont species assemblages adequate for placement within currently accepted lower Paleozoic conodont biozones (Ross and Ross 1996). Sample locations are listed in metric Universal Transverse Mercator coordinates in table 1.1, including the most likely biozone for each sample (Repetski written com. 2007). In general, conodonts having the same biozone as that of the host rock are found within each of the breccia bodies, except for the Siluro-Devonian sample (#2412 in table 1.1) in the lower El Paso Group, Hag Hill Formation (Appendix C). No conodonts from the Middle or Upper Ordovician were found within the El Paso Group-equivalent breccia matrix material. This indicates that either the paleocave system within the El Paso Group was not in existence during the Upper Ordovician, it was completely infilled and later reactivated, or that it was somehow cut off from receiving marine sediment.

As an estimate of burial depth of the El Paso Group in the SFM, the alterations of the conodonts recovered were recorded. The conodont color alteration index (CAI) from the El Paso Group and Ellenburger varies significantly across Texas. In the Llano Uplift region of central Texas, CAI indices vary from 1.0 to 1.5, indicating temperatures of between 40° and 50°C (Kupecz and Land 1991), which equate to a maximum burial depth of only ~400 m, a considerably shallower burial depth than that indicated by Repetski's (1982) estimations for the southernmost SFM (120°–150°C) basis of CAI (3–3.5). This variation indicates that sometime

Sample No.	East	Northing	Elev (m)	Fm Equivalent	Most likely conodont zone
2368	359448	3520725	1640	Cz-RP	<i>Acodus deltatus</i> – <i>Oneotodus costatus</i> Zone through <i>Reutterodus andinus</i> Zone
2369	359437	3520695	1624	UMcK-RP	<i>Oepikodus communis</i> Zone or <i>Reutterodus andinus</i> Zone
2372	359222	3520676	1737	RP	<i>Reutterodus andinus</i> Zone
2373	359409	3520391	1638	HH-RP	Anywhere from the Low Diversity Interval through the <i>Reutterodus andinus</i> Zone
2395	359015	3521700	1738	UMcK-RP	<i>Oepikodus communis</i> or <i>Reutterodus andinus</i> Zone
2405	358977	3521677	1761	RP	<i>Reutterodus andinus</i> Zone
2412	359330	3521624	1580	L.Dev (?) & McK-RP	Lower Devonian/Upper Silurian and <i>Oepikodus communis</i> – <i>Reutterodus andinus</i> Zone
2428	359412	3520330	1658	McK-RP	<i>Acodus deltatus</i> – <i>Oneotodus costatus</i> to <i>Reutterodus andinus</i> Zone

Table 1.1: Locations (UTM Zone 13N) of conodont samples recovered from the SFM. Analysis done by Repetski at USGS Reston, VA, laboratory. formation abbreviations: McK = McKelligon Canyon Formation, UMcK = Upper McKelligon Canyon Formation, RP = Ranger Peak Formation, L.Dev (?) = Lower Devonian/Silurian range, HH = Hag Hill Formation, Cz = Chamizal. Correlation chart insert (plate 1) contains additional information about these zones.

between Ordovician deposition and the present, rocks bearing conodonts were elevated to temperatures of at least 120°C. These values can be used to calculate a range of burial depths using a geothermal gradient range from 25-33°C/km previously used for this area (Stepanek 1984). The results of this calculation indicate that the SFM either experienced a burial depth

between 2.9 and 5 km or they were otherwise heated to the temperatures required to alter conodont specimens. In the Franklin Mountains, Tertiary intrusives near the lower El Paso Group measured section (Repetski 1982, 1988) could have been an area of elevated localized temperature; however, the samples from this study are from several hundred meters above these intrusions and are unlikely to have been altered from intrusion-related temperature increase. Gamma-ray well logs from section 40 in Hudspeth County (next county east of El Paso County) have electric well-log patterns at least 2,700 m deep. The log patterns are similar to those of the Montoya Group from the Permian Basin (Rebecca Harrington 2008, personal com.), which is similar depth to previously published Montoya well log depths from the Dollarhide Field of the Permian Basin that produces from both the Ellenburger and Fusselman (Herald 1957).

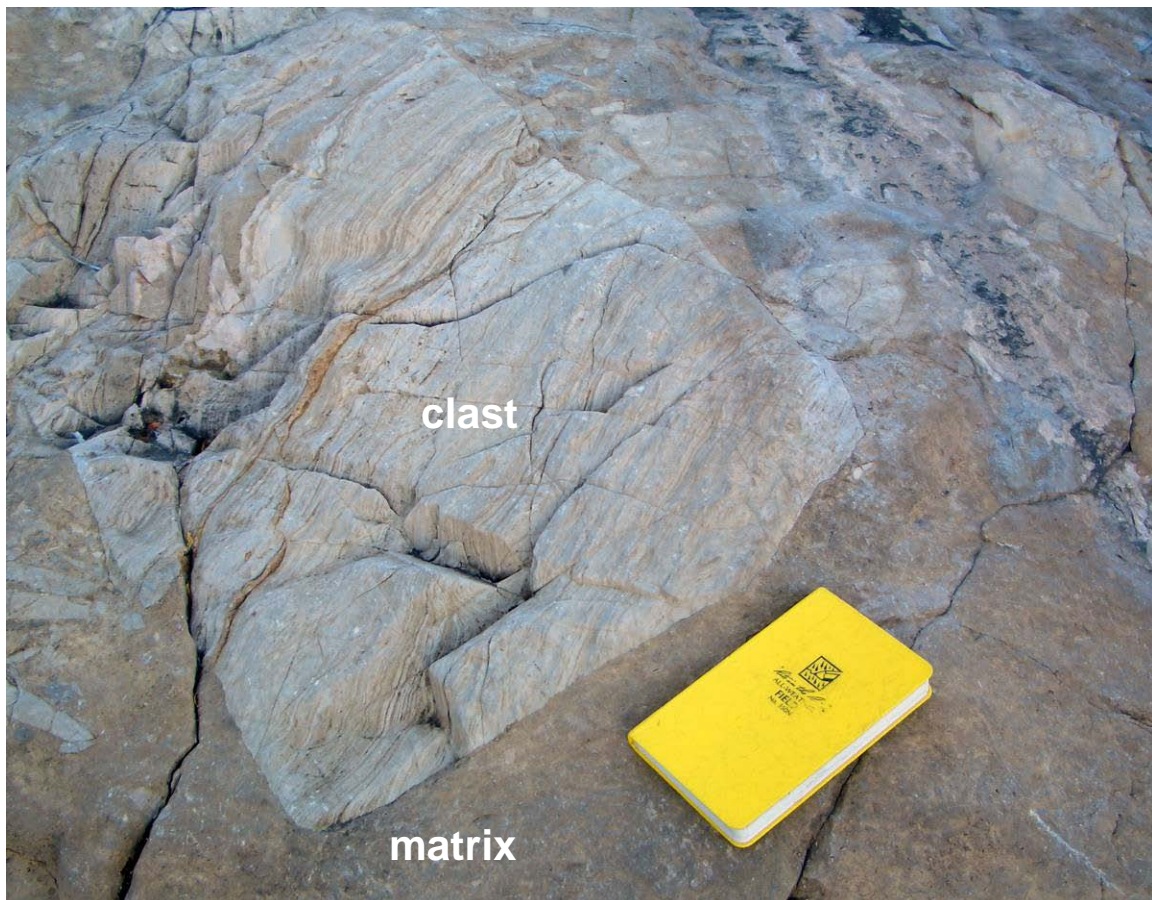


Figure 1.25: Breccia pipe clast and matrix from west side of mountain in Cindy Canyon. Field book is ~20 cm long.

Two samples were processed for palynologic content. They were barren of palynomorphs, so no age or environment interpretations could be made. As is common in barren outcrop samples (Appendix D), the small residue consisted of modern pollen, soil/root fungi, miscellaneous plant fragments, and insect fragments, all of which indicate successful processing and handling of the specimens. This is by no means a full palynological investigation, but initial findings were barren.

1.15 Discussion:

The southwest part of the Great Ordovician Carbonate Bank can be characterized by at least five facies associations (I–V), which range from more distal to shoreline to more proximal and peritidal environments of deposition. Four 3rd order depositional sequences between the latest Cambrian and the end of the Early Ordovician have been identified on the basis of high-frequency stacking patterns (Goldhammer et al. 1993) that have been adapted to the latest geological time scale (Gradstein et al. 2004) and incorporate the entire El Paso Group. It is not possible to determine the full thickness of the El Paso Group in this locality, but it is one of the most complete and well exposed sections in Texas and New Mexico, at ~500 m (Lucia *in press*). A Lower Ordovician passive-margin epeiric shelf was established with warm, tropical, open-marine circulation (Goldhammer et al. 1993; Bickford et al. 2000; Markello et al. 2006). Prolific carbonate sediment production and accumulation from this time make up the El Paso Group.

During the ~10 m.y. period between the latest Early Ordovician and early Late Ordovician, there was extensive subaerial exposure of the El Paso Group strata that was proposed (Lucia 1971, 1995) to be the time when meteoric cave and karst processes modified the uppermost 300 m of the El Paso Group. This karst modified surface and extensive vertical cave system was succeeded by marine limestone deposition that resumed in the Late Ordovician Period (Lucia 1971, 1995). A second period of karst modification occurred at the end of the Silurian at the top

Tippecanoe supersequence boundary (plate I), which connected the El Paso Caverns to these younger Silurian paleocaves through vertical "pipes" allowing material to be transported downward vertically from the Silurian strata into the level of the El Paso Group, some 300 m below. The map pattern of these vertical pipes can be seen on the geologic map in plate II along the western dip slope of the SFM.

Several important questions are related to the development of the karst system of the El Paso region. For example, how much of the paleocave system formed during this Sauk-Tippecanoe unconformity? In plate I, a long-term eustatic sea-level trend is indicated for the entire Ordovician. A brief eustatic fall is shown between the uppermost Ibexian and top Rangerian Laurentian series. No conodont fauna from the Rangerian have been recovered in the study area. In addition, the uppermost Ibexian biozone is present (*R. andinus*). This requires a deviation from eustatic sea level in the El Paso region, and it implies a potential lag in relative sea-level fall along the southwestern flank of Laurentia during peak greenhouse conditions. There have been no Middle Ordovician, Upper Ordovician, or early Silurian fauna found within the matrix material of the breccia fill from various levels within the El Paso Caverns in this or previous studies (Cloud and Barnes 1948; Repetski 1982, 1984; Lucia 1995). It is unusual that marine deposition could follow (open marine Montoya and Fusselman) extensive cave development several hundred meters deep within the El Paso Group, yet no macro or micro fauna have been identified within the cave sediments.

The breccia matrix material has been documented as having laminated silt within sediment-filled caves (Lucia 1995). Some of the best examples of internal sediment lamination are exposed in the "jlc" breccia body (figure 1.20 and plate IV), which is near the base of the McKelligon Canyon Formation ~300 m below the Sauk-Tippecanoe unconformity surface. The presence of laminated sediment indicates deposition in the vadose or high-phreatic zone (Lucia 1971 pg. 202). The vadose zone would therefore need to be ~300 m below the Sauk-Tippecanoe unconformity in order to deposit these laminated sediments. This would require a significant drop

in relative sea-level in the study area. As previously pointed out, the El Paso Group and Montoya Group are both marine limestones deposited along the southwestern passive margin of the Laurentian paleocontinent, likely within ~10 m of relative sea level (Wilson 1993).

A mechanism for extreme base-level lowering of this magnitude has not been identified in the Lower Paleozoic and is problematic. Either these cave sediments were carried into the system during higher-frequency third-order relative sea-level falls or this matrix material entered the system at some later time during tectonic uplift. The most-well-documented period of uplift in this area is during the Laramide orogeny (Carmichael and Ortega 2008). The structural evolution of the El Paso region is highly complicated because it is the intersection of several major North American tectonic terrains, including the controversial "Texas Lineament" (Muehlberger and Dickerson 1989), the southern Ancestral Rocky Mountains (Kluth and Coney 1981; Ye et al. 1996), and a transitional zone between thick and thin-skinned tectonics during Laramide compression and Basin and Range/Rio Grande Rifting (Carmichael and Ortega 2008).

Vertically connected fractures have been cited as the conduit that guided water unsaturated with respect to calcium carbonate deep into the phreatic zone of the El Paso Group during cave formation (Lucia 1995). No evidence has been found for the origin of these fractures, and specifically it is unknown why they are vertically connected in clusters that form the laterally restricted breccia bodies at 1 km spacing. It is possible that some previously unrecognized structural fabric controlled the spacing and location of these breccia bodies but none have been verified. A possible candidate for this could be some level of reactivation of the controversial Grenville "Texas Lineament" proposed by Muehlberger and Dickerson (1989), but the orientation of this structure is perpendicular to the fracture orientation proposed by Lucia (1995).

The size of the SFM breccia bodies is problematic; single cave chambers larger than 12 m across are extremely rare according to modern cave studies (Loucks 1999). It is likely that the breccia bodies observed in the SFM are the result of a composite cave system (*sensu* Loucks 1999) rather than a single event. This alternative model would not require extensive, vertically-

connected fractures and could have formed gradually over time at each third-order depositional sequence boundary (figure 1.3). This style of paleokarst development could lead to a vertically stacked succession of caves forming preferentially above one another from fractures and focused fluid flow from previous, older caves below. These vertically stacked caves would likely be connected during the Sauk-Tippecanoe unconformity, acting as a conduit to focus subsurface groundwater flow.

The critical limitation of this model is that no clear evidence has been identified in the field for multiple cave levels within the breccia bodies mapped. The vertical breccia facies associations indicate continuous collapse of a single large system. Modern composite cave systems tend to build downward at some unknown time scale, with the youngest dissolution occurring deepest in the system (Loucks 1999, Palmer 2007). The global sea level trend for the Ordovician (plate I) is a long-term transgression that is contradictory to the ~10 m.y. falling relative sea level that would be required to create a 300-m-deep cave system along a continental passive margin.

The cumulative stratigraphic thickness of the Sauk and Tippecanoe supersequences in this region is between 780 and 1,000 m (Richardson 1909; Harbour 1972; Seager and Mack 2003). Montoya and Fusselman clasts are common within the breccia bodies within the El Paso Group, and a crude stratigraphic order within the breccia bodies is present. All identifiable breccia clasts were transported stratigraphically downward and occasionally reworked by transport within the paleocave system, resulting in sub-rounded clasts. In a few cases, the crude vertical stacking is significantly violated. Two examples of this are (1) Montoya dolomite and bedded chert clasts (Upham and Aleman?) that have been identified more than 300 m below their original stratigraphic position within breccias north of the Great McKelligon Sag (plate IV, ngms2t), and (2) Siluro-Devonian conodonts that have been identified within breccias located within the Hag Hill Formation within the lower Quarry Breccia matrix material (Appendix C). This would require transport of sediment down over 500 m below the top Fusselman surface during peak greenhouse conditions. These observations indicate an extremely complex subsurface karst

system within the strata rimming the Laurentian paleocontinent during passive-margin conditions with no previously documented tectonic evidence for uplift.

Modern cave systems far exceed this level. The deepest cave currently known, Krubera-Voronja Cave in the Republic of Georgia, more than 2191 m deep and follows a near-vertical path downward. The cave entrance to Krubera is 2300 m above sea level and is within the Arabika Massif of the Gagra Range east of the Black Sea (Ford and Williams 2008). Other tectonically active areas in Eastern Europe, the Alps, and the Appalachians form large vertically extensive chambers, but these are all where tectonic uplift drives base level downward, not at or near sea-level along a passive continental margin such as the El Paso region was during the Lower Paleozoic.

1.16 Conclusions:

Biostratigraphy, chronostratigraphy, sea level and isotopic trends were summarized for the region (plate I). Field observations were integrated with high-resolution airborne lidar data and used to create a geological map of the southern Franklin Mountains at the formation scale (plate II). The sequence stratigraphy of the region was updated and calibrated to the most current geological time scale (figure 1.3) and breccia bodies observed within the SFM were mapped within the stratigraphic framework (figure 1.20 and plate IV). The 3rd order depositional sequences discussed in this study are:

EP 1, which includes Bliss Sandstone through Chamizal dolostone;

EP 2, which includes uppermost Chamizal through lower McKelligon Canyon Formations;

EP 3, which includes the upper McKelligon Canyon through Cindy Formations; and

EP 4, sequence composed of Ranger Peak dolomitic limestones.

These depositional sequences were built upon the previous high-frequency cycle stacking pattern analysis of Goldhammer et al. (1993) and incorporate relative positions of collapse brecciation within this stratigraphic succession. The occurrence of breccia bodies in relationship

to sequence boundaries or sequence boundary zones indicates a possible link between 3rd order depositional sequences and cave formation (plate IV), even though no strong evidence exists for extensive karst directly on these third-order depositional sequence surfaces. This model reduces the magnitude of, if not removes the need for, a vertically connected fracture system of unknown origin to focus unsaturated fluid deep into the El Paso Group strata. Additional work is needed to better constrain size of the original paleocave void required to result in breccias the same size as those preserved in the SFM.

According to previously published cave passage dimensions (Loucks 1999) there is less than a 1.2% probability of a cave passage exceeding 10 m in width. On the basis of these calculations, it would be unlikely, if not impossible that the breccias observed in the SFM originated from a single cave passage unless exposures along the east face are oblique or parallel to the long axis of a near-vertical tabular cave. A possible modern analogue for the El Paso paleocaves could be the spectacular upper passageways within Jewel Cave in the Madison Formation of the Black Hills of South Dakota (Palmer and Palmer 1989) which follow along sub-vertical fractures in the Mississippian Madison Formation.

Conodont biozonation within the El Paso Group breccia matrix material indicates that no definitive older biozone conodonts were found within younger strata. This, along with breccia clast identification in the field, supports downward transport associated with a collapsed paleocave system for both clasts and matrix material. Large Fusselman Dolomite clasts and Siluro-Devonian conodonts recovered from the Ranger Peak and Hag Hill Formation equivalent breccias respectively in the Quarry Breccia are problematic but indicate that conduits capable of transporting sediment stratigraphically downward >500 m were open after deposition and lithification of the Fusselman Formation. This indicates either reactivation of an Ordovician composite paleocave system during top-Fusselman time, or the possibility that a post Fusselman speleogenetic event may be viable alternative models for the El Paso region collapse breccias. The timing of formation of the breccia bodies observed in the SFM is still unclear however; these

breccias were formed by collapse of material into an open void sufficient to allow extensive vertical (downward) transport of clasts and sediment as previously documented (Lucia 1995).

A similar vertical and horizontal distribution of breccia body character is observed in the Ellenburger Group of the Permian Basin (Kerans 1989), where oil and gas wells containing breccia in the upper 90 m below the Sauk unconformity were correlatable regionally. Wells with >600 m thick laterally restricted breccias do not correlate with wells only 400 m away. The large, laterally restricted breccias in the SFM that are spaced at >400 m lend support to this subsurface model. The Permian Basin Ellenburger differs from the SFM in that the Middle Ordovician Simpson Group shales separating the Lower and Upper Ordovician are absent in the SFM.

Chapter Two: Paleocave Mapping and Reconstruction with Hyperspectral, Airborne, and Ground-based Lidar Data; Franklin Mountains, El Paso, Texas

Abstract:

Paleokarst breccia systems are a special type of compound diagenetic-depositional-structural deposit that make up important subsurface hydrocarbon reservoirs and Mississippi Valley Type mineral deposits. The spatial distribution of paleo-caves and associated collapse breccias, and their relationship to fluid flow in subsurface reservoirs continues to be a complex issue. The abrupt vertical and lateral heterogeneities associated with these collapse systems are commonly not well resolved on seismic data and are well below typical hydrocarbon reservoir interwell spacing. The breccias of the Lower Ordovician El Paso Group exposed in the southern Franklin Mountains of west Texas were selected as a subject for outcrop to subsurface analog geological modeling. The southern Franklin Mountains contain a large paleocave system which exposes several paleocave breccias and apparent suprastratal deformation above the collapse horizon.

In order to appropriately model these complex 3D paleokarst geobodies the El Paso Group exposures were mapped in the field and on remote sensing data. The entire outcrop was captured three-dimensionally using scanning airborne light detection and ranging or lidar. These data were used to create a high-resolution 3D digital pointcloud containing approximately 100,000,000 points over the 24 km² study area. The airborne lidar data were enhanced with high-resolution (30 cm) color air photographs and artificially sun-shaded using point-based rendering with normal vectors assigned to each point. Mineralogical attribute data were extracted from AVIRIS hyperspectral imagery and used to locate transitions between dolomitized regions and limestone host rock over the northern third of the study area. Over 100 linear km of lithological contacts were mapped and used to construct a Digital Outcrop Model (DOM).

A computer model was constructed from mapped stratigraphic and structural contacts in 3D and lidar data were used to populate breccia body locations within the model. The spatial distribution of the exposed breccia was used to calculate to determine a variogram ranges for breccia extrapolation within the unknown model cells. The modeling results were then compared to a modern cave system scanned internally with ground-based lidar. The modern cave, Devil's Sinkhole in Rocksprings, Texas was "collapsed" from an open void into a collapsed paleocave breccia body for model validation. This comparison showed similarity of collapse breccia volumes estimated from outcrop mapping and 3D geobody reconstruction from lidar data in the SFM to those calculated from a synthetic collapse of a modern cave.

2.1 Introduction:

Geologists, now, more than ever, are required to analyze, interpret, and convey complex, four-dimensional geological relationships quantitatively (x, y, z, and time). Lidar (light detection and ranging) is a method by which high-precision spatial measurements can be collected. Reliable geological interpretation can be conducted on these data as every laser point from a lidar pointcloud contains a 3D spatial coordinate. The interpretations from lidar data can be used to accurately reconstruct the stratigraphic, structural, and diagenetic architecture of a geological interval of interest. Passive imaging methods such as visible-light photography, multispectral, and hyperspectral imagery offer a semi-quantitative spatial template to understand natural systems. These observation techniques still flatten the Earth onto a 2-D map view. The integration of passive imaging methods with high-resolution lidar adds new life to these data.

In recent years active-remote sensing techniques that include ground-based laser scanning have become a common tool for many field geologists seeking to incorporate high-resolution quantitative spatial 3D data into outcrop modeling (Xu et al. 1999; Xu et al. 2000; Xu, 2000; Adams et al. 2004, 2005; Verwer et al. 2004; Bellian et al. 2005; Murphy et al. 2005; Collins and Kayen 2006; Friedmann and Stamp 2006; Phelps 2006; Bellian et al. 2007; Janson et al. 2007; Lee et al. 2007; Scott 2007; Wawrzyniec 2007; Olariu et al. 2008, Schindel and Cobb, 2008; Phelps et al. 2007, 2008; Roltevatn et al. 2009; Zahm et al. 2009). These studies utilize the 3D point clouds of areas a few square kilometers in size without gridding the data into regularly-spaced digital elevation model (DEM) format (*cf.* Bellian et al. 2005) to conduct stratigraphic mapping directly on the point cloud or point cloud derived triangulated surface data.

Airborne lidar has been used in regional tectonic studies (Kent et al. 2005; Wallace et al. 2006; Blakey et al. 2009), bathymetric and coastal studies (Storlazzi and Logan 2003; Paine et al. 2004; Rosser et al. 2005), impact crater mapping (Herd et al. 2008), and landslide and erosional monitoring (Adams 2002; Sallenger et al. 2002; Rowlands et al. 2003; Jones 2006; Young and Ashford 2006). These previous studies all used airborne lidar to conduct spatial analysis but

created DEM files from the data which although greatly reduces file size for large areas of analysis, reduces, if not removes the possibility to utilize vertical surfaces such as cliff faces, important to stratigraphic studies. Few studies have conducted oblique airborne mapping (Vallet 2007) and none so far have used airborne point cloud data for stratigraphic modeling.

Paleocave systems are spatially complex geological features that are difficult to model (Labourdette et al. 2008). Collapsed paleocave breccias in the southern Franklin Mountains (SFM) of El Paso, Texas offer a well-exposed continuous outcrop of a paleokarst system within the Lower Ordovician El Paso Group (figure 2.1) Previous work in the SFM Lower Paleozoic strata (Richardson 1909; Lucia 1968; LeMone 1968; Harbour 1972; Goldhammer et al. 1993) mapped stratigraphy of the SFM using traditional field methods. Similarly, field studies that mapped large breccia bodies within the El Paso and Montoya Groups described the relationship of breccias to major second order sequence boundaries (Lucia 1971; Kerans and Lucia 1989; Lucia 1995). In addition, mineralogical identification of breccia bodies using high-elevation, hyperspectral image analysis has been conducted (Bellian et al. 2007) but none of these methods offered adequate spatial data to attempt 3D geometric reconstruction of the breccias observed in outcrop.

In this study, integration of field observations, airborne lidar point cloud data, and spectral data (photographs and hyperspectral image analysis) were used to create a 3D geological model to reconstruct paleocave collapse breccia geometry within the El Paso Group strata. The reconstructed collapsed paleocave breccia body from the airborne lidar data was compared to a ground-based lidar pointcloud of a modern cave to validate the model results. Modern cave system modeling has just recently been conducted (Labourdette et al. 2007; Gary et al. 2008; Filippini et al. 2009) and 3D reconstruction of paleocave systems from outcrop is rare (Loucks et al. 2004).

The study area includes 24 km² of airborne lidar data at 0.7 m point spacing over the southern SFM. In addition, a 0.1 m ground-based lidar model from the modern Devil's Sinkhole,

Rocksprings, Texas. The geocellular model contains 10,000,000 grid cells and was built to resemble current geomorphology of the SFM using a combination of observations from this study and previously published data (Lucia 1995; Collins and Raney 2000). The geocellular model contained 177 layers with an average vertical thickness of 5 m over the 3 km x 8 km lateral dimensions.

2.2 El Paso Region Geologic Overview:

The Lower Ordovician El Paso Group exposed in the southernmost Franklin Mountains in El Paso, Texas (figure 2.1) was deposited on a passive continental margin that accumulated mixed carbonates and siliciclastics for approximately 10 m.y. (plate I, figure 2.2). The geologic time scale of Gradstein et al. (2004) is used in this study and sequence boundary ages proposed by Goldhammer et al. (1993) were adapted to this time scale. Four 3rd order depositional sequences are represented in the El Paso Group of the SFM and have been previously documented as EP 1-4 (chapter one, this volume). These depositional sequences are made up of vertically stacked high-frequency cycles that shoal upward. The El Paso Group formation names; Bowen, Hag Hill, Chamizal, McKelligon Canyon, Cindy, and Ranger Peak Formations (plate II, III and figure 2.2) follow the nomenclature of Lucia (1968). These formations consist of a succession of carbonates and some minor siliciclastic contribution concentrated around the sequence boundaries and alternate between subtidal to tidal-flat limestones to dolostones (Kerans and Lucia 1989; Goldhammer 1993).

Evidence for multiple subaerial exposure events has been previously documented (Lucia 1968; LeMone 1968; 1988; Wilson et al. 1993) but significant karst modification has been attributed only to the top El Paso Group unconformity. The top El Paso Group unconformity lasted at least 10 m.y. and defines the Sauk-Tippecanoe second order supersequence boundary (Sloss 1963) and has been proposed as the surface related to extensive meteoric paleocave formation (Kerans and Lucia 1989; Lucia 1995) prior to deposition of the Upper Ordovician Montoya Group.

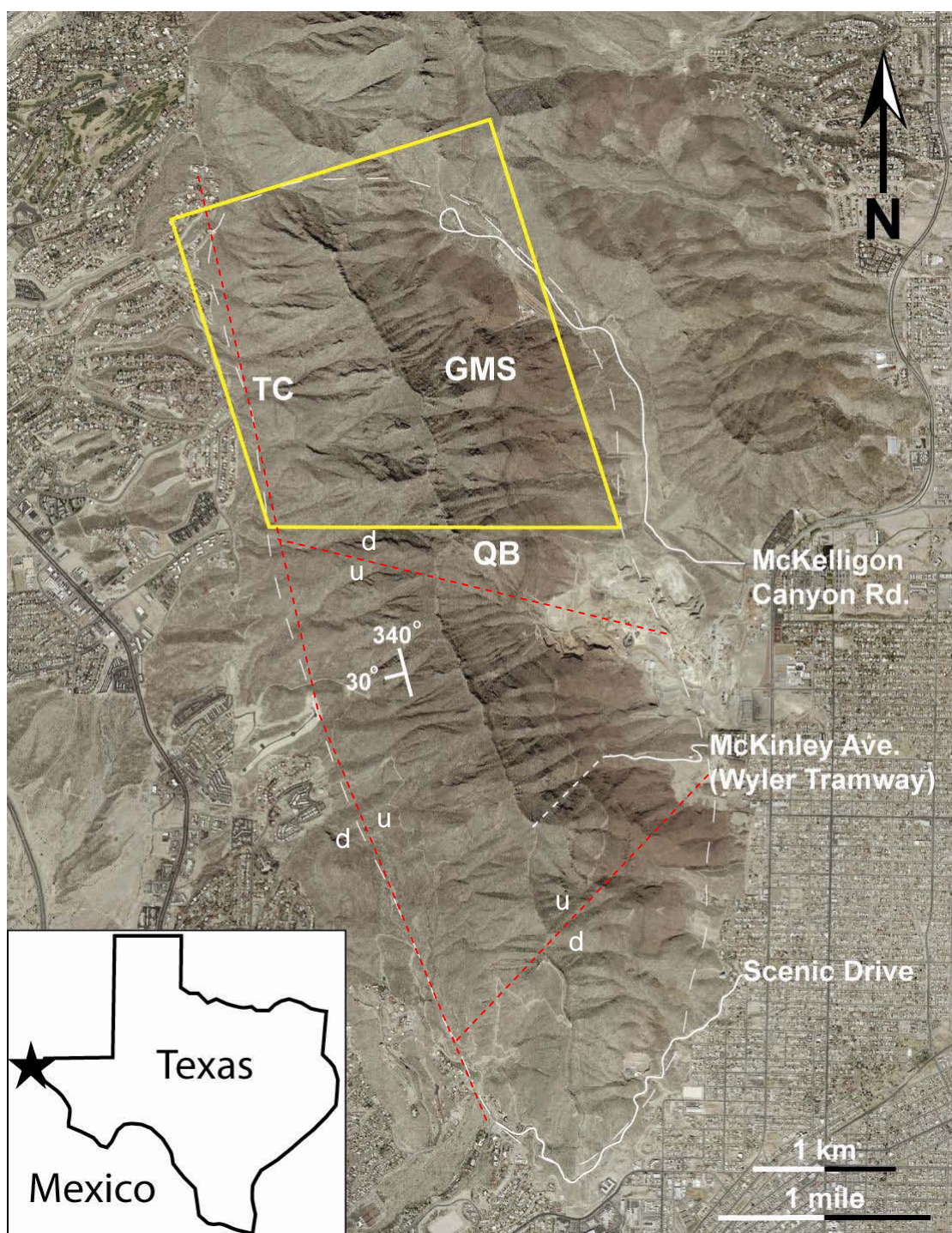


Figure 2.1: The general study area is located by the black star (inset). The yellow box in the main image outlines the AVIRIS hyperspectral coverage area overlapping the study area. Transition Canyon (TC), Great McKelligon Sag (GMS), and Quarry Breccia (QB) are labeled. Dashed white line is lidar study area. 30 cm resolution digital image data was downloaded from the USGS (<http://seamless.usgs.gov>). Red dashed lines show main faults modeled with uplifted (u) and downthrown (d) sense of motion indicated.

The Montoya Group was deposited in craton-wide, open-marine circulation system conditions as evidenced by extensive faunal diversity (Flower 1969) and predominance of bioturbation. The Montoya Group is in paraconformable contact with the El Paso Group and is disconformably overlain by the Silurian Fusselman.

The dominant lithology of the El Paso Group (~500 m) outcrop in the SFM is a dolomitic limestone, with two distinct strataform dolostone units within the relatively thin peritidal-to-supratidal Chamizal and Cindy Formations (plate III). Both of these formations exhibit evidence of subaerial exposure including mudcracks, wavy algal laminated bedding, and mud rip-up clasts but no obvious evidence of karst. These units coincide with the tops of 3rd order depositional sequences EP 1 and EP 3 (figure 2.2). The Chamizal and Cindy Formation dolomites are dominated by medium-crystalline dolomites (~20-50 μ m) and have been interpreted as early reflux in origin (Stepanek 1984; Lucia 1995). Other dolomites are present within the southern Franklin Mountains with larger, fabric destructive dolomite crystals (>50 μ m) that are localized within breccias and associated with selective facies-specific dolomitization penetrating into the host rock (Lucia 1995; Tillotson 2003). In addition, small quantities of coarse crystalline saddle dolomite have been documented both in the Franklin Mountains (Stepanek 1984; Lucia 1995) and in the subsurface Ellenburger Group and on the basis of carbon and oxygen stable-isotope analysis indicates a post-Devonian (Stepanek 1984) emplacement age for the coarser dolomites.

The modern structure of the SFM is the result of Laramide compression followed by Basin and Range/Rio Grande extension during the Cretaceous and Tertiary that brought these Lower Paleozoic rocks to the surface (Carciumaru and Ortega 2008). Deformation continued during Rio Grande Rift-related extension resulting in the northwest-southeast trending fault block observed today with an average dip of 30° west with a strike of 340°. Three large-offset faults that appear to have been

Franklin Mountains, West Texas

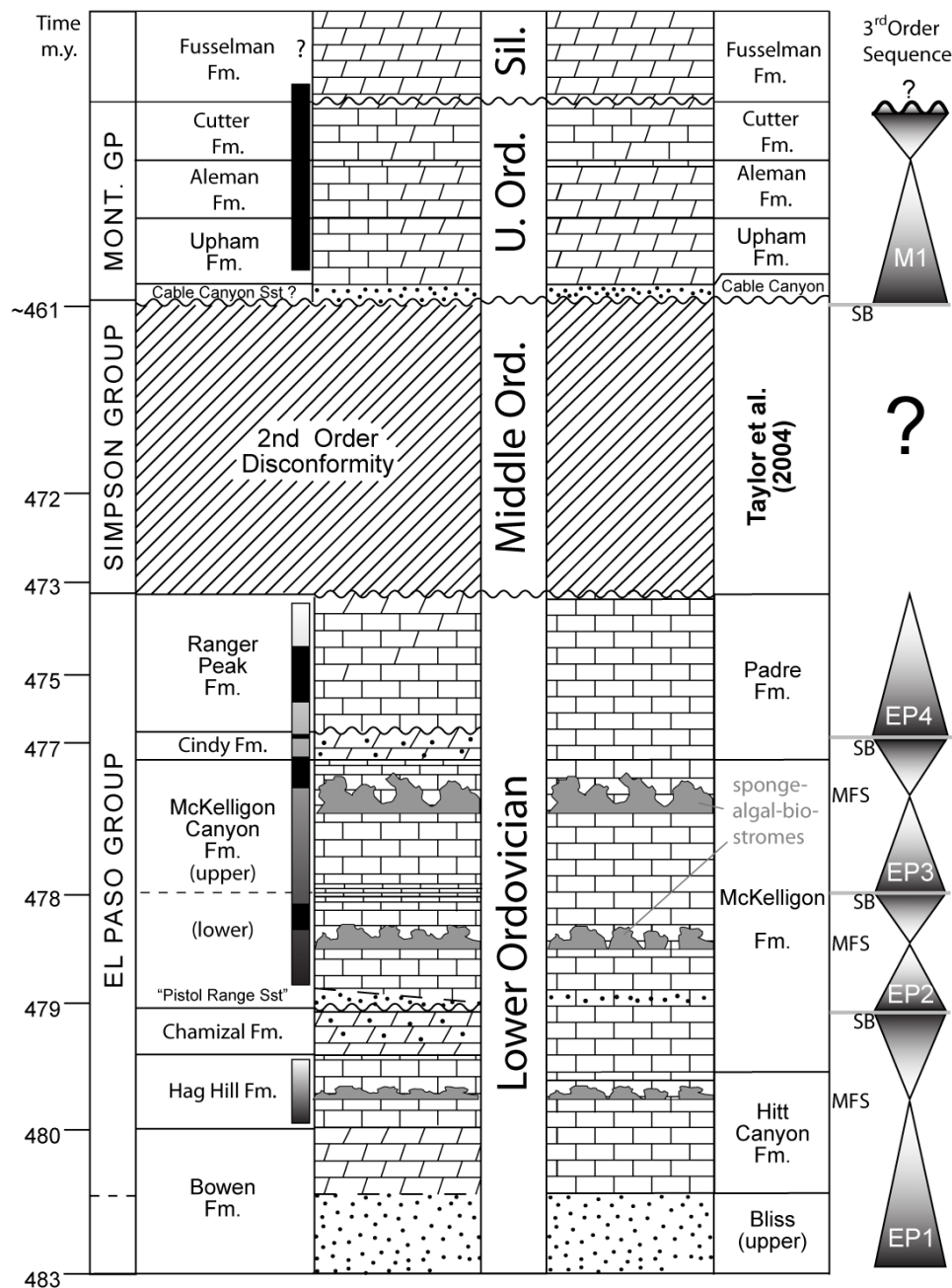


Figure 2.2: Third-order sequences EP1–4 described in text. Lithologic nomenclature after Lucia (1995). Triangle points indicate maximum flooding surfaces (MFS). Stratigraphic chart modified from Bellian et al. (2007) and Goldhammer et al. (1993) and correlated to work of Taylor et al. (2004). Note slightly higher base of the El Paso Group picked by Taylor et al. (dashed line), putting the El Paso Group base within the Bowen Formation. Bars in left column indicated brecciated zones. The gradient fill segments signify upward-fining of clasts within the breccias.

active during this phase of deformation are modeled in this study, the N-S Western Boundary Fault (Harbour 1972; Raney and Collins 2000; Wu 2002), a NW-SE normal fault near Quarry Breccia and the NE-SW normal fault parallel to Scenic Drive (figure 2.1). At least one of these faults has been documented as offsetting collapse paleocave breccias (near QB) within the study area and are most likely related to Rio Grande rifting.

2.3: Model for Timing of Cave Formation:

The most comprehensive published study of the paleocave breccias exposed in the SFM to date is Lucia (1995) which proposed that meteoric diagenesis and cave formation initiated at the top Sauk (El Paso-Montoya Group contact) exposure surface. The El Paso Group caves formed before deposition of the Montoya Group and have been compared to some of the largest known caves (Lucia 1971). Paleocave dissolution did not break through the top El Paso Group surface in the study area as there is no evidence of the overlying Montoya Group thickening into the collapse breccias below and no Middle or Upper Ordovician sediments have been identified within breccia matrix material (Appendix C). On the basis of results from conodont biozones (chapter one, this volume), only during/after collapse did post-El Paso Group material enter the El Paso paleocaves.

The collapse of the El Paso Caverns resulted in laterally restricted and laterally extensive paleocave breccias. The laterally extensive paleocave system formed along the water table limited to the upper 70 m of the El Paso Group at top Sauk time (figure 2.2). The laterally restricted system formed along vertically connected fractures that aided the transport of water unsaturated with respect to calcium carbonate over 300 m deep into the passive margin carbonate platform strata (Lucia 1995). These laterally restricted caves created voids large enough that slabs of El Paso Group could be transported downward vertically over 120 m from their original stratigraphic position. Conodont material transported over 500 m below its stratigraphic equivalent (Appendix C). Only the laterally restricted breccia bodies within the El

Paso Group are modeled in this study as they offer the most complete vertical exposure in outcrop and are somewhat problematic with regard to overall size and shape. These breccias have been interpreted as comparable to the largest caves known, yet would have formed at or near sea level along a passive continental margin without evidence for substantial tectonic uplift. Today's giant caves are dominantly located in areas of active uplift (Ford and Williams 2008).

2.4 Methods and Data:

It was recognized early in this study that the rugged terrain, structural deformation, steep to vertical outcrop faces and desert conditions of the SFM would make field mapping challenging. These same conditions however; preserve excellent exposures of strata with little soil or vegetative cover making it ideal for the integration of traditional field methods with remote sensing data. The digital outcrop model (DOM) workflow outlined by Bellian et al. (2005) was used in this study. Field mapping, global positioning data (GPS), air photographs, hyperspectral image analysis, ground-based and airborne lidar data were all combined to map the geology of the SFM. An important objective was to accurately map the geometry and distribution of the various breccia bodies and their associated contacts with the surrounding host rock.

The resultant DOM of the SFM was used as initial conditioning data in stratigraphic 3D grid (sgrid) in Gocad geological modeling software (Paradigm, Inc. Amsterdam, The Netherlands). The sgrid was built from surfaces mapped on the lidar pointcloud constrained by field observations and then extrapolated throughout the volume. Exposed breccias bodies mapped on the lidar dataset were used to populate the model cells intersecting the outcrop surface in the sgrid as "breccia" (facies code 1) and all other cells were assigned "non-breccia" (facies code 0). Extrapolation using categorical Kriging and categorical conditioned simulation (Dubrule 2003) techniques for property distribution were used to reconstruct possible breccia body geometries within the sgrid. Breccia volume was calculated from the interpolation results and compared to a large laterally restricted modern cave, Devil's Sinkhole. Devil's Sinkhole was chosen for its large

size and recognition as one of the best examples of a large, steep-walled karst depression in the United States (Palmer 2007). Devil's Sinkhole formed in the subsurface and likely due to uplift of the Edwards Plateau of Central Texas and associated fall in water table (Elliott and Veni 1994). In this study the lower portion of Devil's Sinkhole, hence referred to as "Devil's Cave" was laser scanned. The modern cave has not fully collapsed. Therefore, the breccia volumes that could result from its eventual collapse were calculated theoretically using a conservation of volume calculation (equation 2.1) presented below to compare with the SFM collapse breccias.

Patterns derived from the breccia body reconstruction modeling were compared to seismic time-structure maps from the Ellenburger Group draped with amplitude attributes from the Boonsville field (Appendix B) in the Fort Worth Basin. This dataset has been previously compared with the Franklin Mountain breccia geometries (McDonnell et al 2007) as an outcrop analog for collapsed paleocave stratal geometry. Although the breccia bodies within the Ellenburger are not interpreted as sinkholes, the comparison is relevant because the Devil's Sinkhole was a large cave before it broke through to the modern surface similar to the model proposed for the El Paso Group caves (Lucia 1995). These data are presented only for scale reference and not intended to indicate a suitable match between modeled patterns from the SFM and the Boonsville data.

2.4.1 Field methods:

Stratigraphic sections were measured in the field, and used to link previous work (Lucia 1968; Repetski 1982; 1988; Taylor et al. 2004) to the lidar-generated DOM. An informal type section of undisturbed Cambro-Ordovician strata north of Quarry Breccia is presented in plate III. Hand-held GPS locations of samples, stratigraphic contacts including breccia outlines were collected in the field with wide area augmentation system (WAAS) enabled for more accurate location; typically +/- 3 m error in latitude and longitude. Despite enabling WAAS, the GPS readings frequently had high error values (+/- 20 m) due to the steepness of the SFM, deep-cut canyons, and general lack of full-sky view, especially when working on the east face. In these

situations, air-photographic panoramas were used to locate positions manually and later identified on the lidar data (described in the next section). Lidar data were used as the basis for all measurements as it contains the most accurate 3D spatial information for this study (Appendix A). All GPS and photograph locations were adjusted to the lidar data to minimize absolute error.

2.4.2 Airborne lidar data acquisition:

Airborne lidar operates in the same way as ground-based lidar and when treated as a 3D pointcloud and not a DEM (*cf.* Bellian et al. 2005) it can be used to construct a DOM. Typical point spacing of an airborne survey results in a pointcloud with spacing of 1.0 and 2.0 m. Airborne lidar data are frequently used to create DEMs for large-scale geomorphological surface studies (Sallenger et al. 2002; Adams and Chandler 2002; Storlazzi and Logan 2003; Paine et al. 2004; Rosser et al. 2005; Kent et al. 2005; Wallace et al. 2006; Young and Ashford, 2006; Blakey et al. 2009). This resolution or point spacing of airborne lidar is low for use in sequence stratigraphic computer modeling. In addition, these data are, as the name implies, collected from an aircraft, and are intentionally acquired looking down in *map view* from several hundred meters above ground level. This "down-looking" perspective creates data shadows in steep, cliff-forming areas that are parallel to the acquisition angle of the aircraft. Steep cliff faces contain the information stratigraphic modelers require observations from, which has in part lead to the limited if not absence of airborne lidar data integration within published stratigraphic modeling literature. A second limitation is the historically high cost associated with high-resolution airborne lidar acquisition.

In this study a modified acquisition technique was used to minimize shadow effects and maximize cliff-face lidar coverage. An airborne survey was acquired with a close range (eye-safe) instrument from a helicopter flying at low-elevation with maximum sweep angle (+/- 40° from vertical). In addition, the flight plan followed an oblique trajectory to the mountain's structural trend (figure 2.3). Thus, excellent vertical data coverage was attained with few vertical cliff

shadows without the need to fully tilt the lidar unit within the aircraft (Vallet 2008). In addition to the modified lidar acquisition, processing techniques were adapted to more effectively manage the large point cloud files associated with these data. The modified processing techniques were conducted to speed visualization of the data for efficient DOM construction. This will be discussed in the lidar data processing subsection.

An average of 0.7-m point spacing was achieved from airborne lidar data. Due to the intended oblique nature of the data acquisition, "point spacing" is highly variable depending upon the level of vertical change within the sample area. Areas of steeper terrain will have far greater point density per square meter than areas of low vertical change. These data were acquired from a helicopter using a proprietary ALIS-80DS (Airborne Laser Imaging Systems, Calgary, Ab, Canada) which contains two modified Riegl airborne scanning lidar instruments; a forward Q240i and aft Q140i at 50 and 27 Hz (<http://www.riegl.com/products/airborne-scanning/>). Both lidar units in the ALIS-80DS are "whisk broom" style scanners, which means they sweep the laser back and forth across the field of view in the same manner a whisk broom is used. The scanners were set to sweep at with a 10 KHz laser repetition rate with a maximum angle of $\pm 40^\circ$ off nadir (80° total sweep). This provided nearly complete coverage of perpendicular cliff faces.

The data were flown along an oblique ($\sim 345^\circ$) flight path to the structural trend of the mountain (340°) to maximize laser coverage sweeping up the vertical east faces of the westward-dipping monocline (figure 2.3) as well as capturing some of the vertical walls contained within the steep canyons of the western dip slope. The survey was flown at 225 m above ground level to maximize resolution and precision of the laser returns from the ALIS-80DA. The low elevation also helped to maximize vertical cliff-face coverage and reduce data shadows commonly encountered in "down-looking" aircraft survey from higher elevation (Bellian et al. 2005; Vallet 2008).



Figure 2.3: The blue lines are the flight lines as planned for the airborne lidar survey; this flight plan aided in maximizing vertical cliff-face coverage of the steeply westward dipping monocline of the SFM. Metadata for the survey are in Appendix A.

Additional remote sensing data included high-resolution (30 cm resolution) orthophotographs and hyperspectral imagery were co-registered with the pointcloud and were alternately displayed to compare geological interpretation against these various remote sensing data types. These techniques made cross-validation of geological interpretation directly on the lidar data efficient.

2.4.3 Lidar data processing:

The total pointcloud (over 40 km²) was subset to include the area outlined in figure 2.1 (white dashed line) which was 24 km². A desktop personal computer workstation with 16 gigabytes of RAM and 3 gigabytes of graphic card memory and a 64-bit operating system was used to visualize the data. The subset area contained ~100,000,000 individual laser points, a relatively large amount of data to display and manipulate efficiently with computer specifications outlined above. The pointcloud output from the airborne lidar survey was an x, y, z pointcloud (figure 2.4a). A typical non-DEM method for lidar to be displayed is as a triangulated irregular network (TIN) or a 3D mesh and display it with sun-shading algorithm (Bellian et al. 2005) however; the lidar pointcloud from the SFM survey was too large to make single mesh that renders efficiently without decimating important geological detail. Subdividing the pointcloud into multiple files for TIN construction creates inconsistencies along the borders between subareas that can be avoided but require additional processing steps that can be time consuming.

To reduce image rendering delay on the computer, a computer code was written to assign *normals* to each point. A *normal* is a vector that is assigned to an object, in this case a lidar point, to define its orientation or direction in model space (i, j, k). This general type of display is referred to as "point-based rendering" (Gross 2006; Vucini 2008) and is ideal for working with large, unorganized point clouds. By removing the step of creating a TIN to define facets of the DOM (Bellian et al. 2005), fewer rendering operations are required for processing computer graphics. Assigning the normal vector orientation directly to the laser point increases the efficiency of

rendering with the same visual effect as a sun-shaded TIN (figure 2.4b) (Gross 2006). In this way, within computer science, points, lines, and planes are all equally weighted 3D objects which is often the source of confusion when compared to strict mathematical definition of points, lines, and planes.

The computer code used for the airborne lidar data was designed and tested by the author and Reuben Reyes. The computer code was written by Reubin Reyes at the University of Texas at Austin, Bureau of Economic Geology. The normal vectors for each point were calculated from the average angle between the surrounding points and calculating the most likely perpendicular vector to the surrounding points within a user-defined search radius. Point based rendering of the point cloud plus normals for each point was faster than the same level of detail with a TIN surface.

Some stratigraphic contacts were not readily identified on the basis of outcrop shape alone. Moreover, it was not always possible to directly walk along all of these contact surfaces in the field (e.g. vertical cliff face, police firing range, and other restricted access). To assist interpretation in these areas of subdued erosional relief a 30 cm orthophotograph was co-registered (<http://seemless.usgs.gov>) with the airborne lidar data to create a 24 bit color pointcloud for the study area. The orthophotograph contained a high enough resolution (0.3 m spaced pixels) compared to the lidar points (~0.7 m spaced pixels) that every laser point was assigned an 8 bit (0-255) red, green, and blue value (figure 2.4c) along with each calculated normal (i,j,k) vector. Thus, the pointcloud of x,y,z data became x,y,z,i,j,k,r,g,b for each point. The user simply needed to choose which set of attributes to display (normal or color) to toggle back and forth between the data types displayed on the same point cloud.

A subset of the SFM study area to the north of Quarry Breccia (figure 2.1) was covered by an AVIRIS hyperspectral task acquired in 1999. The AVIRIS (airborne visible infrared imaging spectrometer) aircraft-based system collects data in discrete bands of the electromagnetic spectrum that can be used to determine the chemical composition of a target material (Vincent

1997). The passive remote sensing technique of hyperspectral image analysis (reflected natural light between 350 and 1800nm) was used in previous work to identify pixels dominated by calcite versus pixels dominated by dolomite in the area of interest (Bellian et al. 2007). The advantage of this technology is that it offers the user the ability to distinguish mineralogical anomalies, such as dolomitization of a calcite host rock in the target material within and outside the visible spectrum.

In the SFM, two broad categories of dolostone are present within the El Paso Group. Stratal-bound dolomites from a reflux origin within the Cindy and Chamizal Formations and other subsequent dolomite zones associated with large collapse breccias (Stepanek 1984; Lucia 1995). The AVIRIS data were used to aid in mapping mineralogy changes associated with stratigraphy and dolomitization of the collapse breccias, however; the spatial resolution (20 m) reduced the reliability of the AVIRIS data at the scale of 1:2000. These data were co-registered with the airborne lidar data by manually picking control points which further reduced the absolute-position accuracy of the data. Therefore the AVIRIS data were used primarily as a reference for dolomite-calcite boundaries to guide interpretation on air photos and lidar in this study. Processing of these data has been previously documented (Bellian et al. 2007). These data however, still added valuable information in areas lacking good ground-control and picking fault zone contacts along the western bounding faults of the SFM (yellow pixels in figure 2.4C) when combined with high-resolution airborne lidar data.

With the combination of the ground-control points from direct field observations, sun-shaded lidar and the color-draped lidar pointcloud the stratigraphy and associated collapse breccias were mapped across the entire study area. The lidar pointcloud was interpreted in the computer aided design (CAD) software Polyworks (InnovMetric, Ontario, Canada). Stratal terminations and abrupt color changes observed in the lidar data indicated faults, paleocave breccias, or covered intervals. The high-precision of the lidar pointcloud made it possible to extract geographic

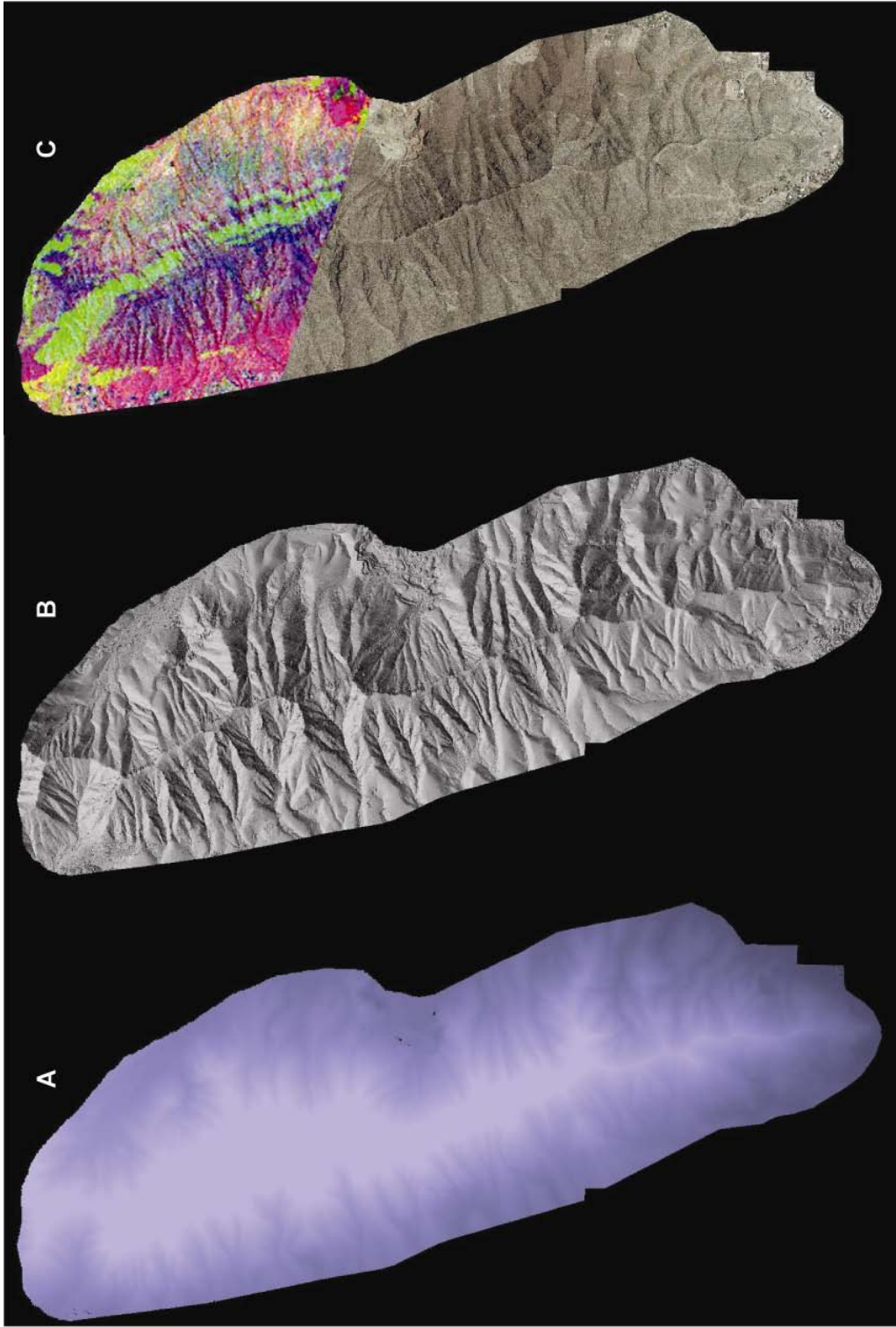


Figure 2.4: Pointclouds shaded with elevation (A), i,j,k vectors (B) and i,j,k plus red, green, and blue pixels from air photos and hyperpectral overlay (C).

coordinates of the points that required validation, and were uploaded to hand-held GPS units for field verification. This process was used to pinpoint areas in need of further investigation over the 24 km² map area. Similarly the process worked in reverse for observations and sample locations from the field. These were imported into the pointcloud and used to constrain interpretation and organize observations. The DOM became a working, interactive, 3-D basemap with a spatial context not possible with flat, 2-D photographs.

2.4.4 DOM construction and modeling:

The DOM constructed in this study was designed to reconstruct possible shapes of collapsed paleocave breccias in 3D from the scatter of lidar-point observations within a sequence stratigraphic and current structural framework. The following steps were required:

- Build stratigraphic surfaces from airborne lidar interpretation.
- Construct sgrid from surfaces and import fault interpretations from lidar data.
- Cut the sgrid with fault surfaces to preserve stratal continuity for property modeling.
- Populate the sgrid with field observation data compiled on lidar pointcloud.

Geological interpretations were conducted in Polyworks on the full-resolution lidar point cloud and transferred to Gocad as polyline files which preserved the spatial integrity of the geological interpretation despite the need to decimate the pointcloud in order to render efficiently (Janson et al. 2007). The stratigraphy and major fault (those with >10m offset) interpretations mapped on the SFM lidar data were used to construct stratigraphic horizons and fault planes that were extrapolated from the lidar point cloud to the edges of the model space (figure 2.5). Surface modeling from a highly variable point distribution such as very close-spaced polyline interpretation from the lidar data line but often very large distances between stratigraphically equivalent lines involves imposing a regional trend on the surfaces modulated by the actual interpreted stratal contacts from the lidar data. This surface construction method produces

geologically reasonable surfaces that incorporate geological conceptual trends that may not be directly extracted from an auto-surface mapping algorithm (Janson et. al. 2007, Phelps et al. 2008).

Two large offset faults (> 10 m) and the main bounding fault along the western edge of the study area were mapped onto the lidar data modified to match field observations from regional maps of the area (Lucia 1995; Collins and Raney 2000; Wu 2002). The points associated with the outline of these fault surfaces along the mountain were used to construct a planar surface to cut and offset the stratigraphic horizons. This process subdivided the model into three large fault blocks with the central block uplifted relative to the southern and northern blocks and allowed breccia body modeling to propagate across the fault within the same stratigraphic interval (figure 2.6). Activity of faults in this region have been documented as late Rio Grande Rift (Carciumaru and Ortega 2008) and can be observed offsetting collapse paleocave breccias, therefore breccias are younger relative to these offsets.

An sgrid was built for the El Paso Group strata between the top of the Ranger Peak and top of the Bliss Formation. An sgrid is a non-orthogonal 3D grid that may be subdivided into cells between horizons (Tinker 1996). The sgrid cells in this study were scaled to 20 x 20 x 5 meters from the original high-resolution lidar data (0.7 meter point spacing) with proportional cell layering. Although this up-scaling from the lidar data may seem drastic, the final sgrid contained over 10,000,000 cells. The model area covers 24 km² with a mean thickness of 402 m and includes the four 3rd order depositional sequences EP 1-EP 4 (figure 2.2).

The sgrid in Gocad was *painted* or assigned cell values. Approximately 100,000 cells were constrained by outcrop data within the model after up-scaling from the full resolution point cloud to the 20 x 20 x 5 m 3D grid. Each model cell intersected by lidar points was assigned a cell value corresponding to breccia or non-breccia (1 or 0 respectively). Population of these data led to a 1% total volume defined as conditioning data from direct field observation. Previous studies have

shown that constructing similar scale models with measured section data alone contain 0.01% or less initial conditioning data (Janson et al. 2007; Bellian et al. 2008; Verwer et al. 2009).

2.4.5 Breccia extrapolation and simulation:

The breccia facies distribution assigned within the sgrid was used to calculate an experimental variogram. An experimental 2D variogram range was calculated in the X-Y plane (latitude and longitude) for incremental azimuth orientations. This was conducted within the Gocad "spatial data analyzer" tool in which a lag distance is user-defined. In this case, lag = 15 m and was run with 40 steps which resulted in a maximum distance of 600 m. The 600 m search distance was chosen as none of the breccia bodies painted into the sgrid exceeded this dimension. The results show that the maximum range value at 160° azimuth was 258 m. The maximum range was in a direction parallel to the outcrop strike of 340° (160° is the inverse of 340°).

Extrapolation of lidar breccias bodies within the DOM used normal Kriging with a spherical variogram with an isotropic range of 258 m based on the spatial statistics calculated directly from the SFM breccia property painted into the sgrid. All undefined cells were populated with breccia or non-breccia facies. Model results and input parameters are in Appendix B.

Sequential indicator simulation (SIS) (Caers 2000) was conducted on breccia body initial condition data from the lidar-painted sgrid. Simulation distributes properties away from the control nodes using the same variogram as the extrapolation above. Both Gaussian and spherical type simulations were used to run symmetrical and asymmetrical ranges (Appendix B). All vertical variogram ranges were set to 100 m. The histogram for the frequency distribution of the breccias was derived directly from the conditioning data and consists of 98% non-breccia and 2% breccias. These values were derived from breccias-to-non-breccia distribution within the interpreted lidar point cloud.

2.4.6 Ground-based lidar of a modern cave:

Before Devil's Sinkhole collapsed, it was a phreatic chamber within the Albian (Cretaceous) Segovia and Fort Terrett formations of the Edwards Group (Rose 1974; Elliott and Veni 1994). Devil's Sinkhole started out as a solution cave, referred to here as Devil's Cave (figures 2.7 and 2.8), which formed in the subsurface and later roof-collapse linked to the cave below to the surface above. The collapse has been attributed to base-level fall which reduced the buoyant effect of water on the overburden. Cave ceiling strength can be reduced by as much as 40% (Loucks 1999; Palmer 2007; Ford and Williams 2008) when a water-filled chamber is emptied. The reduction in ceiling support initiated collapse the ceiling of Devil's Cave resulting in the large debris cone at the center of what is now Devil's Sinkhole (Elliott and Veni 1994). A lidar scan of Devil's Cave is proposed in this study as a volumetric analog for the El Paso Group paleocaves.

The lidar pointcloud of the entire Devil's Sinkhole was collected at ~3 cm point-spacing from atop the debris cone inside the sinkhole, from around the perimeter of the debris cone and from the ground surface looking down into Devil's Cave (figure 2.7). This was the first lidar scan ever conducted in this locality and one of very few scanning lidar acquisitions conducted inside a cave (Murphy et al. 2005). The sinkhole is over 100 m deep from the survey point at the rim of the modern opening and the deepest explored lake-room (figure 2.7). The diameter of Devil's sinkhole ranges from 13 m at the surface opening to over 130 m within the largest area. Data collection began with a reconnaissance mission on January 15th 2004 and required three additional trips over the next two years to complete lidar and photographic coverage.

An Optech ILRIS 3-6-D system was used to collect the lidar data which made it possible to shoot a 360° hemisphere-shaped pointcloud that captured the internal dimensions of the sinkhole. Small passages (less than 3 m in diameter) were not scanned due to scanner limitations in minimum range from scanner to target, and some wall areas were blocked by breakdown material and therefore were also unable to be captured digitally. Flooded passages or the "Lake Rooms" of the NW and SE extent of the sink were not able to be captured (figure 2.7). However,

the upper 75% of the sinkhole was scanned including scans taken from the ground-surface outside of the sinkhole were used to link GPS locations to the internal sinkhole lidar data. This was accomplished by merging scans with GPS locations outside of the cave to scans taken from within the cave that could view the same rock face near the entrance shaft-ground-surface interface just below the surface datum (figure 2.8). All scans were merged into a single point cloud using Polyworks CAD software (InnovMetric, Ontario, Canada).

A 2D mass-balance calculation was used to compare the area of an open modern cave (100% porosity) to a collapsed paleocave (assigned 5% porosity) in 2D by Loucks (1999). A similar technique is used in this study however; the calculation was expanded from 2D to a 3D volume. To simplify this calculation, Devil's Sinkhole void space was divided into two sub-areas above and below the restriction. All points in each of these sub-areas were selected to calculate a sphere using a least-squares, best-fit algorithm built into the CAD software (Polyworks). The upper sphere (figure 2.8) displayed in orange estimated the entrance shaft volume and the lower hemisphere (larger) displayed in light blue estimated the lower chamber (figure 2.8). The 3D mass balance equation used in the volumetric calculation is:

$$(\phi_c \times 4/3 \pi r_c^3) = (\phi_b \times 4/3 \pi r_b^3) \quad (\text{Equation 2.1})$$

where ϕ_c = porosity of the initial cave, r_c = radius of initial cave, ϕ_b = porosity of resultant breccia, and r_b = the radius of the resultant breccia. Spheres were used to approximate volume of the Devil's Sinkhole passages for simplicity (figure 2.8). This equation compares the volume of rock that a spherical object will occupy as a function of its porosity. As porosity increases, volume required decreases. To find the radius of the damage zone after a void has collapsed, equation 2.1 can be simplified to:

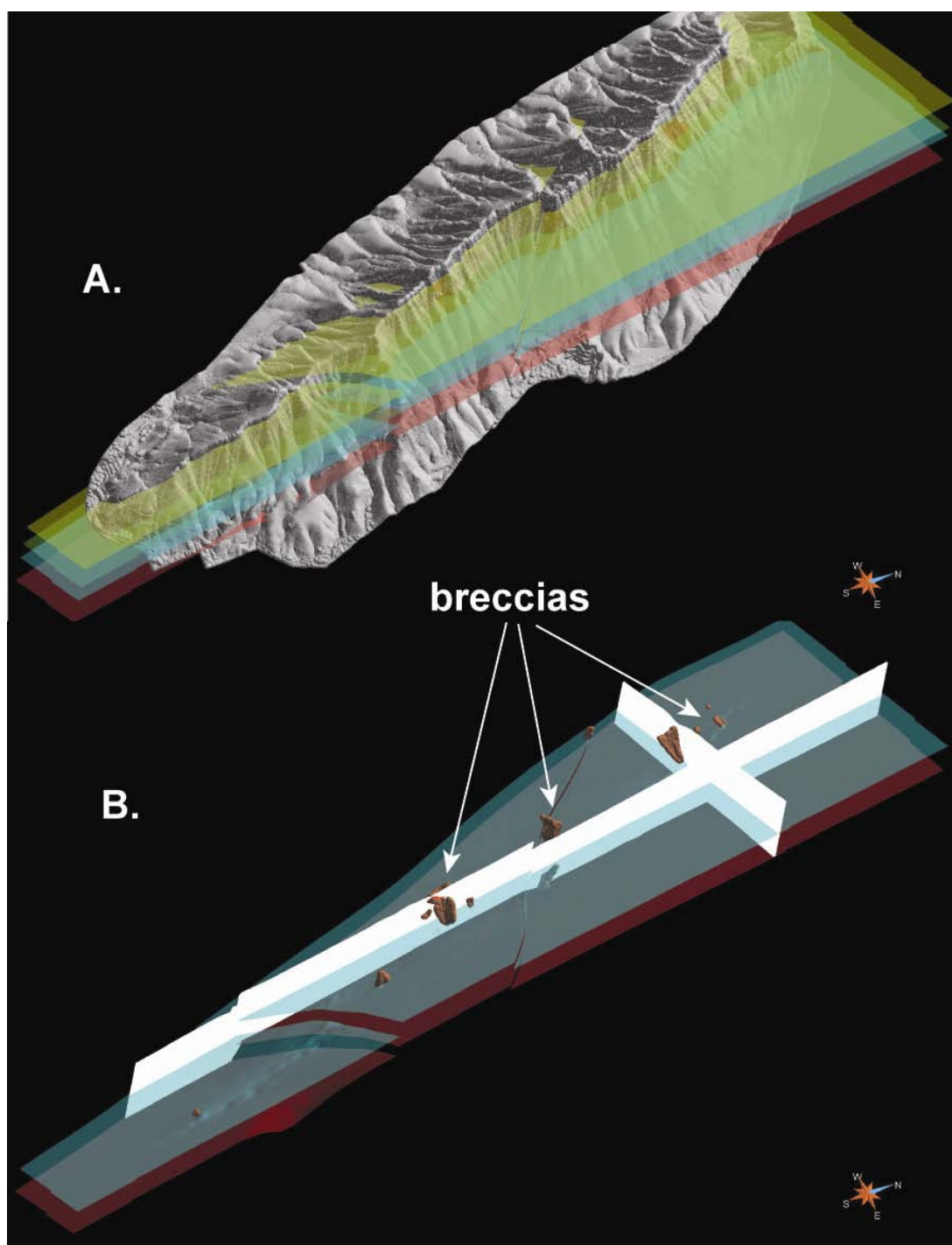


Figure 2.5: The SFM geocellular model includes only two large-offset faults originally mapped by Collins and Raney (2000) and projected onto the airborne lidar data. Stratigraphic horizons are shown in A; red=top Precambrian, blue = top Chamizal, dark green = top lower McKelligon Canyon, and yellow = top Ranger Peak Formation. Breccia outcrop patterns are shown in orange in the lower image (B) with white cross-sections displayed cutting through the model.

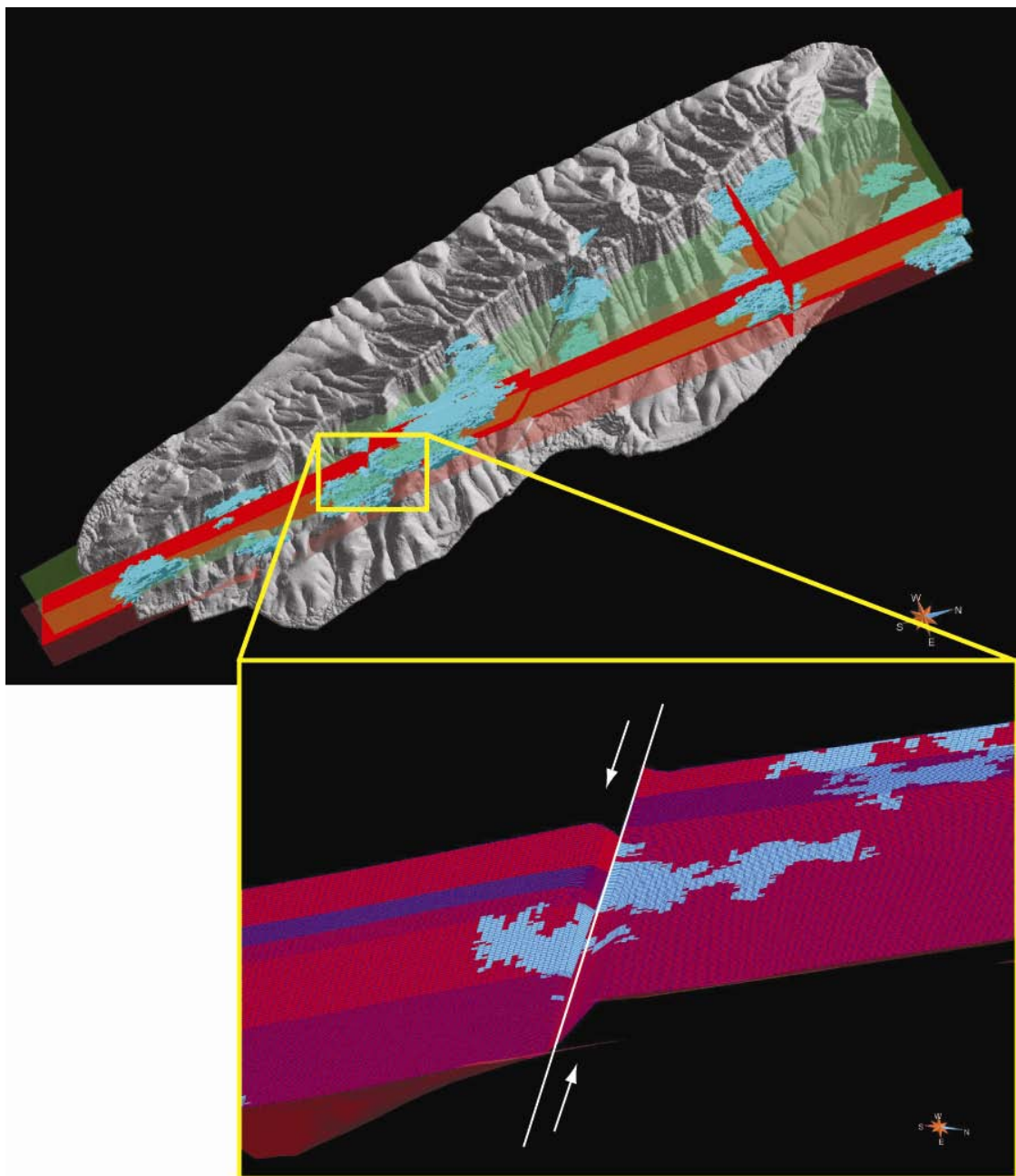


Figure 2.6: To simulate the breccia bodies throughout the model a faulted s-grid was constructed that allowed breccia facies to propagate across the faulted surface (yellow box inset).

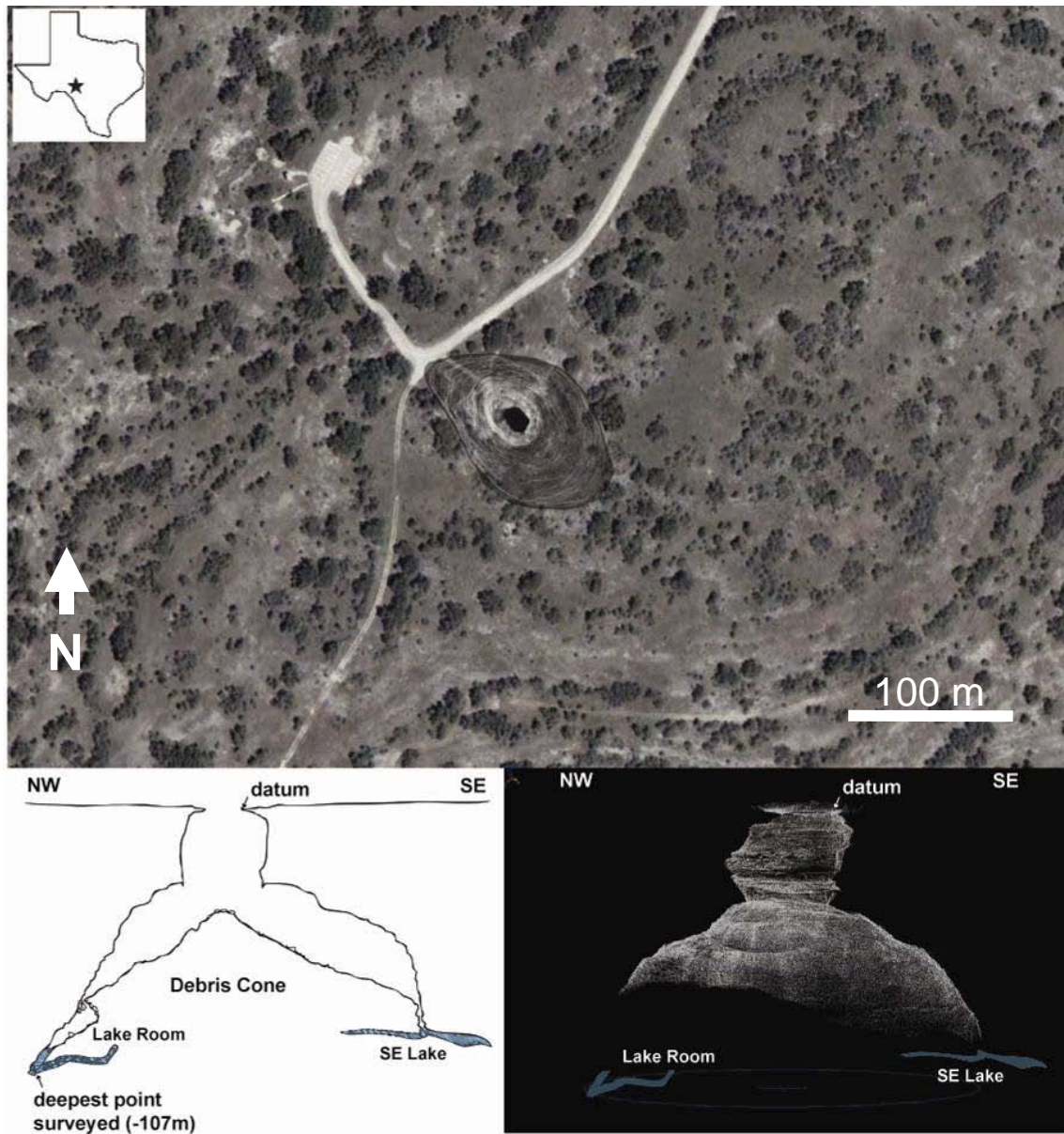


Figure 2.7 Devil's Sinkhole State Natural Area is located in Edwards County, Texas and is formed within the Edwards Limestone on the Comanche Shelf during the Albian (Cretaceous). The surface exposure of the sinkhole is within the Segovia member of the Edwards Limestone which is up to 100m thick. In the upper image and air photo is superimposed with the shape of the lidar survey. Lower left is a line-drawing map modified from Elliot and Veni (1994). The lower right is a lidar scan in the same orientation with lake rooms added graphically as they were too small to laser scan effectively.

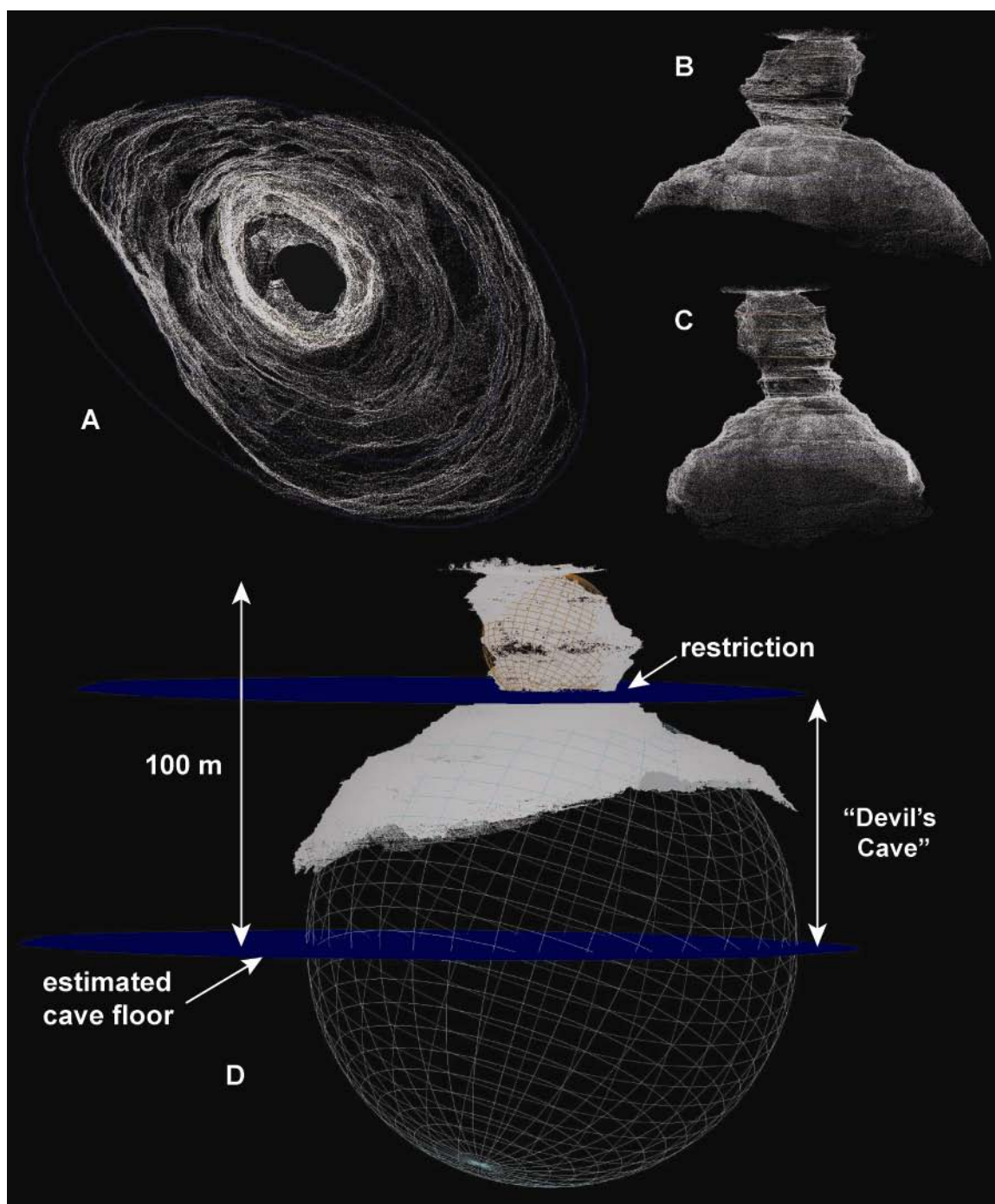


Figure 2.8 Devil's Sinkhole has an ovate shape in plan view (A). Views from the SW (B) and SE (C) show the long axis and short axis respectively. To calculate cave volume, the upper (orange) and lower (blue) chambers were treated separately as a sphere and hemisphere respectively. Cave floor is estimated at the mid-point of the lower sphere (base of the hemisphere) at 100 m below the rim and is the estimation of the cave floor (D) location. Area between the restriction and the estimated cave floor is "Devil's Cave" which represents the void space prior to collapse and conversion of Devil's Cave into Devil's Sinkhole.

$$r_b = [\phi_c \times r_c^3 / \phi_b]^{1/3} \quad (\text{Equation 2.2})$$

The volume of collapse breccia calculated from Devil's Cave was calculated with this equation and results are presented in table 2.1. Breccia volume was used as a comparison factor between the SFM and Devil's Cave examples as the actual shape of the SFM breccia body is not known, nor is the shape that a hypothetically collapsed Devil's Cave would eventually take (figure 2.8). This assessment provides a baseline from which the scale of the paleocave can begin to be assessed by comparing it back to a modern cave void space.

The asymmetry or "ellipticity" of Devil's Sinkhole was measured as an indicator of possible vertically connected fracture network controlling the geometry of this cave similar to the proposed SFM paleocave origins (Lucia 1995). It was noted that Devil's Cave is strongly asymmetric (table 2.2) in a northwest-southeast despite the nearly circular entrance opening. Although no geological mapping of the Devil's Sinkhole has been published, on the basis of these observations it would seem that there is likely a structural fabric controlling the shape of this karst feature.

Devil's Sinkhole	cave r	Cave vol.	DZ r	DZ vol.	φ vol
Objects	meters	cubic meters	meters	cubic meters	5.0%
Upper Sphere Radius (m)*	18.00	24,429.02	48.86	116,640.00	1,221.45
Lower Hemisphere Radius (m)*	65.20	580,498.90	176.98	5,543,356.16	29,024.94

Table 2.1: Volume change expected within the subsurface is calculated assuming initial void porosity of 100%, and a post compaction porosity of 5% (from equations 2.1 and 2.2). Dimensions were extracted from lidar scan of Devil's Sinkhole. Cave r = cave radius in meters, Cave vol. = cave volume in cubic meters, DZ r = damage zone radius in meters, DZ vol. = damage zone volume in cubic meters, φ vol 5% = is the percentage of pore space within the damage zone volume in cubic meters. Compacted porosity in this equation has a significant impact on damaged rock volume.

Devil's Sinkhole Ellipticity				
<u>Devil's Sinkhole Dimesnsions:</u>	<u>Max D(m)</u>	<u>Min D(m)</u>	<u>Depth (m)</u>	<u>Elipcticity</u>
<i>Top Opening</i>	18	13.2	0	1.36
<i>20m above restriction</i>	36.5	25	8.7	1.46
<i>15m above restriction</i>	37.5	26.8	13.7	1.40
<i>10m above restriction</i>	41.2	24.9	18.7	1.65
<i>5m above restriction</i>	36.7	24.2	23.7	1.52
<i>Restriction</i>	30.3	25.6	28.7	1.18
<i>5 m below reserction</i>	48.7	34.3	33.7	1.42
<i>10m below restriction</i>	63.7	45.7	38.7	1.39
<i>15m below restriction</i>	82	54.7	43.7	1.50
<i>20m below restriction</i>	102.5	65.9	48.7	1.56
<i>25m below restriction</i>	118.2	73.1	53.7	1.61
<i>Project 100m level of cave</i>	146	89.9	71.3	1.62
			Mean:	1.51
			STDev	0.10

Table 2.2: A plane was projected through the Devil's Sinkhole pointcloud and moved at 5 m increments down through the point cloud. At each 5 m sample position, all laser points intersecting the plane were selected within a 10 cm tolerance. These points were used to calculate a least-squares ellipse from the data. The mean of the ellipse ratio of maximum distance (Max D) to minimum distance (Min D) was extracted from the best-fit feature extraction tool embedded in Polyworks IMInspect CAD module (InnovMetric, Ontario Canada). The "restriction" and "top opening" ellipticity values were excluded from the mean calculation because they are not representative of the cave structure. These two points represent cave-roof failure that tends to be circular (Esteban and Klappa 1983; Yechieli et al. 2003).

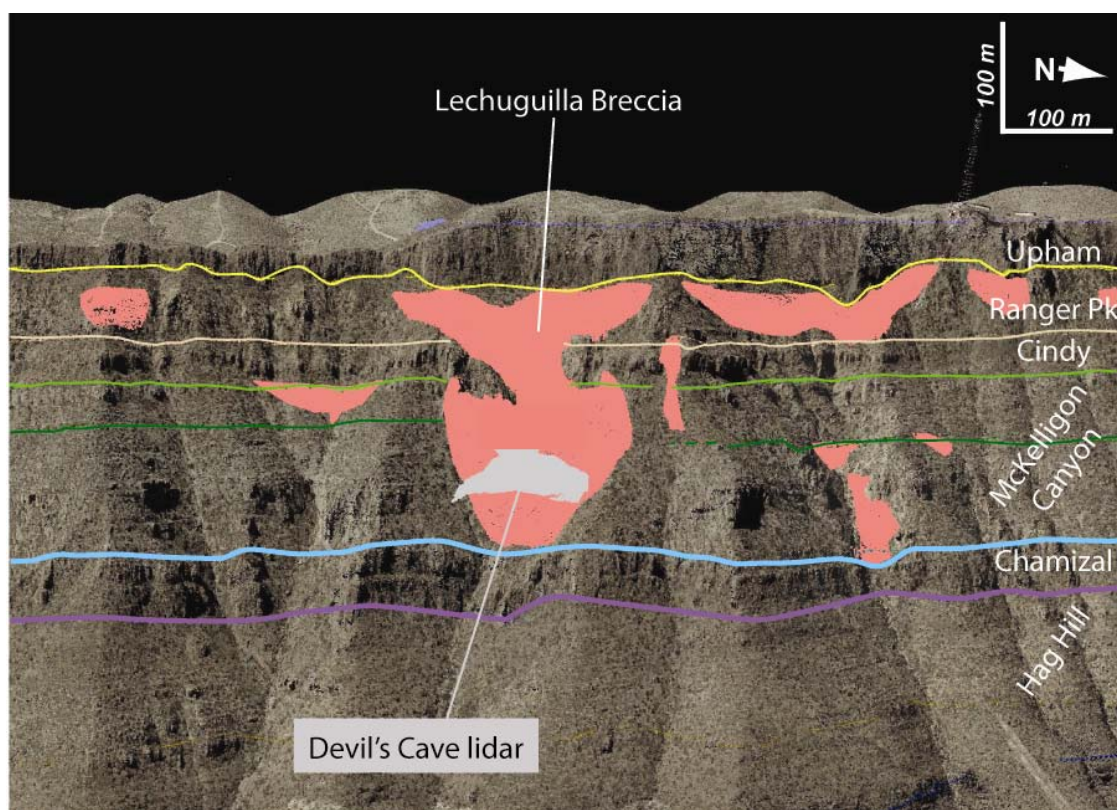


Figure 2.9: Color-draped airborne lidar data shown with stratigraphic contacts near Lechuguilla Breccia (figure 2.1) north of the Wyler Aerial Tramway. The Devil's Cave data are displayed in gray at 1:1 scale. Gray area represents the area of 100% porosity.

SFM Breccia Dimensions	Width (m)	Height (m)
Ranger Peak	100	100
Quarry (lower)	85	175
Quarry (upper)	125	220
Lechuguilla	170	250
Great McKelligon Sag	250	250
Devil's Sinkhole	176	100
(compacted to 5% porosity)		

Table 2.3: Breccia sizes from airborne-lidar data compared to Devil's Sinkhole calculated diameter after the mass balance adjustment using equation 2.2 assuming ~hemispherical internal volume.

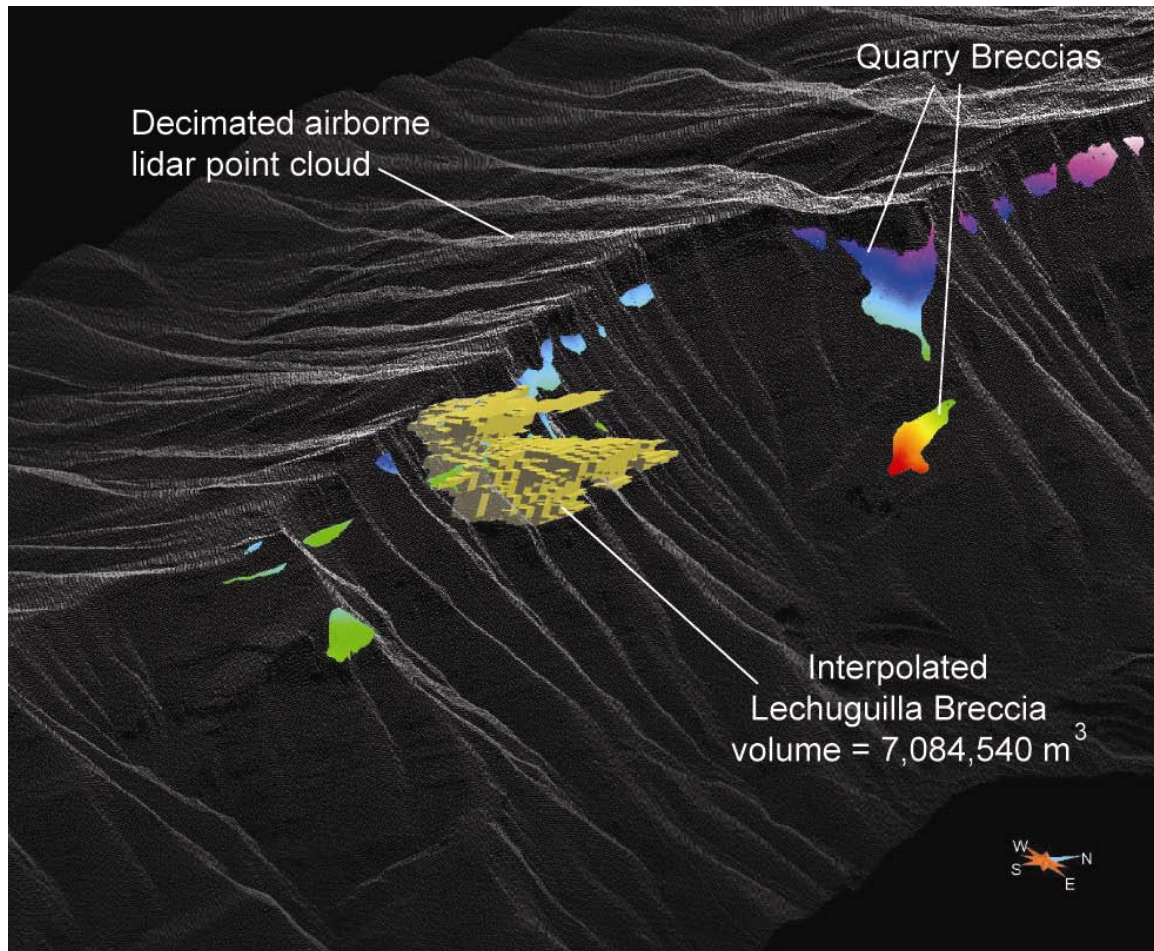


Figure 2.10: The yellow model cells above are the reconstructed breccia body from Lechuguilla Breccia. The total volume from this model run is 7,084,540 m³. Total calculated volume of the estimated Devil's Cave breccia after compaction to 5% porosity is 5,543,356 m³.

2.5: Discussion:

The airborne lidar survey design greatly reduced the effect of data shadows typically encountered from traditional airborne lidar techniques (Bellian et al. 2005; Vallet 2008). The improved vertical coverage from the cliff faces of the SFM made it possible to map third order depositional sequence stratigraphic contacts on the airborne lidar point cloud and directly incorporate field observations into the point cloud. The combination of these data greatly reduced uncertainty in stratigraphic and diagenetic contact definition through iteration between sun-shaded shape attributes and the color-attributes directly on the same point cloud. By assigning

these attributes directly to the points, over 100 million points were simultaneously manipulated without the need to construct a triangulated irregular network or TIN model and break the study area into smaller segments with multiple texture files. This removes cumbersome processing steps when working with large data files (Gross 2006). Directly working with the point cloud also retained full resolution of the original data within the interpretation which reduced computer disk usage and rendered more efficiently on a personal computer workstation.

Interpretations from the point cloud data were transferred digitally into Gocad geological modeling software and reconstruction of the stratigraphy and subsequent paleocave breccia bodies was performed. Data imported from the lidar point cloud was used to populate the Gocad model and calculate spatial statistics. From these input data, a variogram range for property modeling was extracted from field observations. The intermediate steps of model construction and up-scaling from lidar point cloud to 3D geological model are non-trivial tasks but on the basis of this study a clear path between field observations and modeling parameters has been established.

The extrapolation of the Lechuguilla Breccia body using the field-based data for direct variogram range calculation and paleocave breccia reconstruction resulted in a breccia volume similar to that calculated from the collapse of a modern Devil's Cave. It is recognized that this calculation is strongly influenced by the resultant porosity of the collapsed rock volume (equation 2.2) however a compacted rock volume of 5% porosity is not uncommon in the subsurface. Under a collapsed and compacted state, a void the size of Devil's Cave could create a breccia body or damage zone of the same scale as the breccias observed in the SFM (table 2.3) a cave half the size of Devil's Cave compacted to 1% porosity could also easily produce breccias of similar scale. It is also important to recognize that this void would need to be located at the bottom of the breccia body mapped (figure 2.10) as compaction and associated brecciation from cave collapse would not likely affect the cave floor or walls as significantly as the ceiling and overburden. This

has important implications as to the origin of the cave system. If the cave floor was ~300 m below the Sauk-Tippecanoe unconformity, dissolution must have occurred at this depth.

Caves follow permeability pathways and a fracture aperture as small as 0.01 m wide is enough to capture flow through low permeability rock (Lucia 2007; Palmer, 2007; Ford and Williams 2008). Small-scale fractures, of this scale (0.01 m) are common in carbonate rocks but connecting a vertical network of several hundred meters would likely require a focused tectonic event of which there were few within the Paleozoic of the El Paso region. On the basis of ellipticity calculated from Devil's Sinkhole, it is likely that dissolution of Devil's Cave follows a structural fabric (table 2.2). The northwest-southeast orientation is perpendicular to the Balcones Fault of central Texas and situated between the Llano Uplift and the Val Verde Basin (Ewing 1990) however detailed tectonic surface mapping of the area around Devil's Sinkhole has not been well represented in the literature to date (Webster 1980, Ewing 1990). Additional analysis of structural controls influencing the SFM specifically with relation to the observed breccias patterns may provide insight into breccia location, geometry, and timing.

2.6 Conclusions:

The question of scale is fundamental to understanding the origin of paleokarst systems such as those in the SFM. It is apparent from dimensional data presented in this study that a void volume similar in size to the Devil's Cave (tables 2.1 and 2.3) could produce a volume of breccia of similar size to those measured in outcrop in the SFM. The actual shape of this void is dependant upon the original cave shape which will be strongly influenced by tectonic fractures and lithology (Palmer 2007). With the aid of high-resolution airborne lidar an outcrop-based reconstruction of collapsed paleocave breccia was conducted and compared to dimensions from a modern cave. Calculation of collapsed paleocave breccia volume is strongly dependant on the porosity reduction and compaction. The combination of airborne lidar data and ground-based

lidar of an analogous depositional component of the larger system tested a methodology for outcrop-based modeling studies.

The dimensional data extracted from the ground-based lidar of Devil's Sinkhole offered a direct observation of internal geometry and volume associated with a modern sinkhole and indicates that the scale of this type of karst feature is comparable to breccias observed in the SFM outcrops. Within the long and complex depositional, diagenetic, and tectonic history of the El Paso region a combination of various processes is also highly likely. This study is a small step in the direction of understanding the controls on paleocave brecciation in the southern Franklin Mountains but offers more tangible advances in direct link between field observations and geological modeling.

Chapter 3:

Origin of Breccia Bodies within the Southern Franklin Mountains Fault Block, El Paso, Texas

Abstract:

Paleokarst breccias of the southern Franklin Mountains represent one of the best examples of sedimentary breccias of probable solution-enhanced collapse origin observed in the Paleozoic of North America. Four models are evaluated in this study using high-resolution airborne lidar data, remote sensing and field mapping to better constrain timing of the paleocave system and associated breccia formation. These models include fault-damage zone cataclastic brecciation, supersequence meteoric dissolution karst, 3rd order sequence-bounded-composite cave, and solution-enhanced tectonic karst models. Breccia bodies were mapped in outcrop by integrating airborne lidar, oblique and map-view aerial photographs, field observations and previously published data to provide a multi-scale analysis of the southern Franklin Mountains. Tabular breccias bodies previously interpreted as vertical breccias pipes have been re-interpreted as solution-enhanced tectonic karst.

Breccia fabric, orientation and correlation of tabular breccias features were compared in 3D on the sub-meter airborne lidar point cloud in the study area. These data were compared with regional stress fields related to oblique right lateral compression with trends similar to those predicted by a Riedel shear fracture model. The stress field orientation that most closely corresponds to the breccias orientations observed in the field is related to the Laramide orogeny. Results of this work therefore indicate that a fracture-controlled solution-enhanced tectonic karst model may recalibrate speleogenesis by more than 350 million years. This new model proposes Laramide (~70 m.a.) age for the paleocave system in the southern Franklin Mountains driven by thick-skinned deformation of the southern Franklin Mountains strata and are likely unrelated to the top-Sauk second-order supersequence exposure.

3.1 Introduction:

The objective of this research was to use a combination of airborne lidar data and field mapping to better understand the complex 3D geometry and the breccia bodies preserved within the Lower Paleozoic strata of the southern Franklin Mountains (SFM). The interpretation of these breccias is considered in terms of four models, (1) a fault-damage zone model, (2) second-order depositional supersequence water-table to deep-phreatic karst, (3) a third-order sequence-composite-cave model, and (4) a solution-enhanced tectonic karst model. Karst breccias were mapped using oblique aerial photos, GPS, and ground-based lidar, and then transferred to the airborne lidar data to map the 34 breccia bodies along the eastern face of the southern Franklin Mountains. These breccias ranged in outcrop area from 160 m² to nearly 60,000 m². Twelve, near-vertical, tabular breccias were mapped along the western dip slope ranging in size from 960 to 15,500 m².

Results presented here indicate that “laterally restricted” breccia bodies originally mapped by Lucia (1971) can be connected along a limited number of fault planes dipping steeply (60-90 degrees to bedding) parallel to the main bounding normal faults of the Franklin Mountains westward dipping monocline. These breccias will be referred to as *vertical breccias* throughout this study. The alignment of these features was suggested initially by Lucia (1995, 1971), who called upon vertically connected fractures to aid in focusing meteoric water 300-400 m deep into the subsurface to generate the vertical breccia bodies below the “laterally persistent breccias” (Lucia 1971) hence referred to as *strataform breccias* within the uppermost reaches of the El Paso Group exposures (figure 3.2). A structural driver for vertically-connected fractures spanning more than 10 km N-NW trending southern Franklin Mountains (SFM) has not previously been identified, nor has consensus been established as to the detailed-kinematic evolution of the Franklin Mountains in general (Harbour 1972; Ruiz 2004; Scharmann, 2006; Carmiucaru and Ortega 2008). This is likely due to the complex tectonic history the Franklin Mountains and the El Paso region in general (figure 3.1) have experienced. The complex tectonic history is complicated

by extensive and multi-phase diagenesis of the Cambrian through Cretaceous sedimentary section.

Planes parallel to the regional structural strike (340°) and oriented at a high angle to original bedding were constructed to represent the dominant trend of the various fracture/fault orientations. Fracture and fault orientations were measured with a combination of field mapping, linear feature mapping on 30 cm-pixel-resolution aerial and oblique photography, and high-resolution (sub-meter) lidar data from a digital outcrop model (DOM) (Bellian et al. 2005) constructed of the study area. Fault zones in this study were modeled as planes on the basis of geometry in outcrop. Linear features were identified as breccia bodies and fault traces, color-changes observed in high-resolution aerial photography assisted in identification of dolomitization zones, and observations were then field-verified using hand-held global positioning system unit.

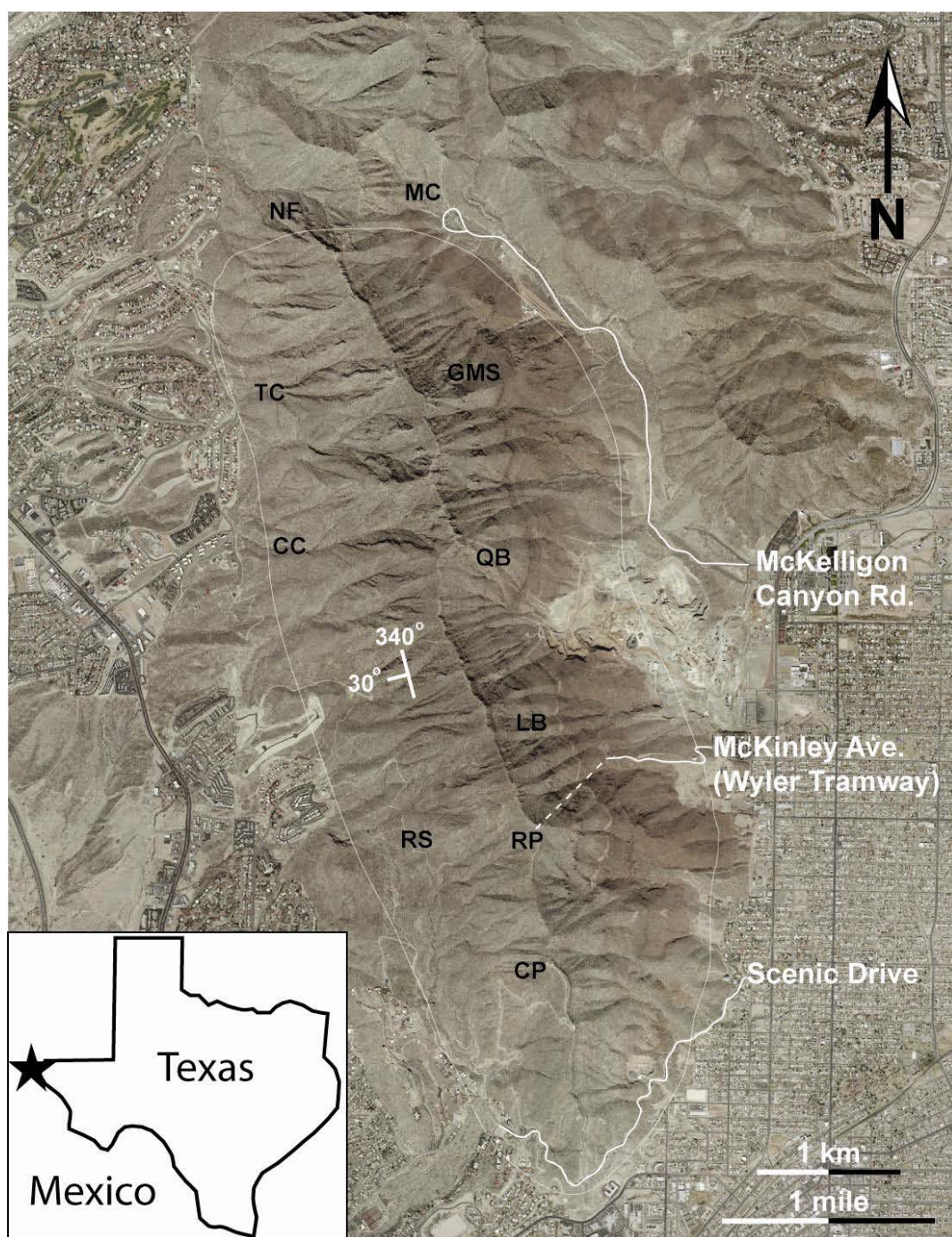


Figure 3.1: The southern Franklin Mountains are surrounded by the city of El Paso, Texas. The study area (star on inset map) covers the 24 square km of the southernmost Franklin Mountains. The thin line defines the area of interest for this study. Average strike and dip are 340 and 30 degrees respectively. Roads are listed for local orientation. CP = Comanche Peak, RP = Ranger Peak, RS = Crazy Cat Rock Slide, LB = Lechuguilla Breccia, QB = Quarry Breccia, CC = Cindy Canyon, TC = Transition Canyon, GMS = Great McKelligon Sag (breccia), MC = McKelligon Canyon, and NF = North Face (breccia). The NF breccia was not mapped in this study but is described by Lucia (1995)

Franklin Mountains, West Texas

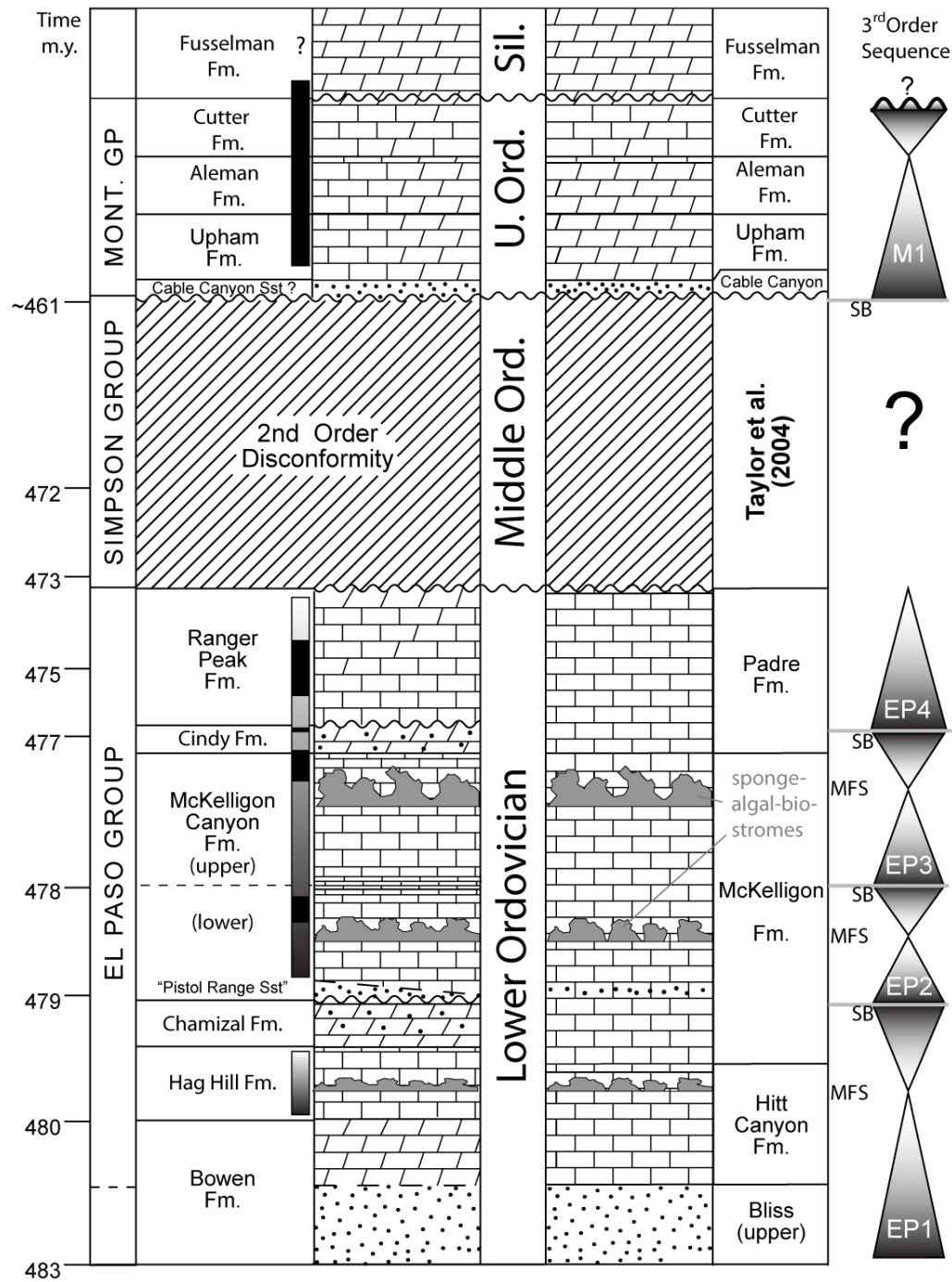


Figure 3.2: The stratigraphy of the El Paso Group as described by Lucia (1968) contains at least three complete third-order depositional sequences and spans a time period of ~ 10 m.y. (chapter 1 of this work). Breccia-prone zones are indicated by the black bars on the left. General clast-size indicated by gradient fill, fining upward.

3.2 Geologic Background:

This study focuses on the origin of the breccia complexes that are contained within the Ordovician through Silurian strata of the SFM. Before this study, previous workers (Stepanek 1984, Lucia 1995; Bellian et al. 2007) tended to concentrate their efforts on the Ordovician stratigraphic section and history to understand these breccias. This study approaches the problem from a more inclusive perspective, examining the entire stratigraphic column of the Franklin Mt section, in addition to the diagenetic history influencing the Paleozoic strata, and finally the structural evolution of the Franklins, from burial in the Paleozoic through uplift and faulting in the Tertiary. A brief overview of the major elements of the SFM geologic/diagenetic/tectonic history is provided below.

3.2.1 Stratigraphy

The El Paso and Montoya Groups of the Franklin Mountains were originally identified by Richardson (1904, 1909) who noted that the 915 m high "basin range" (Basin and Range) that from a distance seems to be a structurally uncomplicated westward dipping monocline. He goes on to note that this is not the case upon close inspection and that the Franklin Mountains are internally, complexly faulted. The study area (figure 3.1) lies along what was the southeastern passive margin of the Early Ordovician (North American) Laurentian craton (figure 3.3). Deposition of marine carbonates with subordinate siliciclastics dominated from the Cambrian through the Carboniferous in a steadily subsiding basin separated by several disconformities but no obvious angular unconformities (Ye et al. 1996; LeMone 1983; Kluth and Coney 1981; Wilson 1970). The El Paso Group was subdivided into six formations (figure 3.2) by Lucia (1968) who also first noted the existence of cave-type collapse breccias (1971). The stratigraphic nomenclature of Lucia (1968) will be used in this work for the El Paso Group.

Outcrop of the Montoya Group is limited for the most part to the Upham and Aleman Formations in the SFM. Small outcrops of the Cutter are scattered along the western dip slope and occasionally along the ridgeline of the SFM.

The Silurian Fusselman Dolomite was also named by Richardson (1908) after Fusselman Canyon at the north end of the SFM. The Fusselman Formation is present only in a few small outcrops along the highest peaks of the SFM near the Great McKelligon Sag (figure 3.1) and can be recognized most readily by a distinctive dolorudstone made of almost entirely pentamerid brachiopods. Clasts of the Silurian dolorudstone are readily identified within breccias occurring within the El Paso and Montoya Groups.

The strata preserved within large west-dipping fault blocks exposes a relatively continuous section of the El Paso and Montoya Groups separated by a ~10 m.y. top-Sauk second-order supersequence from the overlying Tippecanoe second-order supersequence. Subaerial exposure at the top-Sauk 2nd supersequence boundary has been previously identified as the time during which erosion and meteoric cave formation occurred

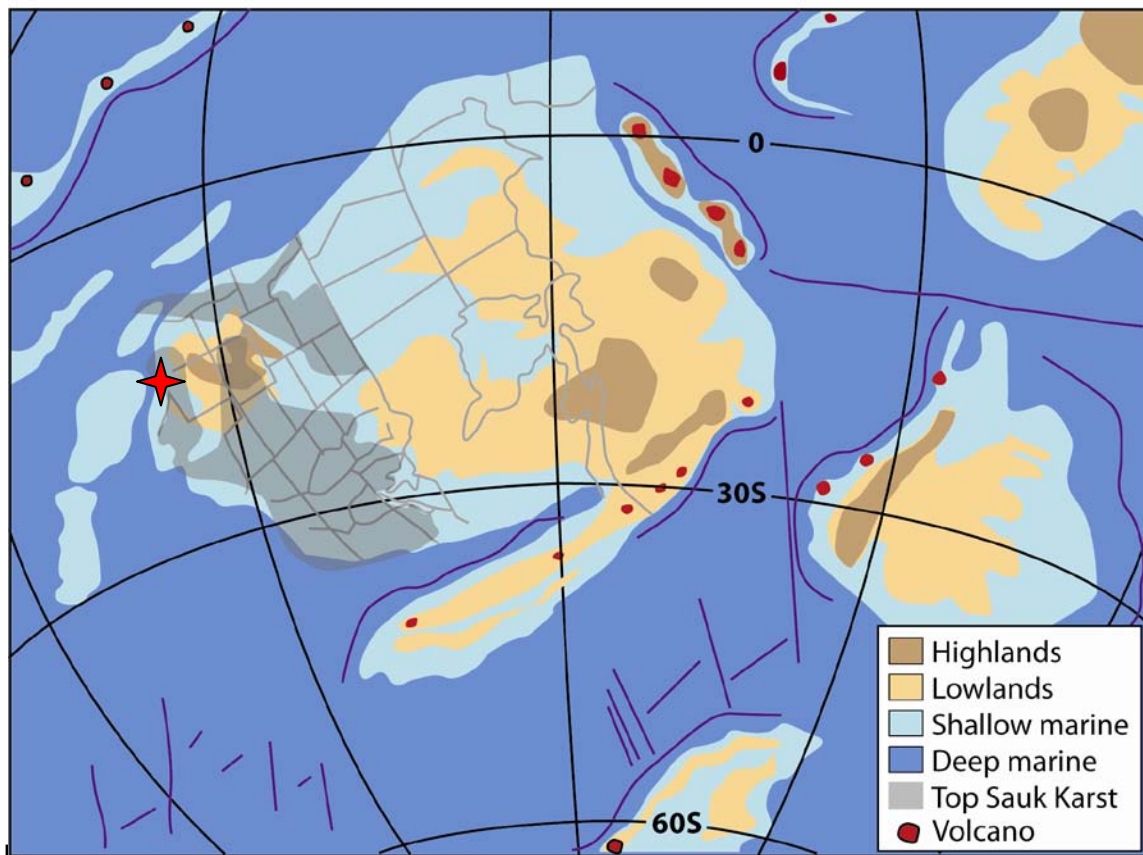


Figure 2.1. Paleogeography of Laurentia during the Early Silurian with (1) the regional patterns of Top-Sauk supersequence-related paleokarst in gray (Paleogeography after Scotese 1986; Top-Sauk karst outline from Palmer and Palmer 1989).

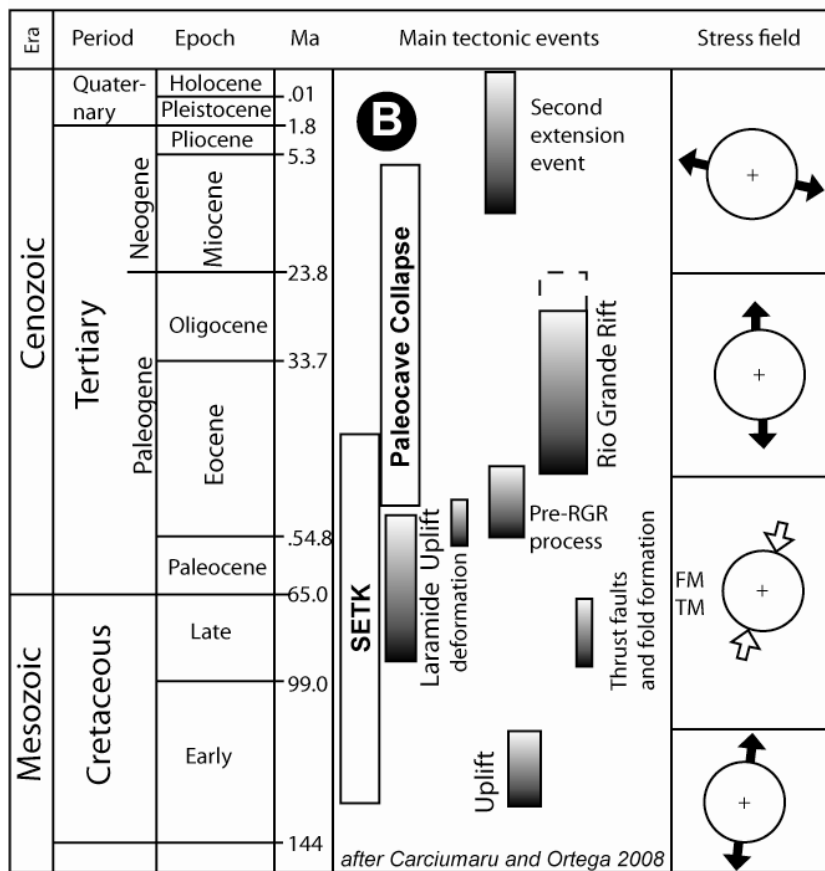
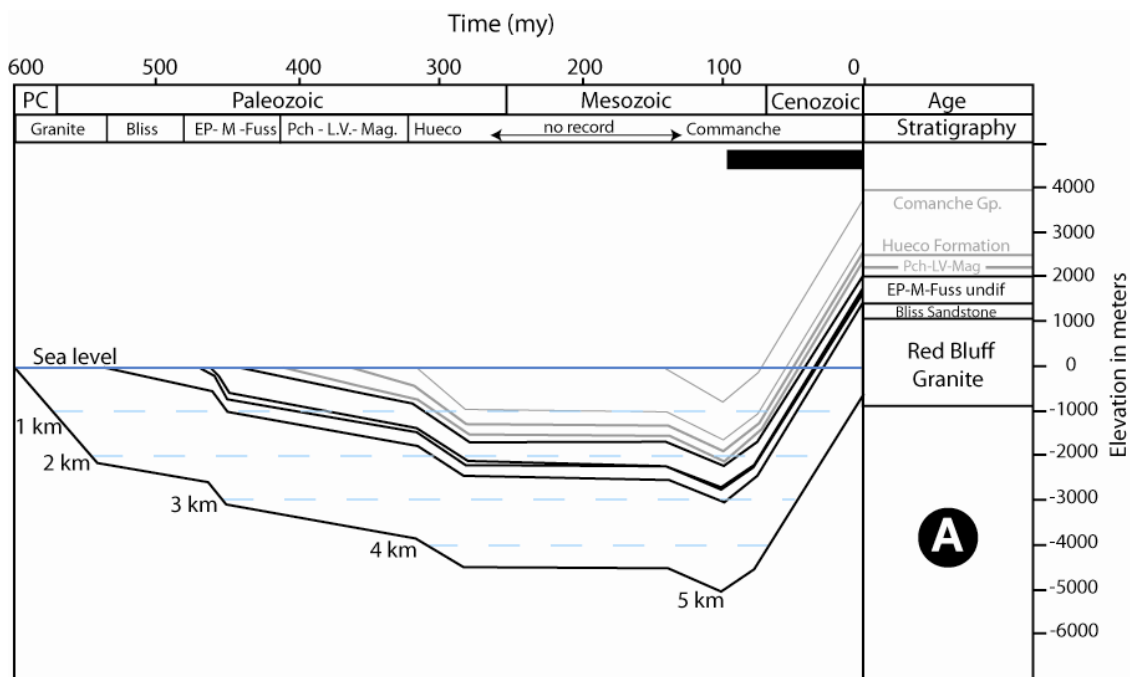


Figure 3.4: Composite burial histories (A) above from published stratigraphic thicknesses (Harbour 1972; Seager and Mack 2003; Carciumaru and Ortega 2008) for the Phanerozoic. EP-M-Fuss = El Paso Group, Montoya Group, and Fusselman Dolomite combined. Pch-L.V.-Mag. = Pecha Shale Lake Valley Group, and Magdelana Group. (Gray text in the stratigraphy column have been eroded leaving Fusselman exposed at the in study area. Younger units are partially preserved in the Northern Franklin Mountains (Harbour 1972). Black bar in upper right corner of (A) indicates detailed diagram (B) of the Early Cretaceous through Holocene major tectonic events and related stress fields that affected the SFM (after Carciumaru and Ortega). FM = Franklin Mountains, TM = Tom Mayes Park SETK = solution-enhanced tectonic karst discussed in text.

within the El Paso Group (Lucia 1995). Deposition of Upper Ordovician Montoya Group carbonates commenced after an unknown thickness of the El Paso Group carbonates was removed as evidenced by the karsted Ranger Peak Formation (Lucia 1995) and regional isopach maps indicating erosional thinning of the El Paso Group to the north (Kottlowski et al. 1969) to a zero-edge some 130 km to the north, near Socorro, NM (~0.3% grade).

A composite burial history curve (figure 3.4A) indicates that the El Paso region was a continuously subsiding basin throughout the Paleozoic. This is reflected in the regional isopach maps for the region (Kottlowski et al. 1963; LeMone 1989; Goldhammer et al. 1993; Ye et al. 1996). Post-Silurian deposition is in stratigraphic continuity with the El Paso Group depositional dip (Harbour 1972; LeMone 1989) with no evidence for substantial tectonic uplift. The first indication of significant uplift (figure 3.4B) in the region occurs during the Late Mesozoic after deposition of an unknown thickness of Cretaceous limestone of the Comanche Series (Harbour 1972). Uplift continued from Laramide through today with three distinct phases of deformation; the Laramide right lateral oblique compression, Rio Grande initial east-west extension and secondary Rio Grande extension (Carciumaru and Ortega 2008).

3.2.2 Diagenetic overview:

The Paleozoic section in the Franklin Mountains is dominated by marine carbonate encompassing a minimum of 1500 m of a total >3000 m of strata that have undergone multiple diagenetic events. Early reflux dolomitization generated strata-bound dolomite in the Chamizal and Cindy Formations (Lucia 1968). At least four discrete phases of dolomitization and three calcite cement stages have been recognized within the SFM study area. Stepanek (1984) documented early stratal dolomite in agreement with Lucia (1968) to be of penecontemporaneous reflux origin. This stratiform dolomite contains $\delta^{18}\text{O}$ values of approximately -2 ‰ (PDB), which is consistent with the proposed early origin. A later burial-related dolomite and even later two-

phase saddle dolomitization occurred perhaps as late as the Tertiary (Stepanek 1984; Lucia 1995). An average burial-phase of micrites (from the Hag Hill, McKelligon, and Fusselman Formations) and breccia fragments and rim cements of approximately -8.5‰ (PDB), followed by a depleted -13.5‰ (PDB) ferroan, zoned calcite and geopetal calcitic silt. Inner zones of saddle dolomite cements with -8.5‰ (PDB) overgrown the calcitic silt followed by an outer ferroan-zoned, depleted saddle dolomite with -14.5‰ (PDB) infilling fractures and small vugs within the breccias. A final phase of non-ferroan sparry calcite flowstone was identified that infills fractures and vugs (Stepanek 1984). On the basis of Stepanek's work a three-phase, post-depositional paragenetic sequence can be recognized in which breccias form and are partially cemented and infilled with calcitic silt followed by a second phase of saddle dolomite cementation from gradually more depleted fluids with a final return to more regional $\delta^{18}\text{O}$ fluid values (-8.5‰).

3.2.3 Breccias

The breccia complexes of the SFM are the single most unique and striking element of the geologic setting of this outcrop belt. Lucia (1971) was the first to treat these breccias in detail, providing maps, cross sections, and a geologic model for breccia formation that focused on the possible formation of these complexes at the Sauk 2nd order sequence boundary. Since these first publications, several authors (Kerans, 1988, Hardage 1996, Loucks, 1999, McDonnell et al. 2007) have cited these breccias as an analog for the subsurface Ellenburger reservoir systems, as well as an analog for top-Lower Ordovician breccias world-wide. The unique aspect of the SFM breccias is the extraordinary vertical extent of the exposure, allowing a full 3D view from below the base of the complexes to all lateral margins, and, to a lesser extent, their upper boundaries.

The vertical breccias form within the McKelligon Canyon Formation and to a lesser extent the Hag Hill Formation (figure 3.2 and plate IV). The five breccias within the McKelligon Canyon

and Hag Hill Formations individually can occupy up to 60,000 m² along the east facing wall of the SFM (table 3.1). The steep, somewhat 2D exposure along the east face of the SFM makes it difficult to determine how far into the mountain (perpendicular to the N-NW outcrop face) these breccias project. In addition, it is also difficult to determine a westward limit for the breccias except in a few cases. Thus, these breccias could be classical cylindrical collapse pipes, or they might represent instead a thin veneer plastered to the side of the mountain. Evidence presented below that was developed as part of the 3D mapping project suggests that many of the breccias did not extend very far into the outcrop in a westerly direction. Chaotic breccias with angular slabs >5 m long, are located near the base of each breccia body indicating "roof-collapse" (*sensu* Kerans 1989) breccias associated with collapse into a large, deep void >50 m below stratigraphic equivalent beds. The roof-collapse zones are between 300-500 m below the Sauk-Tippecanoe unconformity and are in both the McKelligon Canyon and Hag Hill stratigraphic interval. These slab-rich breccias are considered to represent the lowest extent to which dissolution occurred within the El Paso Group hence they likely accumulated near the deepest cave floors. Many of the breccias expose a sharp lower boundary with undisrupted El Paso Group exposures below. The chaotic roof-collapse breccias are generally the only carbonate-breccia material observed that is not dolomitized.

The strataform breccias were identified by Lucia (1971) but not mapped in detail. These breccias are restricted to the middle-upper Ranger Peak Formation where not underlain by McKelligon Canyon Formation equivalent breccias. The *Ranger Peak Breccias* (Lucia 1995), were proposed by him to be the result of bedding-parallel dissolution interfaces similar to those generated at or near the water table. These laterally extensive Ranger Peak breccias system should not be confused with the vertical breccia that occurs within the lower McKelligon Canyon Formation just below the geographic locality of Ranger Peak (figures 3.1, 3.5, and "RP" on plate IV).

Lucia's work (1995) also identified several "breccia pipes" that follow linear trends within the western dip-slope outcrops of the uppermost El Paso and Montoya Groups. Everywhere the Montoya Group is brecciated and the El Paso Group is exposed below it, the El Paso Group is also brecciated. The breccias within the Montoya Group have been previously interpreted as collapsed-cave breccias, formed by upward stoping at a time after the top-Fusselman unconformity (figure 3.6) (Lucia 1995).

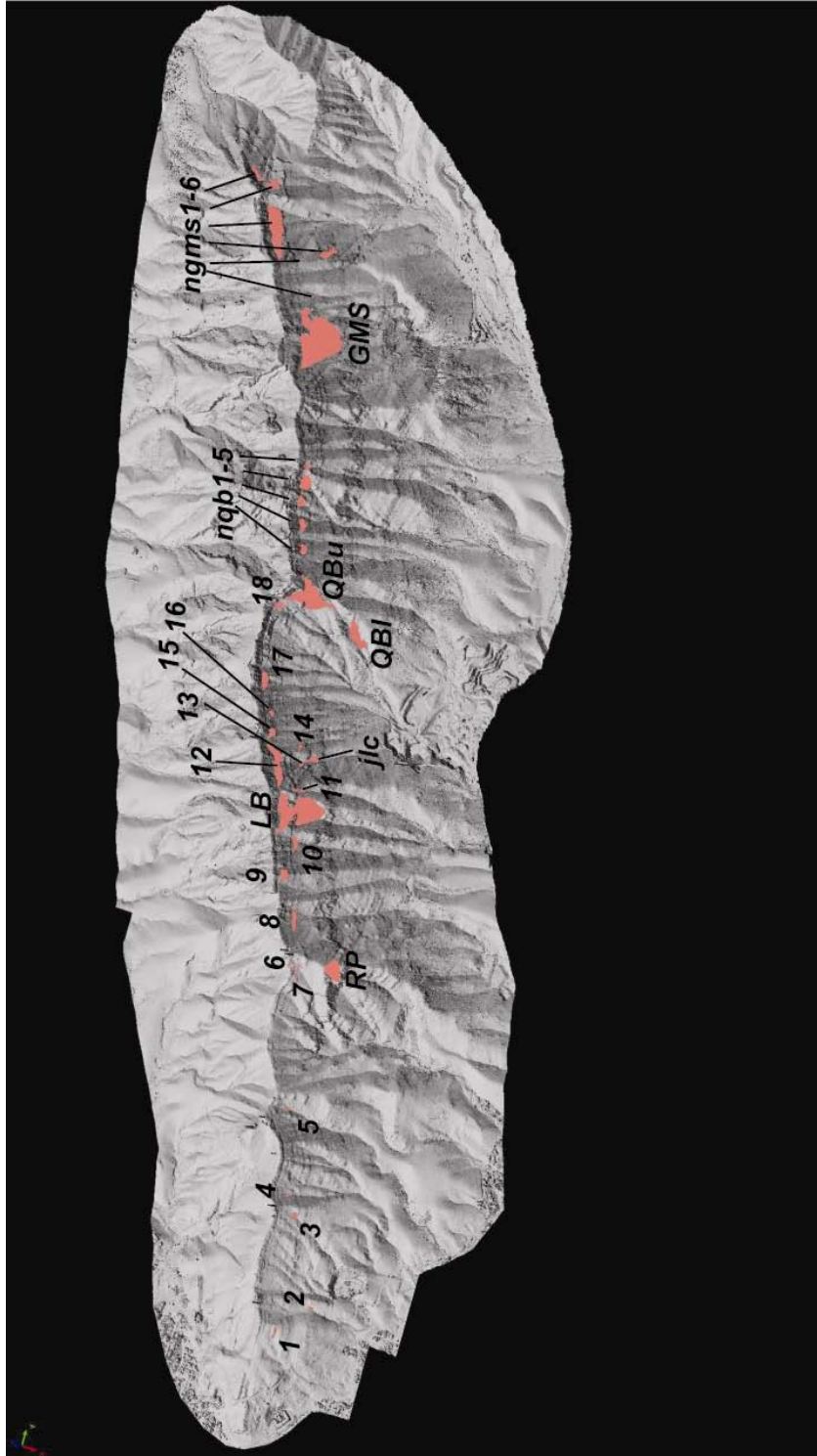


Figure 3.5: Breccias that crop out along the eastern face of the SFM are highlighted in orange. The area of each breccia is labeled in square meters to the right of each breccia name on sun-shaded lidar pointcloud. North is to the right and the lidar field of view is approximately 8 km x 4 km.

The fourth group of breccias is associated with the narrow zones that parallel fault planes. These are restricted to areas with obvious faulting that fit into classical "fault breccia" classification of Sibson (1977). These breccias are monomictic, typically lack fine-grained matrix, and do not resemble the larger breccia bodies previously described. Small exposures (less than 4 m wide but tens of meters in length) are present within the study area near Quarry Breccia and have a shear fabric composed of pulverized host rock with foliated rock fragments less than 10 cm in diameter. These breccias will be discussed briefly in this work as they have little resemblance to the cobble to slab sized, polymictic, matrix-rich, breccias previously described.

3.2.4 Structural history and critical elements:

This region of the southwestern United States experienced the effects of four major Phanerozoic tectonic events beginning with the Ouachita (Flawn, 1961) or Antler-Arbuckle Orogeny (Carboniferous through Permian) and development of the Ancestral Rocky Mountains and the Marathon-Ouachita trend. The effects of this post-Devonian event seems to show little deformation in the El Paso area (Kluth and Coney 1981; Nydegger 1982; Ye et al. 1996). The onset of Laramide compression in the latest Cretaceous to early Tertiary however had significant impact on the sedimentary cover (Richardson 1909; Nelson 1940; Harbour 1972; Fetzner 1992; Wu 2002; Ruiz 2004; Scharmann, 2006; Carmiucaru and Ortega 2008). Subsequent Basin and Range extension followed by Rio Grande extension led to uplift and further complicated the Franklin Mountain tectonic history we observe today. Gravitational sliding continues to affect the SFM outcrops (Lovejoy 1969). It is likely that fractures and faults within the SFM have been reactivated with directional modification during these various events and are truly "complex" fractures in the sense of Drewes (1978).

The late Mississippian-early Pennsylvanian Ancestral Rocky-Mountain orogeny included the Marathon fold and thrust belt, the Orogrande Basin and the uplift of the Diablo Platform (Kluth

and Coney 1981). During this period and throughout the Permian, the El Paso region was a slowly subsiding basin (Ye et al. 1996). Triassic and Jurassic sedimentation is not preserved in the SFM, but no significant structural tilting has been observed between Permian and Cretaceous sediments (Richardson 1909; Harbour 1972). During the Jurassic however, evaporates were deposited that form the detachment for the fold and thrust belt of the Chihuahua Trough immediately to the south of the study area (Carciumaru and Ortega 2008).

Of the numerous tectonic events, it will be argued here that the Laramide compressional event is the most relevant to this study. The early Mesozoic was a time of relative quiescence in the Franklin Mountains region with little to no preserved sediments until the Cretaceous (Harbour 1972). The preserved Cretaceous strata dip at the same angle as Paleozoic strata indicating that there is no structurally-induced angular unconformity present and tilting of the Franklin Mountains strata must therefore postdate the Cretaceous (Richardson 1909; Harbour 1972). Compression along the west coast of North America from the subduction of the Farallon Plate likely did not begin to affect the El Paso region until as late as the Eocene (Nydegger 1982).

The northern edge of the Chihuahua Trough traverses W-NW just south of the Franklin Mountains and is parallel to the United States-Mexico border where an accumulation of sediment in excess of 6,000 m was deposited between the Late Jurassic and Late Cretaceous (Carciumaru and Ortega 2008; Ruiz 2004; Wu 2002; Seager and Mack 1986; Gries and Haenggi 1970). The northern Franklin Mountains expose basement-involved thick-skinned structural features (Karlstrom and Daniel 1993; Carciumaru and Ortega 2008) and the Chihuahua Mountains preserve thin-skinned deformed sedimentary structures of thick sedimentary cover deposited within the Chihuahua trough. This places the SFM at the transition point between these two zones.

The current morphology of the SFM is one of steep topography dipping 30° to the west experiencing ongoing erosion and gravitational sliding (Lovejoy 1969).

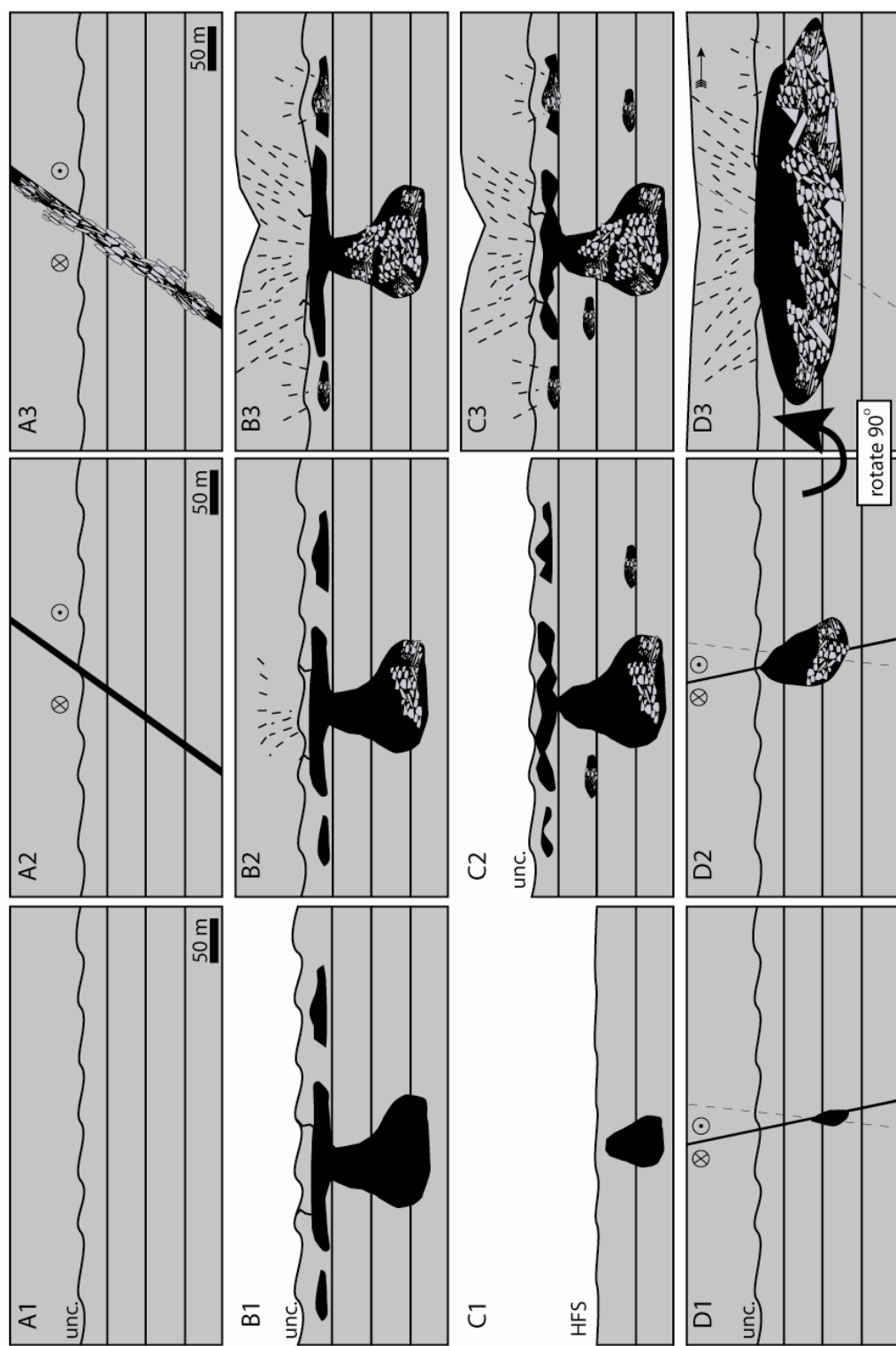


Figure 3.6: Conceptual models for fault driven (A1-3), meteoric karst (B1-3), sequence controlled (C1-3), and soution enhanced fractures (D1-3), 1-3 indicate younger time, "unc." = unconformity, "HFS" = high frequency sequence boundary; models are discussed in the text.

3.3 Models for Breccia Origin:

The origin of a karst collapse breccia is guided by the combination of a mechanical (facies, fractures or bedding planes) driver that is exploited by waters unsaturated with respect to the dominant chemical rock-constituent such as calcite or gypsum (figure 3.7). Once a pathway is established, it will quickly focus flow in the host material (Ford and Williams 2008). In this study, the focusing mechanism that guided dissolution is fracture-driven creating vertical permeability pathways that are solution enhanced. The breccias that form as a result from solution-enhanced tectonic karst would plot along the left half of the diagram below (figure 3.7) but it is important to recognize the dynamic nature of dissolution processes in that any combination of these processes can subsequently completely or partially overprint the other processes.

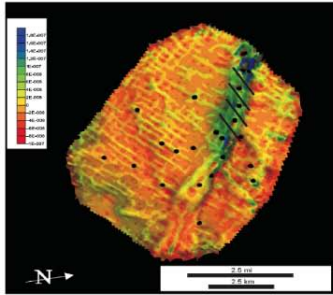
Four models for the origin of breccias observed in the SFM (figure 3.6) in this study are described in this section. (1) A "fault breccia " model following nomenclature revised by Woodcock and Mort (2008) which was based upon the widely accepted fault-rock classification of Sibson (1977) but modified with cave-collapse textural terminology (Loucks 1999), (2) a 2nd order supersequence karst model that suggests meteoric diagenesis as the driving mechanism for solution-cave creation and subsequent collapse and brecciation (Lucia 1995), (3) breccia complexes developed at 3rd order sequence boundaries, calling upon higher-frequency sea-level fluctuations to induce a third-order depositional-sequence-driven subaerial exposure as the mechanism by which cave creation occurred, and (4) a hybrid solution-enhanced tectonic karst model where dissolution is focused along fault surfaces driven by uplift-related gravitational head. In all but the first model, dissolution, void-creation, and internal sedimentation are critical elements in explaining the breccia fabrics.

3.3.1 Fault breccia/gouge model:

By definition, fault breccia implies fault-rock with >30% visible grains greater than 2 mm that are either foliated or non-foliated (Woodcock and Mort 2008). This nomenclature places rocks observed in breccias of the Franklin Mountains within acceptable limits of this classification. The breccia textures observed within the SFM nearly all have >30% visible grains greater than 2 mm. Breccias of interest for this work are large, polymictic, chaotic to crackle breccias that occur in irregular pods along the east face of the SFM (figure 3.5) and do not appear to be classic fault breccias or fault gouge (*sensu* Sibson 1977) typical of shear zones. The mechanics however are relevant to later models in this study and therefore will be discussed briefly here.

In the model summary diagram below (figure 3.6A), a fault breccia is the result of mechanical grinding of *fault-rocks* (*cf.* Sibson 1977) and incorporating these locally derived clasts into the fault breccia. Fault/gouge breccias can be foliated but in reactivated systems this foliation may be completely destroyed as fault motion changes during different stress conditions (Drewes 1978). The orientation of the stress applied in conjunction with the fault displacement, and cohesive rock strength, will determine the magnitude and style of the resultant damage zone. The details of fault damage zones with relation to mechanical stratigraphy in carbonates are an area of active research and are not well understood (Ferril and Morris 2008; Zahm et al. 2009). Fault breccias produced in carbonates will generally follow the fault orientation and be laterally restricted to some proportion of its offset and would be modified by fault-rock strength (Ferril and Morris 2008; Zahm et al. 2009).

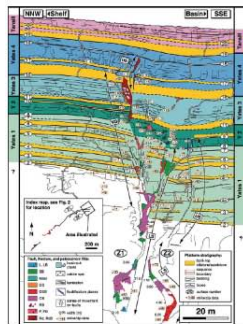
Breccia bodies distinctly tabular, elongate parallel to tectonic grain, textures typically monomict involving host rock and late dolomite cement. Minimal internal sediment or material from younger horizons



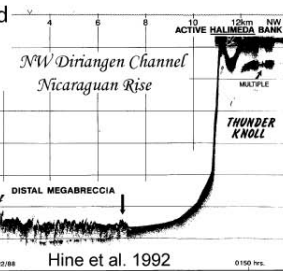
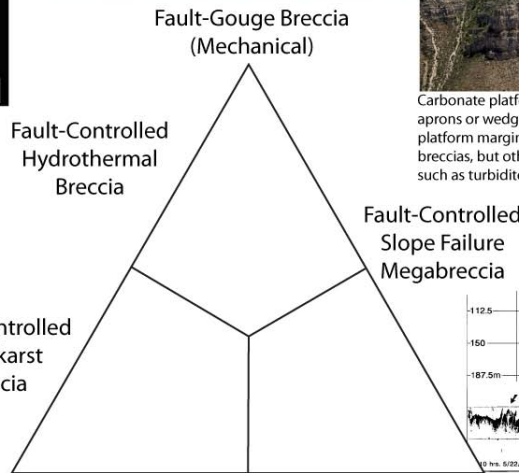
Fault gouge breccias have no textural sorting, no evidence of fluid movement and deposition of breccia or matrix, geometry is distinctly tabular parallel to tectonic fabric



Carbonate platform-margin breccia systems form linear aprons or wedges that thin progressively away from the platform margin. No "internal sediments" are associated with breccias, but other normal background sedimentation occurs such as turbidites and hemipelagites.



Breccia bodies distinctly tabular, elongate parallel to tectonic grain, textures diverse including laminated infills of different ages, typically show some combination of syndepositional growth/offset.



Karst Collapse Megabreccia

Platform-Margin Blue Hole Collapse

Forereef Debris Flow Megabreccia



Major paleokarst systems are characterized by vertically extensive breccia pipes, laterally extensive breccias associated with water-table dissolution, and some element of preferred alignment of karst dissolution features associated with fracture-controlled flow. "Internal sediments" may have laminations.



Carbonate platform-margin breccia systems form linear aprons or wedges that thin progressively away from the platform margin. No "internal sediments" are associated with breccias, but other normal background sedimentation occurs such as turbidites and hemipelagites.

Figure 3.7. The geometry of a breccia body is controlled by a combination of mechanical and/or chemical origin. This ternary diagram separates fault-dominated from karst-dominated and forereef-type collapse breccias. A continuum of breccias types and overprinting of textures is possible. The breccias in this study would plot on the left half of this diagram.

3.3.2 Second-order depositional supersequence meteoric karst model:

In this model, originally proposed for the SFM by Lucia (1971), prolonged subaerial exposure of carbonate strata is proposed to generate caves at the water table and down into the deep phreatic zone during second order sea-level fall-to-lowstand (figure 3.6B). This event would have begun at the top-Sauk unconformity, but then later reactivated in association with different phases of fluid migration and collapse at 10-100 m.y. intervals with amplitudes of 50-100 m, and rise-and-fall rates of 1-3 cm/1000 yr (Goldhammer et al. 1991). The solution-cave system would have propagated along vertically connected fractures creating deep-phreatic shafts that dissolve the host rock several hundred meters below the water table. This cave system partially collapses without destroying the cave-roof-rock and is covered by the next succession of marine carbonates. After lithification of these younger carbonates partial collapse causes some of this upper Ordovician overburden to transport into the underlying Lower Ordovician caves as a collapse breccia.

A second phase of cave-formation occurs at a later time following similar logic with base-level fall/lowstand; however, dissolution follows the collapse-related fracture system induced by the collapse of the previous phase, connecting both meteoric systems together. The resultant succession of strata is hydrologically linked and allowed large clasts (> 50 cm) to be transported down into the re-activated void of the upper reaches of the lower system (figure 3.8). Finally the system may be exposed to reactive fluids along preferential permeability pathways created by the collapsed karst system (Lucia 1995) or may act as a high-permeability pathway for

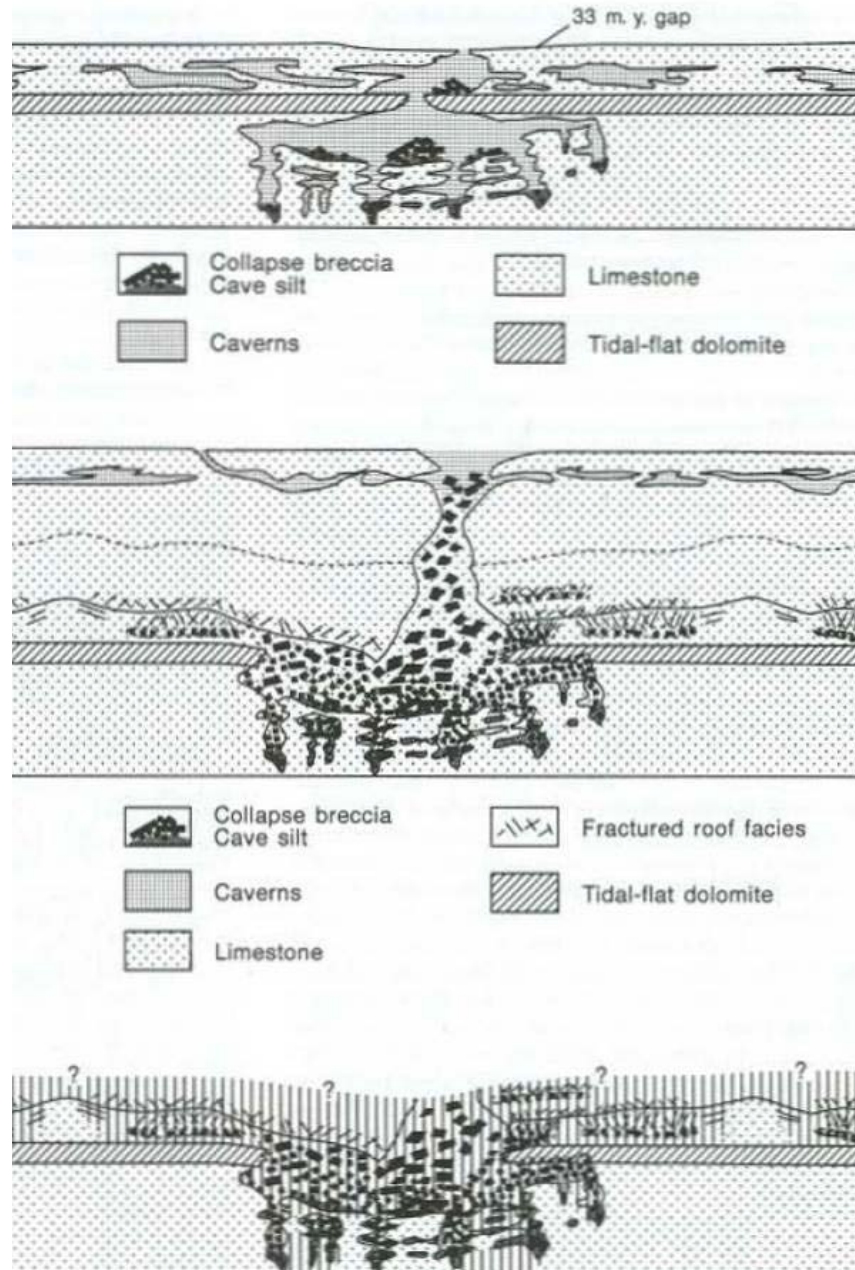


Figure 3.8: Second-order supersequence meteoric dissolution karst model (after Lucia 1995) progressing from the meteoric system (top) to the collapse and diagenesis after the second karst event (bottom). Vertical lines indicate "post-Fusselman dolomitization" (after Lucia 1995).

fluid flow during burial, thereby focusing late dolomitization or similar late diagenetic processes/products.

3.3.3 3rd order sequence composite cave model:

This model was proposed and described previously (chapter 1 of this work) and therefore will be only briefly reviewed here. In this model (figure 3.6C), sequential dissolution occurs at third-order sea-level fall-lowstand creating a vertically stacked composite cave system (Loucks 1999). These fluctuations occur at 1-10 m.y. intervals and have amplitudes of 50-100 m and rise-and-fall rates of 1-10 cm/1000 yr (Goldhammer et al. 1991). Each successive cave system capitalizes on the preferential pathways from its predecessor to focus fluid flow along the developing composite system occurring at third order sequence boundaries (Tinker et al. 1995). With the appropriate duration and environmental conditions during the early Paleozoic (chapter 2 this volume), dissolution of large solution caves may have developed.

This speleogenetic model uses a modern sinkhole as an analog for shape and size of the voids required to result in rock volumes similar to those estimated for the SFM breccias. This model offers an alternative timing for numerous small caves to form and coalesce into one large system at a second order supersequence lowstand. The composite cave system roof did not fail until sufficient burial of the system had occurred, sometime after lithification of the Montoya. Data from subsurface reservoirs (Tinker et al. 1995; Loucks 1999) illustrates that a caves may remain open even under several hundred meters of burial depth. A factor to consider in this scenario is the influence a fluid-filled void versus an air-filled void and the effects a compromised beam (fractured roof) would have on the room size (Loucks 1999) and eventual collapse.

A critical aspect of this karst model, and of the 2nd-order paleokarst model, is the ability to demonstrate syn-Lower Ordovician timing of the dissolution events and subsequent transgression and infill. The upper surface of these breccia bodies can nowhere be shown to be in depositional

contact with immediately overlying strata, thus leaving in doubt the timing of breccia/cave formation. Regardless, this multisurface model could more easily explain the distribution of breccias within the upper half of the El Paso Group by suggesting that they had formed associated with several unconformities rather than only the top-El Paso Group surface.

3.3.4 Solution-Enhanced Tectonic Karst Model:

The solution-enhanced tectonic fracture meteoric karst model, referred to here as the SETK model, has not been formally proposed previously, however informal discussions have been documented within private industry since the 1960's (Bridges, 1967 written communication; Lucia personal communication). In more recent studies of Lower Paleozoic carbonate strata (Woodcock et al. 2008; Tarasewicz et al. 2005) the concept of combined dissolution along fracture systems has been gaining interest. Additionally, the importance of fracture orientation to the existence of the paleokarst system has been recognized by the currently accepted 2nd order supersequence meteoric karst model (Lucia 1995) for cave formation. Explanation of the origin of these fractures with respect to brecciation and the required precursor cave system has yet to be documented.

In the SETK model, thick-skinned, oblique compression induces synthetic Riedel shear fractures at ~10 and ~75 degrees to the main oblique fault (Woodcock and Schubert 1994). This tectonic regime creates three primary orientation of fractures related to oblique compression sub-parallel to the principal stress direction (figures 3.4B and 3.6D). The fault-generated fracture network could provide a permeability system through which solution enhancement would be focused. The source of these fluids is dependent upon the dynamics of the specific setting in which these systems form. The migrating fluids unsaturated with respect to calcite may enlarge the fracture aperture exponentially with time, further focusing regional fluid flow and development of large solution-cave systems (Dreybrodt and Gabrovšek 2002) that later may collapse. Fracture-driven cave formation has been extensively modeled and is widely accepted as a

common (if not the most common) focusing mechanism in speleogenesis (Palmer 2007; Ford and Williams 2008). In all but the first of these models a precursor connected fracture network is required to focus flow and allow dissolution cave to form into which overburden may collapse downward stratigraphically (assuming bedding is not overturned).

The remainder of this paper will discuss methods and results of the research carried out to resolve the complex tectonic and karst history of the SFM and will then reconsider the relative merits of the four models covered above.

3.4 Methods:

Field mapping of the breccias in an attempt to correlate geometries in 3D proved ineffective. Although individual breccias could be examined, establishing a link from one breccia body to the next proved exceptionally difficult. Likewise, ground-based lidar was attempted but the lack of acceptable vantage points from which to acquire data was a significant obstacle to data quality. It was recognized that resolution of the origin of the SFM breccias was a 3D spatial problem that required special treatment. Thus, in September 2006, the RCRL set out to capture the entire SFM outcrop belt with airborne lidar data to provide a spatial high-resolution DEM for mapping and 3D modeling.

The airborne lidar survey acquired for this research contains over 200 million laser XYZ points matched to airborne orthophotographs from March, 2002 (www.seamless.usgs.gov) for the entire area. Stratigraphic contacts were digitized manually onto a sun-shaded airborne lidar point cloud calibrated to ground-control points. Photographic panoramas oblique to the outcrop, acquired during the lidar survey were also used in calibration of stratigraphic interpretation and construction of the DOM. Bedding contacts; strike, dip, fracture and fault orientations, as well as faults traced with GPS were incorporated into the DOM. All GPS coordinates were projected onto the airborne lidar data which had an average elevation error of +/- 0.009 m (appendix A).

Where sufficient exposure was available on airborne lidar data a 3D least-square median plane was calculated to extract average bedding or fault dip. This process worked best for projecting dipping stratigraphic surfaces from the east face of the mountain into the steep dip-slope canyons along the west side of the mountain. In this way bedding discontinuities related to fault offsets were readily identified. Fault traces that were traced over long distances (>100 m) also could be used to extract fault plane strike and dip. The erosional profile of the SFM made determination of fault strike less prone to error than fault dip as most fault surfaces were more confidently traced along bedding surfaces.

Fault scarps where exposures are partially covered by alluvium such as the Western Boundary Fault (WBF) (figure 3.9) were identified by meter-scale topographic anomalies visible on the lidar data. These vertical anomalies were used to identify covered faults and used to create fault planes from lidar points extracted along fault trace. Results from this fault-plane mapping method were used to project planes and their potential intersection points onto the eastern SFM outcrop face (figure 3.9). With this method, complex 3D geometries of the intersection between dipping strata and steeply dipping faults were visualized in 3D space. The high-resolution lidar data also made it possible to view stratigraphy and fault associations from various perspectives with present-day structural dip removed (figure 3.9 and 3.10).

Breccia outlines from the east face of SFM were digitized and projected along planes perpendicular to the WBF. The projected results were examined for grouping or clustering along linear trends parallel to the WBF. This comparison although visible in map view can not easily be compared along the 340° regional strike of the SFM due to the structure and natural erosional profile of the mountain. The projected outlines, collapsed onto the perpendicular 2D plane, were projected along the regional strike vector for both breccia bodies and dolomite halos surrounding the breccias for the observations along the east face. The variance of each projected cluster was measured by extracting the difference between the minimum and maximum distance of each

breccia and/or dolomite halo to the WBF (figure 3.11) and recorded in table 3.1. The projection plane was then rotated about the WBF in 3° increments in the positive and negative direction along compass from the regional strike and cluster spacing was again measured and recorded in table 3.1. This process was repeated six times to +/- 10° from regional strike (340°) of the WBF.

All lidar points that fall within each breccia outline were extracted as a subset point cloud and a three-dimensional least squares distance vector was calculated intersecting all points. This vector was within 1.5° of regional strike of the WBF. The orientation of this vector was then used to compute a plane parallel to this trend and rotated about this vector 180° in 1° increments. Distance from the plane to all lidar points that fall within breccias outlined in this work were calculated and recorded in frequency plots of the distance of each lidar breccia point to the plane (along a vector normal to the plane). A zero value on the X axis is equivalent to the plane position (figure 3.13). Each group of plots, in 10° rotational increments were graphed together and are and were visually inspected for normal distribution about the plane position with the highest frequency of occurrence and least amount of scatter.

The area of each breccia was calculated using a triangular-area summation of from all nearest neighbor points and recorded in table 3.2. The "width" or difference between the minimum and maximum distance of each breccia body from the WBF was calculated and recorded in table 3.2. In other words, a triangular mesh was constructed for each breccia body and the total area for all triangles was calculated.

Near-vertical, tabular breccias along the western dip slope with limited vertical exposure were mapped within the lower Upham Formation and uppermost Ranger Peak Formation. A different strategy was used to extract trends preserved within these strata. Each breccia was mapped by selecting all of the lidar points within the breccias body from which a point cloud subset was saved. A best-fit least squares vector was calculated for each point cloud subset (figure 3.14). The strike of this vector was recorded in table 3.3 along with the summation

triangulated 3D area of each linear trend point cloud. This method extracted the orientation and area of each breccia body with limited user bias.

Rose diagrams from field measurements of faults and fracture orientations along with lidar-derived fault traces were generated. Lidar line-segments taken along fault traces were used to create vectors. These vectors were weighting by magnitude and treated as strike and dip measurements. Similarly, field-measured fault strike and dip measurements were weighted by the offset of each fault multiplied by a factor of 100 to approximate fault length from offset. These two types of measurements were combined to produce rose diagrams for observations within the study area and were in agreement with previously published regional bedding and fault orientations (Harbour 1972; Thomas 1974; Stacy 1991; Fetzner 1992; Wu 2002; Carciumaru 2005; Scharman 2006; Carciumaru and Ortega 2008).

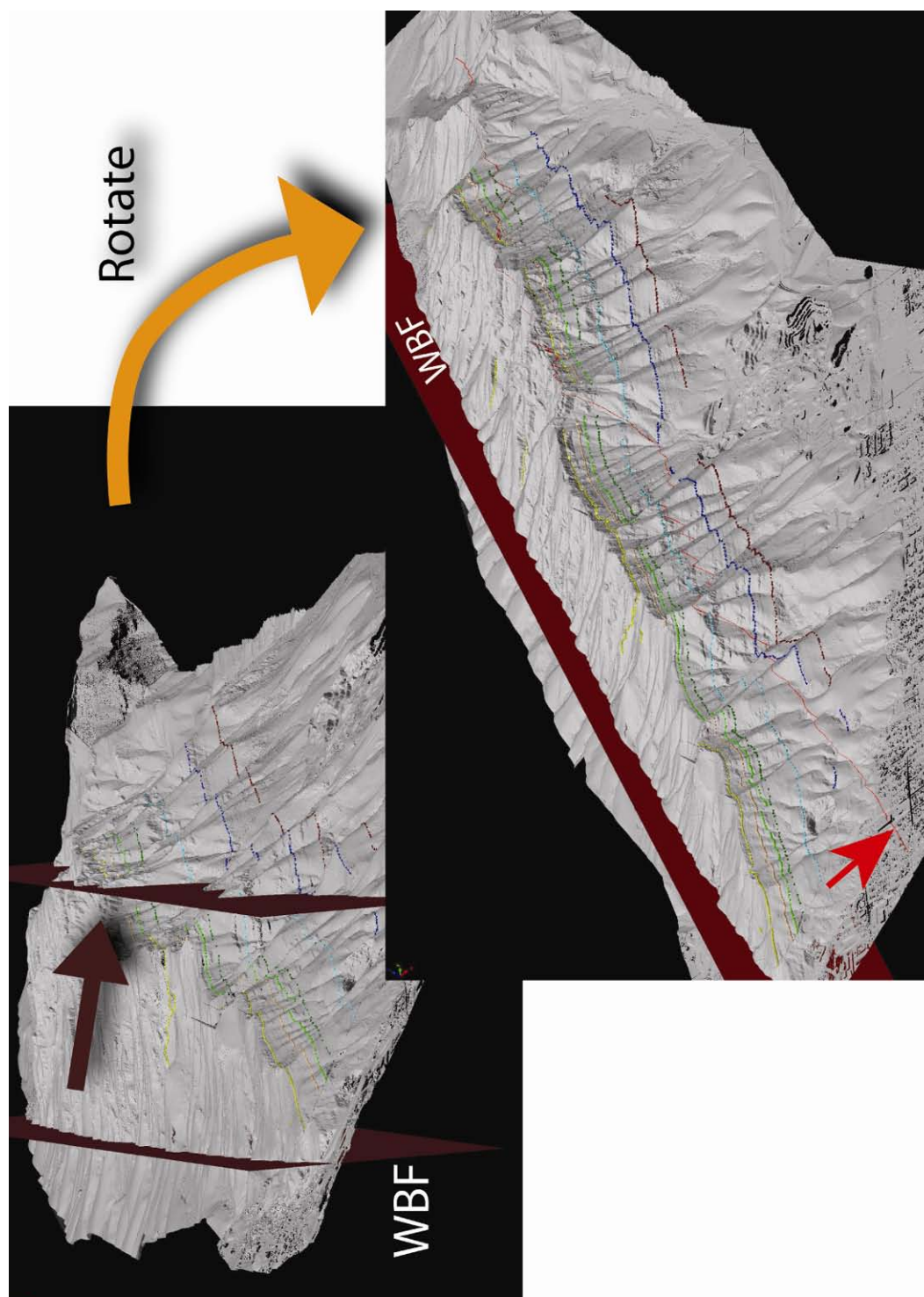


Figure 3.9: Upper left illustrates the projection of the Western Boundary Fault (WBF) to the range front. The lower right image is rotated to show the intersection of the projected fault trace with the outcrop erosional profile (red arrow); projected WBF has been removed so as not to obscure the view.

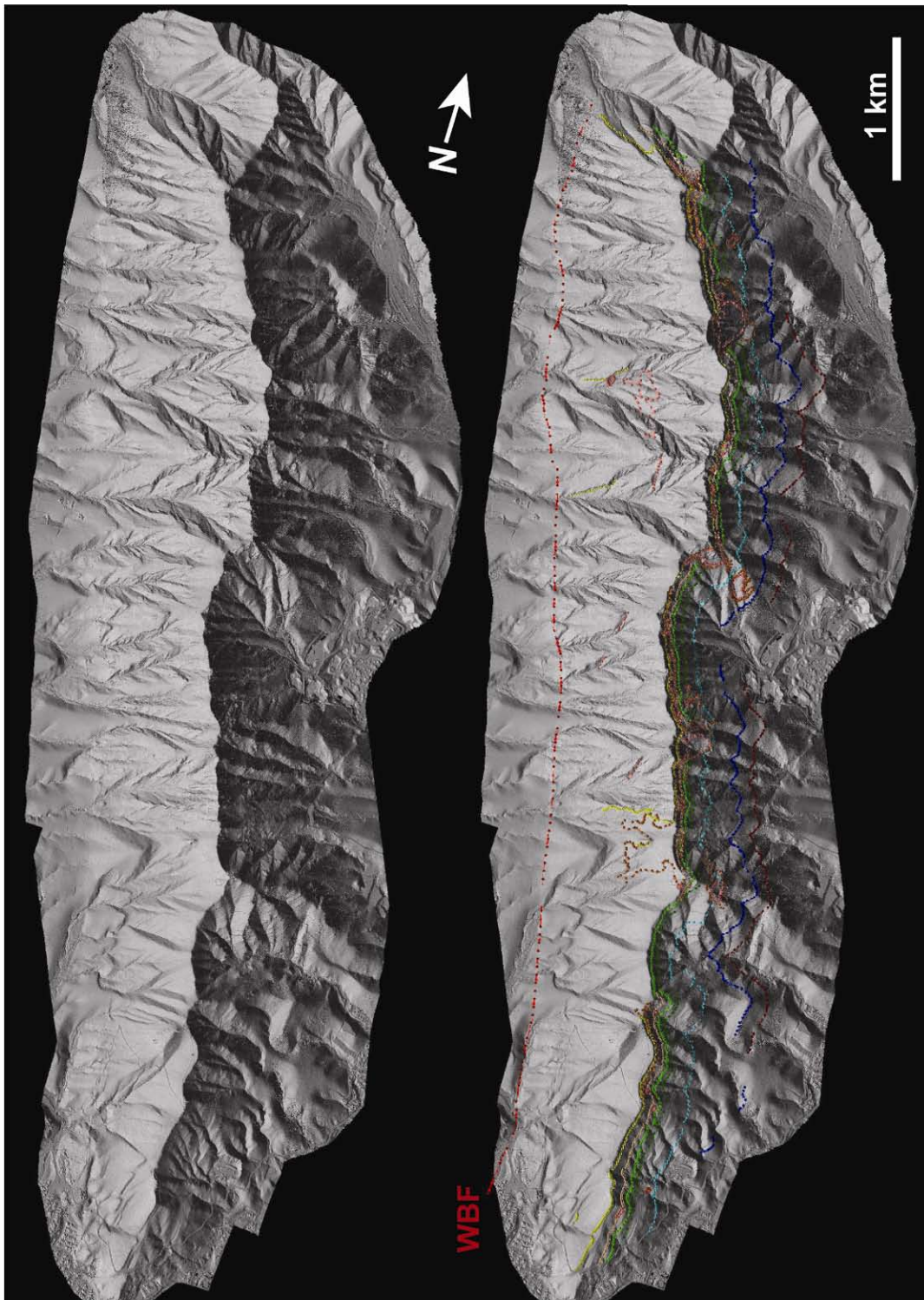


Figure 3.10: Upper image illustrates the fault scarp visible through the alluvium. The fault trace is highlighted in red in the lower image.

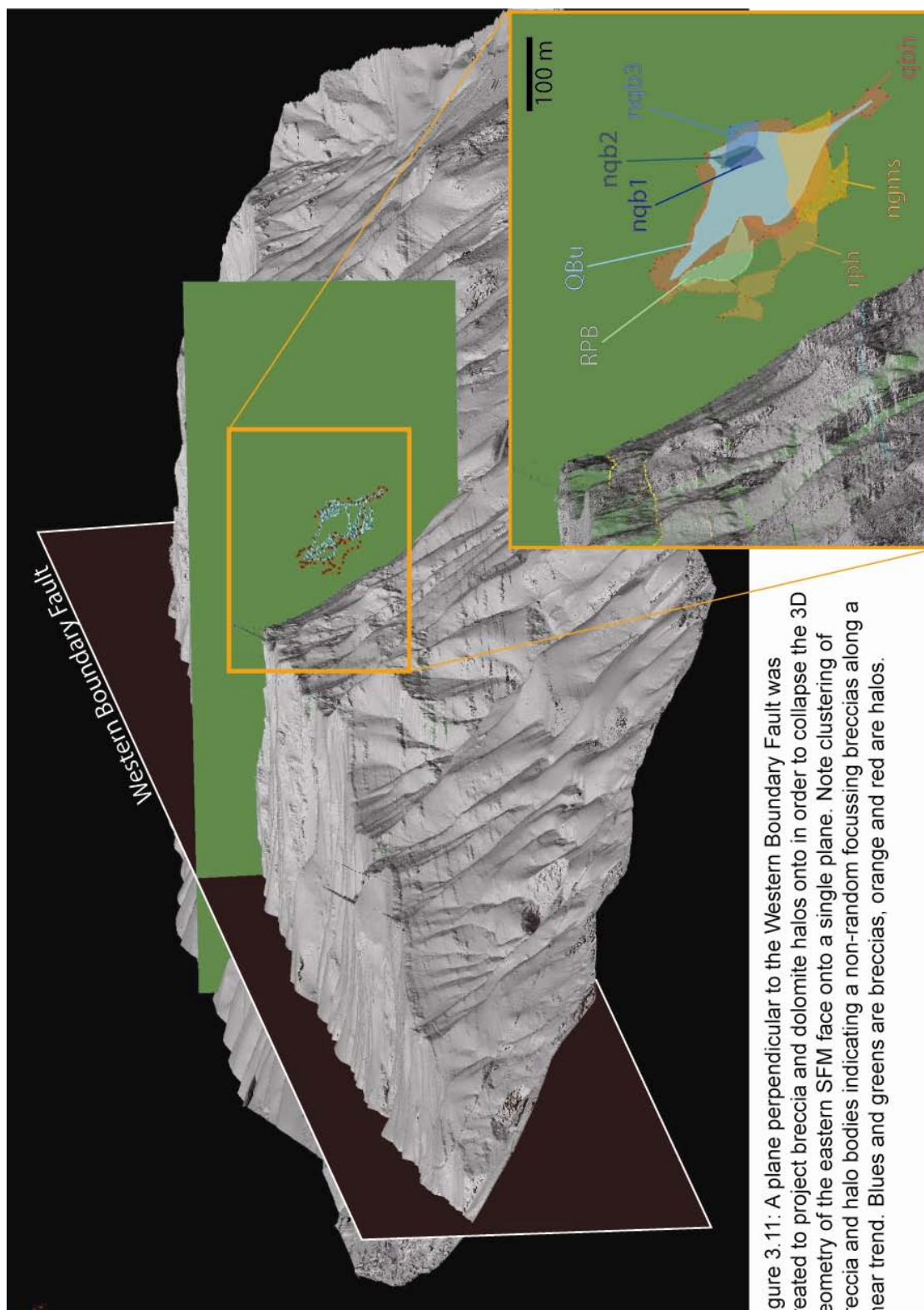
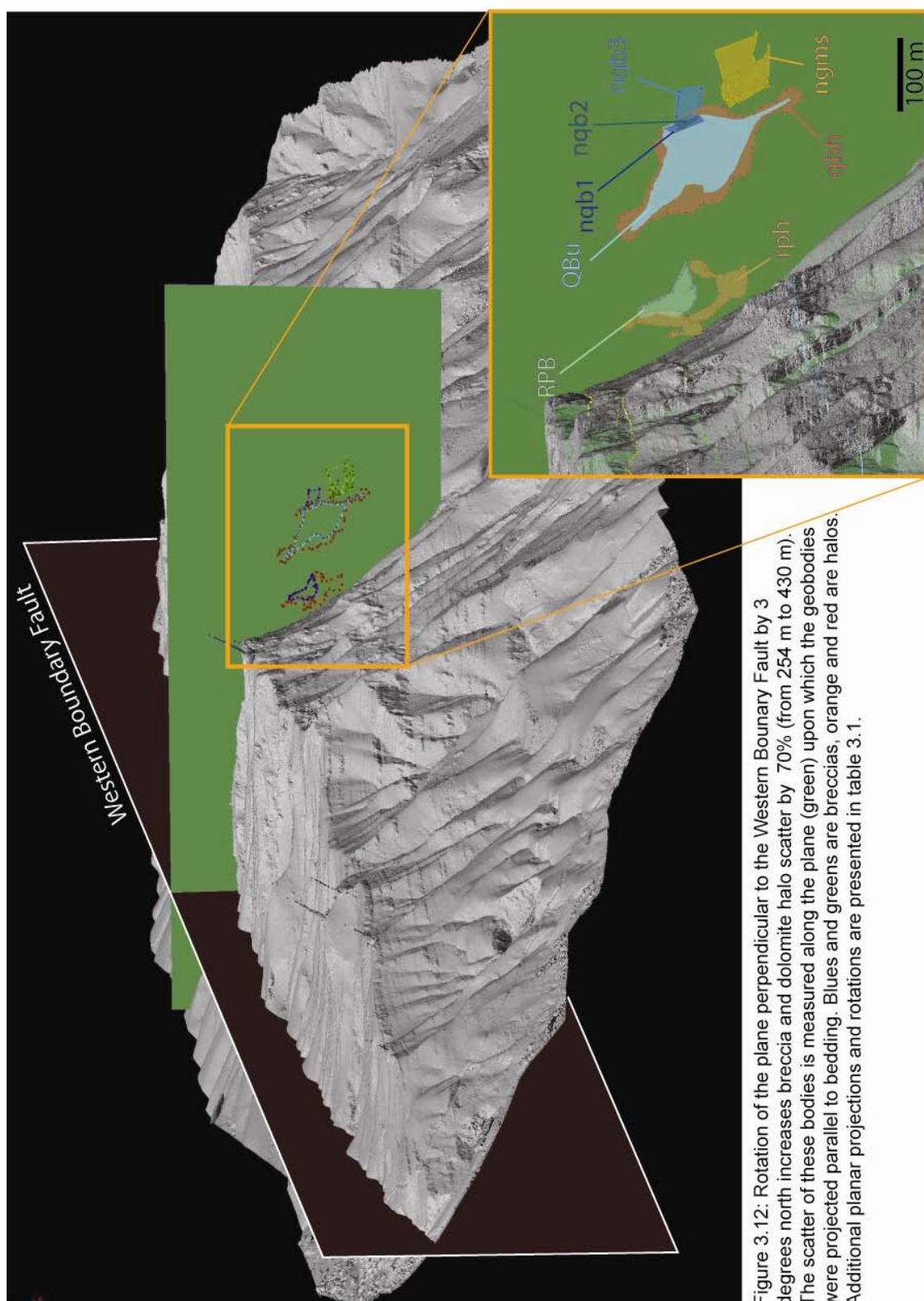


Figure 3.11: A plane perpendicular to the Western Boundary Fault was created to project breccia and dolomite halos onto in order to collapse the 3D geometry of the eastern SFM face onto a single plane. Note clustering of breccia and halo bodies indicating a non-random focussing breccias along a near trend. Blues and greens are breccias, orange and red are halos.



<u>Flat-Cluster</u>	<u>Rotation</u>	<u>Width</u>	<u>% change</u>
QB Hi	0	248	0%
QB Hi Rot 3N	-3	430	73%
QB Hi Rot 3S	3	275	11%
QB Hi Rot 6S	6	389	57%
QB Hi Rot 6N	-6	611	146%
QB Hi Rot 10N	-10	897	262%
QB Hi Rot 10S	10	810	227%

Table 3.1: Six rotations of the projection plane (green plane in figure 3.9 and 10) are presented in this table. The maximum scatter from each projected breccia was measured parallel to the projection plane from edge to edge of the cluster of objects. The per cent change from the plane normal to the regional Western Boundary Fault to each of the six rotated orientations (+/- 3°, 6°, and 10°) indicates a rapid reduction in spatial correlation with only a few degrees of rotation.

3.5 Observations:

In complex, rugged terrain like the SFM a seemingly simple task, such as walking out a fault or fracture quickly becomes extremely difficult due to vertical cliffs and numerous closely spaced canyons. High-resolution lidar was used to map strata and identify discontinuities potentially related to faults with offsets of >2 m and breccias that are larger than 160 m² along the east face of the SFM (figure 3.5, plate 2). High-resolution lidar data offers a quantitative base map from which geological observations can be compared in 3D. The following section will be divided into fault orientations, fracture plane orientations and breccia geometry.

3.5.1 Main Boundary Faults:

There are numerous faults and fractures in the SFM that vary in offset from zero along small fractures to over 6000 m along the Eastern Boundary Fault uplifting the Precambrian basement adjacent to Tertiary alluvium. The Western Boundary Fault Zone is a complex of several closely-spaced parallel faults across a zone ~60 m wide (Harbour 1972; Stacy 1991; Wu 2002) with a 340° trend. The fault zone can be traced along the base of the western dip slope of the SFM. Within the WBFZ along the entire Franklin Mountain chain both steeply dipping normal and reverse faults between 50-70° east have been documented (Harbour 1972; Wu 2002) with an

average dip of 30° to the west. In the SFM, this fault scarp is commonly covered by Tertiary alluvium but continuous segments can be identified between scattered outcroppings in the lidar data for several hundred meters each (figure 3.9, 3.10). The scarp traces can be connected to extrapolate a continuous fault interpretation along the entire SFM. From this interpretation a median value was extracted to construct a plane representing the average trend of the WBFZ. The relief on this fault trace is insufficient to calculate a reliable dip angle for the fault plane. Therefore, field measurements from faults parallel to the WBFZ on the dip slope of the SFM were compared to previously published fault dips (Harbour 1972; Wu 2002) and were all with +/- 10 degrees of 60° so a near vertical dip to depositional bedding dip was used (figure 3.9).

Faults parallel to the WBF that are exposed along the eastern face of the SFM follow an extremely serrate pattern tracing up from the Precambrian granite to the top of the El Paso Group over a distance of a km or less. The complexity of this fault trace makes it exceedingly difficult to follow in the field and would likely not be recognized without the aid of lidar data (red arrow in figure 3.9). Nineteen of the thirty-four breccias that crop out along the eastern face of the SFM (plate IV) occur between +/- 125 m to the east and west of the fault plane in figure 3.9. In addition, the upper half of the upper Quarry Breccia is also partially intersected within these limits. An accurate palinspastic reconstruction of the three fault blocks identified in the regional map of the area (Collins and Raney 2000) could include as many as 10 additional breccia bodies within these limits but reliable slickensides to determine true sense motion have not been identified.

3.5.2 Breccia locations and geometries:

Breccias are subdivided into two groups, those that crop out along the eastern face of the SFM, and those that are exposed along the western dip slope. A total of 34 breccias larger than 160 m² were mapped along the east face of the SFM (figure 3.5, plate IV). These breccias have been described above and generally have somewhat random fill type but all are collapse cave

breccias. In the breccias that penetrate down into the McKelligon Canyon Formation, breccia clasts retain original stratigraphic order (figure 3.2) with oldest and largest protolith clasts at the base of each breccia followed by younger and gradually smaller clasts above.

All breccia names with numerical characters in their names increase from south to north, for example ngms1 is the southernmost of the "ngms" breccias and ngms6 is the northernmost. Four of the seven largest outcrop areas of breccia (table 3.1, yellow highlights) have been previously described as "vertically extensive" (Lucia 1995) and include from south to north, the Ranger Peak (RP), Lechuguilla (LB), Quarry (QBu), and Great McKelligon Sag (GMS) breccias (figure 3.5, plate IV). The largest of the remaining three, ngms4, was previously mapped as part of the laterally continuous breccia within the Ranger Peak Formation, as was number 12 breccia; Quarry Breccia lower (QBl) was noted but not discussed (Lucia 1995). The nqb1-5 breccias were included as part of Lucia's Ranger Peak laterally continuous water table karst, as were numbers 9, 12, 15, 16, 17, ngms5 and 6. Breccias not previously documented are 1-8, 10, 13, 14 and ngms 1-3. In general these breccias are ovate to in outcrop expression. One breccia within the study area not included in this work but previously identified by Lucia (1995) is the "North Face" which occurs at the northern end of the study area (figure 3.1).

There are 10 western dip slope near-vertical, tabular breccias identified in this study that were more than 25 m wide from southeast-to-northwest and several hundred meters in length (figure 3.14). There are likely more yet to be discovered. These tabular breccias occur primarily within the lowermost Montoya Group and to a lesser extent the uppermost El Paso Group and range in size from 960 to over 15,000 m² and all have a general NE trend. The alignment of these breccias is apparent in map view but are particularly striking when structural dip has been removed (figure 3.14) by rotating the airborne lidar data set to return bedding to original orientation. The tabular breccias are chaotic and appear clast-supported with sub-angular to rounded clasts and a fine-grained dolomite matrix and clasts. Clast size ranges from 0.1 to 1.0 m.

There is stratigraphic offset along these linear breccias that can be identified in both lidar data and field observations that is down to the east as much as 30 m.

3.5.3 Fracture plane orientations and breccia geometry:

The alignment of breccias in the SFM indicates a structural fabric likely controls their distribution. To test for alignment, breccia bodies were collapsed onto planes perpendicular to the WBF the dominant structural feature in the SFM. All of the breccias exposed on the east face of the SFM align into two clusters. Each breccia was mapped on the lidar data as were the associated dolomite halos. The breccias and halos were then projected onto a 2D plane perpendicular to the WBFZ (figure 3.8) described previously in this chapter. When planes were rotated away from the WBFZ orientation by more than $\pm 3^\circ$, the clusters rapidly broke apart (figures 3.11 and 12). To illustrate this, the distance from edge to edge of the farthest spread objects parallel to 2D projection plane was measured and recorded in table 3.2. With as little as -3° of rotation there is a 73% increase in the cluster size. The asymmetry of increase in the positive and negative rotation may be contributed to the natural variation of the WBFZ or slight rotational ($\sim 1^\circ$) error of the projection plane or the WBFZ plane. A vector was defined using a least squares method for all points within breccia bodies (figure 3.5 pink highlights). The orientation of this vector was 342.7° ; the strike of the MBF was measured in the field with an average of 340° and calculated from the fault scarp traces of the WBF from the lidar data to be 341.5° (figure 3.8). All of these values are less than $341.5 \pm 1.5^\circ$ degrees and within acceptable error tolerance.

To test for sensitivity of the alignment of breccias to dip angle of the fault plane, the data points within the breccia outlines for all breccias that crop out on the east face were selected and the frequency distribution of signed distance from the plane was calculated (figure 3.13). This was conducted at 1° increments for angles between $0-180^\circ$ to bedding to test for the best fit dip plane

that intersects the breccia point cloud. It is important to recognize that two most likely clusters should result from this test. The first would be the plane parallel to the erosional profile of the SFM and the second should be the most likely dip plane for the fault/fracture trend connecting the breccia bodies. Over 1.7 million breccia point samples were calculated in this process. The two planes with the least variance are a normal distribution that is parallel to the dip slope (erosional slope bias) shown in green in figure 3.13 and a bimodal distribution parallel to the calculated dip from the WBFZ shown in red in figure 3.13 which are ~30 East dip and ~60° E dip respectively.

Fracture, fault and fault trace orientations were plotted as a rose diagram (figure 3.14). The combined result shows three preferred orientations. The first and most extensive is the WBFZ discussed earlier with dominant orientation at 340° with >>100 m offset. The second follows linear breccias along the dip slope with variable offset (0-40 m) and contains collapse breccias with a trend of 355° which is ~15° east of the WBF orientation. The last shows variable offset from 0-10 m with a trend of 55° which is ~75° east of the WBF orientation. If a Riedel Shear model is applied with NE-SW compression dilatational faults would form at approximately 10 and 75 degrees NE of the WBF. There is a good agreement between the fracture planes mapped and those predicted by a Riedel shear model.

Linear trends from the dip-slope were mapped on lidar data and used to construct a feature length-weighted rose diagram of orientations. Each line segment mapped along a linear feature was plotted weighted by the length of the segment. Due to the nature of the outcrop, the most confidently identified linear features are exposed along the dip slope. These measurements therefore come almost exclusively from the Montoya Group. The orientations of the fractures fall into three groups. Group one is parallel to the WBFZ, the second group is between 10 and 20° east of the WBFZ and the third group is between 60 and 80° east of the WBFZ (figure 3.14).

Breccia	Area (m ²)	Width m	Lucia (1995, 1971)
1	889	52	n/a
2	555	26	n/a
3	952	31	n/a
4	414	12	n/a
5	741	21	n/a
6	254	30	n/a
7	652	74	n/a
RP	8,458	64	Ranger Peak
8	2,805	26	"laterally continuous"
9	2,426	35	n/a
10	2,279	22	noted but not discussed
LB	38,579	179	Lechuguilla Breccia
11	1,092	39	Lechuguilla Breccia
12	10,011	78	n/a
FJC	2,338	59	"sediment filled cave"
13	988	22	"laterally continuous"
14	561	19	"laterally continuous"
15	2,019	13	"laterally continuous"
16	678	19	"laterally continuous"
17	3,227	28	"laterally continuous"
18	1,821	40	Quarry Breccia (faulted segment)
QBI	12,297	80	noted but not discussed
QBu	26,742	182	Quarry Breccia
nqb1	2,127	23	"laterally continuous"
nqb2	2,563	23	"laterally continuous"
nqb3	2,488	42	"laterally continuous"
nqb4	6,162	66	"laterally continuous"
nqb5	1,004	21	"laterally continuous"
GMS	59,679	142	Great McKelligon Sag
ngms1	424	20	n/a
ngms2	161	17	n/a
ngms3	4,530	60	n/a
ngms4	20,692	103	"laterally continuous"
ngms5	3,136	74	"laterally continuous"
ngms6	2,319	97	"laterally continuous"
MIN	161	12	
MAX	59,679	182	
AVG	3,168	53	
Total	226,063	1,839	

Table 3.2: Summary of breccia area (m²), and width (m) from south to north along the SFM. Width is calculated from the difference between minimum and maximum distance from the outcrop face parallel to the Western Boundary Fault. Breccias previously documented by Lucia (1995, 1971) in the column at the far right. Yellow highlighted cells are the seven largest breccias mapped. Area is calculated from the 3D summation of the triangular area between all points.

Linear Feature		Area (m ²)	Strike°	Length
Pipe Plane Crash		1,600	10	83
Pipe West of Lechuguilla		7,297	12	228
Pipe North of Two Towers A		960	4	122
Pipe North of Two Towers B		4,588	4	182
Pipe South of Transition A		10,175	-5	132
Pipe South of Transition B/C		15,479	-5	300
Pipe North of Transition A		8,892	7	255
Pipe North of Transition B		6,173	5	138
Pipe North of Transition C		2,960	6	72
	MIN	960	-5	72
	MAX	15,479	12	300
	AVG	6,458	4	168
	Total	58,124	38	1,512

Table 3.3: Tabular feature dimensions calculated from the lidar data polygons from the 3D summation of the triangular area between all points. Negative values are west of north.

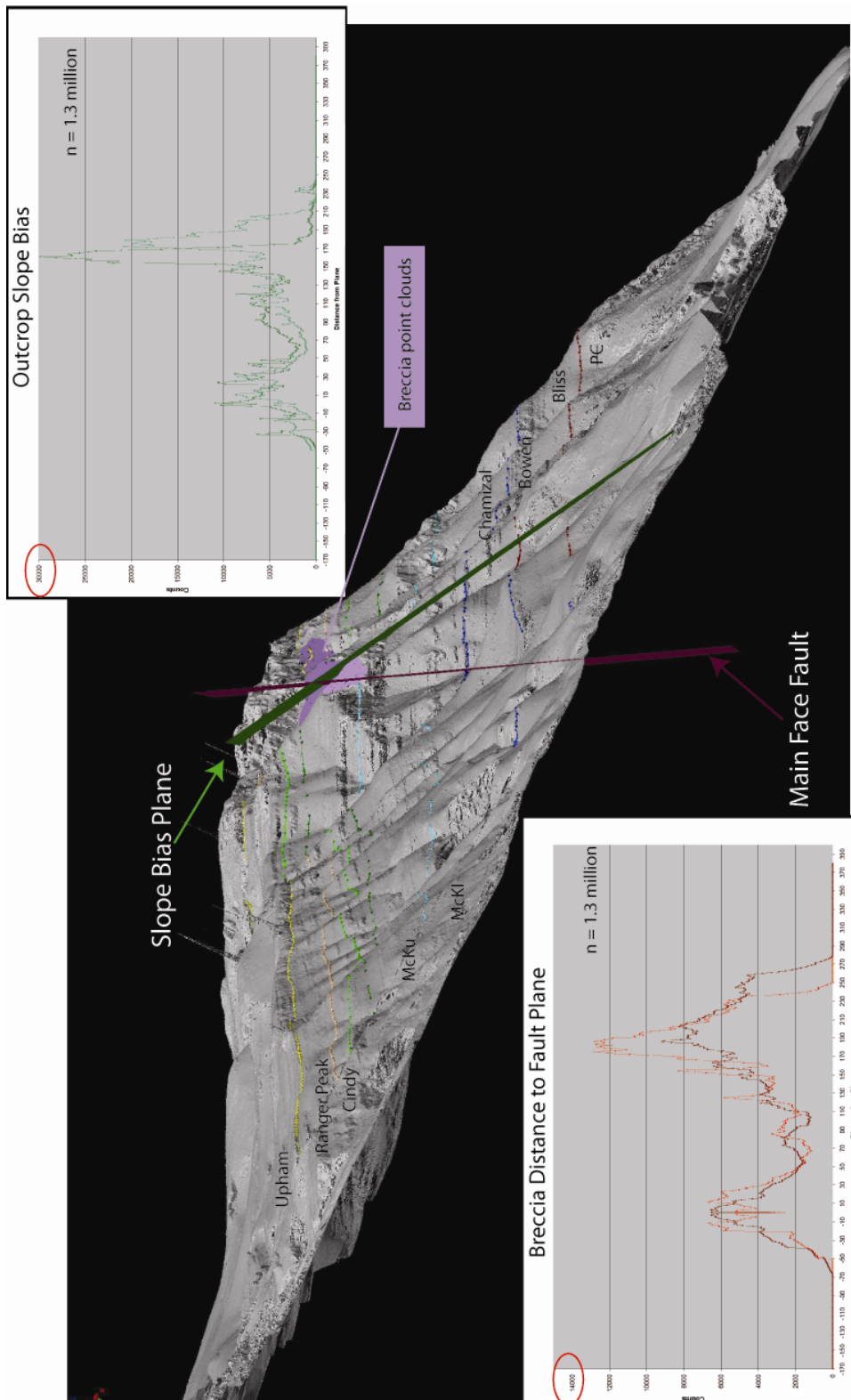


Figure 3.13: Lidar data from outcrops may impose bias for spatial analysis. In this example, the green slope bias plane illustrates the erosional plane of the outcrop that influences points plotting within 170 m of the Main Face Fault (upper right). The lower graph illustrates the bimodal distribution of breccia bodies centered at 0 and 190 m (lower left, x-axis). Note the y-axis scale change between these two graphs (red circles). Alignment of the fault plane parallel to the outcrop erosional face induces a strong bias in the data analysis.

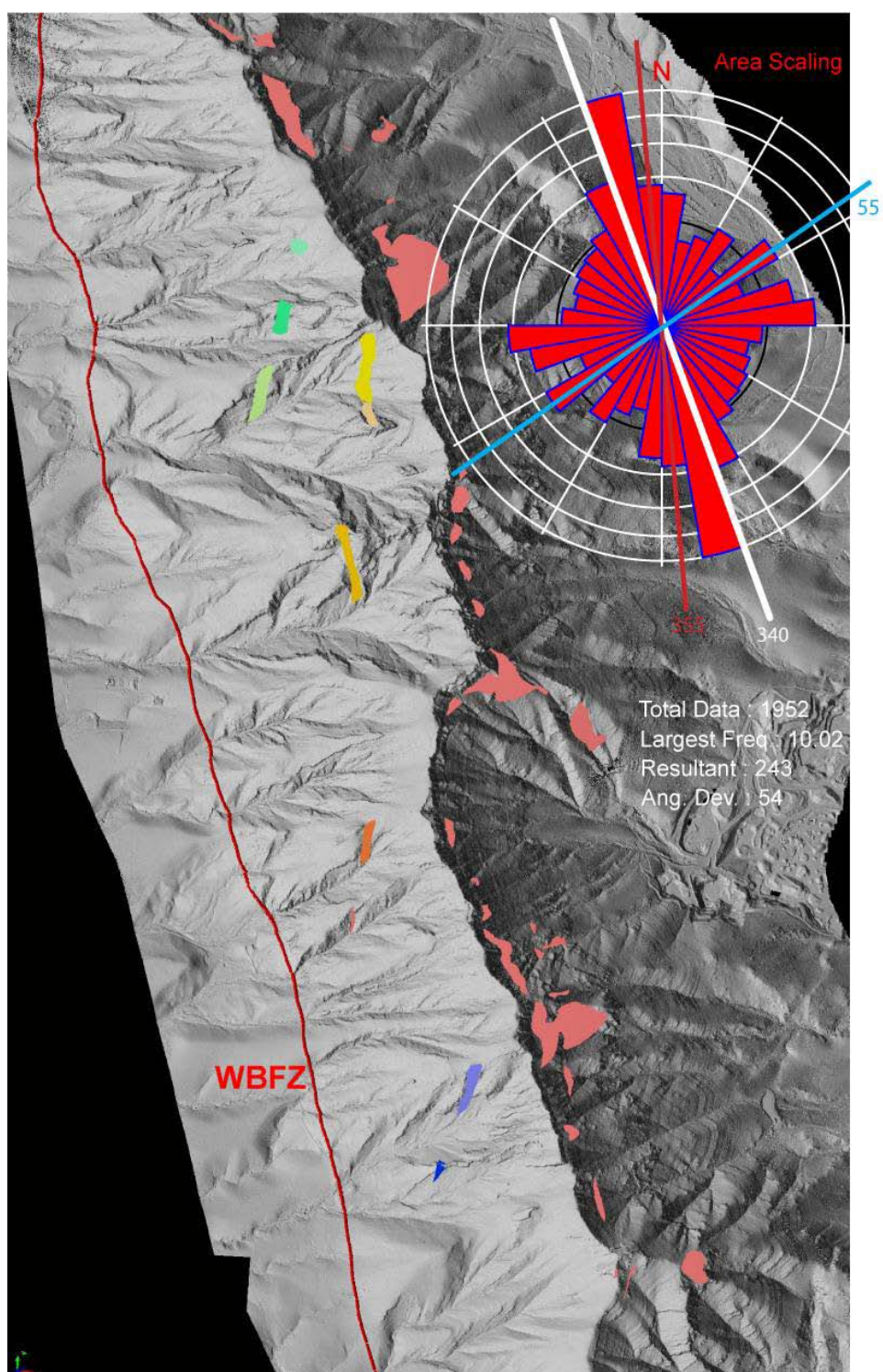


Figure 3.14: View of linear breccias along the western dip slope. Pink highlights are breccias mapped along the eastern footwall and the green, yellow, orange, and blue outlines are the linear breccias. Linear breccias align to the Riedel shear orientation (red line at 355° in rose diagram) which are oblique to the WBFZ labeled in red.

3.6 Discussion:

Lidar data were used to map fracture and fault orientations (displayed as planes) in the SFM that range in size from a >2 m of offset to over 2000 m. The primary orientations observed for these linear features match up with those of a right lateral compression regime and closely following the orientations predicted by a Riedel shear model (figure 3.8). The only post-Lower Ordovician periods documented in the El Paso region that produced thick-skinned NE-SW compression were the Carboniferous Antler Orogeny (Ancestral Rocky Mountains) and the Cretaceous-Tertiary Laramide Orogeny. In order to evaluate the four models presented for breccia origin (figure 3.6) within the SFM, each model's strengths and weaknesses will be discussed in the following section within the context of the observations and data presented in this paper.

3.6.1 Fault breccia/gauge model:

The complexity of fault damage zone analysis in carbonate strata is an area of recent interest (Tarasewicz et al. 2005; Woodcock et al. 2006; Ferrill and Morris 2008; Woodcock et al. 2008). A fault model such as the one proposed in figure 3.4 would not produce polymictic, nonfoliated, chaotic breccias like those observed in the SFM. Narrow (<4 m wide) monomictic breccias are present in the Franklin Mountains but do not contain the complex fill and stratal relationships observed in the larger collapse breccias and are typically less than a few meters in width. This model is therefore not likely to be a good choice for the formation of the extensive brecciation observed in the SFM.

3.6.2 Second-order supersequence meteoric karst model:

This is the currently accepted model for southern Franklin Mountain (SFM) breccia origin and relative timing of formation (Lucia 1995). On the basis of field mapping and cross-cutting

relationships and breccia composition, two types of breccias were identified. The first is a laterally restricted breccia cutting downward stratigraphically several hundred meters below a second order supersequence boundary erosional unconformity. The second breccia type is a laterally-extensive breccia restricted to the uppermost limestone unit, the Ranger Peak Formation just below the top Sauk second-order sea level fall that is overlain by the dolomitized Montoya Group strata. Both of these karst events are interpreted to have initiated during exposure of the Lower Ordovician strata before deposition of the Upper Ordovician strata. The Upham Formation (basal Montoya Group) does not change thickness over collapsed paleocave zones indicating it was deposited, lithified and likely even dolomitized before collapse into the El Paso Caverns (plate IV).

According to Lucia's (1995) model, the El Paso caverns formed at the end of the Lower Ordovician, top Sauk supersequence including both laterally restricted (deep phreatic) and laterally extensive (water table karst). This open cave system did not receive any additional Mid-Late Ordovician sediments during subsequent transgression and burial of the Sauk-Tippecanoe unconformity and cavern system by Late Ordovician Montoya Group. Voids of sufficient size remained open for later collapse (post Silurian) of Upper Ordovician and younger lithified strata several hundred meters below their stratigraphic equivalent levels into these voids. A vertically connected fracture zone oriented 340° controlled the position of the laterally restricted breccias to transmit fluids unsaturated with respect to calcium carbonate over 300 m into the subsurface or base level must have dropped several hundred meters on a passive margin of the North American craton.

The strengths of this model are that it offers an explanation for the cross-cutting relationships of strata and breccias in outcrop. As a Lower Paleozoic karst event it allows for ample time for various stages of dissolution and dolomitization to occur. The collapse of open caves would explain vertical displacement of clasts by collapse downward stratigraphically.

Laminated matrix was likely carried by fluids moving down from above (Lucia 1995) in open voids within the El Paso caverns before collapse of the system.

The weaknesses of this model are:

- The vertical extent of collapse breccias below the unconformity surface requires extremely large base-level fluctuation (~300 m). A vertically connected fracture network has been suggested account for this but it is difficult to explain on the tectonically-stable, passive, continental margin of Laurentia. What was the driver for hydrologic head to transport unsaturated waters vertically through 300 m of El Paso Group strata?
- It is difficult to explain the lack of Middle and Upper Ordovician sediment or fauna within the paleocave matrix if speleogenesis occurred during the Middle Ordovician exposure event. The exposure was followed by marine transgression and deposition of the Upper Ordovician Montoya Group yet the cave system appears to have remained completely shut off to marine sediment input.
- Laminated matrix material has been reported infilling pore spaces and small caves parallel to El Paso Group depositional bedding (Lucia 1995). The lamina orientations have been used as supporting evidence for top-Sauk paleocave origin yet no data have been presented as to the strike and dip of laminated sediment. Moreover, lamina have been stated to most likely have formed within the uppermost phreatic zone (Lucia 1971, 1995) yet evidence cited (Lucia 1995, his figures 17-19) is from the lower Lechuguilla Breccia near the base of the McKelligon Canyon Formation (plate IV). This would require the upper phreatic zone to be 300 m below the Sauk unconformity or >500 m below the top Fusselman unconformity to deposit these sediments. Field observations from this study and previously noted by Lucia (1995) concur that laminations are often

disrupted by clasts and have highly irregular and contorted laminations. The conclusion from these observations is that the orientations of lamina need to be better constrained or should not be used as support of the top-Sauk unconformity model.

- Large (20-30 cm) rounded clasts of saddle dolomite (plate IV) along with Montoya clasts were identified within the mid-McKelligon Canyon equivalent breccias (ngms2t and ngms2b, plate IV). Saddle dolomite ages from the SFM have been previously assigned as post-Devonian late stage vug-filling cements (Stepanek 1984) and must have been transported down through at least 600 m of the Ordovician, Silurian, and Devonian strata to reach this level of the cave system (figure 3.8). Devonian strata in the El Paso region are the Percha Shale which indicate a restricted, poorly oxygenated marine setting (Seager and Mack 2003).
- It has been shown (Loucks 1999) through evidence of oil exploration and production drill-bit drops that subsurface caves can remain open well below 600 m of burial. Why did the El Paso caverns collapse post-Devonian but have no post-Devonian matrix material? This is problematic but may suggest that collapse occurred after erosion of the over post-Devonian material or some reason for Devonian collapse needs to be identified. Other mechanisms such as falling base-level are more difficult to explain without substantial tectonic uplift.
- Upham Formation sediment has been reported as deposited around blocks of the Ranger Peak Formation near the mouth of Transition Canyon (Lucia 1971, pg 192). No Upham sediments have been found in this study within the Ranger Peak Formation. Thin veins of Cable Canyon sandstone however, have been identified filtering down into the uppermost Ranger Peak Formation.

3.6.3 3rd order composite cave model:

This model was proposed in chapter 1 of this work and calls upon dissolution of smaller caves occurring at 3rd order depositional sequence lowstand creating a vertical stack of caves. These caves build upward through the stratigraphic column gradually collapsing into the underlying cave until; a catastrophic failure occurred sometime after deposition of the Upper Ordovician deposition strata.

The strengths of this model are that it removes the requirement of massive sea level fluctuations by constructing a composite cave system at shorter term 3rd order lowstands that may or may not fully expose the platform. Laser-derived dimensions from simulated mechanical compaction of a modern cave (chapter 2) are capable of producing similar size breccias to those observed in the SFM. Estimates of atmospheric CO₂ values for the Late Ordovician (Berner 1997) could induce rapid dissolution of carbonates and related speleogenesis during 3rd order sea level fluctuations. Like the previous model, there is ample time is available post Silurian for several phases of documented fluid rock interactions (Stepanek 1984). Similar logic is used for this higher frequency model as the 2nd order supersequence model, except caves form along fracture patterns formed by lower caves inducing localized fractures under the weight of overburden gradually forming larger vertically stacked caves. Final breakthrough at some time after the Silurian connected the whole system allowing transport of Montoya and Fusselman clasts into the El Paso Group stratigraphic level. This removes the need for a preexisting vertically-extensive and connected fracture network to act as a conduit for fluids to travel deep into the subsurface.

Weaknesses of this model are:

- Breccias described in chapter 1 of this study indicate a uniform transition from larger roof-collapse slab-breccias into smaller collapse material and finally crackle breccias within the overburden. No strong field evidence has been identified to

suggest the vertical breccias within the SFM follow the multi-storey, coalesced-collapsed paleocave hypothesis of Loucks (1999). It is possible that each of the higher-order paleocaves were connected into one large vertical cave during top-Sauk exposure and later collapsed but evidence for this model would have been destroyed in the process.

- No significant karst surfaces have been found on top of the higher-order sequence boundaries that might be associated with extensive dissolution and karstification (Luicia 1995). Even though a connection to the surface is implied by both the 3rd order sequence composite cave model and the 2nd order meteoric model; both models require deposition of the Montoya Group above the open cave with little if any Montoya sediments being deposited within the cave fill. Thus, a lack of evidence for surface karst on the higher order surfaces seems to be a relatively minor problem if speleogenesis is taking place below the surface.
- Laminated cave sediment could be explained by this model as depth to the phreatic interface would be less extreme than in the previous model. This is in conflict with the internal breccia-fill pattern previously not indicating a coalesced collapsed paleocave system.
- One of the most common speleogenetic models is that caves grow downward as base level falls (Palmer 2007). The 3rd order composite cave model violates this model for meteoric speleogenesis. This model does have bias toward modern caves being the only extensive dataset available as submerged cave exploration is extremely dangerous. It seems logical that cyclicity must exist within speleogenesis at some interval governed by environmental conditions.

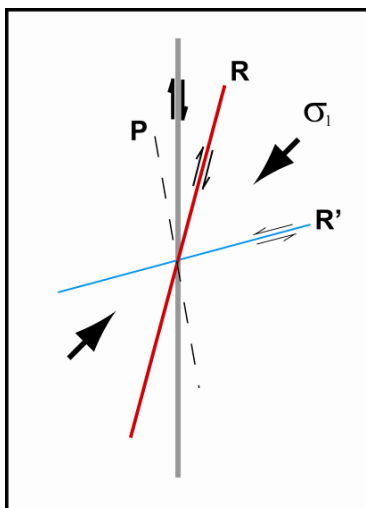
3.6.4 Solution-Enhanced Tectonic Fracture Model:

In the previous two syn-Paleozoic meteoric karst models, a fracture network is required to focus fluid through relatively low permeability limestones and dolostones. The question addressed in the solution-enhanced tectonic karst model presented here is a source for a stress regime that matches the observed linear breccia patterns within the SFM. In addition, this model provides the necessary hydraulic gradient for vertically extensive dissolution. The SFM experienced no less than four significant tectonic episodes between the deposition of the El Paso Group and the recent including the Antler/Arbuckle and Laramide orogenies, Basin and Range, and Rio Grande rifting. Drewes (1978) pointed out that complex structures, similar to those that acted upon in the SFM will often lead to conflicting interpretations (*cf.* Harbour 1972; Seager and Mack 1986; Karlstrom and Daniel 1993; Wu 2002; Ruiz 2004; Scharmann, 2006; Carciumaru and Ortega 2008).

There is general consensus on the principal stress orientations (NE-SW) during Laramide compression in the latest Cretaceous to early Tertiary (figure 3.4B). The Cretaceous strata disconformably overlie the Paleozoic strata (Richardson 1909; Harbour 1972) so there is no evidence for structural tilting in the Triassic and Jurassic and the general trend throughout the Paleozoic was that of a subsiding basin with ancestral highs to the east, west and north (Harbour 1972).

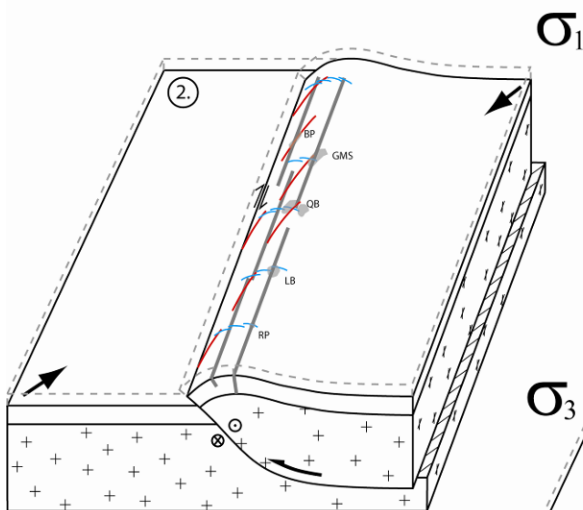
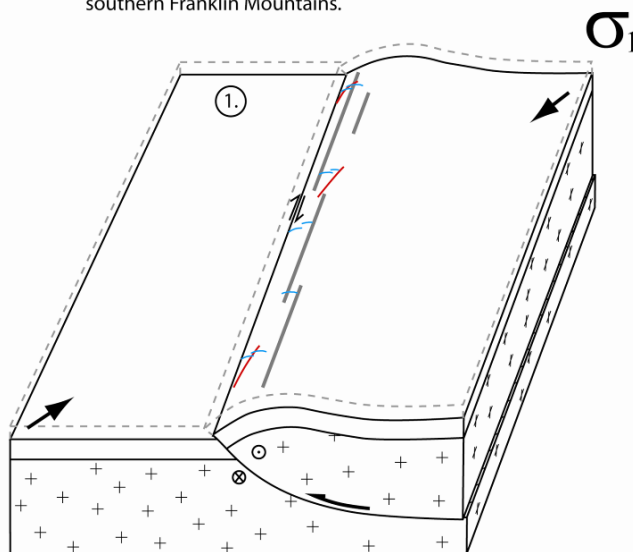
The strengths of this model are that a Laramide age for speleogenesis removes the need for extreme sea-level fluctuation in the Lower Paleozoic greenhouse conditions. Laramide timing also fits best with the very strong fault-parallel orientation of the breccia bodies and their tabular, lineament-constrained distribution. The SETK model offers a tectonic driver capable of producing uplift to initiate falling base level and/or mixing of fluids migrating up along permeable beds within the Paleozoic strata from the Chihuahua trough.

Figure 3.15 (opposite): This block diagram illustrates the early stages of deformation (1) within the SFM during onset of Laramide oblique right lateral compression followed by uplift and fracture development following Riedel shear predicted orientations (2), and finally Basin and Range/Rio Grande extension (3) exposing and uplifting the SFM to their current position. For clarity, only the largest breccias and one “breccia pipe” are included in this diagram; from south to north they are RP = Ranger Peak Breccia, LB = Lechuguilla Breccia, QB = Quarry Breccia, GMS = Great McKelligon Sag, and BP = “breccia pipe” (*sensu* Lucia 1995).



The Riedel Shear model (modified from Woodcock and Schubert 1994) is a predictive model for fracture orientation in an oblique compressional regime such as the El Paso region was under the influence of during the late Laramide Orogeny. Linear fault breccias have been identified on lidar data and field-verified that indicate similar fracture orientations predicted by this model.

1.) Early phase of Laramide compression in the El Paso region resulted in thick-skinned tectonic low-angle thrusting of the El Paso Group sediments and basement. The NE-SW compression developed Riedel shear fractures R (red) and R' (blue). These dilational fractures were solution enhanced to form the breccia pipes exposed on the dip slope of the southern Franklin Mountains.



2.) Breccias form along gentle upward block of El Paso Group and become solution-enhanced as regional fluid flow is focussed along these preferential pathways. With continued uplift voids eventually collapse.

3.) Basin and Range and Rio Grand extension in the El Paso region uplift the breccias and exposes them currently along the eastern face of the southern Franklin Mountains.

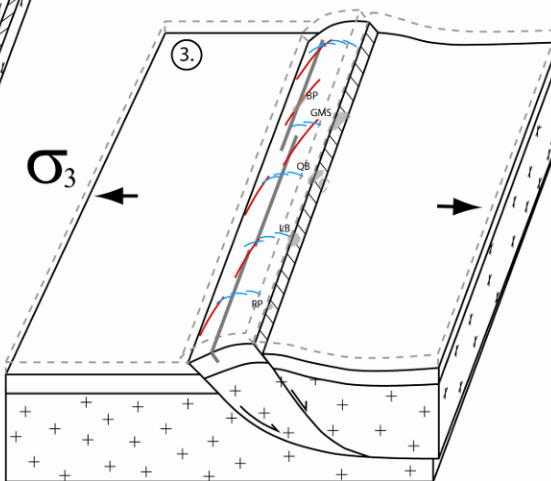


Figure 3.15: (caption on facing page)

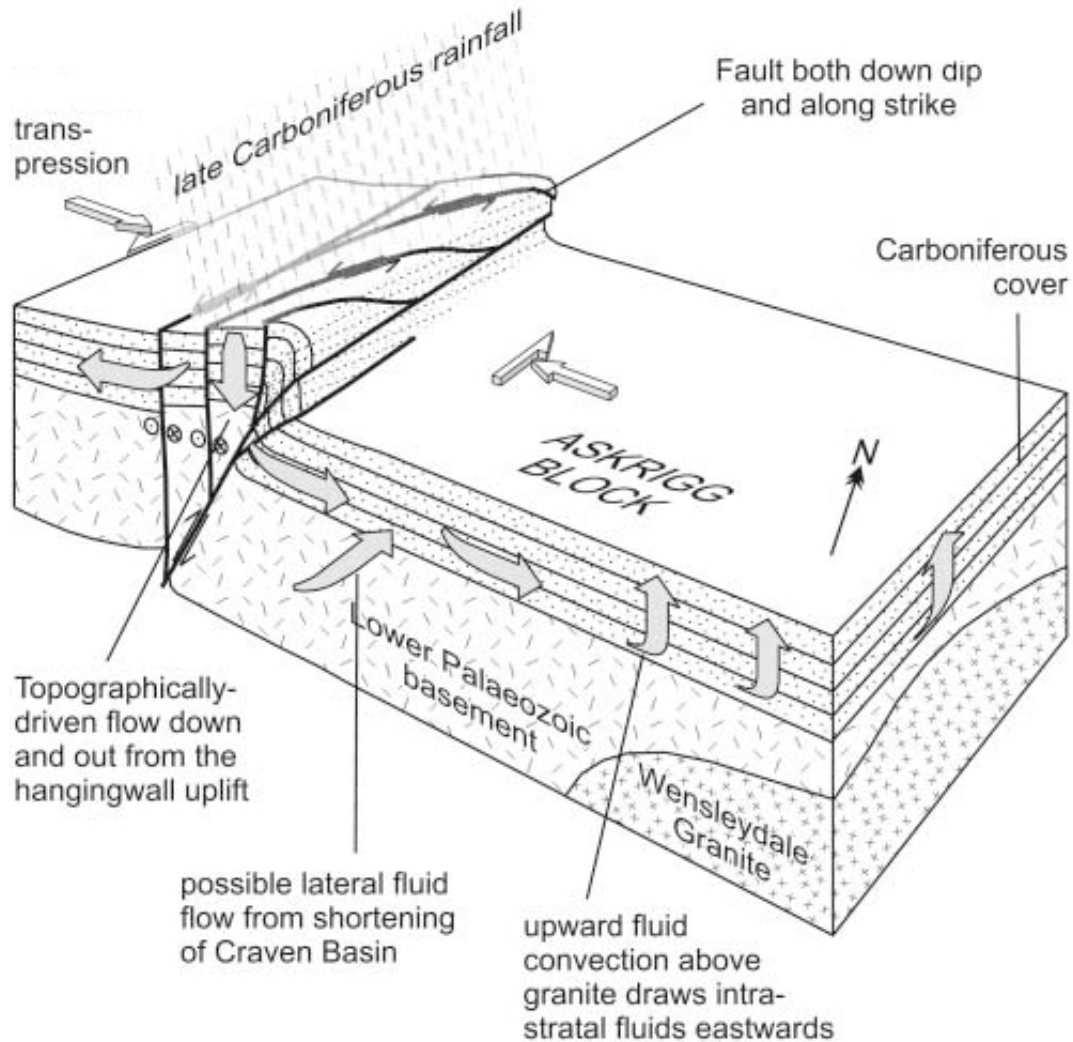


Figure 3.16: The Dent Fault model (after Woodcock et al. 2008) is a mirror image to the SFM solution-enhanced tectonic karst model. Fluid migration along fractures induced by the Dent fault left lateral compression (labeled as transpression above) in combination with basinal fluids offer a potential mixing-zone, deep dissolution that could continue as uplift progresses.

The weaknesses of the SETK model are:

- Less time is available for dolomitization of the breccia bodies.
- There are no Late Paleozoic clasts or sediment (post-Devonian) present within the breccias. This would require erosion of these sediments prior to collapse of the paleocave system.

- If the paleocaves formed during uplift, what mechanisms would drive collapse of the caverns? It is possible that Rio Grande rifting caused failure of roof strata within the paleocaves but evidence for this has yet to be identified.
- If laminated internal sediment were proven to be parallel to deposition bedding dip of the El Paso Group, this sediment would need to be deposited before the final stages of uplift (Rio Grande rift) responsible for the current SFM morphology, dipping 30° to the west.
- In addition, assuming a Laramide origin for the initiation of the caves within the El Paso region, what mechanism would be called upon to induce collapse?

3.6.5 Analogous solution-enhanced tectonic karst model:

A similar model to the solution-enhanced tectonic model proposed in this study was documented that produced chaotic breccias adjacent to the left-lateral, oblique, compressional Dent fault in NW England (Tarasewicz et al. 2005; Woodcock 2008). The Dent fault is a mirror image of the SFM structures within Lower Paleozoic mixed siliciclastics and carbonates with thick-skinned, basement involved oblique compression produced warping of the Paleozoic strata. This tectonic uplift created a vertical fracture network capable of transmitting meteoric fluids 2-2.5 km into the subsurface that likely enhanced fracture apertures. Riedel fractures and strike-parallel fractures formed during compression and initiated a vertical fracture network required for vertical fluid migration >2 km into the subsurface. Woodcock et al. (2008) indicate that meteoric water migrating laterally toward the system may focus along vertical fractures in a system like the SFM. In addition, Woodcock et al. (2008) also noted that the uplifted terrain would provide a hydraulic head for downward migration of fluids along the fracture system assuming sufficient precipitation available to sustain groundwater levels sufficient to approximate topography (figure 3.15). Fluids migrating from the >6 km-deep Chihuahua trough migrated laterally or slightly up-gradient early in the Laramide oblique right lateral compression and followed along 340° oriented faults (figure

3.15). Large paleocaves formed in the subsurface would be prone to collapse with falling base level during continued uplift. The buoyant effect of water on the cave ceiling has been previously estimated to contribute as much as 40% of the cave-roof support (Loucks 1999, 2004); emptying of the cave passage could induce collapse. This is only made more volatile with a fractured ceiling beam (White and White 1963; Loucks 1999) reducing the stability of a chamber.

Breccias reported along the Dent fault (Tarasewicz et al. 2005; Woodcock et al. 2006; Woodcock et al. 2008; Mort and Woodcock 2008) have been classified as chaotic collapse breccias and range in size from +/-10 m from the fault core within the hanging wall to +/- 50 m from the fault core in the foot wall. These values are constant with the width measurements extracted from lidar data of the SFM (table 3.2 and 3.3).

Montoya clasts observed within El Paso Group stratigraphic equivalent breccias retain the same dolomite crystal size and weathering appearance as *in situ* strata. Breccia clasts of the Montoya have been reported to retain heavier $\delta^{18}\text{O}$ values than the matrix material (Stepanek 1984). In addition, Stepanek (1984) also reported the Montoya, Ranger Peak, Cindy, Chamizal and Devonian Conutillo Formation as retaining heavier $\delta^{18}\text{O}$. This indicates that the Montoya was likely dolomitized before collapse. Additionally saddle dolomite clasts are within breccias in the McKelligon Canyon Formation. Saddle dolomite from the SFM is zoned and has inner $\delta^{18}\text{O}$ values of -8.5 and outer zones of -14.5 PDB (Stepanek 1984). Work in the subsurface has placed saddle dolomites with similar $\delta^{18}\text{O}$ values occurring between Devonian and Permian (Kupecz and Land 1991). Cave formation during the Devonian is unlikely as the Conutillo Formation is dominantly a subtidal wackestone and the El Paso Group would be even more deeply buried below base level enhancing the problems associated with deep-fluid migration in cave formation.

3.7 Conclusions:

The breccias of the southern Franklin Mountains offer a world class example of collapsed paleocave breccias but the timing of brecciation and associated precursor caves remains in question. On the basis of data presented, the type section of top-Sauk meteoric paleokarst may be related to a 340° Laramide oblique right-lateral compression and associated Riedel (R) and to a lesser degree Conjugate Riedel (R') shear orientation identified on both lidar and ground-control data. This model suggests that the vertical breccias of the El Paso Group paleocave system may be over 300 million years younger than previously thought. Additional research on solution-enhanced tectonic karst is needed to verify this model but this study highlights several observations that warrant further inspection. Some of these observations are:

- Orientation of breccia bodies with respect to regional tectonics
- Hydrology required to induce dissolution and cave formation
- Age of breccia matrix material
- Organization and lithology of breccia clasts

The combination of field mapping and high-resolution airborne lidar data interpretation made it possible to expand upon the previous work in this region and emphasized the importance spatially accurate and precise data in addressing geologically complex questions. This study combined various aspects of structure, diagenesis, and sequence stratigraphy to evaluate a paleokarst system. Numerous further studies should follow from ground work presented here. Suggested additional studies include paleomagnetic analysis of the host rock and breccia matrix material, detailed stable and radiogenic isotopic analysis, careful fluid inclusion analysis, and a full kinematic study of the Laramide to recent. The study of paleokarst is extremely complicated as the evidence of what formed the original cave has been removed and overprinted by subsequent geological events.

APPENDIX A:

Franklin Mountain LIDAR Project Metadata:

Description:

The University of Texas contracted Digital World Mapping to provide a lidar survey of the Franklin Mountain range located in El Paso, Texas. DWM's proprietary lidar system acquired data over 42km² between Sept 8th and 11th, 2006. In addition, a control network was established and a kinematic survey was completed in order to ensure data integrity.

Bounding Coordinates:

West_Bounding_Coordinate: -106.51227565
East_Bounding_Coordinate: -106.45188444
North_Bounding_Coordinate: 31.87400342
South_Bounding_Coordinate: 31.77541499

Spatial Reference Information:

Grid Coordinate System Name: Universal Transverse Mercator, Zone 13
Horizontal Datum Name: NAD83
Vertical Datum Name: NAVD88
Undulation model used to covert to MSL: Geoid03

Acquisition Parameters:

Flight Altitude: 225m
Laser Scanning Frequency: Fore laser 50hz, Aft laser 27hz
Laser Firing Rate: 10Khz

System Calibration

The calibration of Digital World's lidar system is performed at the onset and completion of each project. The system calibration consists of two components. First is to measure the lever arms between the three main sensors, the laser, GPS antennae and the IMU. Second, is the measurement of the small angle differences in the way the IMU and the laser are mounted in relation to each other. The roll, pitch and heading are measured to 0.05° accuracy or better. The calibration flight was performed on Sept 8th, 2006.

Data Quality Information:

The elevations of the kinematic ground points were compared to the elevations from the ground thin data set. The accuracies found are as follows:

	(meters)
Average dz	0.009
Root mean square	0.065 (Hard Surface)
Std deviation	0.064

GPS Control Network:

```
*****
* NETWORK - WEIGHTED GPS NETWORK ADJUSTMENT      *
*                                                  *
* (c) Copyright Waypoint Consulting Inc., (2000) *
*                                                  *
* VERSION: 6.03                                  *
*                                                  *
* FILE: E:\LiDAR_Projects\Texas_Franklin Mountains\Static\Franklin.net
*****
```

DATE(m/d/y): Sun. 9/10/06 TIME: 21:08:49

DATUM: 'WGS84'
GRID: Grid: UTM, Zone 13
SCALE_FACTOR: 1.0000
CONFIDENCE LEVEL: 95.00 % (Scale factor is 2.4479)

INPUT CONTROL/CHECK POINTS

STA_ID	TYPE	--	LATITUDE	--	LONGITUDE	--	ELLHGT	--	HZ-SD	V-SD
TXEL	GCP-3D	31	41 29.43839	-106	16 17.60392	1123.159	0.00500	0.00500		
wsmn	CHK-3D	32	24 25.67427	-106	20 59.35088	1205.182				

INPUT VECTORS

SESSION NAME	VECTOR(m)	-----	Covariance (m) [unscaled]	-----
	DX/DY/DZ		standard deviations in brackets	
HORI to VFW1 (1)	-19641.5270	6.0396e-008	(0.0002)	
	12003.9600	5.5909e-008	2.6906e-007	(0.0005)
	9857.0320	-1.1451e-008	-7.1238e-008	5.7558e-008 (0.0002)
HORI to wsmn (1)	1159.6746	2.1080e-004	(0.0145)	
	41806.4390	5.9605e-005	7.3232e-005	(0.0086)
	64593.3980	-2.2991e-005	-1.6853e-005	2.1338e-005 (0.0046)
TXEL to HORI (1)	3553.9510	6.8688e-008	(0.0003)	
	624.2580	5.3839e-008	2.6760e-007	(0.0005)
	2721.4340	-1.8139e-008	-1.1432e-007	1.6671e-007 (0.0004)
TXEL to RED2 (1)	3558.5480	4.0760e-007	(0.0006)	
	622.8160	2.7206e-007	7.3692e-007	(0.0009)
	2721.2510	-2.1359e-007	-4.4242e-007	5.2482e-007 (0.0007)
TXEL to VFW1 (1)	-16087.5530	2.4985e-007	(0.0005)	
	12628.2880	2.2771e-007	9.8686e-007	(0.0010)
	12578.3940	-7.7190e-008	-4.5262e-007	5.3076e-007 (0.0007)

```

TXEL to wsmn (1)      4713.6316  3.1659e-004 (0.0178)
                     42430.7471  3.7613e-005 7.0128e-005 (0.0084)
                     67314.8040 -2.0112e-005 -2.5381e-005 4.1026e-005 (0.0064)

VFW1 to wsmn (1)      20801.1940  1.1050e-004 (0.0105)
                     29802.4860  2.4373e-005 4.1239e-005 (0.0064)
                     54736.3935 -1.1153e-005 -1.1964e-005 1.5019e-005 (0.0039)

```

```

*****
      OUTPUT VECTOR RESIDUALS (East, North, Height - Local Level)
*****

```

SESSION NAME	-- RE -- (m)	-- RN -- (m)	-- RH -- (m)	- PPM -	DIST - (km)	STD - (m)
HORI to VFW1 (1)	0.0006	0.0000	-0.0107 \$	0.427	25.0	0.0006
HORI to wsmn (1)	-0.0038	0.0162	-0.0101	0.253	77.0	0.0175
TXEL to HORI (1)	0.0004	-0.0066	-0.0194 \$	4.523	4.5	0.0007
TXEL to RED2 (1)	0.0000	0.0000	0.0000	0.000	4.5	0.0013
TXEL to VFW1 (1)	-0.0013	0.0159	0.0705 \$	3.010	24.0	0.0013
TXEL to wsmn (1)	0.0049	0.0071	0.0276	0.362	79.7	0.0207
VFW1 to wsmn (1)	0.0048	-0.0096	-0.0101	0.223	65.7	0.0129

RMS	0.0030	0.0100	0.0303			

\$ - This session is flagged as a 3-sigma outlier

```

*****
      CHECK POINT RESIDUALS (East, North, Height - Local Level)
*****

```

STA. NAME	-- RE -- (m)	-- RN -- (m)	-- RH -- (m)
wsmn	-0.0061	0.0061	-0.0002

RMS	0.0061	0.0061	0.0002

```

*****
      CONTROL POINT RESIDUALS (ADJUSTMENT MADE)
*****

```

STA. NAME	-- RE -- (m)	-- RN -- (m)	-- RH -- (m)
TXEL	0.0000	0.0000	0.0000

RMS	0.0000	0.0000	0.0000

```

*****
      OUTPUT STATION COORDINATES (LAT/LONG/HT)
*****

```

STA_ID	-- LATITUDE --	-- LONGITUDE --	- ELLHGT -	ORTHOHGT
HORI	31 43 11.78995	-106 14 14.68793	1197.2380	1221.2961
RED2	31 43 11.78342	-106 14 14.50503	1197.2455	1221.3034
TXEL	31 41 29.43839	-106 16 17.60392	1123.1591	1147.3184
VFW1	31 49 26.14316	-106 28 19.23944	1297.0387	1320.9698
wsmn	32 24 25.67447	-106 20 59.35111	1205.1819	1228.8907

 OUTPUT STATION COORDINATES (GRID)

STA_ID	- EASTING - (m)	- NORTHING - (m)	- ELLHGT - (m)	ORTHOHGT (m)
HORI	382761.7224	3510059.7063	1197.2380	1221.2961
RED2	382766.5342	3510059.4506	1197.2455	1221.3034
TXEL	379489.8242	3506945.3893	1123.1591	1147.3184
VFW1	360688.7987	3521863.5625	1297.0387	1320.9698
wsmn	373063.8738	3586366.0672	1205.1819	1228.8907

 OUTPUT VARIANCE/COVARIANCE

STA_ID	SE/SN/SUP (95.00 %)	----- CX matrix (m)----- (not scaled by confidence level) (m) (ECEF, XYZ cartesian)			
HORI	0.0123	2.5056e-005			
	0.0123	4.5313e-008	2.5220e-005		
	0.0123	-1.4908e-008	-9.3474e-008	2.5129e-005	
RED2	0.0123	2.5408e-005			
	0.0123	2.7206e-007	2.5737e-005		
	0.0125	-2.1359e-007	-4.4242e-007	2.5525e-005	
TXEL	0.0122	2.5000e-005			
	0.0122	-1.2162e-019	2.5000e-005		
	0.0122	7.4156e-020	-8.5045e-020	2.5000e-005	
VFW1	0.0123	2.5085e-005			
	0.0123	7.3643e-008	2.5343e-005		
	0.0123	-2.1460e-008	-1.3146e-007	2.5157e-005	
wsmn	0.0210	8.3260e-005			
	0.0139	1.2430e-005	4.4053e-005		
	0.0180	-5.6901e-006	-5.3944e-006	3.2289e-005	

 VARIANCE FACTOR = 408.7505

Note: Values < 1.0 indicate statistics are pessimistic, while
 values > 1.0 indicate optimistic statistics. Entering this
 value as the network adjustment scale factor will bring
 variance factor to one.

Appendix B

DOM results for 3 interpolations and 9 simulations:

Southern Franklin Mountains Simulation Model Parameters										
Run name:	Type	Type	Method	Type	NonBre %	Brec %	Var. R1	Var. R2	Var. Vert.	Trend °
<i>Interp_01</i>	Interpolation	Continuous	SKriging	Spherical	98.00%	2.00%	258	258	100	0
<i>Interp_02</i>	Interpolation	Continuous	SKriging	Spherical	98.00%	2.00%	258	387	100	0
<i>Interp_03</i>	Interpolation	Continuous	SKriging	Spherical	98.00%	2.00%	387	258	100	0
<i>SIS_01</i>	Simulation	Categorical	SIS	Spherical	98.00%	2.00%	258	258	100	0
<i>SIS_02</i>	Simulation	Categorical	SIS	Spherical	98.00%	2.00%	258	172	100	0
<i>SIS_03</i>	Simulation	Categorical	SIS	Spherical	98.00%	2.00%	387	258	100	0
<i>SIS_04</i>	Simulation	Categorical	SIS	Gaussian	98.00%	2.00%	258	258	100	0
<i>SIS_05</i>	Simulation	Categorical	SIS	Spherical	98.00%	2.00%	258	172	100	0
<i>SIS_05_G</i>	Simulation	Categorical	SIS	Gaussian	98.00%	2.00%	258	172	100	0
<i>SIS_06</i>	Simulation	Categorical	SIS	Spherical	98.00%	2.00%	387	258	100	0
<i>SIS_07</i>	Simulation	Categorical	SIS	Spherical	98.00%	2.00%	387	172	100	0
<i>SIS_08</i>	Simulation	Categorical	SIS	Gaussian	98.00%	2.00%	387	172	100	0

Twelve simulations were run with different variogram ranges as defined by spatial statistics extracted directly from the interpreted lidar data. Dimensional information extracted from a modern cave setting was used to define the asymmetric (elliptical) ranges for breccia distribution simulation of a meteoric paleokarst system. This table is a duplicate of table 2.4. The SFM field area covers the east (left) side of each image.

Each modeling run is a 3D solution to the input parameters in the table above. Each simulation conforms to some degree to the underlying seismic image. The most similar by visual comparison is SIS_01 which uses an asymmetric variogram range in r1 = north-south and r2 = east-west. The second choice is SIS_07 which created larger individual cave bodies but fewer of them. This simulation used the rmin and rmax value based on the Devil's Sinkhole ellipticity factor applied to the SFM variogram range calculated from the lidar initial condition data. These models are very simplistic but are intended more for the illustration of the technique than providing a comprehensive spatial analysis.

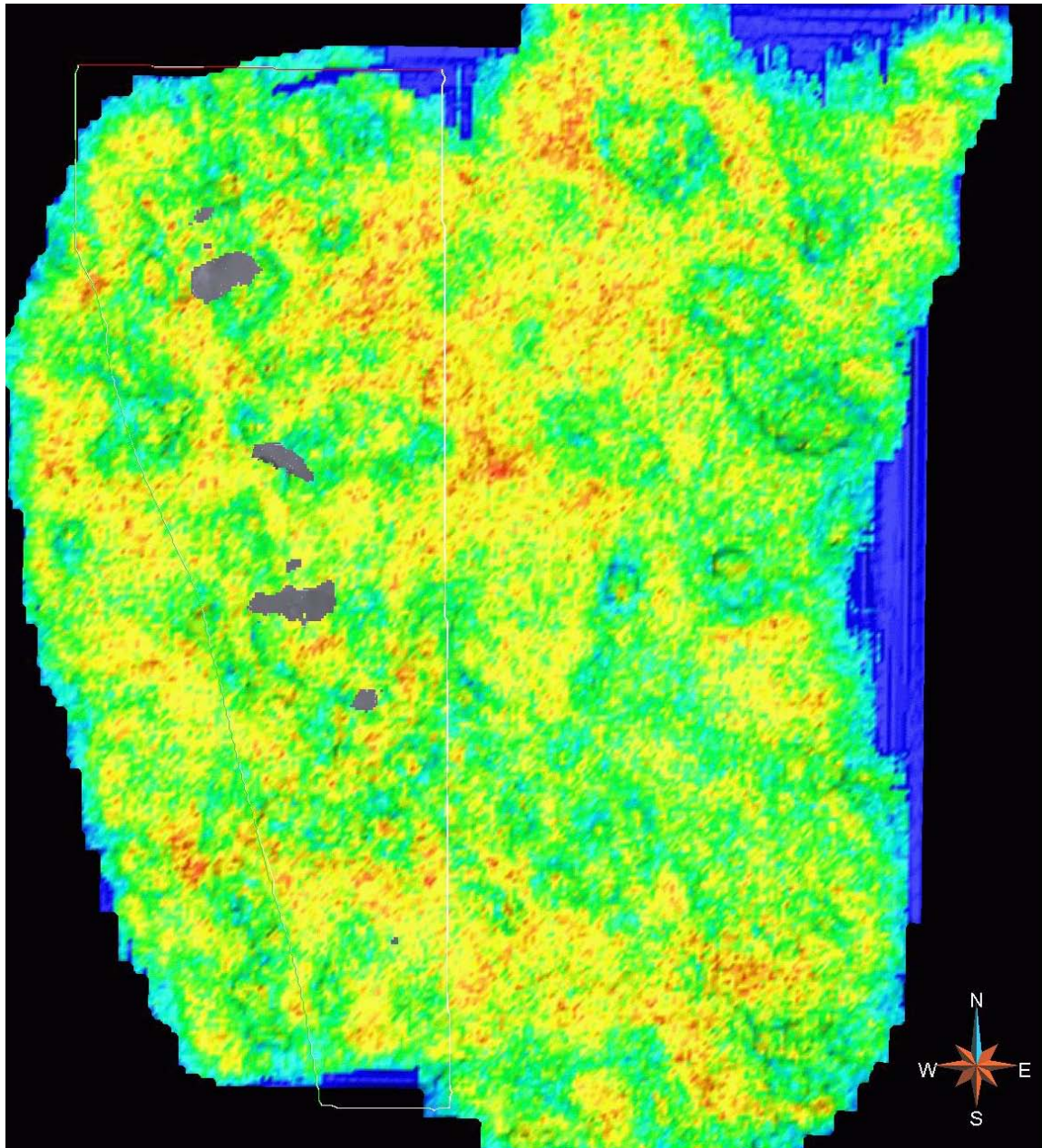


Figure B.1: Interp_01 interpolation parameters: Gray bodies are the interpolated paleocave dimensions from a symmetrical variogram range ($r_1=r_2=258$ m). The range value of 258 m was calculated from the distribution initial condition data "painted" into the Gocad sgrid. These values were initialized from the average of the point attributes that fell within the nearest sgrid cell. The shape of the breccia bodies interpolated is very similar to the input shape extracted from the lidar. The interpolation method does not allow for breccia population without connection to initial condition breccia values. Basemap image is absolute average amplitude attribute draped over the top Ellenburger time-structure map from the Boonsville field in the northern Fort Worth Basin.

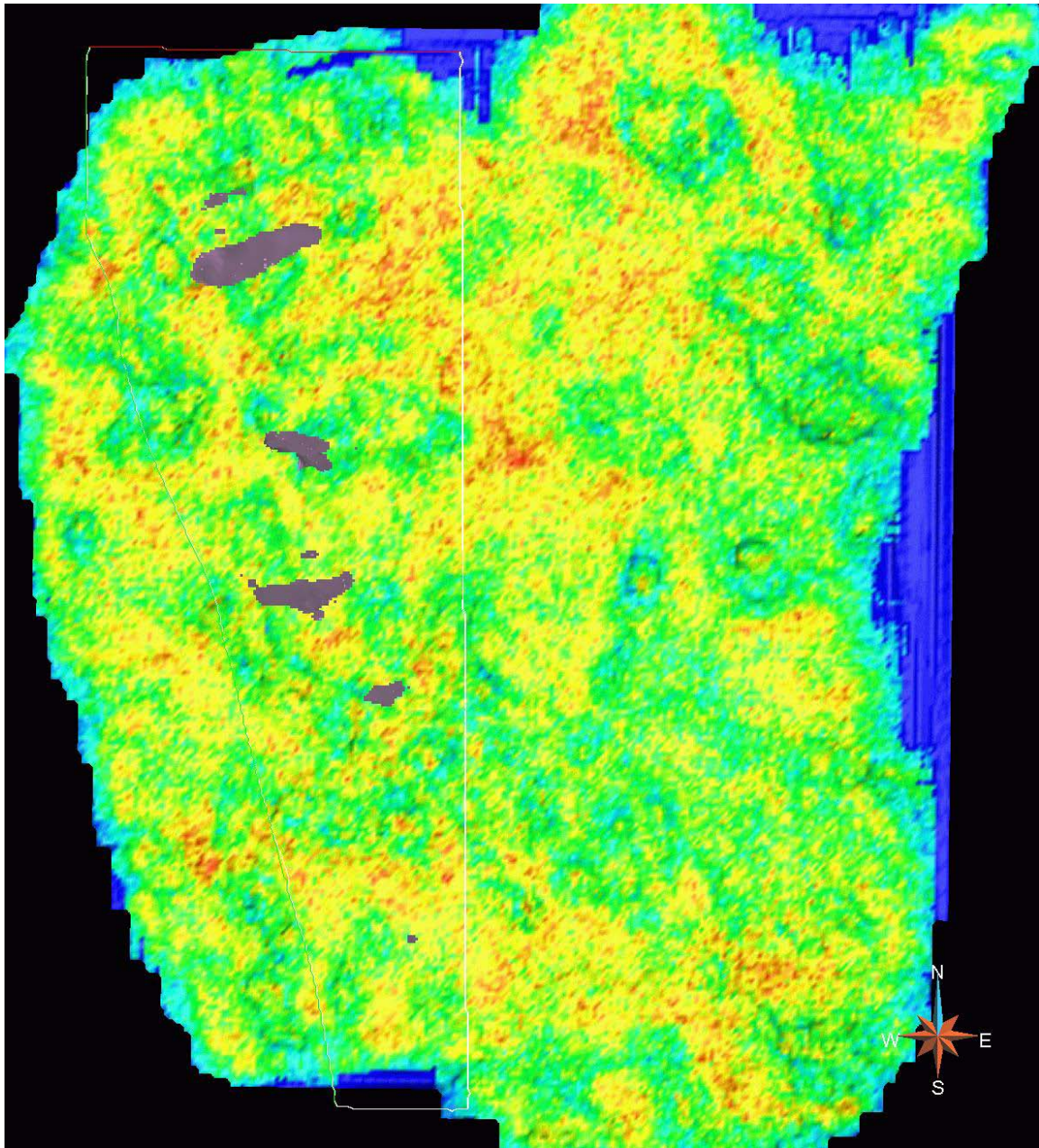


Figure B.2: Interp_02 interpolation parameters: Brown bodies are the interpolated paleocave dimensions from an asymmetrical variogram range ($r_1 = 258$ m and $r_2 = 387$). The range value of 258 m was calculated from the distribution initial condition data "painted" into the Gocad sgrid. The r_2 range of 387 is 1.5 times r_1 (based on ellipticity from Devil's Sinkhole; table 2.2). These values were initialized from the average of the point attributes that fell within the nearest sgrid cell. The shape of the breccia bodies interpolated is very similar to the input shape extracted from the lidar. The interpolation method does not allow for breccia population without connection to initial condition breccia values.

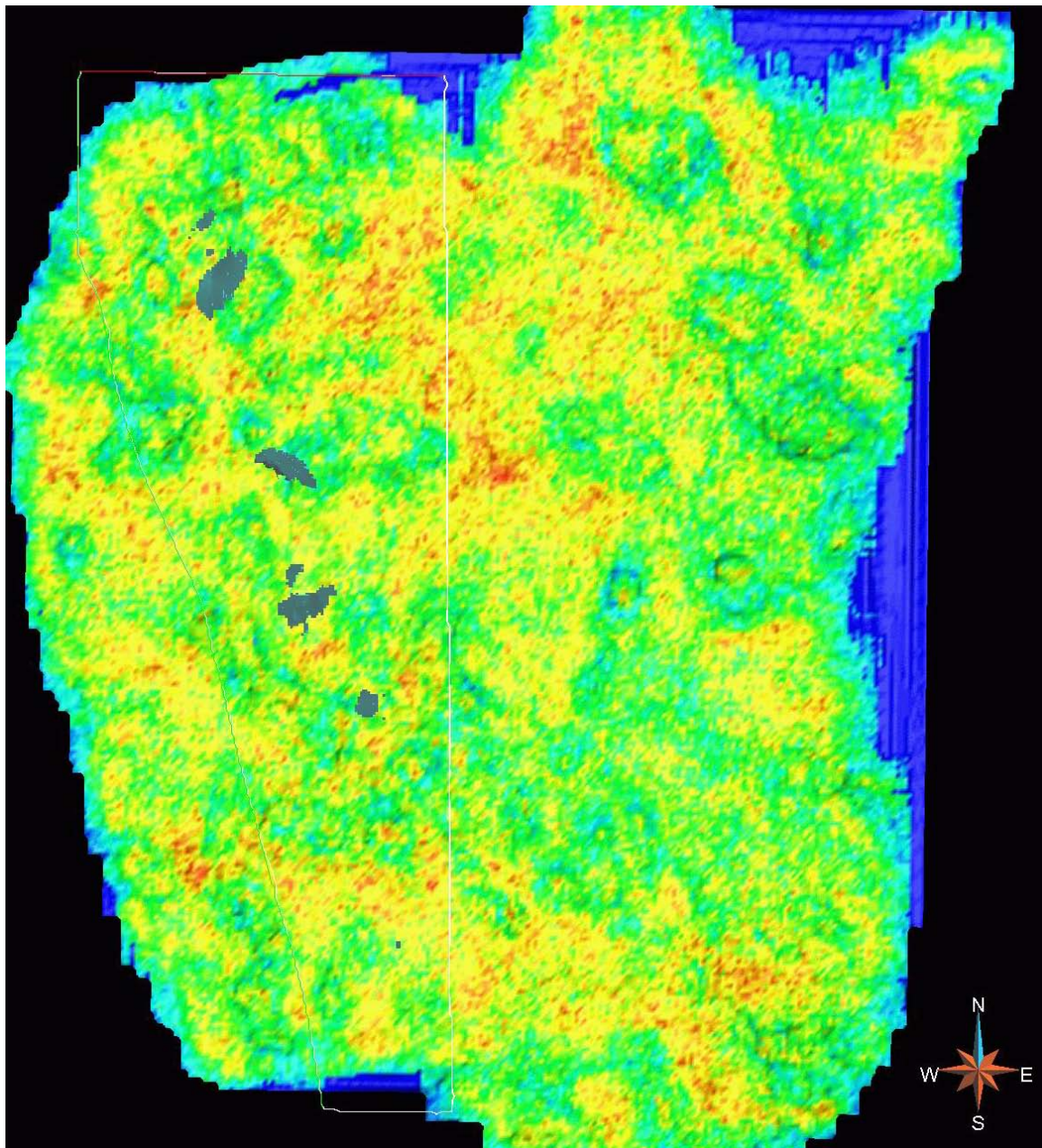


Figure B.3: Interp_03 interpolation parameters: Blue-green bodies are the interpolated paleocave dimensions from an asymmetrical variogram range ($r_1 = 357$ m and $r_2 = 258$). The range value of 258 m was calculated from the distribution initial condition data "painted" into the Gocad sgrid. The r_2 range of 387 is 1.5 times r_1 (based on ellipticity from Devil's Sinkhole; table 2.2). These values were initialized from the average of the point attributes that fell within the nearest sgrid cell. The shape of the breccia bodies interpolated is very similar to the input shape extracted from the lidar. The interpolation method does not allow for breccia population without connection to initial condition breccia values.

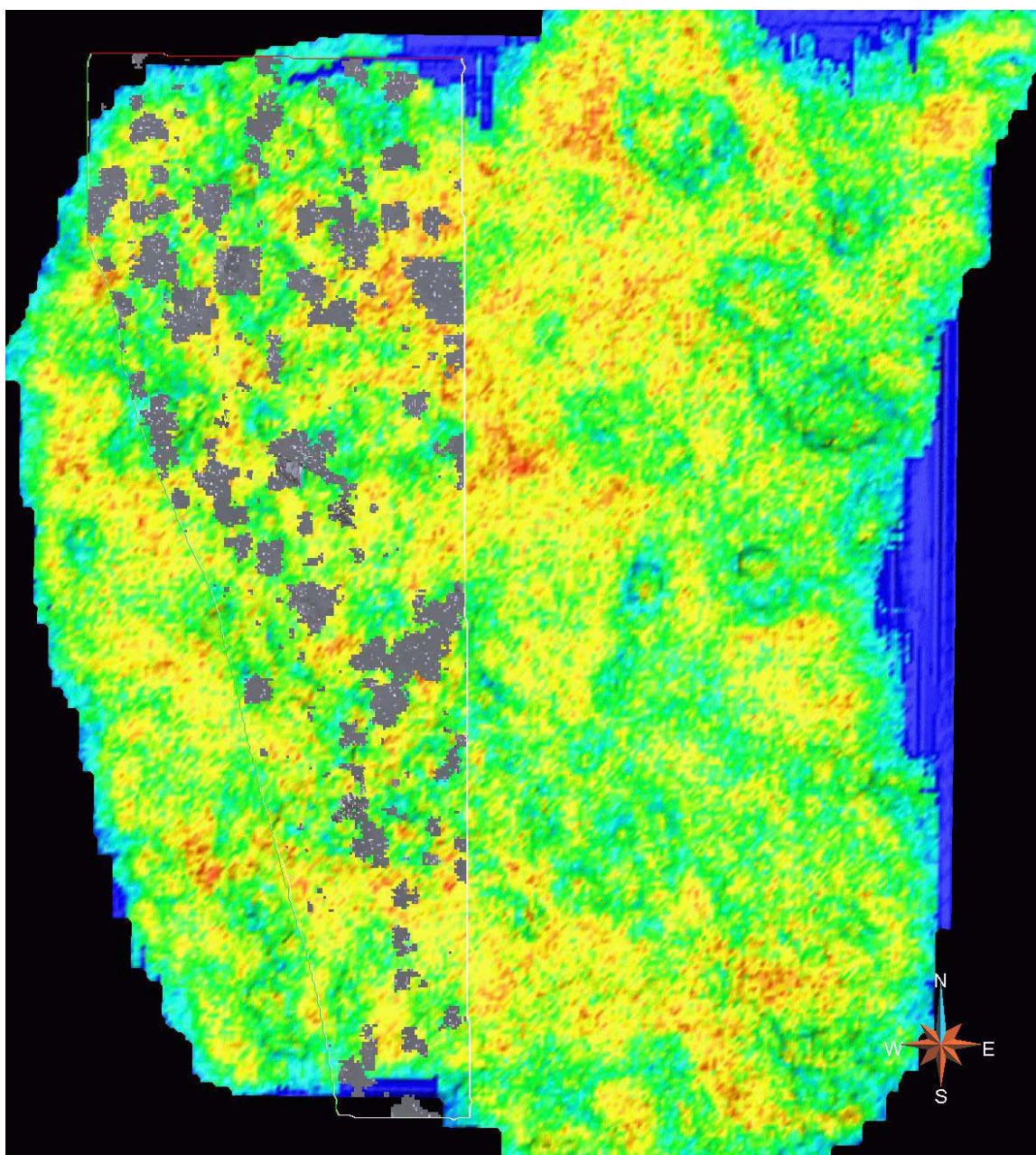


Figure B.4: SIS_01 simulation parameters: Gray bodies are the simulated paleocave dimensions from a symmetrical variogram range ($r_1 =$ and $r_2 = 258$). The range value of 258 m was calculated from the distribution initial condition data "painted" into the Gocad sgrid. These values were initialized from the average of the point attributes that fell within the nearest sgrid cell. The shape of the breccia bodies interpolated is very similar to the input shape extracted from the lidar. The interpolation method does not allow for breccia population without connection to initial condition breccia values.

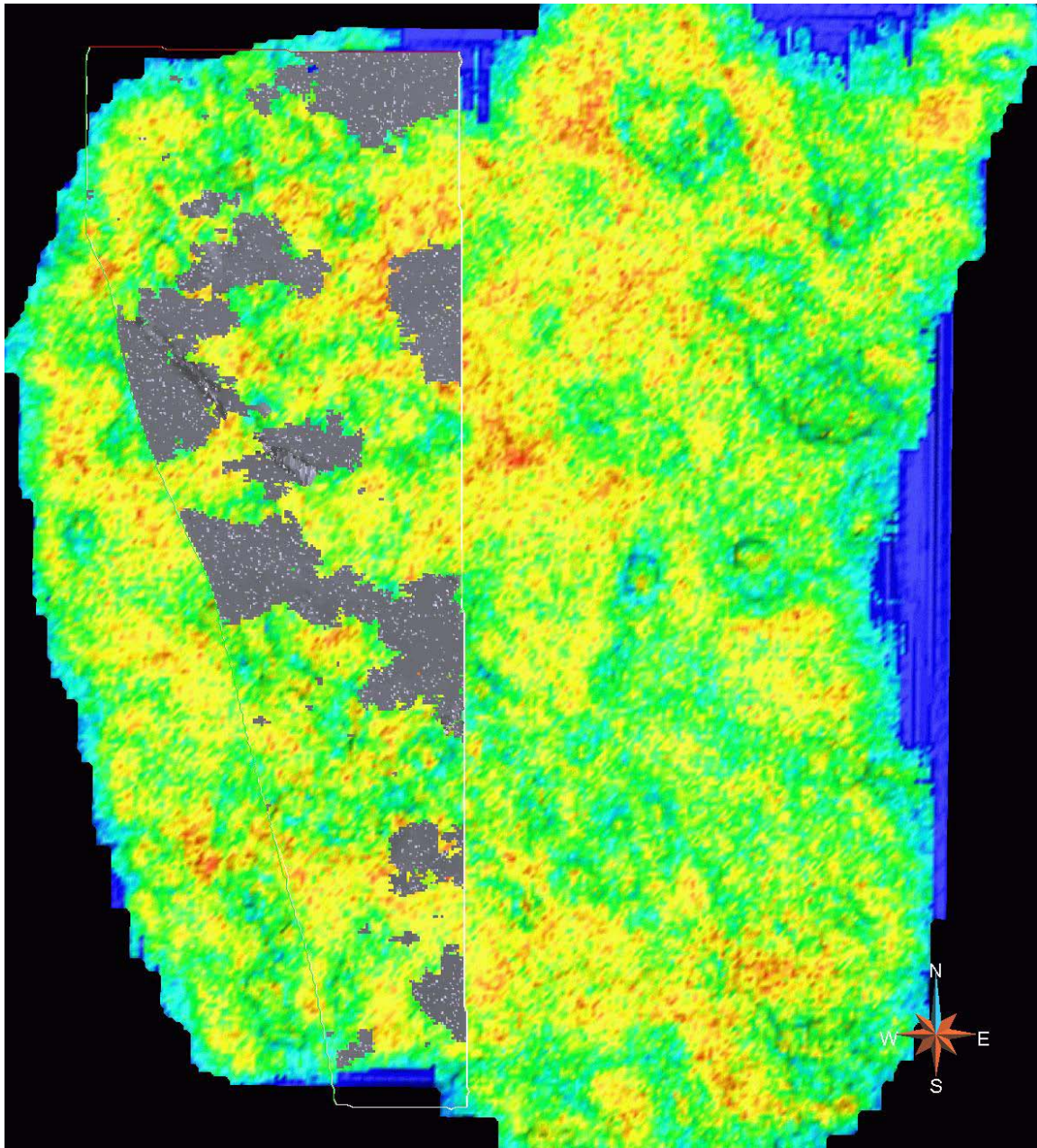


Figure B.5: SIS_02 simulation parameters: Gray bodies are the simulated paleocave dimensions from an asymmetrical variogram range ($r_1 = 357$ m and $r_2 = 172$). The range value of 258 m was calculated from the distribution initial condition data "painted" into the Gocad sgrid. The r_1 range of 387 is 1.5 times r_1 (based on ellipticity from Devil's Sinkhole; table 2.2). R_2 is $258/1.5$. These values were initialized from the average of the point attributes that fell within the nearest sgrid cell. The shape of the breccia bodies interpolated is very similar to the input shape extracted from the lidar. The interpolation method does not allow for breccia population without connection to initial condition breccia values.

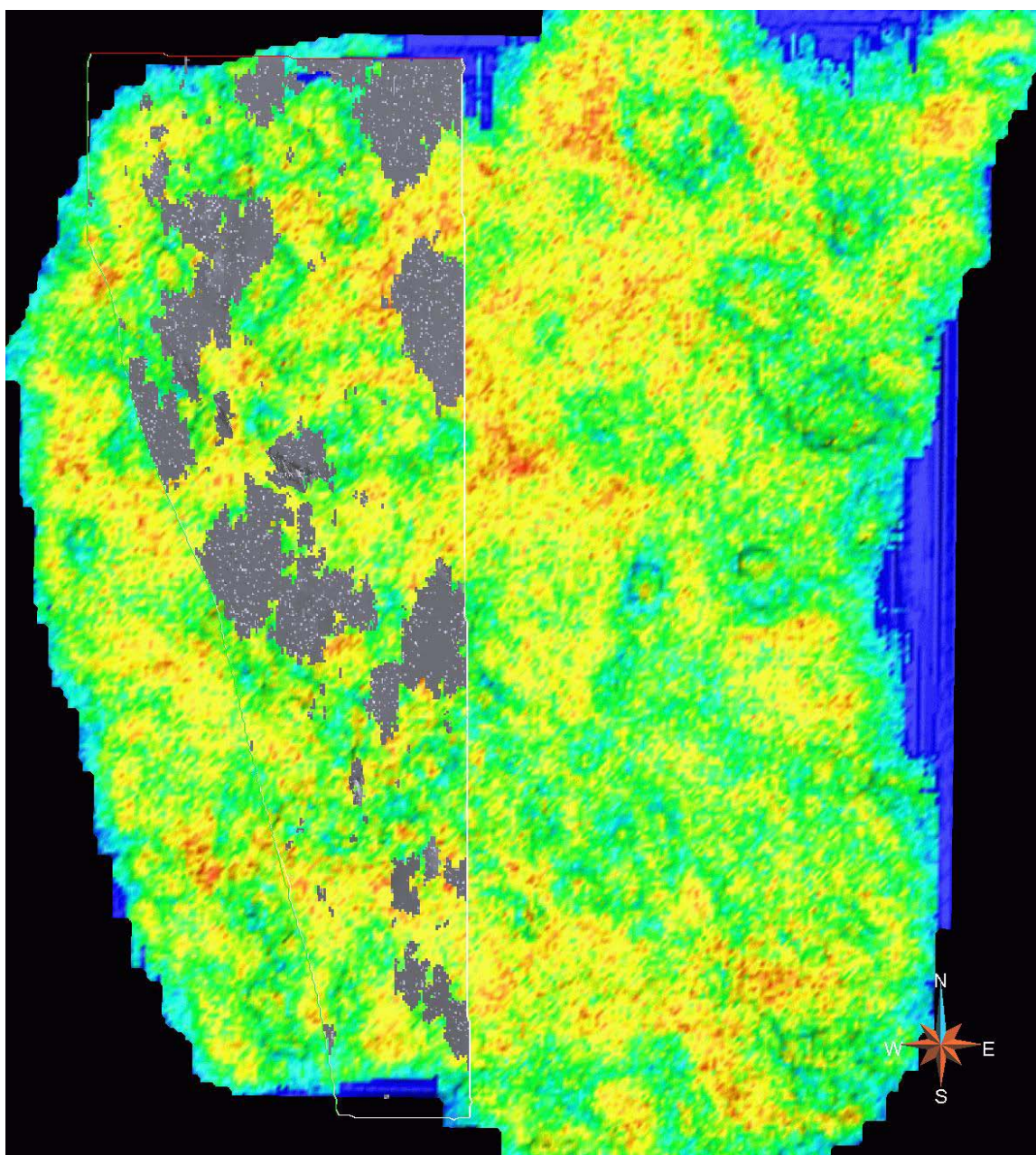


Figure B.6: SIS_03 simulation parameters: Gray bodies are the simulated paleocave dimensions from an asymmetrical variogram range ($r_1 = 357$ m and $r_2 = 258$). The range value of 258 m was calculated from the distribution initial condition data "painted" into the Gocad sgrid. The r_1 range of 387 is 1.5 times r_1 (based on ellipticity from Devil's Sinkhole; table 2.2). These values were initialized from the average of the point attributes that fell within the nearest sgrid cell. The shape of the breccia bodies interpolated is very similar to the input shape extracted from the lidar. The interpolation method does not allow for breccia population without connection to initial condition breccia values.

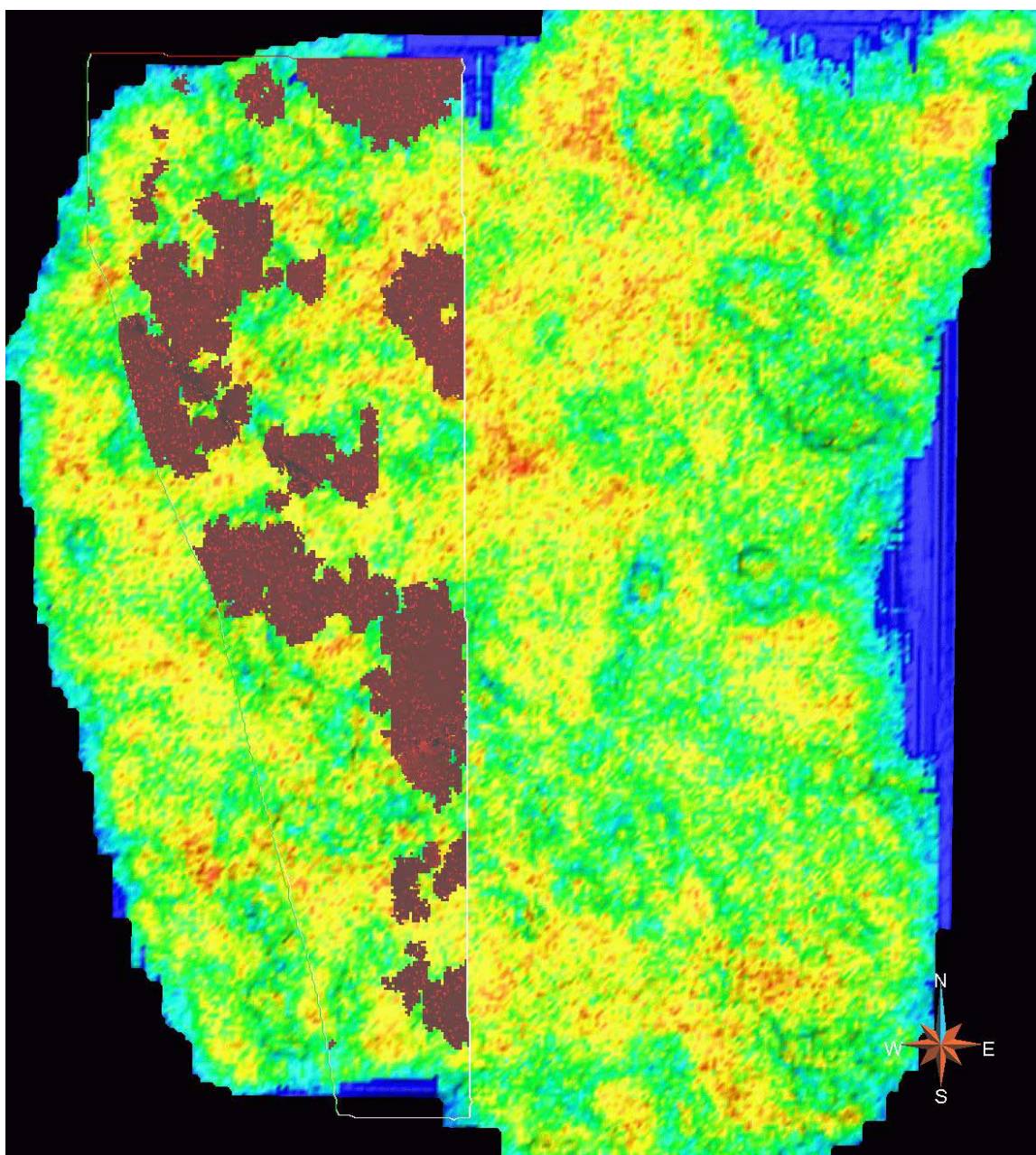


Figure B.7: SIS_04 simulation parameters: Red bodies are the simulated paleocave dimensions from a symmetrical variogram range ($r_1 = 258 \text{ m} = r_2$). The range value of 258 m was calculated from the distribution initial condition data "painted" into the Gocad sgrid. These values were initialized from the average of the point attributes that fell within the nearest sgrid cell. The shape of the breccia bodies interpolated is very similar to the input shape extracted from the lidar. The interpolation method does not allow for breccia population without connection to initial condition breccia values.

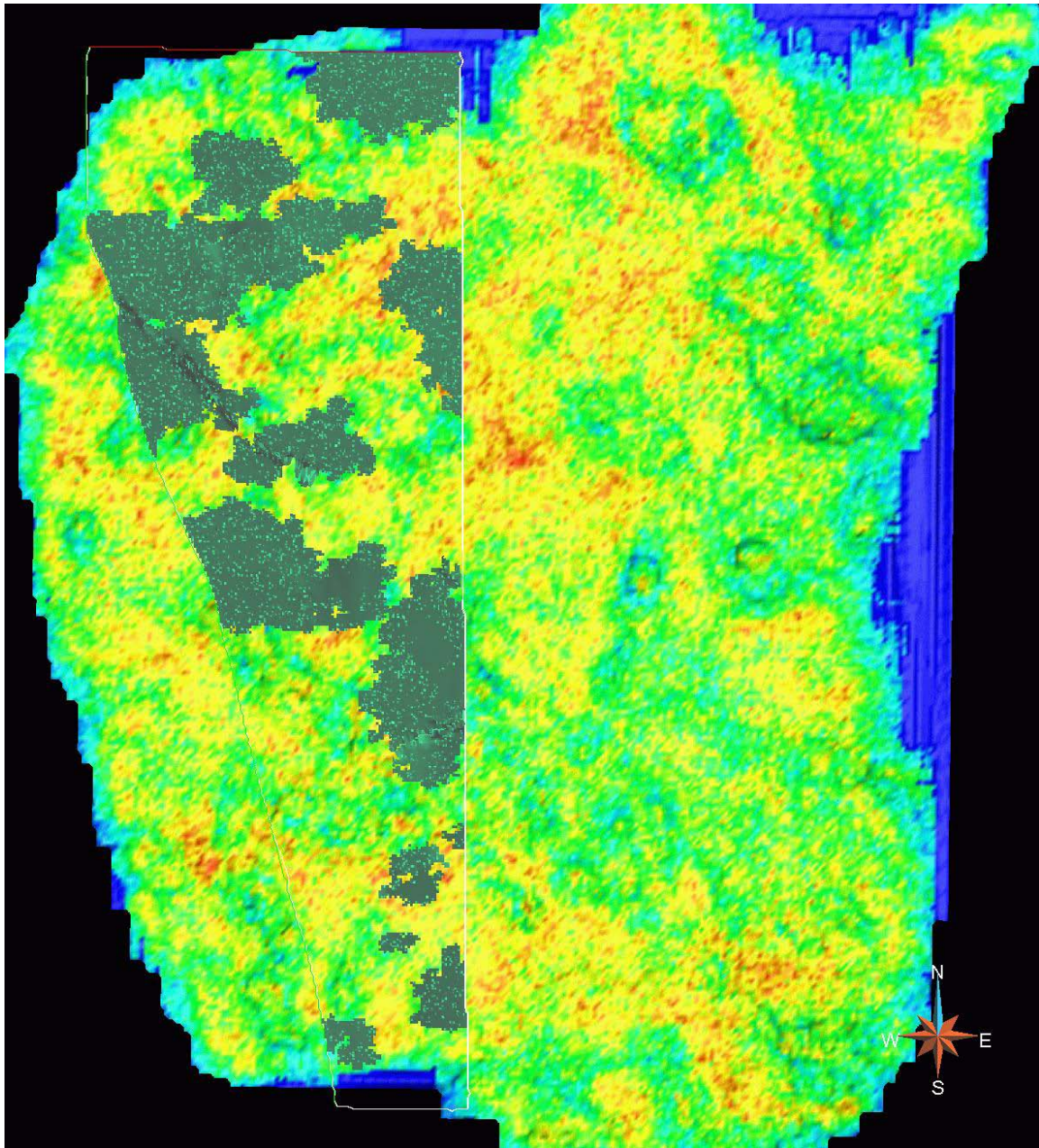


Figure B.8: SIS_05 simulation parameters: Green bodies are the simulated paleocave dimensions from an asymmetrical variogram range ($r_1 = 258$ m and $r_2 = 172$). The range value of 258 m was calculated from the distribution initial condition data "painted" into the Gocad sgrid. The r_2 range of 172 is $258/1.5$ (based on ellipticity from Devil's Sinkhole; table 2.2). These values were initialized from the average of the point attributes that fell within the nearest sgrid cell. The shape of the breccia bodies interpolated is very similar to the input shape extracted from the lidar. The interpolation method does not allow for breccia population without connection to initial condition breccia values.

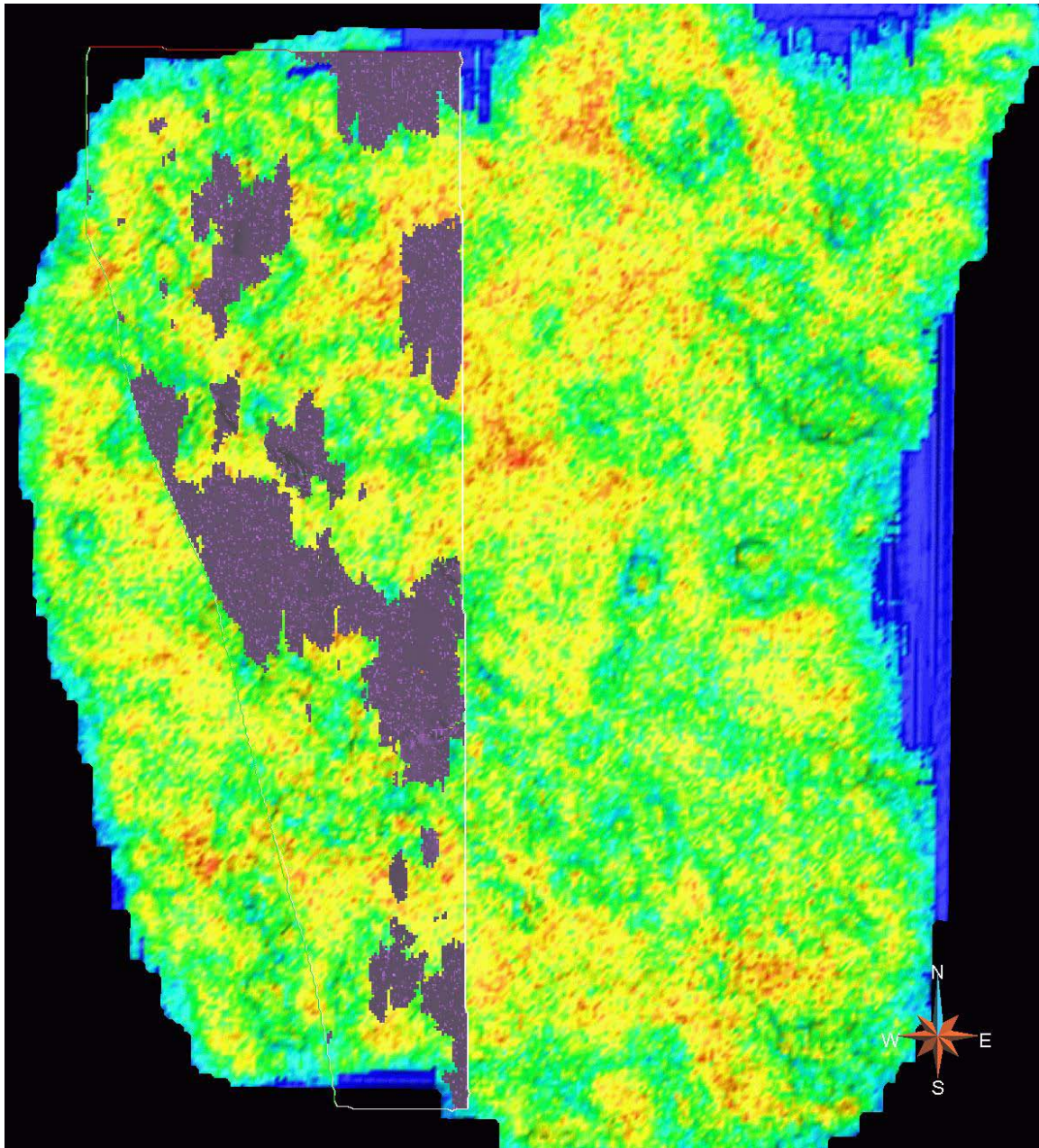


Figure B.9: SIS_05G simulation parameters: Purple bodies are the simulated paleocave dimensions from an asymmetrical variogram range ($r_1 = 258$ m and $r_2 = 172$). The range value of 258 m was calculated from the distribution initial condition data "painted" into the Gocad sgrid. The r_2 range of 172 is 258/1.5 times (based on ellipticity from Devil's Sinkhole; table 2.2). These values were initialized from the average of the point attributes that fell within the nearest sgrid cell. The shape of the breccia bodies interpolated is very similar to the input shape extracted from the lidar. The interpolation method does not allow for breccia population without connection to initial condition breccia values.

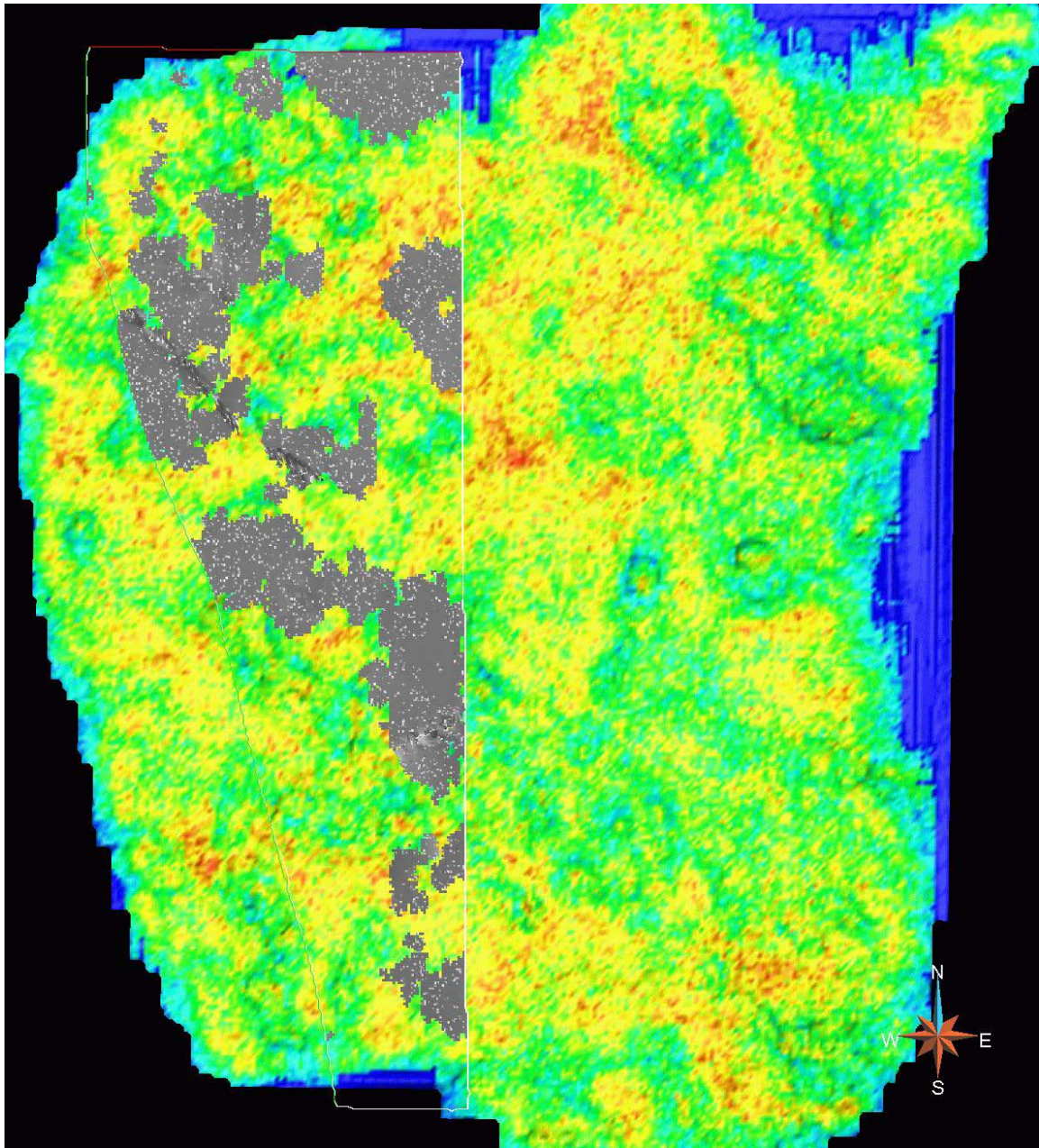


Figure B.10: SIS_06 simulation parameters: Gray bodies are the simulated paleocave dimensions from an asymmetrical variogram range ($r_1 = 357$ m and $r_2 = 258$). The range value of 258 m was calculated from the distribution initial condition data "painted" into the Gocad sgrid. The r_1 range of 387 is 1.5 times r_1 (based on ellipticity from Devil's Sinkhole; table 2.2). These values were initialized from the average of the point attributes that fell within the nearest sgrid cell. The shape of the breccia bodies interpolated is very similar to the input shape extracted from the lidar. The interpolation method does not allow for breccia population without connection to initial condition breccia values.

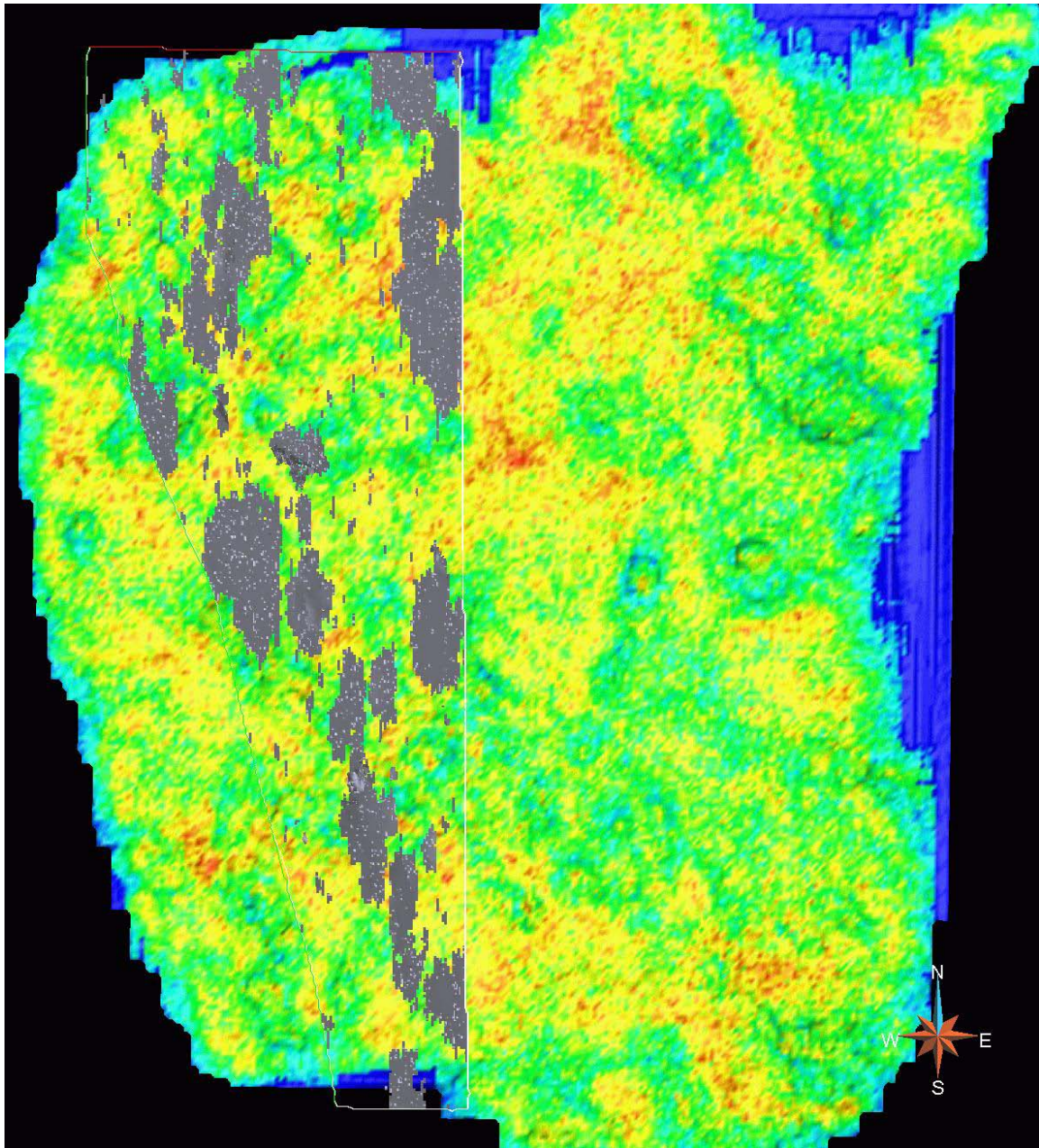


Figure B.11: SIS_07 simulation parameters: Gray bodies are the simulated paleocave dimensions from an asymmetrical variogram range ($r_1 = 357$ m and $r_2 = 172$). The range value of 258 m was calculated from the distribution initial condition data "painted" into the Gocad sgrid. The r_1 range of 387 is 1.5 times r_1 (based on ellipticity from Devil's Sinkhole; table 2.2). The r_2 range is $258/1.5$ as a minimum range. These values were initialized from the average of the point attributes that fell within the nearest sgrid cell. The shape of the breccia bodies interpolated is very similar to the input shape extracted from the lidar. The interpolation method does not allow for breccia population without connection to initial condition breccia values.

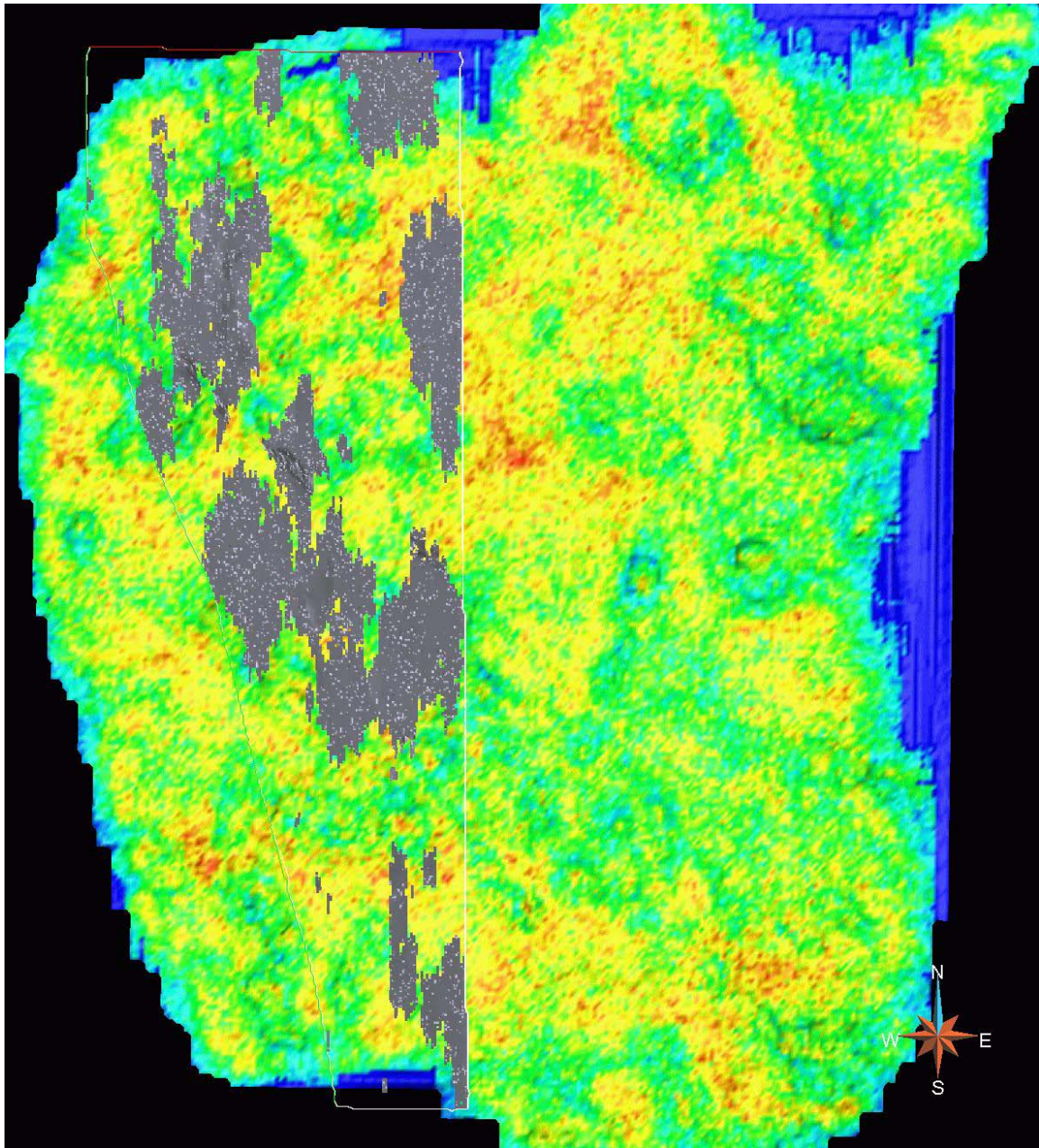


Figure B.12: SIS_08 simulation parameters: Gray bodies are the simulated paleocave dimensions from an asymmetrical variogram range ($r_1 = 357$ m and $r_2 = 172$). The range value of 258 m was calculated from the distribution initial condition data "painted" into the Gocad sgrid. The r_1 range of 387 is 1.5 times r_1 (based on ellipticity from Devil's Sinkhole; table 2.2). The r_2 range is $258/1.5$ as a minimum range. These values were initialized from the average of the point attributes that fell within the nearest sgrid cell. The shape of the breccia bodies interpolated is very similar to the input shape extracted from the lidar. The interpolation method does not allow for breccia population without connection to initial condition breccia values.

Appendix C

El Paso Group Conodont Samples

All samples collected and photographed by the author.

Conodont processing and species identification

conducted by:

Dr. John Repetski

United States Geological Survey

Reston, VA

and

Dr. Stephen Leslie

James Madison University

Harrisonburg, VA

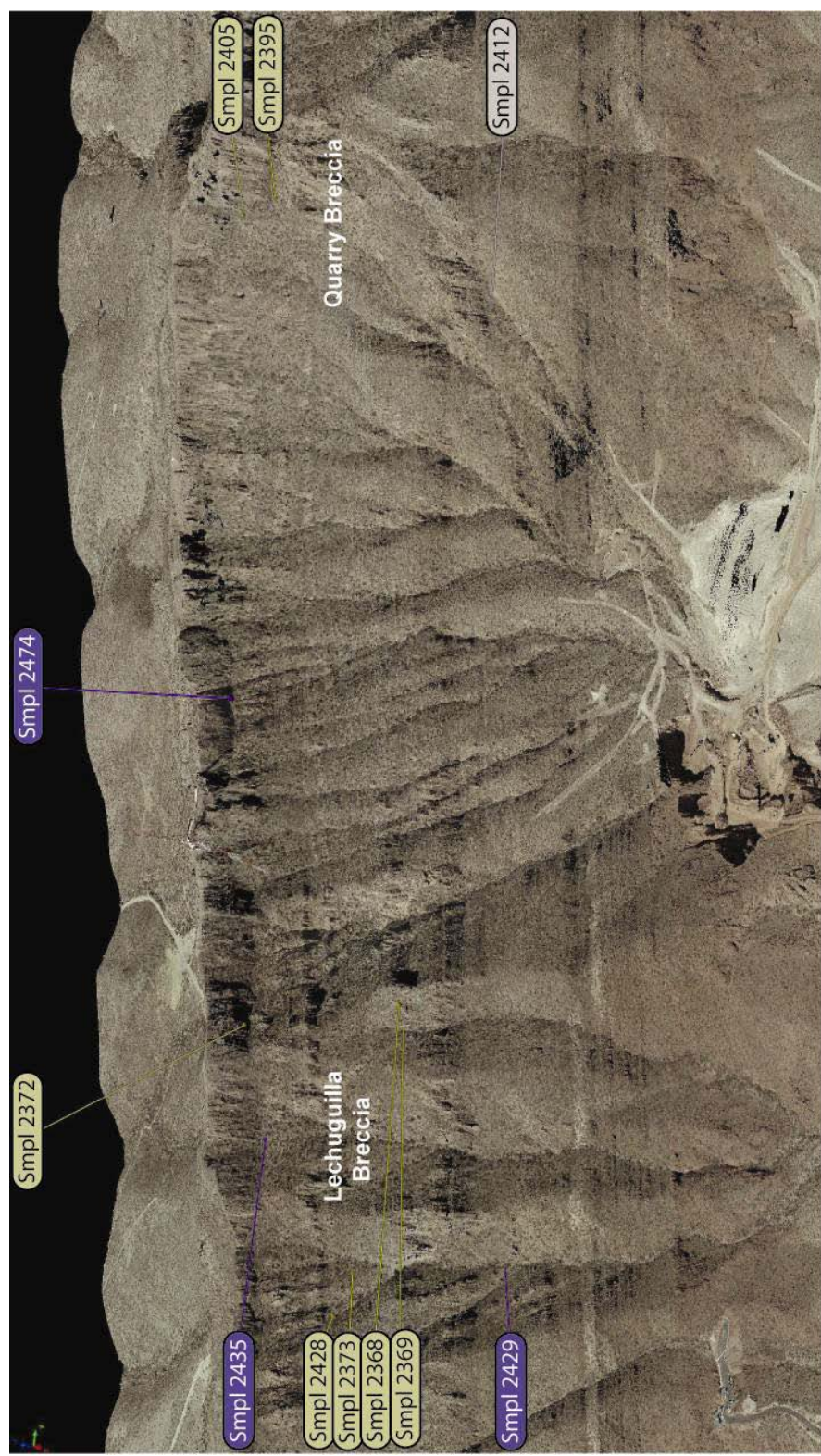


Figure C.1: Conodont sample location map. Geographic coordinates for each are listed in table 1.1.

Figure C.2: Sample 2368

Sample collected from fjl "cave fill" north of Lechuguilla Breccia just below the lower biostrome top. Uppermost Chamizal (Uppermost Hitt Canyon) through Ranger Peak (O. costatus through R. andinus Zones).



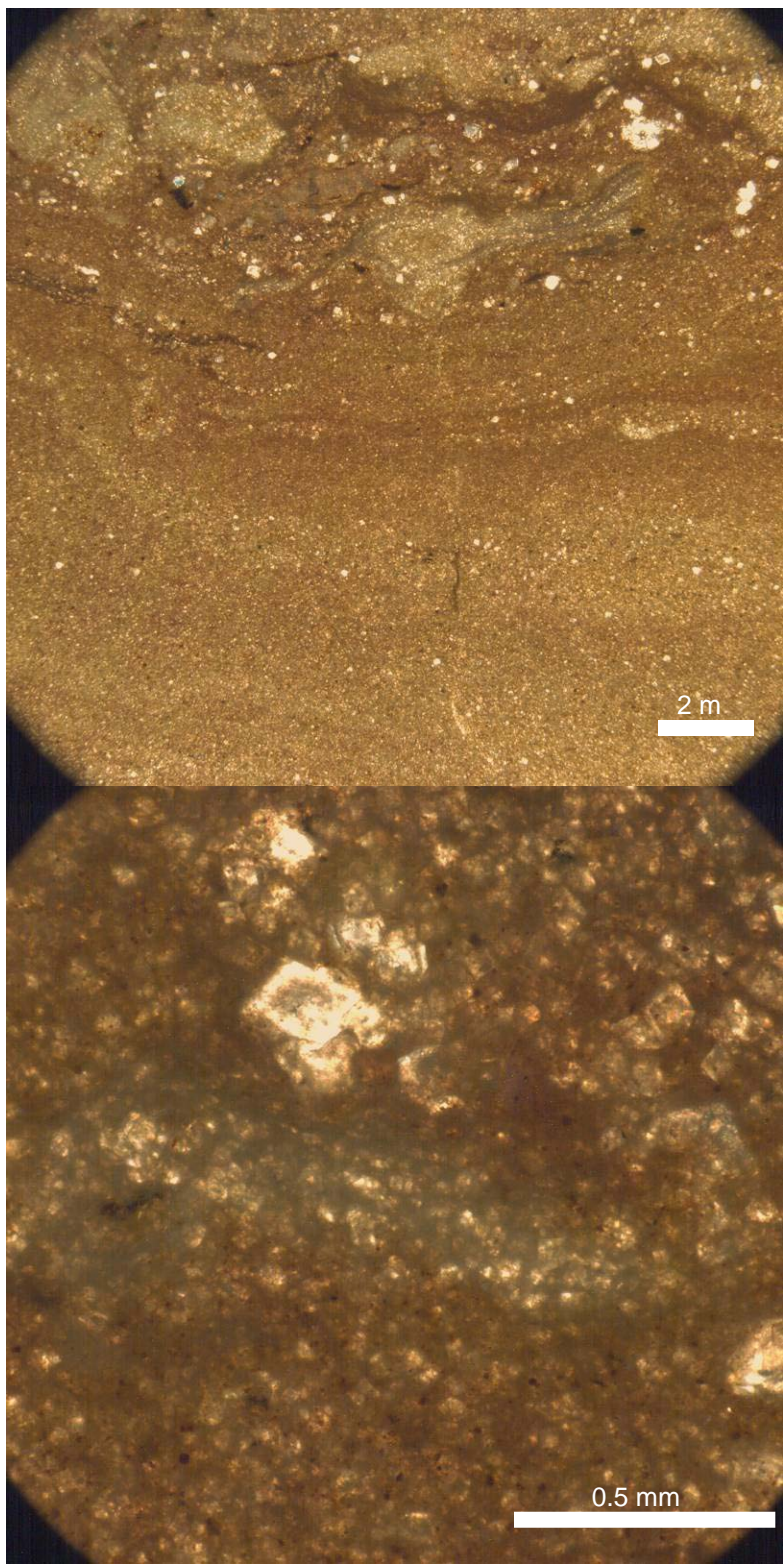


Figure C.3:

Sample 2368

Low magnification
photomicrograph of

sample 2368 thick section.

This is a finely laminated
dolosilt with large (100-300
μm) dolomite crystals.

Upper image is at 1x and
lower is 9.2 x.

THIS SAMPLE HAS BLUE
EPOXY.

Mild to no reaction with
10% HCl, possible slight
de-dolomitaztion?

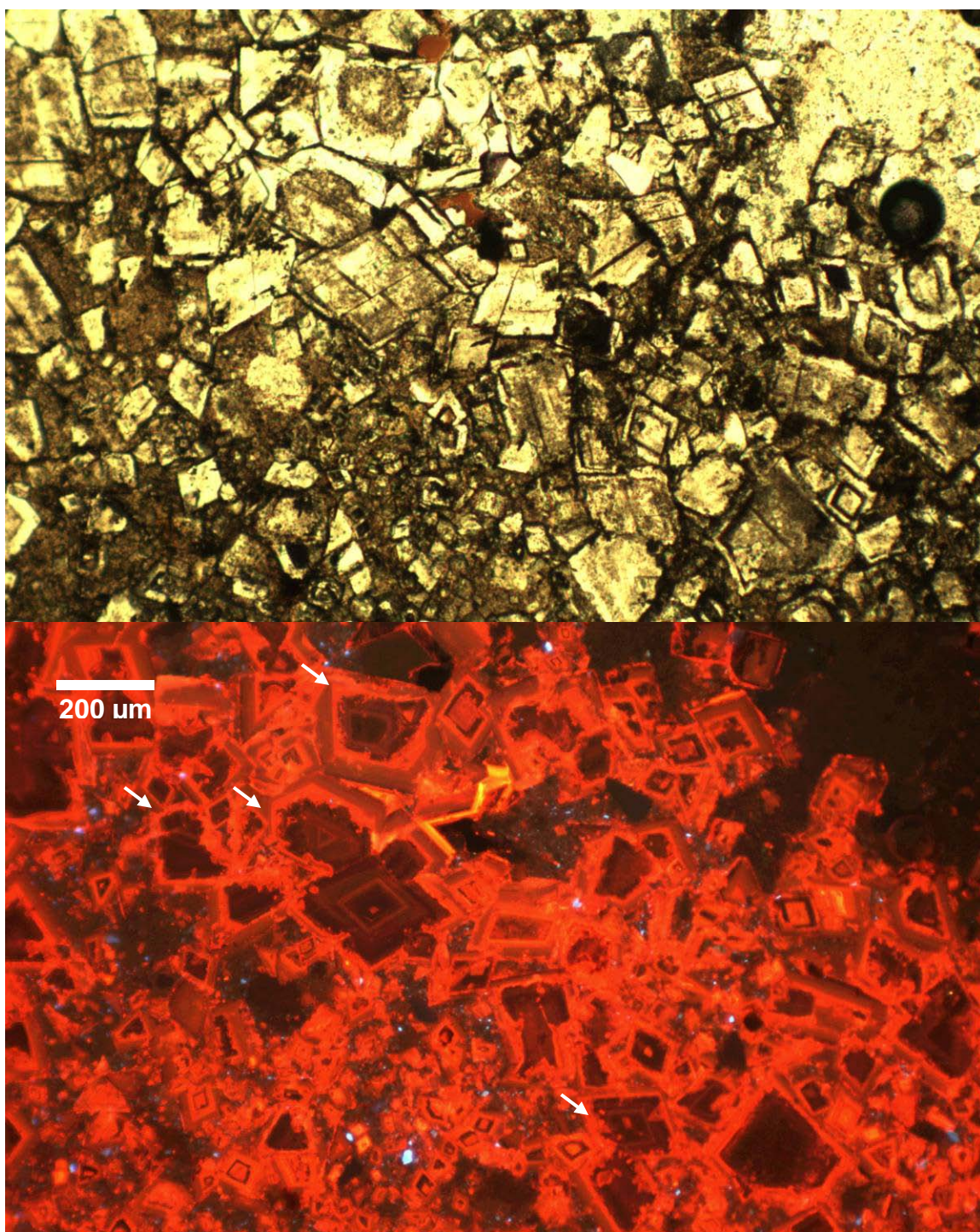


Figure C.4: Sample 2368, upper image in plane polarized light, lower image is CL. CL illumination shows abraded/corroded dolomite crystals (white arrows, lower image) indicating either corrosion from multiple fluid migrations and/or abrasion via transport of grains. Distinct banding of both darker crystals and younger rims indicates a complex fluid-rock interaction within the matrix material of the El Paso Group Breccias. Image was taken using 10X magnification.

Figure C.5: Sample 2369

Taken from just below the lower biostrome contact lateral (north) to fill “cave sediment” canyon one canyon north of Lechuguilla Breccia. Upper McKelligon Canyon through Ranger Peak (*O. comminus* or *R. andinus* Zone).



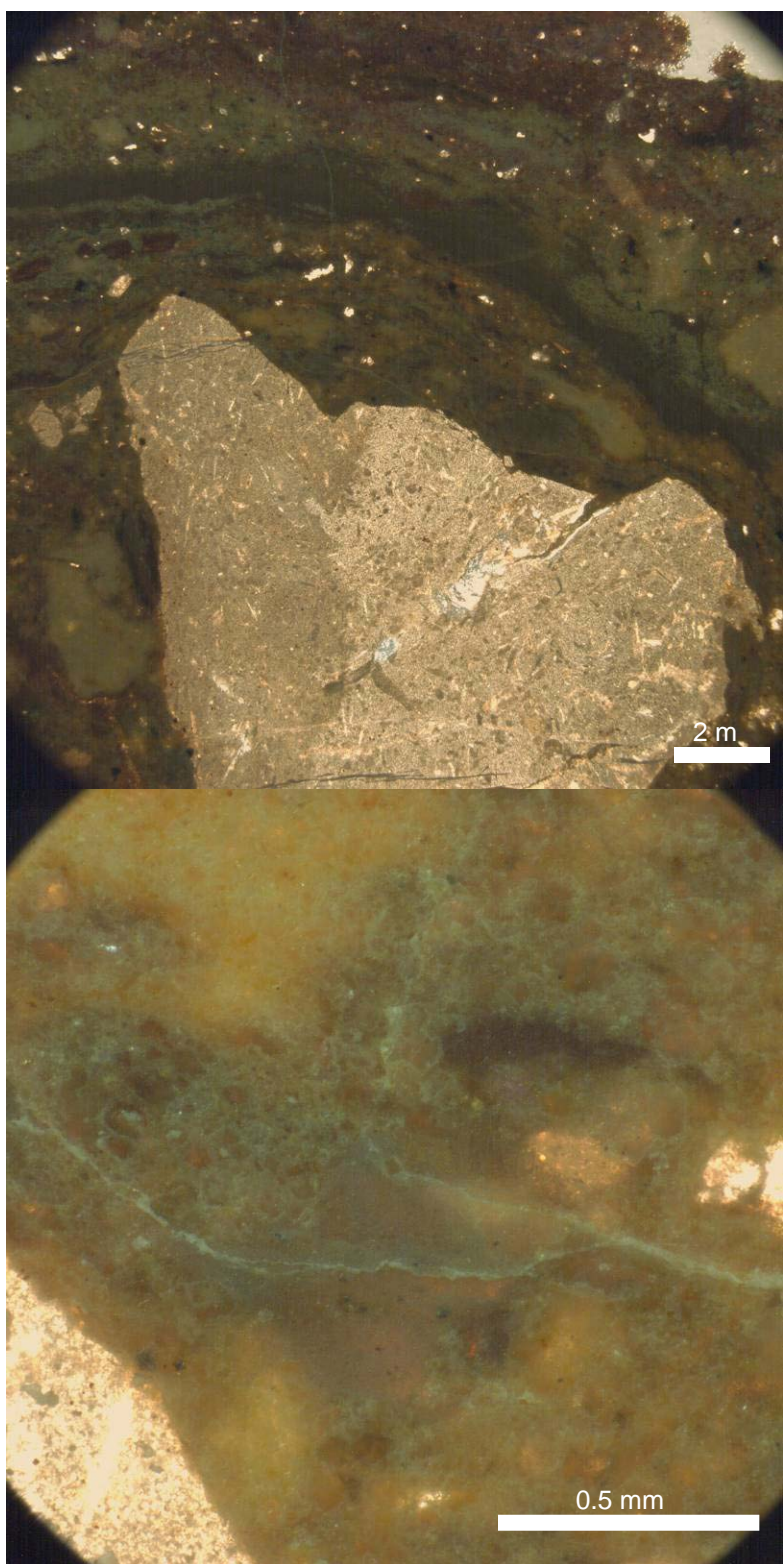


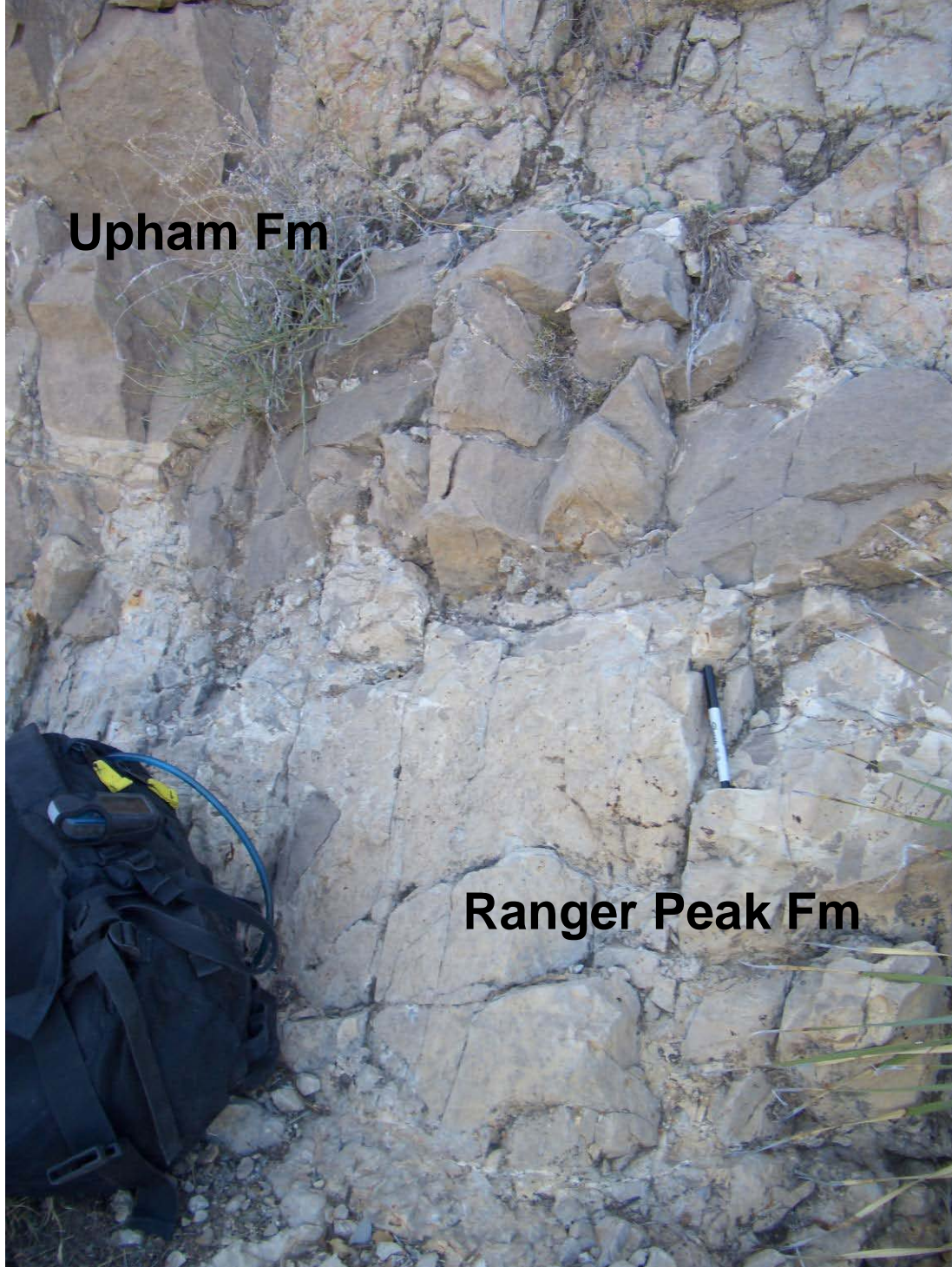
Figure C.6:

Sample 2369:
Low magnification
photomicrograph of
sample 2369 thick
section. Upper image is
at 1x and lower is 9.2 x.
Large rock fragment in
upper image is
dolomite, as does seem
to be the matrix
material.

Localized reaction
(calcite-replaced
crinoids/sponge
fragments).

Figure C.7: Sample 2372

Directly above north flank of Lechuguilla Breccia, just south of Lucia's "limestone pillar" in the white sediment to the left of pen. Range is from Low Diversity Interval through R. andinus which translates to Hag Hill (middle Hitt Canyon) through Ranger Peak (Padre Fm) Formations.



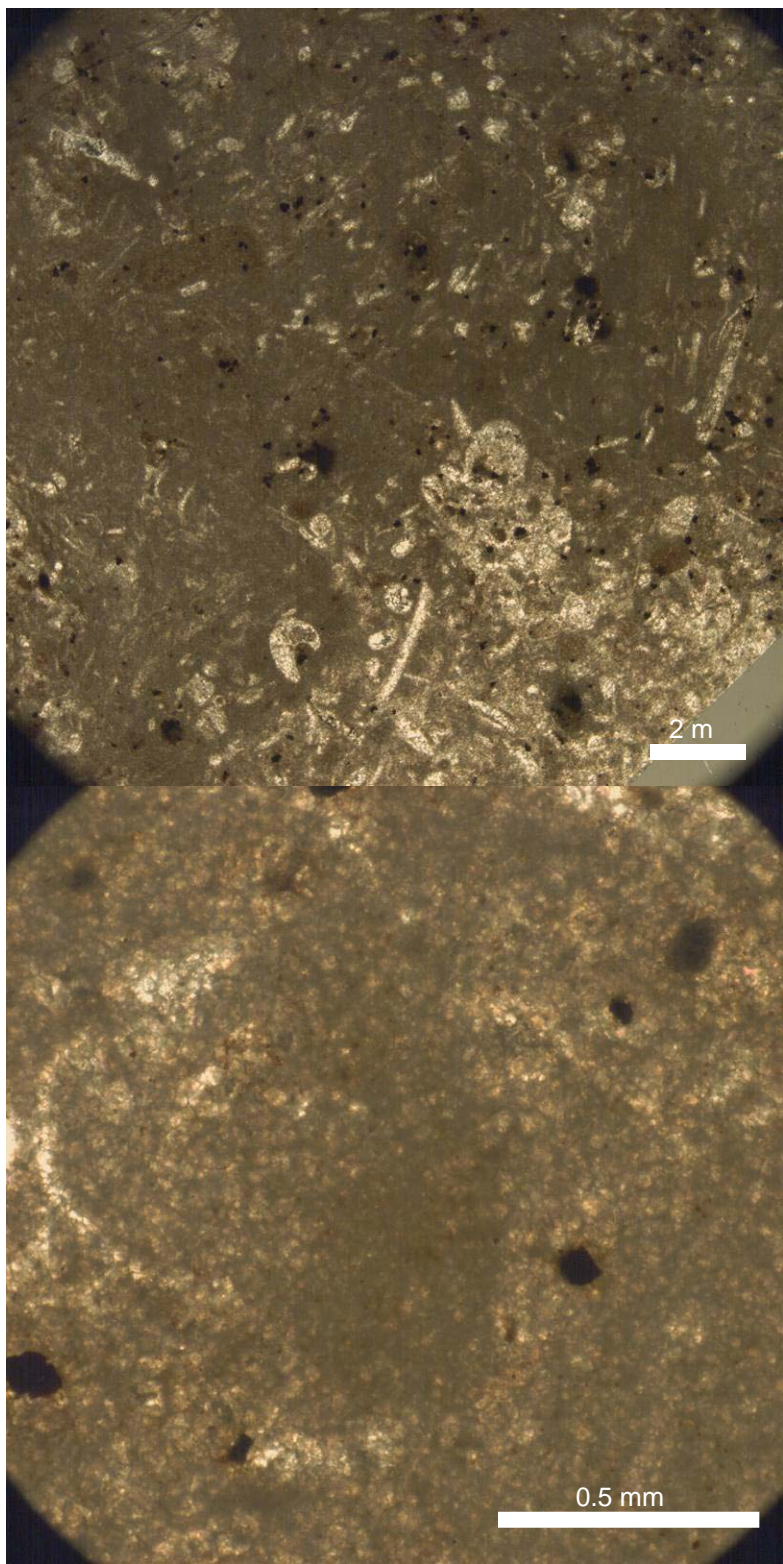


Figure C.8:
Sample 2372
Low magnification
photomicrograph of
sample 2372 thick
section. Dolomitized
spiculitic skeletal
packstone with
unknown dark
patches. Upper image
is at 1x and lower is
9.2 x.

THIS SAMPLE HAS
BLUE EPOXY.

No reaction with 10%
HCl.

Figure C.9: Sample 2373

South of LB on south side of small fault with red silt between upper and lower biostromes of McKelligon Canyon Fm. Hag Hill (Middle Hitt Canyon) to Ranger Peak age conodonts (anywhere from Low Diversity Interval through R. andinus Zone).



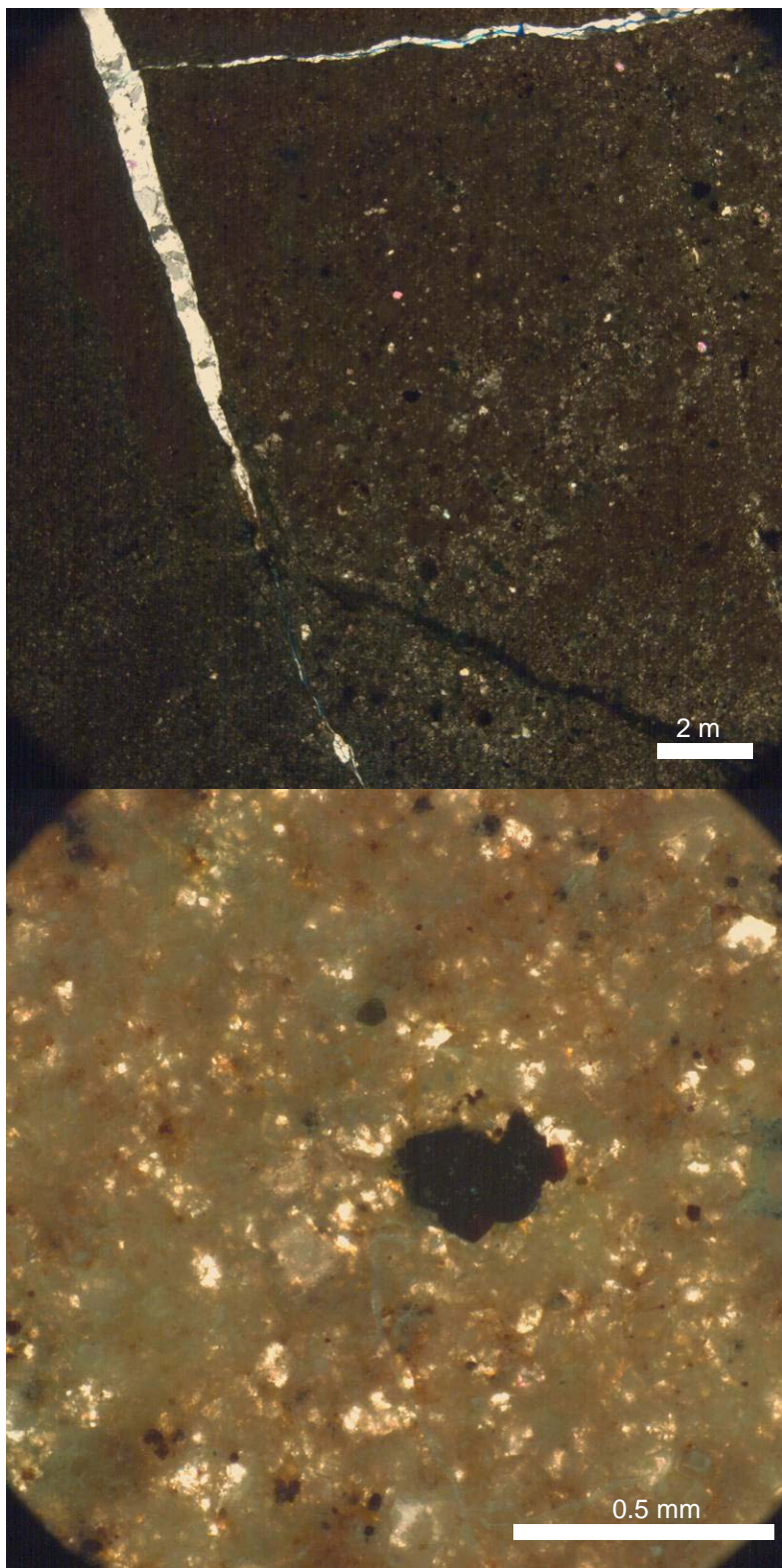


Figure C.10:

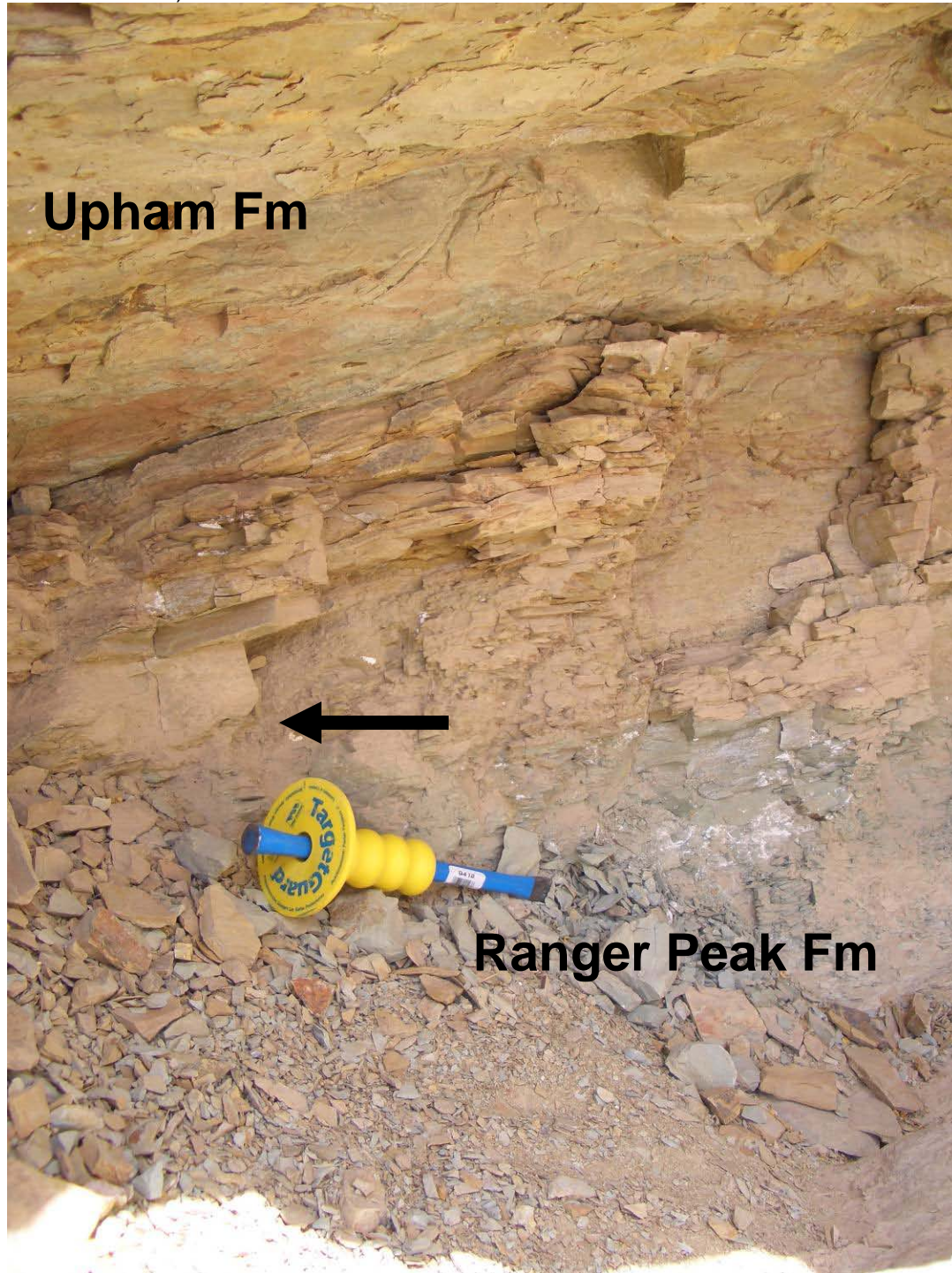
Sample 2373
Low magnification
photomicrograph of
sample 2373 thick
section. Calcite-filled
fractures reaction
with 10% HCl. Some
large (100-300 μm)
dolomite crystals in
fine crystalline
dolomitic matrix.
Upper image is at 1x
and lower is 9.2 x.

THIS SAMPLE HAS
BLUE EPOXY.

Localized reaction
with 10% HCl, along
fractures.

Figure C.11: Sample 2395

Taken from the top of the El Paso Group contact with the Montoya (Upham Fm). Black arrow points to actual sample taken. Upper McKelligon Canyon through Ranger Peak (O. comminus or R. andinus Zone).



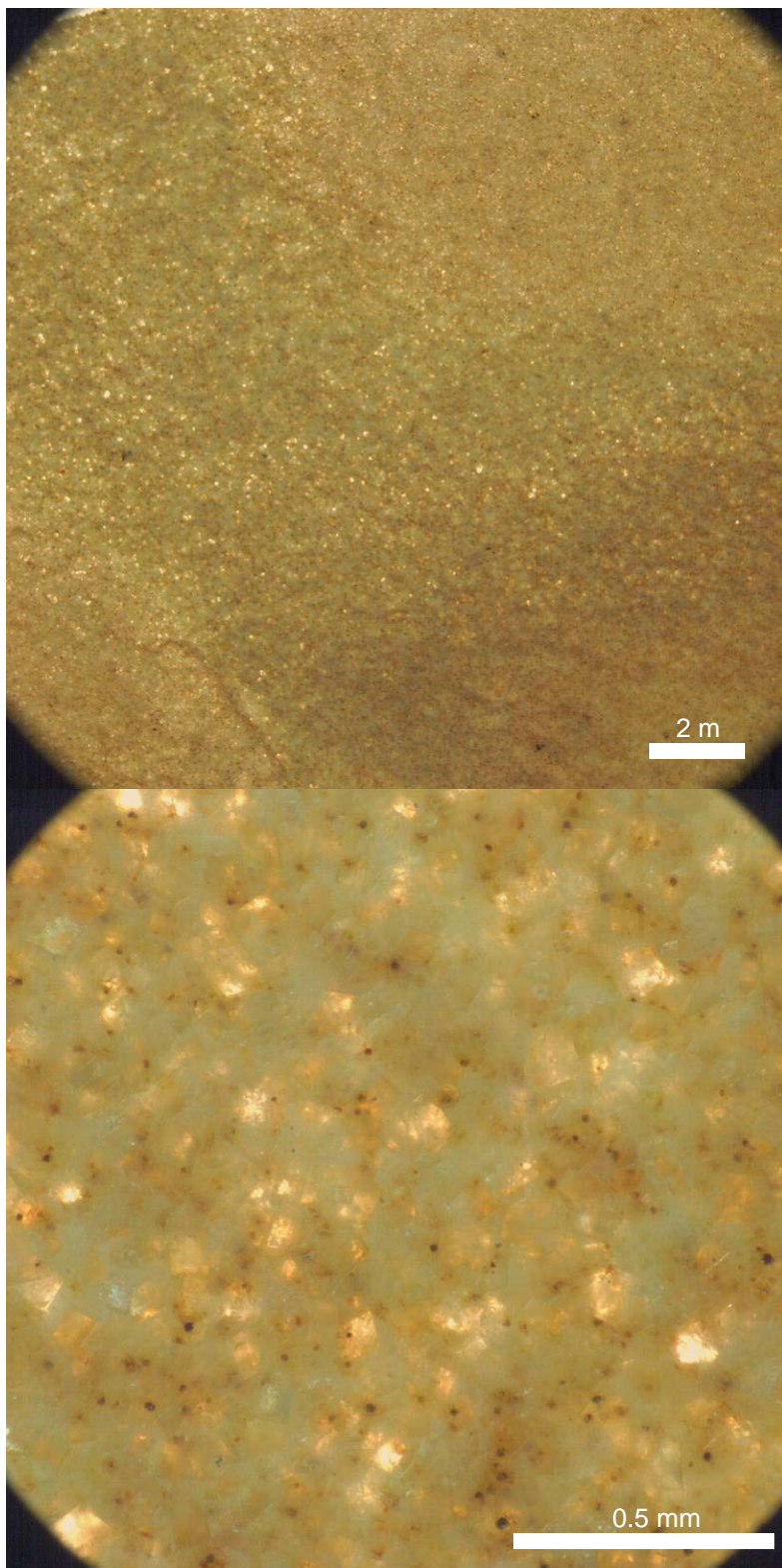


Figure C.12:

Sample 2395

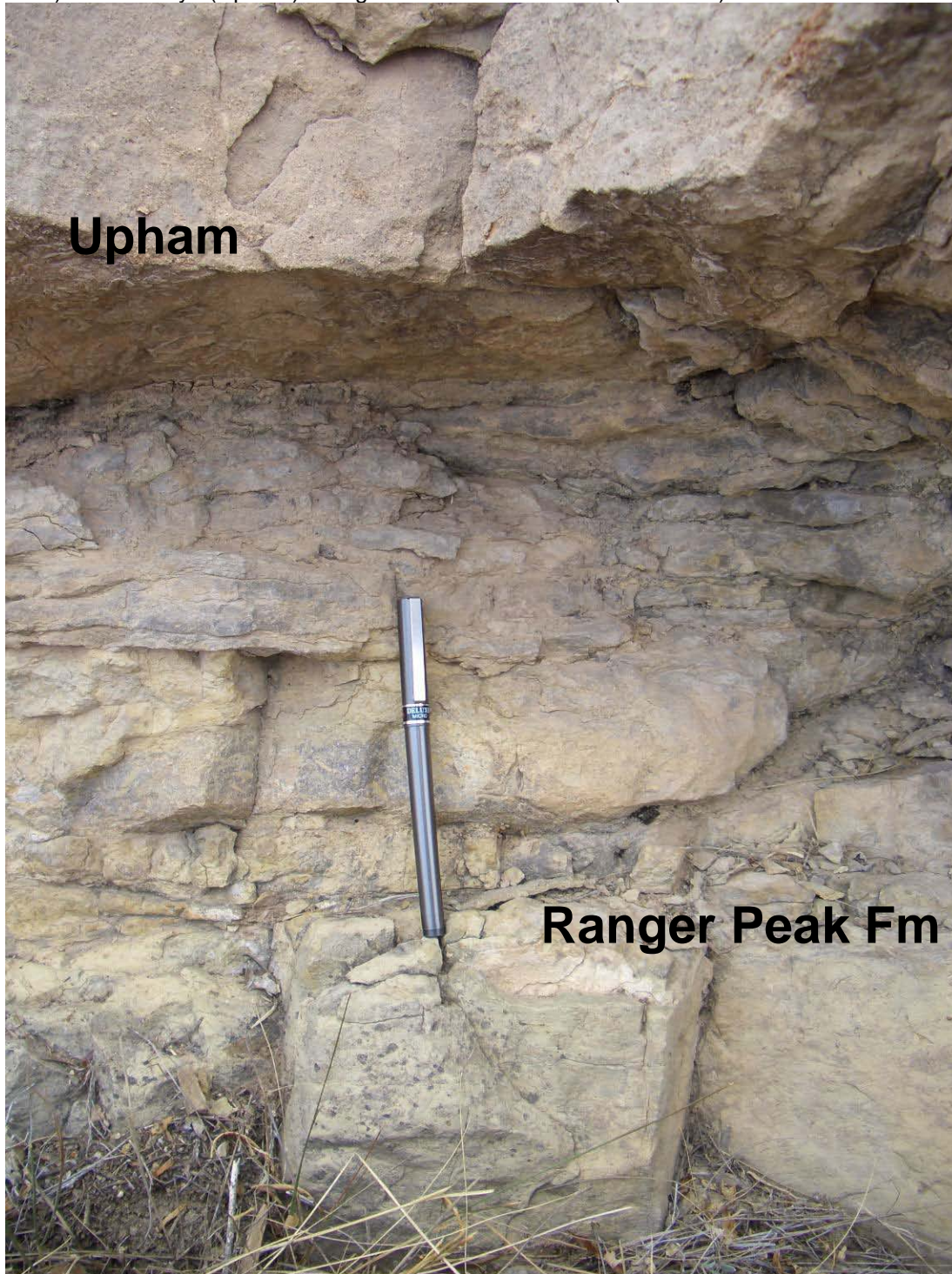
Low magnification photomicrograph of sample 2395 thick section. This is a fine swirled-texture dolosilt (?) with large (100-300 μm) crystals. Upper image is at 1x and lower is 9.2 x.

No reaction with 10% HCl.

Figure C.13:

Sample 2405

Taken from south side of fault near 2395 from greenish horizon contact between El Paso (Ranger Peak) and Montoya (Upham). Ranger Peak conodont zone (*R. adinus*).



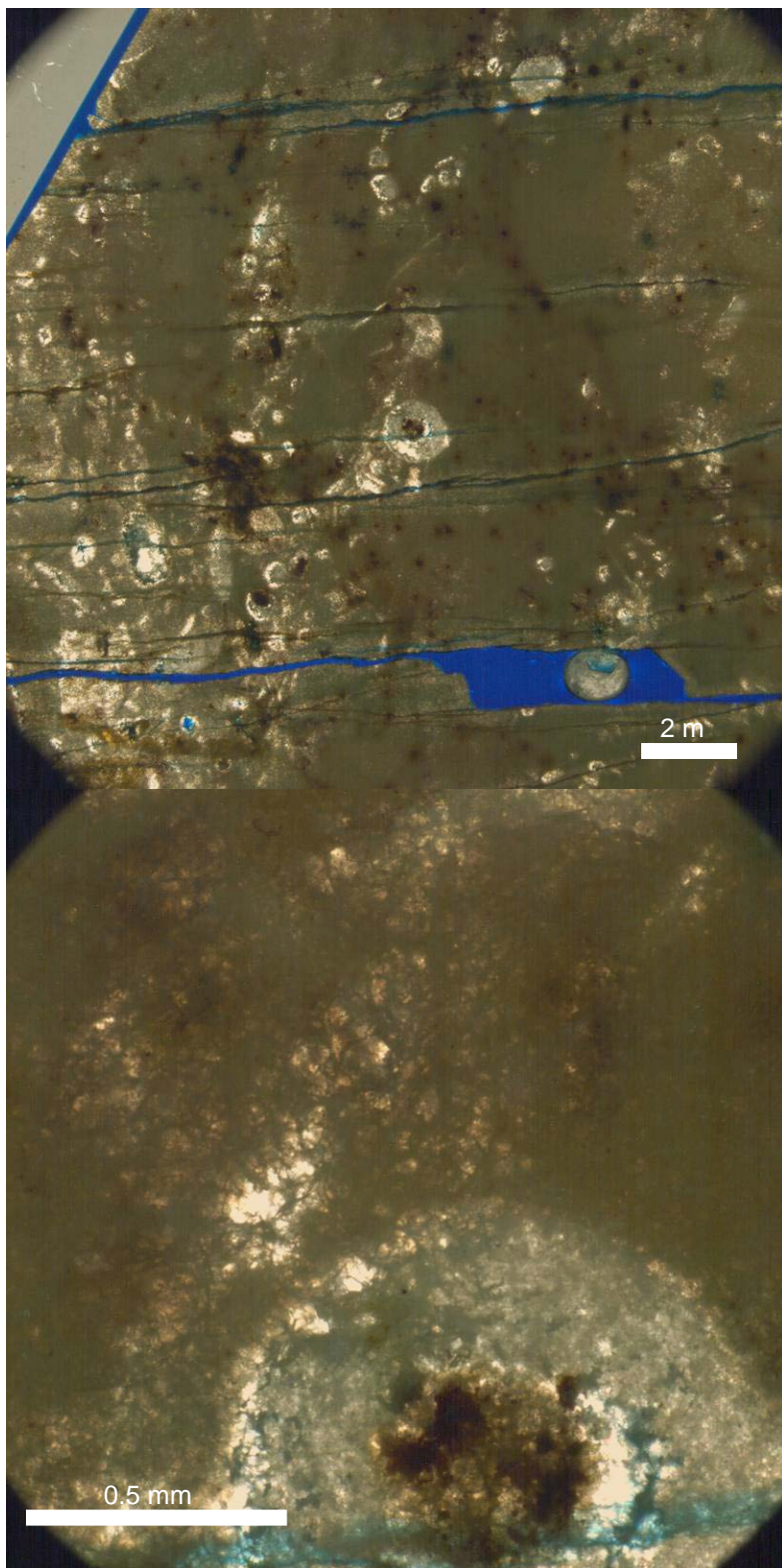


Figure C.14:

Sample 2405

Low magnification photomicrograph of sample 2405 thick section. This is a fractured crinoidal (?) dolopack-dolowackstone (?) with medium (20-100) crystals. Upper image is at 1x and lower is 9.2 x.

THIS SAMPLE HAS BLUE EPOXY.

No reactoin with 10% HCl.

Figure C.15: Sample 2412:

Taken from deepest breccia mapped. Lower 1/3 of the El Paso Group (Hag Hill of Lucia/Hitt Canyon). Yellow matrix material from north-side of lower Quarry Breccia. Lower Devonian/Silurian PLUS O. comminus to R. andinus Zone (two zone present, not a range).



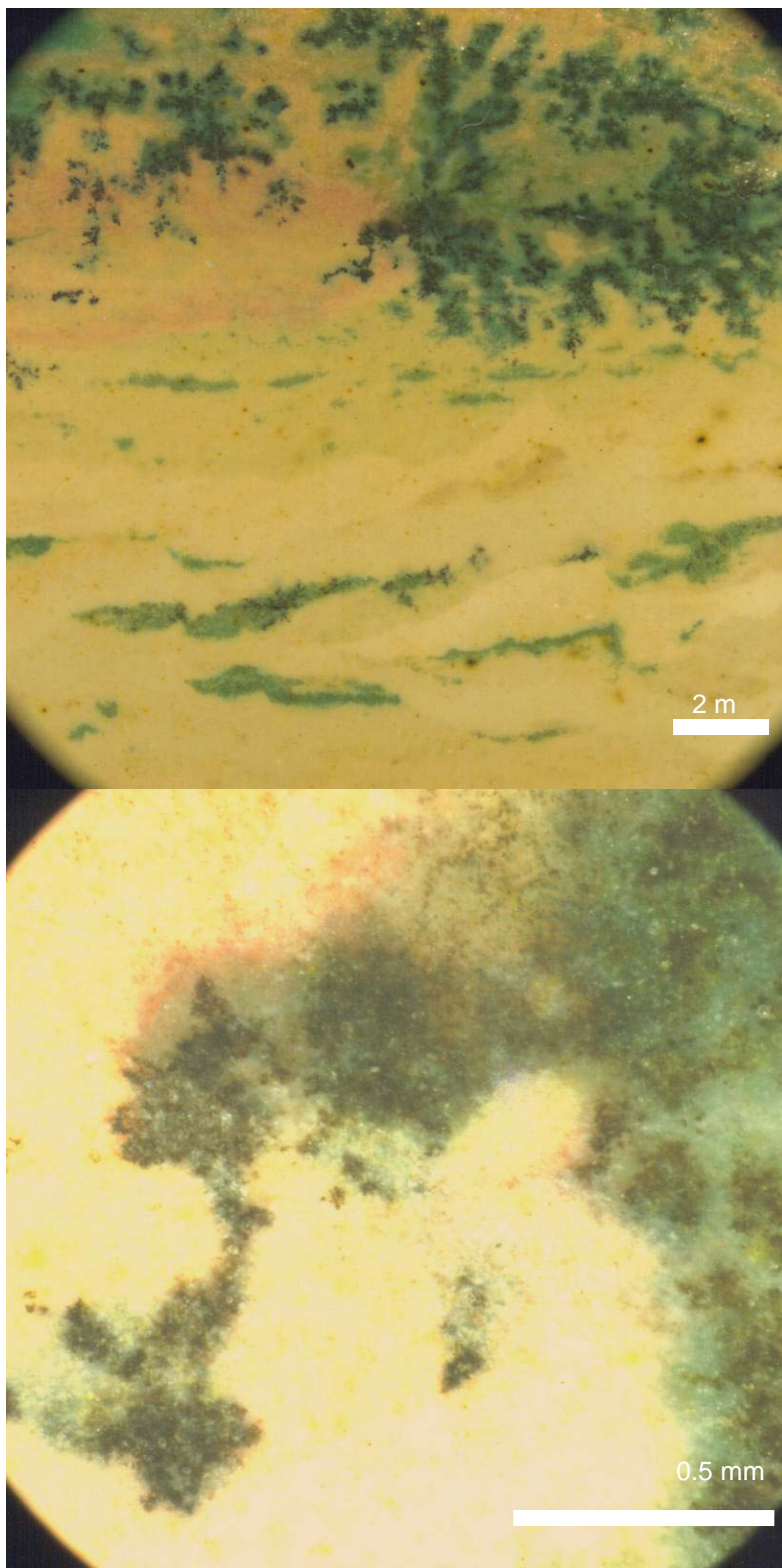


Figure C.16:

Sample 2412:

Low magnification
photomicrograph of
sample 2412 thick
section. This is a
dolomudstone. Upper
image is at 1x and
lower is 9.2 x.

THIS SAMPLE HAS
BLUE EPOXY.

No reaction with 10%
HCl.

Figure C.17: Sample 2428

At the McKelligon-Cindy (Padre Fm) contact near small fault offset (<1m offset) fault. *O. costatus* to *R. andinus* Zone. No thick section for this sample.



Figure C.18: Sample 2429

No conodonts from this sample taken from Lower Hag Hill/Bowen level within distinct red banded zone (soil?). No reaction to 10% HCl.



Figure C.19: Sample 2435

No conodonts in this sample taken from fill above Lechuguilla Breccia near El Paso/Montoya contact. Very mild reaction to 10% HCl (recent calcite replacement?).



Figure C.20: Sample 2447

No conodonts in this sample. Sample location is near the dolomitic limestone near the Scenic Drive section measured by Repetski (1984). No reaction to 10% HCl. Sample is a laminated yellow dolosilt (?). Location is not shown on overview figure at beginning of Appendix C.



Figure C.21: Sample 2474

No conodonts in this sample; looks like the standard red-Ranger Peak matrix. Calcite (fracture fill or possible dedolomite?) with mild reaction to 10% HCl. Sample just below this contact of Montoya and Ranger Peak below radio towers north of Lechuguilla Breccia.



Appendix D

**Palynology of samples from the Lower Ordovician (Ellenburger equivalent) El Paso Group
outcrop breccia matrix material, El Paso, Texas.**

Prepared by: Pierre A. Zippi, Ph.D.

Biostratigraphy.com, LLC

Garland, Texas

U.S.A.

June 18th 2008

**Palynology of samples from Lower Ordovician (Ellenburger age) collapse breccia outcrop,
El Paso, Texas.**

Pierre A. Zippi, Ph.D., Biostratigraphy.com, LLC July 18, 2008

Executive summary:

Two samples from an outcrop of Lower Ordovician (Ellenburger age) collapse breccia in El Paso, Texas were analyzed for palynology to determine age and paleoenvironment of deposition.

Both samples were barren of palynomorphs. No age, environment, or thermal maturity interpretations can be made.

As is common in barren outcrop samples, the small residue consisted of modern pollen, soil/root fungi, miscellaneous plant fragments and insect fragments.

**Palynology of samples from Lower Ordovician (Ellenburger age) collapse breccia outcrop,
El Paso, Texas**

P. Zippi, Biostratigraphy.com, LLC, Dallas, TX

Introduction:

Two samples were submitted for palynological age determination by J. Bellian of the Bureau of Economic Geology, University of Texas, Austin. One sample was mixed host rock and infill, while the second was concentrated infill.

Methods:

Samples were crushed. Carbonate minerals were dissolved using HCl and silicate minerals removed using HF. The organic residue was washed with HNO₃ followed by a wash with ammonia or KOH. A heavy liquid separation was used to remove the insoluble minerals. The residues were sieved through a 10 m mesh screen to remove small particles that would be unidentifiable in transmitted light microscopy. Residues were mounted on a coverslip with polyvinyl alcohol and fixed to a microscope slide with elvacite. Samples were examined at a minimum of 500X. Personnel: The palynological sample processing was performed by Global Geolab, Ltd. and Biostratigraphy.com, LLC. Slides and residues were shipped to Biostratigraphy.com, LLC in Garland, TX. Dr. Pierre Zippi performed the palynological analyses, project coordination, palynological quality control, final interpretation and reporting. Sample analysis results: All samples were barren of fossil palynomorphs.

040608H-1 Barren of fossil palynomorphs. Modern contamination.

040508D-2 Barren of fossil palynomorphs. Modern contamination.

Conclusion:

No conclusions can be drawn from the results. Recovery of modern contamination is common with barren outcrop samples and indicates that the lab processing successfully concentrated the small amounts of organics associated with the rocks.

Recommendations:

If possible, a darker more organic rich lithology should be sampled. If only weathered material is available, then strip away the more heavily contaminated surficial material and sample the more protected underlying material. Acquire the darkest fine grain lithology available: dark siltstone, carbonaceous claystone, fine grain (organoclasts) lignites and coals are best.

References Cited:

- Adams, E. W., Schroder, S., et al., 2004, Digital reconstruction and stratigraphic evolution of a microbial-dominated, isolated carbonate platform (Terminal Proterozoic, Nama Group, Namibia): *Journal of Sedimentary Research* v. 74, no. 4, p. 479-497.
- Adams, E. W., Grotzinger, J. P., Watters, W. A., Schroeder, S., McCormick, D. S., and Al-Siyabi, H.A., 2005, Digital characterization of thrombolite-stromatolite reef distribution in a carbonate ramp system (terminal Proterozoic, Nama Group, Namibia): *AAPG Bulletin*, v. 89, no. 10, p. 1293-1318.
- Bellian, J.A., Kerans, C., and Jennette, D.C., 2005, Digital outcrop models: applications of terrestrial scanning lidar technology in stratigraphic modeling: *Journal of Sedimentary Research*, v. 75, no. 2, p. 166-176.
- Bellian, J.A., Beck, R.A., and Kerans, C., 2007, Analysis of hyperspectral and lidar data: remote optical mineralogy and fracture identification: *Geosphere*, v. 3, no. 6, p. 491-500.
- Bellian, J.A., Janson, X., and Harris, M., 2008, Carbonate Digital Outcrop Reservoir Models: from Lidar to MPS Simulation, American Association of Petroleum Geologists Annual International Meeting Official Program, April 9th-12th, Cape Town, South Africa, v. 15, p. 8.
- Bellian, J.A., Kerans, C., and Repetski, J., 2010, The Great American Carbonate Bank, Southern Franklin Mountains of the Desert Southwest, El Paso, Texas, *in* The Cambro-Ordovician Sauk Sequence of Laurentia - The Geology and Petroleum Potential of the Great American Carbonate Bank, SEPM James Lee Wilson Memorial Special Volume, *in press*.
- Berner, R.A., 1997, The rise of plants and their effect on weathering and atmospheric CO₂: *Science*, v. 227, p. 544-546.
- Bickford, M.E., Soegaard, K., Nielsen, K.C., and McLelland, J.M., 2000, Geology and geochronology of Grenville-age rocks in the Van Horn and Franklin Mountains area, west Texas: implications for the tectonic evolution of Laurentia during the Grenville: *Geological Society of America Bulletin*, v. 112, p. 1134-1148.
- Blakey, R.C., 2009, North American paleogeographic maps, <http://jan.ucc.nau.edu/~rcb7/nam.html>, accessed January 08, 2009.
- Bliefnick, D. M., 1992, Karst-related diagenesis and reservoir development in the Arbuckle Group, Paschall No. 2 core, Wilburton field, Oklahoma, in M. P. Candelaria and C. L. Reed, eds., *Paleokarst, karst related diagenesis and reservoir development: Examples from Ordovician-Devonian age strata of west Texas and the mid-continent: Permian Basin Section SEPM Publication No. 92-33*, p. 137- 152.
- Caers, J. (2000). Adding local accuracy to direct sequential simulation. *Mathematical Geology*, October, 32(7):815-850.
- Carciumaru, D.D., 2005, Structural geology and tectonics on the northern Chihuahua Trough, The University of Texas at El Paso, Ph.D. dissertation, 109 pp.

- Carciumaru, D. and Ortega, R., 2008, Geological structure of the northern margin of the Chihuahua trough: Evidence for controlled deformation during Laramide Orogeny, *Boletín de la Sociedad Geológica Mexicana*, Vol. 60, n.1, 2008 p. 43-69.
- Clemons, R.E., 1989, The Ellenburger-El Paso connection; Lower Ordovician shelf carbonates, *in* The lower Paleozoic of West Texas and southern New Mexico; modern exploration concepts: Society of Economic Paleontologists and Mineralogists, Permian Basin Chapter, Publication 89-31, p. 85-104.
- Clemons, R.E., 1998, Geology of the Florida Mountains, southwestern New Mexico: New Mexico Bureau of Mines and Mineral Resources Memoir 43, University of New Mexico Publications in Geology, 112 p.
- Cloud, P.E., and Barnes, V.E., 1948, The Ellenburger Group of central Texas: University of Texas, Austin, Publication 4821, 473 p.
- Collins, B.D. and Kayen, R., 2006, Applicability of terrestrial LIDAR scanning for scientific studies in Grand Canyon National Park, Arizona *Open-File Report - U. S. Geological Survey*, OF 2006-1198:27 pp.
- Collins, E.W., and Raney, J.A., 2000, Geologic Map of West Hueco Bolson, El Paso Region, Texas, The University of Texas Bureau of Economic Geology, Scott W. Tinker, Director.
- Drewes, H., 1978, The Cordilleran orogenic belt between Nevada and Chihuahua, *Geological Society of America Bulletin*, v. 89, p.641-657, Doc. no. 90501.
- Dreybrodt, W., and Gabrovsek, F., 2002, Basic processes and mechanisms governing the evolution of karst, *in* Evolution of karst; from prekarst to cessation; proceedings, Gabrovsek, Zalozba ZRC, Slovenia (2002) p. 115-154.
- Dubrule, Oliver, 2003, Introduction to Geostatistics, SEG Short Course Notes, Society of Economic Geologists, 176 pp.
- Dunham, R.J., 1969, Early vadose silt in Townsend mound (reef), New Mexico (*in* Depositional environments in carbonate rocks; a symposium) *Special Publication - Society of Economic Paleontologists and Mineralogists*, Special Publication 14, 139-181.
- Dutton, S.P., Kim, E.M., Broadhead, R.F., Breton, C.L., Raatz, W.D., Ruppel, S.C., and Kerans, C., 2005, Play analysis and digital portfolio of major oil reservoirs in the Permian Basin: The University of Texas at Austin, Bureau of Economic Geology Report of Investigations No. 271, 287 p., CD-ROM.
- Elliot, W.R. and Veni, G., eds. 1994, The Caves and Karst of Texas, 1994 NSS Convention Guidebook, National Speleological Society, Huntsville, Alabama, 342 p.
- Esteban, M., and Klappa, C.F., 1983, Subaerial exposure environment, *in* Carbonate Depositional Environments, American Association of Petroleum Geologists Memoir 33, pp. 1-54.
- Ewing, 1990, Tectonic Map of Texas, University of Texas at Austin, Bureau of Economic Geology, Austin, Texas.

- Ferrill, D.A. and Morris, A.P., 2008, Fault zone deformation controlled by carbonate mechanical stratigraphy, Balcones fault system, Texas, AAPG Bulletin, Mar 2008; 92: 359 - 380.
- Fetzner, K.R., 1992, The interpretation of principal strains from calcite twins in the Franklin Mountains, Texas: The University of Texas at El Paso, Master's thesis, 51 p.
- Figures, S.H., 1987, Geology and geophysics of the Pipeline Complex, northern Franklins Mountains, El Paso, Texas. Dissertation: The University of Texas at El Paso, El Paso, Texas. 331 p.
- Flawn, P.T., 1961, The subsurface Ouachita structural belt in Texas and southeast Oklahoma (*in* The Ouachita system) *Publication - University of Texas, Bureau of Economic Geology*, pp. 65-81.
- Flower, R.H., 1969, Early Paleozoic of New Mexico and the El Paso region Guidebook, *in* El Paso Geological Society, Annual Field Trip No. 3, p. 31-101.
- Ford, D.C. and Williams, P.W., 2008, Karst hydrology and geomorphology, Wiley and Sons Publishing, West Sussex, United Kingdom 562 pp.
- Gary, M.O., Fairfield, N., Stone, W.C., Wettergreen, D., Kantor, G., Sharp, J.M., Jr., 2008, 3-D mapping and characterization of Sistema Zacaton from DEPTHX (Deep Phreatic Thermal Explorer), Proceedings of the 11th Multidisciplinary Conference on Sinkholes and the Engineering and Environmental Impacts of Karst, American Society of Civil Engineers Geotechnical Special Publication no. 183, pp. 202-212.
- Ginsburg, R.N., 1982, Actualistic depositional models for the Great American Bank (Cambro-Ordovician) (abs.), *in* Eleventh International Congress on Sedimentology, Abstracts of Papers, p. 114.
- Goldhammer, R.K., Oswald, E.J., and Dunn, P.A., 1991, The hierarchy of stratigraphic forcing: an example from Middle Pennsylvanian shelf carbonates of the Paradox Basin, *in* Franseen, E. K., Watney, W. L., Kendall, G.C.St.C., and Ross, W., eds., *Sedimentary Modeling: Computer Simulations and Methods for Improved Parameter Definition*: Kansas Geological Survey Bulletin 233, p. 361-414.
- Goldhammer, R.K., Lehmann, P.J., and Dunn, P.A., 1993, The origin of high-frequency platform carbonate cycles and third-order sequences (Lower Ordovician El Paso Gp, West Texas); constraints from outcrop data and stratigraphic modeling: *Journal of Sedimentary Research*, v. 63, p. 318-359.
- Gradstein, F.M., Ogg, J.G., and Smith, A.G., 2004, *A Geologic Time Scale*: Cambridge University Press, 585 p.
- Gross, Markus, 2006, Graphically Speaking, *IEEE Computer Graphics and Applications*, September/October 2006, p. 96-99.
- Hammes, U., Kerans, C., and Lucia, F.J., 1996, Development of a multiphase cave system; Ellenburger Formation, Lower Ordovician, West Texas (*in* Permian Basin oil and gas fields; keys to success that unlock future reserves, Martin,) *Publication - West Texas Geological Society* (1996), 96-101 139-141.

- Harbour, R. L., 1972, Geology of the Northern Franklin Mountains, Texas and New Mexico: U.S. Geological Survey Bulletin 1298, 129 p.
- Hardage, B. A., D. L. Carr, D. E. Lancaster, J. L. Simmons, R. Y. Elphick, V. M. Pendleton, and R. A. Johns, 1996, 3-D seismic evidence of the effects of carbonate karst collapse on overlying clastic stratigraphy and reservoir compartmentalization: *Geophysics*, v. 61, p. 1336– 1350.
- Harland, W.B., Armstrong, R.L., Cox, A.V., Craig, L.E., Smith, A.G., and Smith, D.G., 1989, *A Geologic Time Scale*: New York, Cambridge University Press, 128 p.
- Harper, D.T., 2006, The Ordovician biodiversification; setting an agenda for marine life, *in* *Exploring life and environments through time; celebrating the 40th anniversary of Paleo-3: Palaeogeography, Palaeoclimatology, Palaeoecology*, v. 232, no. 2-4, p. 148-166.
- Haubold, H. 1999, Alteration of magnetic properties of Palaeozoic platform carbonate rocks during burial diagenesis (Lower Ordovician sequence, Texas, USA), *in* Tarling, D.H., and Turner, P., eds., *Palaeomagnetism and diagenesis in sediments*: Geological Society, London, Special Publications, 151, p. 181-203.
- Hayes, P.T., 1975, Cambrian and Ordovician rocks of southern Arizona and New Mexico and westernmost Texas: U.S. Geological Survey Professional Paper P 0873, 98 p.
- Hendricks, L., 1952, Correlation between surface and subsurface sections of the Ellenburger group of Texas: University of Texas, Austin, Report of Investigations No. 11, 44 p.
- Herald, F.A., 1957, Occurrence of oil and gas in West Texas, Texas University Publication, Includes papers by various authors not cited individually, August 1957, no. 5716, 443 pp.
- Hine, A.C., Locker, S.D., Tedesco, L.P., Mullins, H.T., Hallock, P., Belknap, D.F., Gonzales, J.L., Neumann, A.C., and Snyder, S.W., Megabreccia shedding from modern, low-relief carbonate platforms, Nicaraguan Rise, *Geological Society of America Bulletin*, Aug 1992; 104: 928 - 943.
- Howe, H.J., 1959, Montoya group stratigraphy (Ordovician) of Trans-Pecos Texas [-New Mexico]: *AAPG Bulletin*, v. 43, p. 2285-2332.
- Janson, X., Kerans, C., Bellian, J.A., and Fitchen, W., 2007, Three-dimensional geological and synthetic seismic model of Early Permian redeposited basinal carbonate deposits, Victorio Canyon, west Texas, *AAPG Bulletin*, v. 91, no. 10, p. 1405-1436.
- Kadhi, A, 1970, Structure of the Tom Mays park area, Franklin mountains, El Paso County, Texas, University of Texas at El Paso, El Paso, TX, United States, Master's thesis.
- Karlstrom, K.E. and Daniel, C.G., 1993, Restoration of Laramide right-lateral strike slip in northern New Mexico by using Proterozoic piercing points; tectonic implications from the Proterozoic to the Cenozoic, *Geology (Boulder)*, vol. 21, no. 12, pp. 1139-1142.
- Kelley, V.C., and Silver, C., 1952, Geology of the Caballo Mountains: New Mexico Bureau of Mines and Mineral Resources Memoir 49, University of New Mexico Publications in Geology, 4, 286 p.

- Kerans, C., 1988, Karst-controlled reservoir heterogeneity in Ellenburger Group carbonates of West Texas: AAPG Bulletin, v. 72, no. 10, p. 1160-1183.
- Kerans, C., 1989, Karst-controlled reservoir heterogeneity and an example from the Ellenburger Group (Lower Ordovician) of West Texas: The University of Texas at Austin, Bureau of Economic Geology Report of Investigations No.186, 40 p.
- Kerans, C., and Lucia, F.J., 1989, Recognition of second, third, and fourth/fifth order scales of cyclicity in the El Paso Group and their relation to genesis and architecture of Ellenburger reservoirs, in Cunningham, B. K., and Cromwell, D. W., eds., The lower Paleozoic of West Texas and Southern New Mexico modern exploration concepts: Society of Economic Paleontologists and Mineralogists, Permian Basin Section, Publication 89-31, p. 105-110.
- Kluth C.F. and Cooney, P.J., 1981, Plate tectonics of the Ancestral Rocky Mountains, *Geology* v.89, p.10-15, January, 1981.
- Kottlowski, F.E., 1963, Paleozoic and Mesozoic strata of south-western and south-central New Mexico: New Mexico Bureau of Mines and Mineral Resources Bulletin 79. 100p.
- Kottlowski, F.E. and Pray, L.C., 1967, Silurian outcrops of southcentral and southwestern New Mexico in Symposium--Silurian-Devonian rocks of Oklahoma and environs, *Tulsa Geological Society Digest* (1967), v. 35 p. 209-230.
- Kottlowski, F.E., LeMone, D.V., and Foster, R.W., 1969, Early Ordovician highlands of Precambrian rocks and their associated facies *Guidebook - El Paso Geological Society, Annual Field Trip*, (3), p.134-142.
- Kottlowski, F.E., LeMone, D.V., and Foster, R.W., 1973, Remnant mountains in Early Ordovician seas of the El Paso region, Texas and New Mexico: *Geology*, v. 1, p. 137-140.
- Kupecz, J.A., and Land, L.S., 1991, Late-stage dolomitization of the Lower Ordovician Ellenburger Group, west Texas, *Journal of Sedimentary Research*, v. 61: p. 551-574.
- Kyle, J.R., 1976, Brecciation, alteration and mineralization in the Central Tennessee zinc district: *Economic Geology*, v. 71, p. 892-903.
- Labourdette, R., Lascu, I., Mylroie, J., and Roth, M., 2007, Process-Like Modeling of Flank-Margin Caves: From Genesis to Burial Evolution, *Journal of Sedimentary Research*, Nov; v. 77: p. 965 - 979.
- Lee, K., Tomasso, M., Ambrose, W., and Bouroullec, R., 2007, Integration of GPR with stratigraphic and lidar data to investigate behind-th-outcrop 3D geometry of a tidal channel reservoir analog, upper Ferron Sandstone, Utah; *Leading Edge*, August 2007 v. 26, p. 994-998.
- LeMone, D.V., 1968. The Canadian (Lower Ordovician) El Paso Group of the Southern Franklin Mountains, El Paso County, Texas: *West Texas Geological Society Guidebook* 68-55, p. 76-81.

- LeMone, D.V., 1969, The Cambrian-Ordovician rocks of West Texas and southern New Mexico, *in* Border Stratigraphy Symposium: New Mexico Bureau of Mines and Mineral Resources Circular104, p. 17-25.
- LeMone, D.V., 1988, Sequence stratigraphy of the Tobosa Basin-related Paleozoic sediments of the Franklin Mountains, El Paso County, Texas and Dona Ana County, New Mexico, *in* Franklin Mountains, Tobosa Basin; related sequences: American Association of Petroleum Geologists, Southwest Section, El Paso, p. 28-58.
- LeMone, D.V., 1989, Sequence stratigraphy of the Tabosa Basin-related Paleozoic sediments of the Franklin Mountains, El Paso County, Texas and Dona Ana County, New Mexico *in* The lower Paleozoic of West Texas and southern New Mexico; modern exploration concepts, *Publication - Society of Economic Paleontologists and Mineralogists, Permian Basin Chapter* (1989), n.89-31 p. 71-83.
- Loper, D.E., Werner, C.L., Chicken, E., Davies, G., and Kincaid, T., 2005, Coastal Carbonate Aquifer Sensitivity to Tides, American Geophysical Union EOS, n. 39, Sept. 27th, 2005, p. 353-328.
- Loucks, R.G., and Hanford, R., 1992, Paleocave-reservoir networks; their origin and recognition, *The Bulletin of the Houston Geological Society*, December 1992, v. 35 (4): p. 24-25.
- Loucks, R.G., and Anderson, J.H., 1984, Depositional facies and porosity development in Lower Ordovician Ellenburger Dolomite, Puckett Field, Pecos County, Texas, *in* Carbonate reservoir rocks: SEPM Core Workshop, v. 1, p. 1-31.
- Loucks, R.G., 1999, Paleocave carbonate reservoirs; origins, burial-depth modifications, spatial complexity, and reservoir implications: AAPG Bulletin, v. 83, p. 1795-1834.
- Loucks, R.G., Mescher, P.K., and McMechan, G.A., 2004, Three-dimensional architecture of a coalesced, collapsed-paleocave system in the Lower Ordovician Ellenburger Group, central Texas: AAPG Bulletin, v. 88, p. 545-564.
- Lovejoy, E.P., 1968, Conjectural Dating, by Means of Gravity Slide Masses, of Cenozoic Tectonics of the southern Franklin Mountains, *in* El Paso Geological Society Annual Field Trip Guidebook 2, p. 32-33.
- Lovejoy, E.P. 1969, The Infra-Paleozoic contact, southern Franklin Mountains, Guidebook - El Paso Geological Society, Annual Field Trip 3: p. 104-109.
- Lucia, F.J., 1968, Sedimentation and palaeogeography of the El Paso Group: West Texas Geological Society Guidebook 68-55, p. 61-75.
- Lucia, F.J., 1971, Lower Paleozoic history of the western Diablo Platform, west Texas and south central New Mexico; *in* Robledo Mountains, New Mexico, Franklin Mountains, Texas; 1971 field conference guidebook Soc. Econ. Paleontol. Mineral.; Permian Basin Section, , (1971) p. 174-214.
- Lucia, F.J., 1988, Lower Paleozoic collapse brecciation and dolomitization, Franklin Mountains, Texas (*in* Franklin Mountains, Tobosa Basin; related sequences, Keller,) American Association of Petroleum Geologists, Southwest Section, El Paso, TX, p. 75-113.

- Lucia, F.J., 1995, Lower Palaeozoic cavern development, collapse, and dolomitization, Franklin Mountains, E1 Paso, Texas, *in*: Budd, D.A, Saller, A.H., and Harris, P.M., eds., Unconformity and porosity in carbonate strata: American Association of Petroleum Geologists Memoir 63, p. 137-152.
- Lucia, F.J., 2007, Carbonate Reservoir Characterization, second ed., Springer, New York, 233 figs., 336 p.
- Lucia, F.J., 2010, Top Sauk Paleokarst, a review, *in* The Cambro-Ordovician Sauk Sequence of Laurentia, The Geology and Petroleum Potential of the Great American Carbonate Bank, SEPM James Lee Wilson Memorial Special Volume, *in press*.
- Markello, J.R., Koepnick, R.B, Waite, L.E, and Collins, J.F., 2006, The carbonate analogs through time (CATT) hypothesis and the global atlas of carbonate fields—A systematic and predictive look at Phanerozoic carbonate systems, *in* Lukasik, J., and Simo, T. eds., Controls on carbonate platform and reef development: SEPM Special Publication 89,
- McDonnell, A., Loucks, R.G., and Dooley, T., 2007, Quantifying the origin and geometry of circular sag structures in northern Fort Worth Basin, Texas: Paleocave collapse, pull-apart fault systems, or hydrothermal alteration? AAPG Bulletin, Sep 2007; v. 91: p. 1295 - 1318.
- Montañez, I.P., and Read, J.F., 1992, Fluid-rock interaction history during stabilization of early dolomites, Upper Knox Group (Lower Ordovician), U.S. Appalachians: Journal of Sedimentary Petrology, v. 62, no. 5, p. 753-778.
- Montañez, I.P., and Osleger, D.A., 1993, Parasequence stacking patterns, third-order accommodation events, and sequence stratigraphy of Middle to Upper Cambrian platform carbonates, Bonanza King Formation, southern Great Basin, *in* Carbonate sequence stratigraphy; recent developments and applications: AAPG Memoir 57, p. 305-326.
- Mound, M.C., 1968, Conodonts and biostratigraphy of the lower Arbuckle Group (Ordovician), Arbuckle Mountains, Oklahoma: Micropaleontology, v. 14, no. 4, p. 292-334.
- Muehlberger, W.R., and Dickerson, P.W., 1989, A tectonic history of Trans-Pecos Texas, *in* Sedimentation and tectonics of western North America; Volume 3, Structure and stratigraphy of Trans-Pecos Texas, *in* Field trips for the 28th International Geological Congress: American Geophysical Union, p. 35-54.
- Murphy, D., 2005, www.devoniantimes.org; last updated July 9, 2005.
- Murphy, P.J., Parr, A.A., Strange, K., Hunter, G., Allshorn, S., Halliwell, R.A., Helm, J., and Westerman, A.R., 2005, Investigating the nature and origins of Gaping Gill Main Chamber, North Yorkshire, UK, using ground penetrating radar and lidar, *Cave and Karst Science*, 32(1):25-38.
- Mussman, W.J., Montanez, I.P., and Read, J.F., 1988, Ordovician Knox paleokarst unconformity, Appalachians *in*: Paleokarst, Springer-Verlag, New York, pp. 211-228.
- Nelson, L.A., 1940, Paleozoic stratigraphy of the Franklin Mountains, west Texas, Bulletin of the American Association of Petroleum Geologists, vol. 24,no. 1, pp. 157-172.

- Nydegger, G.L., 1982, The Las Vegas-El Paso Gap; a review of the southern part of the Cordilleran overthrust belt, *in* Geologic studies of the Cordilleran thrust belt, Powers, Rocky Mt. Assoc. Geol., Denver, CO, United States (1982) 391-407
- Olariu, M.I., Ferguson, J.F., Aiken, C.V., and Xu, X., 2008, Outcrop fracture characterization using terrestrial lidar scanners: Deep-water Jackfork sandstone at Big Rock Quarry, Arkansas, *Geosphere*; Feb. 2008; v. 4: 247-259.
- Palmer, A.N., 2007, Cave geology: Dayton, Ohio, Cave Books, 454 p.
- Palmer, A.N., and Palmer, M.V., 1989, Geologic history of the Black Hills caves, South Dakota (*in* Black Hills symposium, Pisarowicz,) *The NSS Bulletin* (December 1989), 51(2):72-99.
- Phelps, R.M., 2006, Sequence Stratigraphic and Architectural Characterization of a Permian Carbonate Ramp, upper San Andres Formation, Last Chance Canyon, New Mexico [unpublished M.S. thesis]: The University of Texas at Austin: Austin, 170 p.
- Phelps, R.M., and Kerans, C., 2007, Architectural Characterization and Three-Dimensional Modeling of a Carbonate Channel–Levee Complex: Permian San Andres Formation, Last Chance Canyon, New Mexico, U.S.A. *Journal of Sedimentary Research*, Nov 2007; 77: 939 - 964.
- Phelps, R.M., Kerans, C., Janson, X., Scott, S.Z., and Bellian, J.A., 2008, Three-dimensional modeling and sequence stratigraphy of a carbonate ramp-to-shelf transition, Permian Upper San Andres Formation, *Sedimentology*, v. 55: 1777-1813 doi: 10.1111/j.1365-3091.2008.00967.x.
- Playton, T.E., 2008, Characterization, variations, and controls of reef-rimmed carbonate foreslopes, University of Texas at Austin, Austin, TX, United States, Doctoral thesis, 302 pp.
- Pope, M.C., 2002, Cherty facies of the Late Ordovician Montoya Group, southern New Mexico and western Texas; implications for Laurentia oceanography and duration of Gondwana glaciation, *in* *Geology of White Sands: New Mexico Geological Society Guidebook 53*, p. 159-165.
- Pope, M.C., and Steffen, J.B., 2003, Widespread, prolonged late Middle to Late Ordovician upwelling in North America: a proxy record of glaciation? *Geology*, v. 31, p. 63-66.
- Pranter, M.J., Ellison, A.I., Cole, R.D., and Patterson, P.E., 2007, Analysis and modeling of intermediate-scale reservoir heterogeneity based on a fluvial point-bar outcrop analog, Williams Fork Formation, Piceance Basin, Colorado, *AAPG Bulletin*, v.91, p. 1025-1051.
- Pray, L.C., 1953, Upper Ordovician and Silurian stratigraphy of Sacramento Mountains, Otero County, New Mexico, *AAPG Bulletin*, Aug 1953; 37: 1894 - 1918.
- Pray, L.C., 1958 Fenestrate bryozoan core facies, Mississippian bioherms, southwestern United States, *Journal of Sedimentary Research*, Sep 1958; 28: 261 - 273.
- Read, J.F., 1982, Geometry, facies, and development of Middle Ordovician carbonate buildups, Virginia Appalachians: *AAPG Bulletin*, v. 66, p. 189-209.

- Repetski, J.E., 1982, Conodonts from El Paso Group (Lower Ordovician) of western-most Texas and southern New Mexico: New Mexico Bureau of Mines and Mineral Resources, New Mexico Institute of Mining and Technology, Memoir 40, 121 p.
- Repetski, J.E., 1988, Ordovician conodonts from the Bliss Sandstone in its type area, west Texas: New Mexico Bureau of Mines and Mineral Resources Memoir 44, p.123-127.
- Richardson, G.B., 1904, Report of a reconnaissance in Trans-Pecos Texas north of the Texas and Pacific railway: University of Texas, Austin, Mineral Survey Bulletin 9, 119 p.
- Richardson, G.B., 1908, Paleozoic formations in Trans-Pecos Texas, *American Journal of Science* (June 1908), 25(150):474-484.
- Richardson, G.B., 1909, Description of the El Paso Quadrangle, Texas: U.S. Geological Survey, Geological Atlas Folio 166, 86 p.
- Rolevatn, A., Buckley, S., Howell, J.A., and Fossen, H., 2009, Overlapping faults and their effect on fluid flow in different reservoir types: A LIDAR-based outcrop modeling and flow simulation study; AAPG Bulletin, v. 93: 407-427.
- Rose, Peter B., 1974, Edwards Group, surface and subsurface, central Texas, The Bulletin of the Houston Geological Society, September, vol. 17, no.1. p.3.
- Ross, C.A., and Ross, J.R.P., 1996, Silurian sea-level fluctuations (*in* Paleozoic sequence stratigraphy; views from the North American Craton) *Special Paper - Geological Society of America* (1996), 306 187-192.
- Ruiz, A., 2004, An integrated analysis of the Laramide orogeny, and the effects of the Rio Grande rift in southern New Mexico and west Texas [Master's Thesis]: University of Texas at El Paso.
- Ruppel, S.C., James, E.W., Barrick, J.E., Nowlan, G.S., and Uyeno, T.T., 1996, High-resolution $^{87}\text{Sr}/^{86}\text{Sr}$ chemostratigraphy of the Silurian: implication for event correlation and strontium flux: *Geology*, v. 24, p. 831-834.
- Sando, W.J., 1964, Stratigraphic importance of corals in the Redwall Limestone, northern Arizona, *U. S. Geological Survey Professional Paper* (1964), C39-C42.
- Scharman, M.R., 2006, Structural constraints on the Laramide shortening and Rio Grande Rift extension in the central Franklin Mountains, El Paso County, Texas: The University of Texas at El Paso, Master's thesis, 83 p.
- Schindel G., and Cobb, A.B., 2008, The Devils Sinkhole lidar study, Rocksprings, Edwards County, Texas, *Bulletin of the South Texas Geological Society* (April 2008), 48(8):47-54.
- Scotese, C.R., 2002, PALEOMAP website, 2002, <http://www.scotese.com>.
- Scott, S.Z., 2007, Application of ground-based LIDAR to constrain topographic strike-variability and facies proportions of progradational San Andres Formation clinoforms, Last Chance Canyon, NM, University of Texas at Austin, Austin, Tx, Master's Thesis (May 2007) 110 pp.

- Seager, W.R., and Mack, G.H., 2003, Geology of the Caballo Mountains, New Mexico: New Mexico Bureau of Mines and Mineral Resources, Memoir 49, 136 p.
- Sheehan, P.M., and Harris, M.T., 1997, Upper Ordovician-Silurian macrofossil biostratigraphy of the eastern Great Basin, Utah and Nevada, *in* Early Paleozoic biochronology of the Great Basin, Western United States: U.S. Geological Survey Professional Paper 1579-C, p. 89-115.
- Sibson, R.H., 1977, Fault rocks and fault mechanisms, *Journal of the Geological Society*, Mar 1977; 133: 191 - 213.
- Sloss, L.L., 1963, Sequences in the cratonic interior of North America: *Geological Society of America Bulletin*, v.74, p. 93-114.
- Sloss, L.L., 1988, Forty years of sequence stratigraphy: *Geological Society of America Bulletin*, v. 100, p. 1661-1665.
- Stacy, J.K., Julian, F.E., and LeMone, D.V., 1992, Structural and tectonic development of McKelligon Canyon, southern Franklin Mountains, El Paso County, Texas, *in* Paleokarst, karst-related diagenesis, and reservoir development; examples from Ordovician-Devonian age strata of West Texas and the Mid-Continent: *Society of Economic Paleontologists and Mineralogists, Permian Basin Chapter, Publication 92-33*, p. 195-201.
- Stepanek, B. E., 1984, Diagenesis of Paleokarst Collapse Breccias--The Ordovician El Paso and Montoya Groups, West Texas, The University of Michigan, Master's Thesis, 13 figs, 33 p.
- Stepanek, B. E., 1988, Dolomitization of Paleokarst Collapse Breccias-The Ordovician El Paso Group, Franklin Mountains, West Texas, *in* Franklin Mountains Tobosa Basin Related Sequences, El Paso Geological Society and The Southwest Section of the AAPG, February pp. 114-141.
- Suhm, R.W. and Ethington, R.L., 1975, Stratigraphy and Conodonts of Simpson Group (Middle Ordovician), Beach and Baylor Mountains, West Texas, *The American Association of Petroleum Geologists Bulletin*, v. 59, n. 7 p. 1126-1135.
- Tarasewicz, J.P.T., Woodcock, N.H., and Dickson, A.D., 2005, Carbonate dilation breccias: examples from the damage zone to the Dent Fault, northwest England *Geological Society of America Bulletin*, May 2005; 117: 736 - 745.
- Taylor, J.F., and Repetski, J.E., 1995, High-resolution trilobite and conodont biostratigraphy across the Cambrian-Ordovician boundary in southcentral New Mexico, *in* Cooper, J.D., Droser, M.L., and Finney, S.C., eds., *Ordovician Odyssey: Short papers for the Seventh International Symposium on the Ordovician System: Society for Sedimentary Geology (SEPM), Pacific Section, Book 77*, p. 133-136.
- Taylor, M.E., 1997, Early Paleozoic Biochronology of the Great Basin, Western United States, U.S. Geological Survey Professional Paper 1579, 115 p.
- Taylor, J.F., Myrow, P.M., Ripperdan, R.L., Loch, J.D., and Ethington, R.L., 2004, Paleooceanographic events and faunal crises recorded in the Upper Cambrian and Lower

Ordovician of west Texas and southern New Mexico: Geological Society of America Field Guide 5, fld005-11, 18 p.

- Tillotson, B. A., 2003, Bed and facies scale selectivity during late-stage dolomitization: Lower Ordovician El Paso Group, Franklin Mountains, West Texas: The University of Texas at Austin, Master's thesis 110 pp.
- Tinker, S.W., Ehrets, J.R., and Brondos, M.D., 1995, Multiple karst events related to stratigraphic cyclicity; San Andres Formation, Yates Field, West Texas, *in* Unconformities and porosity in carbonate strata, *AAPG Memoir* (1995), 63 213-237
- Troutman, T.J., 2004, Reservoir characterization, paleogeomorphology, and genesis of the Mississippian Redwall Limestone paleokarst, Hualapai Indian Reservation, Grand Canyon area, Arizona, U.S.A., University of Texas at Austin, Austin, TX, United States, Master's thesis (2004) 221 pp.
- Vallet, J., 2008, High Precision LiDAR Mapping for Complex Mountain Topography, proceedings of the 6th Annual ICA Mountain Cartography Workshop; Mountain Mapping and Visualization, Lenk, Switzerland, February 2008 pp. 249-254.
- Verwer, K., Kenter, J. A. M., Maathuis, B. and Della Porta, G., 2004, Stratal patterns and lithofacies of an intact seismic-scale Carboniferous carbonate platform (Asturias, northwestern Spain): A virtual outcrop model, *in* A. Curtis and R. Wood, eds., Geological prior information: Informing science and engineering: Geological Society (London) Special Publication 239, p. 29– 41.
- Verwer, K., Merino-Tomé, O., Kenter, J.A.M., and Della Porta, G., 2009, Evolution of a High-Relief Carbonate Platform Slope Using 3D Digital Outcrop Models: Lower Jurassic Djebel Bou Dahar, High Atlas, Morocco, *Journal of Sedimentary Research*, Jun 2009; 79: 416 - 439.
- Vucini, E., Moller, T., Groller, M.E., 2008, Efficient reconstruction from non-uniform point sets, *Visual Computing*, v. 24, 555-563, DOI 10.1007/s00371-008-0236-x.
- Wawrzyniec, T.F., McFadden, L.D., Ellwein, A., Meyer, G., Scuderi, L. McAuliffe, J., and Fawcett, P., Chronotopographic analysis directly from point-cloud data: A method for detecting small, seasonal hillslope change, Black Mesa Escarpment, NE, Arizona, *Geosphere*, Dec 2007; 3: 550-567.
- Webby, B.D., Paris, F., Droser, M.L., and Percival, I.G., 2004, The great Ordovician biodiversification event: Columbia University Press, 484 p.
- Webster, R.E., 1980, Structural Analysis of Devils River Uplift-Southern Val Verde Basin, Southwest Texas, *AAPG Bulletin* v. 64 no. 2, pp. 221-241.
- Wilson, J.L., 1970, Upper Paleozoic history of the western Diablo Platform, West Texas and south-central New Mexico *in* The geologic framework of the Chihuahua tectonic belt; a symposium in honor of Ronald K. de Ford), West Texas Geological Society, Midland, TX, United States (1970) 24-26.
- Wilson, J. L., Medlock, P., et al., 1993, Paleokarst within the Knox Group of Alabama, east side of the Black Warrior Basin: Paleokarst Related Hydrocarbon Reservoirs: v. 18, p. 245-274.

- Woodcock N.H. and Shubert, C., 1994, Continental strike-slip tectonics, *in* Continental deformation, Hancock, Pergamon Press, Tarrytown, NY, (1994) 251-263,
- Woodcock, N.H, Omma, J.E., and Dickson, J.A.D., 2006, Chaotic breccia along the Dent Fault, NW England: implosion or collapse of a fault void? *Journal of the Geological Society*, May 2006; 163: 431 - 446.
- Woodcock, N.H., Sayers, N.J., and Dickson, J.A.D., 2008, Fluid flow history from damage zone cements near the Dent and Rawthey faults, NW England, *Journal of the Geological Society*, Jul 2008; 165: 829 - 837.
- Woodcock, N.H. and Mort, K., 2008, Classification of fault breccias and related fault rocks *Geological Magazine*, May 2008; 145: 435 - 440.
- Wu, Kaiwen, 2002, The structural geology and tectonics of the southern Franklin Mountains in El Paso County: The University of Texas at El Paso, Master's thesis, 67 p.
- Xu, X., Aiken, C. L., Bhattacharya, J. P., Corbeanu, R.M., Nielsen, K. C., McMechan, G. A., and Abdelsalam, M. G., 2000, Creating virtual 3-D outcrop: *The Leading Edge*, v.19, no. 2, p. 197-202.
- Xu, X., 2000, Three-dimensional virtual geology; photorealistic outcrops, and their acquisition, visualization and analysis University of Texas at Dallas, Richardson, TX, United States, Doctoral thesis (2000) 170 pp.
- Xu, X., Aiken, C. L., and Nielsen, K. C., 1999, Real time and the virtual outcrop improve geological field mapping: *Eos, Transactions, American Geophysical Union*, v. 80, no. 29, p. 317-322.
- Yapp, C.J. and Poths, H., 1992, Ancient atmospheric CO₂ pressures inferred from natural goethites *Nature (London)* (January 1992), 355(6358):342-344.
- Ye, H., Royden, L., Burchfiel, C., and Schuepbach, M., 1996, Late Paleozoic deformation of interior North America; the greater ancestral Rocky Mountains *AAPG Bulletin*, Sep 1996; 80: 1397 - 1432.
- Yechieli, Y., Abelson, M., Wachs, D., Shtivelman, V. Crouvi, O., and Baer, G., 2003, Formation of sinkholes along the shore of the Dead Sea; preliminary investigation (*in* Sinkholes and the engineering and environmental impacts of karst; proceedings, Beck,) *Geotechnical Special Publication* (2003), 122 184-192.
- Zahm, C., Zahm, L., and Bellian, J.A., 2009, Integrated Fracture Prediction Using Sequence Stratigraphy within a Carbonate Fault Damage Zone, Texas, USA, *Journal of Structural Geology*, in press.

Vita

Jerome A. Bellian was born in Lakewood, Ohio, on December 13, 1971, the son of Joseph G. and Joan C. Bellian. He is a graduate of Walsh Jesuit High School in Stow, Ohio, and attended Miami University in Oxford, Ohio for both his Bachelor's and Master's degrees (1995 and 1998, respectively). After graduation Jerome took a position with Exxon Production Research Company in Houston, Texas, where he worked until October 2000, when he joined the Bureau of Economic Geology in Austin, Texas. Jerome began his Ph.D. studies at The University of Texas at Austin under Dr. Charles Kerans in 2004 and completed his studies while working full time as a researcher at the Bureau of Economic Geology. Jerome is currently employed by the Chevron Energy Technology Company in San Ramon, California.

Permanent Address: 810 El Quanito Drive, Danville, CA 94526

Dissertation was typed by the author.

Plates:

NOTE:

The plates included in this section require a 36 inch (91.5 cm) wide plotter with roll-feed to print at full scale.

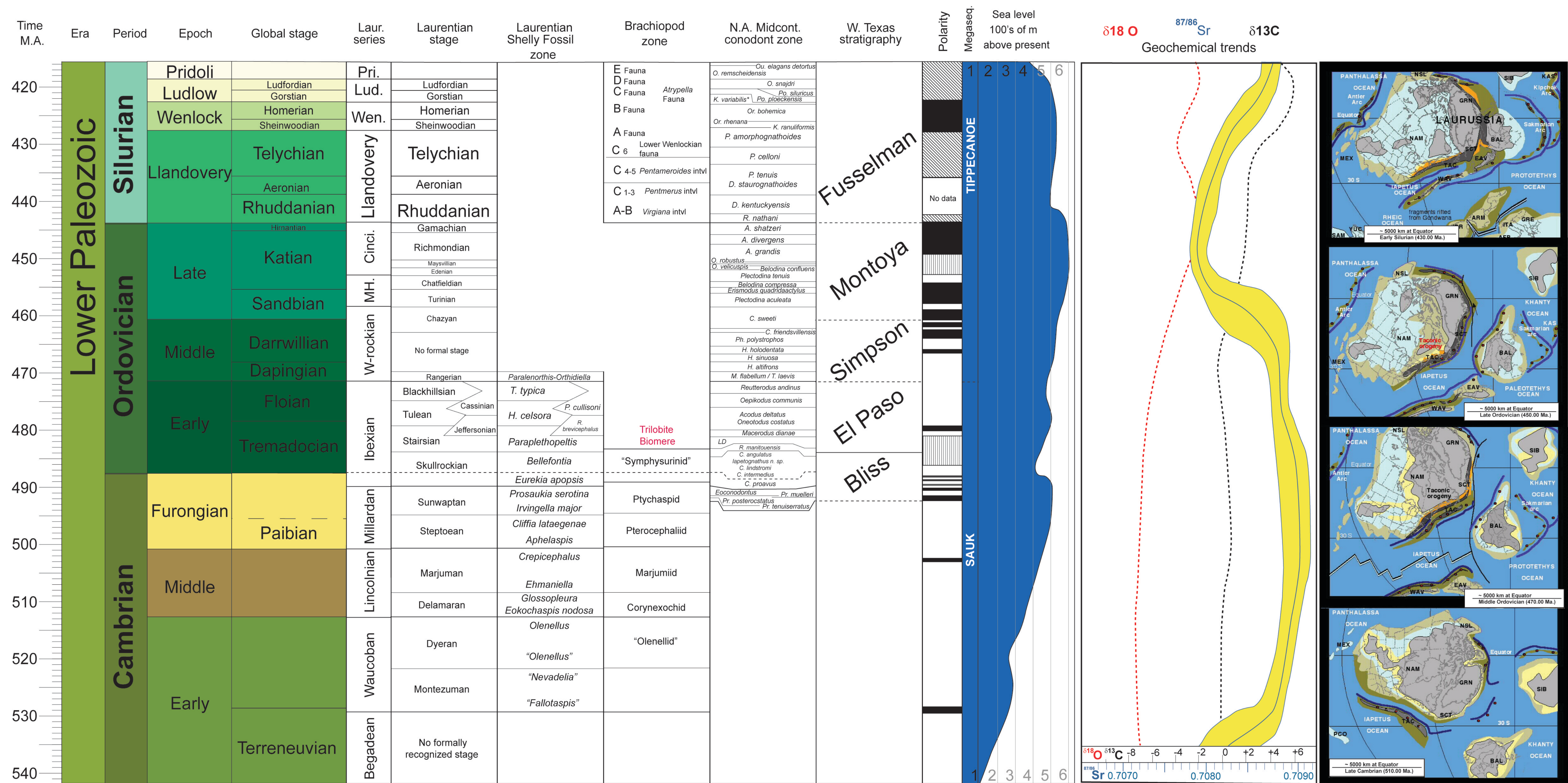


Plate I: Summary of most recent geological time scale, era, period, epoch, global stages, polarity, biomere, and sea level curve (Gradstein et al. 2004) with Laurentian Series and Stage (this volume). Laurentian stage abbreviations are: Pri. = Pridolian, Lud. = Ludlowian, Wen. = Wenlockian, Cinc. = Cincinnati, MH. = Mowhawkian, W-rockian = Whiterockian. Laurentian Shelly Fossil Zone (this volume) abbreviations: T. = *Tripodus*, P.= *Petigurus*, R. = *Ranasasus*, and H. = *Hintzeia*. Silurian conodont zones after Gradstein et al. (2004) and Ruppel et al. (1996) with the following abbreviations: Po. = *Polygnathoides*, K. = *Kockelella*, Or. = *Orzarkodina*, P. = *Pterospirifer*, D. = *Distomodus*, R. = *Rexroadus*. Ordovician conodont abbreviations A. = *Aphelognathus*, O. = *Oulodus*, C. = *Cahabagnathus*, Ph. = *Phragmodus*, H. = *Histiodelia*, M. = *Microzarkodina*, T. = *Tripodus*, LD. = "Low Diversity Interval," R. = *Rossodus*, C. = *Cordylodus*, and Pr = *Protoconodontus* (Taylor and Repetski 1995). Brachiopod Zones are after Sheehan and Harris (1997). Carbon, Oxygen, and Strontium curves after Markello et al. (2006). Paleogeographic reconstructions of Laurentia and surrounding land masses; proto-North America (NAM) with modern USA state boundaries outlined (after Blakey 2009). Details of relative positions of the Bliss through Fusselman here are found in figure 1.3.

